Dissipative Dynamics of Stars, Planets, and Black Holes

Thesis by
Linhao Ma

In Partial Fulfillment of the Requirements for the
Degree of
Doctor of Philosophy

CALIFORNIA INSTITUTE OF TECHNOLOGY
Pasadena, California

2024
Defended May 1, 2024

Linhao Ma
ORCID: 0000-0001-6117-5750

ACKNOWLEDGEMENTS

I am grateful to my thesis advisor, Professor Jim Fuller, for his patient guidance and mentorship over the years. I would also like to thank Professor Philip F. Hopkins for advising me on parts of the works in this dissertation. It is through the countless interactions and innovative discussions with them that I have been able to complete this thesis and grow as a researcher.

I extend my thanks to my family and friends for their unwavering support over the past five years, especially during the pandemic. I am also grateful for the musical works of the greatest composers, particularly those by Richard Wagner, which have been my pillar of strength during challenging times.

The scientific context of this dissertation has greatly benefited from in-depth discussions with my colleagues. I would like to thank Evan Bauer, Corinne Charbonnel, Tassos Fragos, Claude-Andrè Faucher-Giguére, Ylva Götberg, Emily Hu, Luke Zoltan Kelley, Georges Meynet, Holly Preece, Richard Townsend, and many others for their valuable comments on the works presented here. I am also thankful to Selma de Mink and the Max Planck Institute for Astrophysics for organizing the 2023 Kavli Summer Program, which facilitated many of these discussions.

I am grateful to the members of my thesis defense committee: Professor Jim Fuller, Professor Philip F. Hopkins, Professor Andrew Howard, Professor E. Sterl Phinney, and Professor Charles Steidel, for their constructive feedback on this thesis. I also pay special tribute to the Caltech computer cluster "Wheeler," where many numerical calculations in this dissertation were performed. Wheeler was retired permanently on April 30, 2024, the day before I defended this thesis.

The works presented in this dissertation are supported by the following fellowships and grants: the Robert A. Millikan Graduate Fellowship, the Kavli Summer Program in Astrophysics Fellowship, the David and Barbara Groce Travel Fund, NSF 1715847, NSF 1911233, NSF CAREER Grant 1455342, NASA 80NSSC18K0562, NASA HST-AR-15800.001-A, JPL 1589742, and NASA 20-XRP20 2-0147.

ABSTRACT

In this dissertation, I present a series of theoretical works on two important dissipative mechanisms in the universe, namely dynamical friction and tidal dissipation. I discuss the physics of these processes, and investigate how they will affect the dynamical evolution of stars, planets, and black holes.

I develop a new sub-grid dynamical friction estimator based on the discrete nature of N-body simulations. This estimator avoids the ambiguously defined quantities in Chandrasekhar's dynamical friction formula. I test the estimator in the GIZMO code, and find that it agrees well with high-resolution simulations where dynamical friction is fully captured. The additional computational cost with this estimator is negligible, making it an efficient and implementable solution to sub-grid dynamical friction modeling.

I study the dynamics of massive black hole seeds in high-redshift galaxies. I analyze the direct N-body integration of seed black hole trajectories with high-resolution cosmological simulations, and calculate the dynamics of randomly generated test particles in post-processing with dynamical friction. I find that seed black holes less massive than $10^8\,M_\odot$ (i.e. all but the already-supermassive seeds) cannot efficiently sink to the galactic center in typical high-redshift galaxies. This finding provides new constraints on the formation models of super-massive black holes in the most distant galaxies.

I study the effects of tidal resonance locking for exoplanet systems, in which the planet locks into resonance with a tidally excited stellar gravity mode. I find that due to nonlinear mode damping, resonance locking in Sun-like stars likely only operates for low-mass planets ($M \lesssim 0.1\,M_{\rm J}$), but in stars with convective cores it can likely operate for all planetary masses. The orbital decay timescale with resonance locking is typically comparable to the star's main-sequence lifetime, corresponding to a wide range in effective stellar quality factor ($10^3 < Q' < 10^9$), depending on the planet's mass and orbital period. I make predictions for several individual systems and examine the orbital evolution resulting from both resonance locking and nonlinear wave dissipation.

I investigate the tidal spin-up of subdwarf B (sdB) star binaries. I directly calculate the tidal excitation of internal gravity waves in realistic sdB stellar models, and integrate the coupled spin–orbit evolution of sdB binaries. I find that for canonical

sdB ($M_{\rm sdB} = 0.47\,M_\odot$) binaries, the transitional orbital period below which they could reach tidal synchronization in the sdB lifetime is ~ 0.2 days, with weak dependence on the companion masses. This value is very similar to the tidal synchronization boundary evident from observations.

I investigate the scenario of tidal spin-up of Wolf–Rayet–black-hole binaries, which is a possible way to form the fast-rotating black holes observed from gravitational wave events. I directly calculate the tidal excitation of oscillation modes in Wolf–Rayet star models, determining the tidal spin-up rate, and integrating the coupled spin–orbit evolution for Wolf–Rayet–black-hole binaries. I find that for short-period orbits and massive Wolf–Rayet stars, the tidal interaction is mostly contributed by standing gravity modes, in contrast to Zahn's model of traveling waves which is frequently assumed in the literature. I show that tidal synchronization is rarely reached in Wolf–Rayet–black-hole binaries, and the resulting black hole spins have $a \lesssim 0.4$ for all but the shortest period ($P_{\rm orb} \lesssim 0.5\,{\rm d}$) binaries.

PUBLISHED CONTENT AND CONTRIBUTIONS

[1] Linhao Ma and Jim Fuller. "Tidal Spin-up of Black Hole Progenitor Stars". In: *The Astrophysical Journal* 952.1 (2023), p. 53. DOI: 10.3847/1538-4357/acdb74.
L.M. carried out the research and participated in the writing of the manuscript.

[2] Linhao Ma et al. "A new discrete dynamical friction estimator based on N-body simulations". In: *Monthly Notices of the Royal Astronomical Society* 519.4 (2023), pp. 5543–5553. DOI: 10.1093/mnras/stad036.
L.M. carried out the research and participated in the writing of the manuscript.

[3] Linhao Ma and Jim Fuller. "Orbital Decay of Short-period Exoplanets via Tidal Resonance Locking". In: *The Astrophysical Journal* 918.1 (2021), p. 16. DOI: 10.3847/1538-4357/ac088e.
L.M. carried out the research and participated in the writing of the manuscript.

[4] Linhao Ma et al. "Seeds don't sink: even massive black hole 'seeds' cannot migrate to galaxy centres efficiently". In: *Monthly Notices of the Royal Astronomical Society* 508.2 (2021), pp. 1973–1985. DOI: 10.1093/mnras/stab2713.
L.M. carried out the research and participated in the writing of the manuscript.

TABLE OF CONTENTS

LIST OF ILLUSTRATIONS

LIST OF TABLES

Chapter 1

INTRODUCTION

Dissipative processes, which transform the kinetic energy into thermal energy, are ubiquitous in shaping the dynamical evolution of celestial bodies. They connect the large-scale gravitational forces to the small-scale micro-physics processes in stars and galaxies. Their outcomes leave unique fingerprints on astronomical observations, and understanding them is crucial to learn about the universe we live in.

This dissertation is a disquisition on dissipation. I will present a series of theoretical works concerning two major dissipative mechanisms related to astrophysical systems, namely dynamical friction, and tidal dissipation. I will discuss the physics of these processes, and show how they could affect the dynamics of stars, black holes and planets.

In the following sections of this introductory chapter, I will talk about the basic physics of dynamical friction and tidal dissipation, and their related contexts on black hole inspiral and stellar oscillations. I will then introduce the questions and existing efforts on these topics. Finally, I will give a detailed outline of the remaining chapters of this dissertation, which aim to address these questions.

1.1 Dynamical Friction and Black Hole Inspiral

Physics of Dynamical Friction

The physics of dynamical friction can be traced back to the pioneering work of S. Chandrasekhar in 1943 [6], and is illustrated in the left panel of Figure 1.1: when a massive object ("test particle") travels through a sea of lighter objects ("background particles"), it experiences numerous two-body scattering processes due to its gravitational interaction with these background particles. In each of these two-body scatterings, the test particle will exchange some of its momentum with the other background particle. As a result, the test particle gradually loses its momentum as it travels, after undergoing many scatters. This is dynamically equivalent to an effective "friction force" acting on the test particle, and this process is hence called dynamical friction.

With this picture, we shall be able to derive the strength of dynamical friction

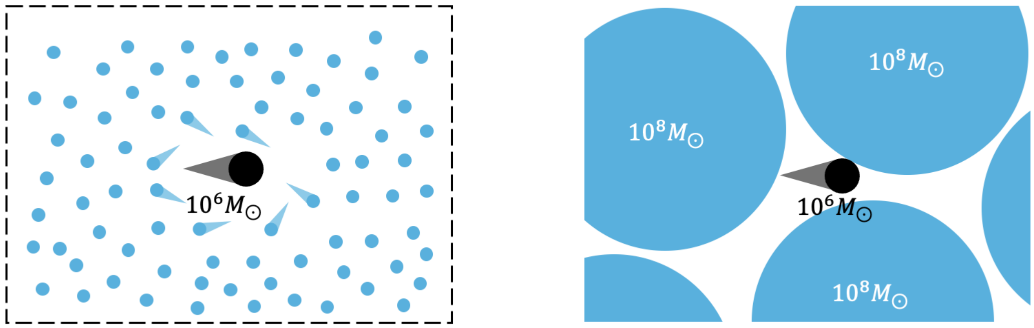

dynamical friction

in simulations, sub-grid DF needed

Figure 1.1: A sketch of dynamical friction explained. **Left**: When a massive particle (e.g., a black hole of 10^6 solar-masses) passes through a sea of lighter particles, it experiences numerous two-body scattering with these lighter particles. As its momentum is continuously transferred to the lighter particles, the massive particle effectively feels a "friction" and loses its momentum. This process is called dynamical friction. **Right**: In realistic N-body simulations, the light physical particles (e.g., stars and dark matter particles) are often not resolved, and are instead represented by massive simulation particles with some spatial distribution and extension. As two-body scattering with these simulation particles are different from that with physical particles, we need sub-grid treatment of dynamical friction to resolve the full dynamics of individual massive physical particles.

from first principles [6]. We first consider the two-body scattering between a test particle with mass M and velocity $\mathbf{v}_M$, and a background particle with mass m and velocity $\mathbf{v}_m$. For weak encounters ($m \ll M$), the trajectory of the test particle can be approximated as a straight line. If we coordinate this trajectory with a one-dimensional distance parameter s, then during the whole scattering process (from $s \to -\infty$ to $s \to \infty$), the change of the test particle velocity can be derived from the standard equations of gravitational two-body scattering. It is given by:

$$\Delta \mathbf{v}_\parallel = \frac{2\,m\,\mathbf{V}}{M+m}\left[1+\frac{b^2\,V^4}{G^2\,(M+m)^2}\right]^{-1}, \tag{1.1}$$

where $\mathbf{V} \equiv \mathbf{v}_m - \mathbf{v}_M$ is the velocity of m in the rest frame of M, G is the gravitational constant and b is the impact parameter of the scattering process.

We then assume the background particles form a homogeneous medium, such that their phase space distribution can be written as $\mathcal{N}(\mathbf{x}, \mathbf{v}_m) = n f(\mathbf{v}_m)$. In the rest frame of M, the background particle moves a distance of $V\mathrm{d}t$ in an infinitesimal period of time $\mathrm{d}t$. The infinitesimal phase space volume filled with the background particles that shift the velocity of the test particle by $\Delta\mathbf{v}_{||}$ is then given by $V\mathrm{d}t\mathrm{d}p\mathrm{d}q\mathrm{d}^3\mathbf{v}_m$, where p and q are the two spatial coordinates perpendicular to the direction of motion $\hat{\mathbf{V}}$. We can then sum up all background particles in the phase space volumes to get the collective change of $\mathbf{v}_M$:

$$\mathrm{d}(\mathbf{v}_M)_{\mathrm{all}} = \int \Delta\mathbf{v}_{||}\, nf(\mathbf{v}_m)V\mathrm{d}t\mathrm{d}p\mathrm{d}q\mathrm{d}^3\mathbf{v}_m\,. \tag{1.2}$$

From the above expression we can move the $\mathrm{d}t$ term to the left hand side, and this gives an effective acceleration of dynamical friction:

$$\mathbf{a}_{\mathrm{DF}} \equiv \frac{\mathrm{d}(\mathbf{v}_M)_{\mathrm{all}}}{\mathrm{d}t} = \int \Delta\mathbf{v}_{||}\, nf(\mathbf{v}_m)V\mathrm{d}p\mathrm{d}q\mathrm{d}^3\mathbf{v}_m\,. \tag{1.3}$$

For a homogeneous distribution of background particles, the integrand in Equation 1.3 only depends spatially on the impact parameter b. We hence express the (p, q) plane in polar coordinates (b, ϕ), which allows us to write $\mathrm{d}p\mathrm{d}q = b\mathrm{d}b\mathrm{d}\phi$. This allows us to re-express Equation 1.3 as:

$$\begin{aligned}
\mathbf{a}_{\mathrm{DF}} &= \int \Delta\mathbf{v}_{||}\, nf(\mathbf{v}_m)Vb\mathrm{d}b\mathrm{d}\phi\mathrm{d}^3\mathbf{v}_m \\
&= \int \frac{2\,m\,\mathbf{V}}{M+m}\left[1 + \frac{b^2\,V^4}{G^2\,(M+m)^2}\right]^{-1} nVb\mathrm{d}b\mathrm{d}\phi f(\mathbf{v}_m)\mathrm{d}^3\mathbf{v}_m \\
&\approx 2G^2M\rho\int \mathrm{d}b\mathrm{d}\phi \int \frac{\mathbf{V}}{V^3} f(\mathbf{v}_m)\mathrm{d}^3\mathbf{v}_m\,,
\end{aligned} \tag{1.4}$$

where we assumed $b^2V^4 \gg G^2(M+m)^2$ and $M \gg m$ for weak encounters, and substituted the background mass density $\rho = mn$. If the background particles are distributed over a range of impact parameters between b_{min} and b_{max}, the spatial part of the integral can be carried out, and we arrive at the final expression of dynamical friction:

$$\mathbf{a}_{\mathrm{DF}} = -4\pi G^2 M\rho\ln\Lambda \int \frac{\mathbf{v}_M - \mathbf{v}_m}{|\mathbf{v}_M - \mathbf{v}_m|^3} f(\mathbf{v}_m)\mathrm{d}^3\mathbf{v}_m\,, \tag{1.5}$$

where $\ln\Lambda \equiv \ln(b_{\mathrm{max}}/b_{\mathrm{min}})$ is called the Coulomb logarithm.

We can see from Equation 1.5 that when the test particle moves faster than the background particles ($v_M > v_m$), the dynamical friction acceleration is in the opposite direction of $\mathbf{v}_M$, which means the test particle feels an effective fiction. We also see that the strength of dynamical friction is proportional to the mass of the test particle M. This means dynamical friction is the most efficient for massive objects, e.g., massive black holes wandering around in galaxies.

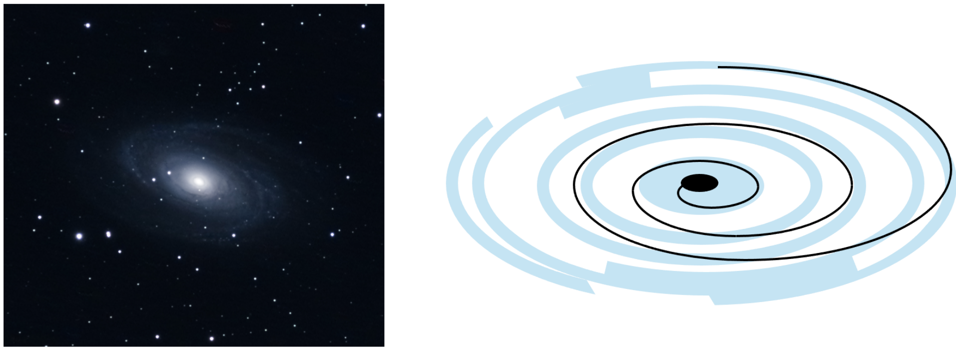

Figure 1.2: **Left**: Supermassive black holes are found in many galactic centers, e.g., the $7 \times 10^7\, M_\odot$ black hole in the center of Bode's galaxy (shown, captured with an 81mm apochromatic telescope at the Joshua Tree National Park in California). **Right**: Dynamical friction could cause the inspiral of massive black holes. As these black holes lose their orbital angular momentum due to dynamical friction, they will sink to the galactic center in a certain amount of time, which naturally explains the observations.

Black Hole Inspiral

Observations have confirmed the existence of super-massive black holes in many galactic centers, whose masses can be thousands to billions of times the mass of the sun [19, 20, 12]. These black holes are believed to have undergone a prior orbital inspiral phase, such that they end up sinking into the galactic center. During the inspiral, they loses their orbital angular momentum due to dynamical friction, as illustrated in Figure 1.2.

To estimate the timescale of the black hole inspiral phase, we make use of the dynamical friction formula (Equation 1.5). We assume the background particles in the galaxy (stars, gas, dark matter) can be described with a Maxwellian distribution of velocity, characterized by an isotropic Jeans dispersion σ. The dynamical friction to decelerate a black hole with mass M is then given by [4]:

$$\mathbf{a}_{\mathrm{DF}} = -\frac{4\pi G^2 M \rho \ln \Lambda}{v_M^2} \frac{\mathbf{v}_M}{v_M} \times \left[\mathrm{erf}\left(\frac{v_M}{\sqrt{2}\sigma} \right) - \sqrt{\frac{2}{\pi}} \frac{v_M}{\sigma} \exp\left(-\frac{v_M^2}{2\sigma^2} \right) \right]. \tag{1.6}$$

If the black hole is on a circular orbit inside the galaxy at a radius r_{orbit}, its orbital velocity is then given by $v_M = \sqrt{G m_{\mathrm{enclosed}} / r_{\mathrm{orbit}}}$, where $m_{\mathrm{enclosed}} = m(r < r_{\mathrm{orbit}})$ is the enclosed galactic mass inside the orbit. The dynamical friction inspiral timescale is then the time needed for the black hole to damp its velocity:

$$t_{\rm inspiral} = \frac{v_M}{|\mathbf{a}_{\rm DF}|} \,. \tag{1.7}$$

To estimate the numerical value, we note that the velocity dispersion for a typical high-redshift galaxy is $\sigma \simeq 200\,\mathrm{km/s}$. The observed flatness of the rotation curves further suggests an isothermal density profile of the galaxy with a constant circular velocity $v_M \sim \sigma$ [40]:

$$\rho(r) = \frac{v_M^2}{4\pi G R_{\rm orbit}^2} \,. \tag{1.8}$$

The value of the Coulomb logarithm depends on the spatial extension of the galaxy, which is ambiguously defined. Nevertheless, the order of the Coulomb logarithm is insensitive to the exact $b_{\rm max}$ selected due it logarithmic dependence on the impact parameter. We hence set $\ln\Lambda = 10$ in an ad hoc manner. With the above values, the inspiral timescale is given by:

$$t_{\rm inspiral} \simeq 0.92 \left(\frac{M}{10^8 M_\odot}\right)^{-1} \left(\frac{R_{\rm orbit}}{2\,\mathrm{kpc}}\right)^2 \mathrm{Gyr}\,, \tag{1.9}$$

which means a super-massive black hole of $10^8 M_\odot$ created near ($\lesssim 2\,\mathrm{kpc}$) the galactic center has a good chance to sink in 1 Gyr. This can explain their existence in low-redshift galactic centers we observe today.

1.2 Stellar Tides and Oscillations

The rise and fall of sea levels have been noticed by humans since ancient times, but it was only until 1687 when Sir Isaac Newton firstly gave a satisfactory physical explanation of tides [33]. The studies on stellar tides are even more recent, and their detailed modeling has not been established until the second half of the 20th century, partially due to the lack of knowledge for stellar structure and evolution. The tides on stars can be classified into equilibrium tides and dynamical tides, and they can both shape the dynamical evolution of the star and its companion which provides the tidal potential.

Equilibrium Tides

In the left panel of Figure 1.3, we show the classical picture of equilibrium stellar tides. The orbiting companion exerts a time-varying tidal potential on the star. As the fluid of the star responds to this tidal potential, the star has some hydrostatic deformation, and rises a tidal bulge. In the absence of dissipation in the tides, the

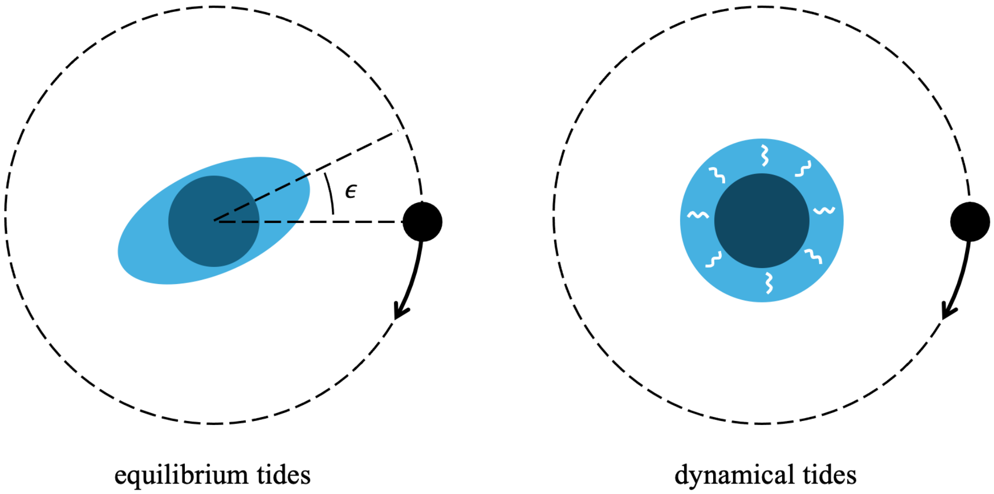

Figure 1.3: **Left**: The scenario of equilibrium tides explained. The orbiting companion object has a time-varying tidal potential on the star, and rises a tidal bulge that rotates with the orbit. The dissipation of this tidal bulge creates a phase-lag of ϵ after the orbit of the companion. **Right**: The scenario of dynamical tides explained. The same time-varying tidal potential excites the internal stellar oscillations in the star. Tidal dissipation is then caused by the damping of these oscillations.

tidal bulge would co-rotate with the companion's orbit. However, as the bulge has internal viscous dissipation, it never catches up with the orbit of the companion, and is instead left behind by a phase lag of ϵ.

For equilibrium tides, [21] defines the tidal quality factor Q as the ratio between the energy stored in tides E_0, and the dissipation of tidal energy in a complete orbital cycle:

$$\frac{1}{Q} \equiv \frac{1}{2\pi E_0} \oint \left(-\frac{\mathrm{d}E}{\mathrm{d}t} \right) \mathrm{d}t \,. \tag{1.10}$$

When ϵ is small, [26] shows that this tidal quality factor is related to the phase-lag ϵ by:

$$Q = \frac{1}{2\epsilon} \,. \tag{1.11}$$

Hence, the value of ϵ reflects the efficiency of the dissipative mechanisms, and larger ϵ (smaller Q) corresponds to more efficient tidal dissipation.

Dynamical Tides

Unlike equilibrium tides, dynamical stellar tides are not the hydrostatic deformation of stars under the tidal potential from their companions. Instead, they are internal stellar oscillations that are excited by the tidal potential, as shown in the right panel of Figure 1.3. For this reason, dynamical tide are also known as tidally excited oscillations (TEOs).

To understand the excitation mechanism of dynamical tides, we write down the equations of stellar oscillations under a tidal potential U. For a non-rotating, spherically symmetric star, this set of equations can be obtained with linear perturbation theory over the static equations of stellar structures [43]:

$$\begin{aligned}
\text{continuity equation}: &\quad \delta\rho + \nabla\cdot(\rho\boldsymbol{\xi}) = 0\,, &(1.12)\\
\text{energy equation}: &\quad \frac{\delta P + (\boldsymbol{\xi}\cdot\nabla)\,P}{P} = \Gamma_1\frac{\delta\rho + (\boldsymbol{\xi}\cdot\nabla)\,\rho}{\rho}\,, &(1.13)\\
\text{momentum equation}: &\quad \frac{\partial^2\boldsymbol{\xi}}{\partial t^2} = -\frac{\nabla\delta P}{\rho} + \frac{\nabla P}{\rho^2}\delta\rho - \nabla\delta\phi - \nabla U\,, &(1.14)\\
\text{Poisson's equation}: &\quad \nabla^2\delta\phi = 4\pi G\delta\rho\,, &(1.15)
\end{aligned}$$

where P, ρ, ϕ are the pressure, density, and self-gravity potential inside the star, and $\delta P, \delta\rho, \delta\phi$ are their Eulerian perturbation values. t is the time coordinate and $\boldsymbol{\xi}$ is the Lagrangian perturbed vector displacements of the fluid. $\Gamma_1 = (\partial\ln P/\partial\ln\rho)_{\text{adiabatic}}$ is the adiabatic index of the fluid, assuming an adiabatic energy equation.

The above equations can be combined to the following equation of the perturbation variable $\boldsymbol{\xi}$ [38]:

$$\frac{\partial^2\boldsymbol{\xi}}{\partial t^2} + C\cdot\boldsymbol{\xi} = -\nabla U\,, \tag{1.16}$$

where C is a linear operator that satisfies $C\cdot\boldsymbol{\xi} = \rho^{-1}[-\nabla(\Gamma_1 P\nabla\cdot\boldsymbol{\xi}) + (\nabla\cdot\boldsymbol{\xi})\nabla P - (\nabla\boldsymbol{\xi})\cdot(\nabla P) + \rho(\boldsymbol{\xi}\cdot\nabla)\nabla\phi + \rho\nabla\delta\phi]$. To solve this equation, we note that we can first solve the eigenvalue problems of the *free oscillation equation*:

$$\frac{\partial^2\boldsymbol{\xi}}{\partial t^2} + C\cdot\boldsymbol{\xi} = 0\,, \tag{1.17}$$

whose set of eigensolutions $\{\boldsymbol{\xi}_\alpha\}$ satisfies

$$C\cdot\boldsymbol{\xi}_\alpha = \omega_\alpha^2\boldsymbol{\xi}_\alpha\,. \tag{1.18}$$

Clearly, this set of solutions $\{\boldsymbol{\xi}_\alpha\}$ is the internal stellar oscillations without the excitation of the tidal potential. We define a inner product over the vector space spanned by $\{\boldsymbol{\xi}_\alpha\}$ as $\langle\boldsymbol{\xi}_\alpha|\boldsymbol{\xi}_\beta\rangle \equiv \int_{\text{star}}\boldsymbol{\xi}_\alpha^*\cdot\boldsymbol{\xi}_\beta\,\rho\mathrm{d}V$. We can show that C is a Hermitian operator with this inner product. This means $\{\boldsymbol{\xi}_\alpha\}$ satisfies the orthogonal relations:

$$\langle\boldsymbol{\xi}_\alpha|\boldsymbol{\xi}_\beta\rangle = \delta_{\alpha\beta}\,, \tag{1.19}$$

and they form a complete basis for all stellar oscillations. We can then expand the general solution to equation 1.16 as

$$\boldsymbol{\xi}(t) = \sum_{\alpha} a_{\alpha}(t)\boldsymbol{\xi}_{\alpha}\,, \tag{1.20}$$

where $a_{\alpha}(t)$ is the expansion coefficient that describes the amplitude of $\boldsymbol{\xi}_{\alpha}$ under tidal excitation. By substituting the above expansion into Equation 1.16, and taking the inner product of $\boldsymbol{\xi}_{\beta}$ with it, we can make use of the orthogonal relation to get:

$$\ddot{a}_{\alpha}(t) + \omega_{\alpha}^{2} a_{\alpha} = -\langle\boldsymbol{\xi}_{\alpha}|\nabla U\rangle\,. \tag{1.21}$$

We see that the equation for the expansion coefficients is a driven harmonic oscillator equation. The force term $-\langle\boldsymbol{\xi}_{\alpha}|\nabla U\rangle$ describes the coupling between the tidal force and the free oscillation $\boldsymbol{\xi}_{\alpha}$, and it produces the tidal forcing of the oscillation. Hence, in the picture of dynamical tides, it is the individual stellar oscillations that are excited by the tidal force from the companion, and the oscillations damp due to their own non-adiabatic dissipative mechanisms.

Stellar Oscillations

We now discuss the details of the free stellar oscillations that can be excited by the tidal force, i.e. the eigensolutions $\{\boldsymbol{\xi}_{\alpha}\}$. We adopt the Cowling approximation [8], which allows us to ignore the perturbations of the internal gravity $\delta\phi$. The equations for the free oscillations now become:

$$\text{continuity equation}: \quad \delta\rho + \nabla\cdot(\rho\boldsymbol{\xi}) = 0\,, \tag{1.22}$$

$$\text{energy equation}: \quad \delta P + (\boldsymbol{\xi}\cdot\nabla)\,P = c_{\mathrm{s}}^{2}(\delta\rho + (\boldsymbol{\xi}\cdot\nabla)\,\rho)\,, \tag{1.23}$$

$$\text{momentum equation}: \quad \frac{\partial^{2}\boldsymbol{\xi}}{\partial t^{2}} = -\frac{\nabla\delta P}{\rho} + \frac{\nabla P}{\rho^{2}}\delta\rho\,, \tag{1.24}$$

where $c_{\mathrm{s}}^{2} \equiv \Gamma_{1}(P/\rho)$ is the square of the adiabatic sound speed. Assuming that the background stellar profiles (P and ρ) are spherically symmetric and only depend on r, the continuity equation can be expressed in spherical coordinates:

$$\delta\rho + \frac{\partial\rho}{\partial r}\xi_{r} + \frac{\rho}{r^{2}}\frac{\partial}{\partial r}(r^{2}\xi_{r}) + \rho\nabla_{\perp}\cdot\boldsymbol{\xi}_{\perp} = 0\,, \tag{1.25}$$

where $\nabla_{\perp}$ is the angular part of the del operator. The energy equation reduces to:

$$\delta P + \xi_{r}\frac{\partial P}{\partial r} = c_{\mathrm{s}}^{2}(\delta\rho + \xi_{r}\frac{\partial\rho}{\partial r})\,, \tag{1.26}$$

which can be further rewritten as the following form:

$$\frac{\delta\rho}{\rho} = \frac{1}{\Gamma_1}\frac{\delta P}{P} + \frac{N^2}{g}\xi_r\,, \tag{1.27}$$

where $N^2 = g(\Gamma_1^{-1}(\partial \ln P/\partial r) - \partial \ln \rho/\partial r)$ is the square of the Brunt–Väisälä frequency inside the star [44]. This frequency (also known as the buoyancy frequency) is the oscillatory frequency for a perturbed fluid element under the restoring forces from buoyancy.

For an perturbed eigensolution δQ, we can assume it has the standard harmonic dependence over time, i.e. $\delta Q \propto e^{-i\omega t}$. The momentum equation then reduces to:

$$\rho\omega^2\xi_r = \frac{\partial}{\partial r}\delta P + g\delta\rho\,, \tag{1.28}$$

$$\rho\omega^2\boldsymbol{\xi}_\perp = \nabla_\perp\delta P\,. \tag{1.29}$$

Equations 1.27 and 1.28 can be combined to cancel the $\delta\rho$ terms to yield:

$$\frac{\partial}{\partial r}\delta P + \frac{g}{c_\mathrm{s}^2}\delta P + \rho(N^2 - \omega^2)\xi_r = 0\,, \tag{1.30}$$

where only partial derivatives on the radial direction are involved. Equations 1.25 and 1.29 can also be combined to the following equation where the $\boldsymbol{\xi}_\perp$ terms are canceled:

$$\delta\rho + \frac{\partial\rho}{\partial r}\xi_r + \frac{\rho}{r^2}\frac{\partial}{\partial r}(r^2\xi_r) + \frac{1}{\omega^2}\nabla_\perp^2\delta P = 0\,, \tag{1.31}$$

where the only angular derivative is the one with the angular Laplacian operator $\nabla_\perp^2$, whose eigenfunctions are spherical harmonics Y_l^m. This suggests us to separate the angular dependence of δP as $\delta P \propto Y_l^m$, such that:

$$\nabla_\perp^2\delta P = -\frac{l(l+1)}{r^2}\delta P = -\frac{L_l^2}{c_\mathrm{s}^2}\delta P\,, \tag{1.32}$$

where $L_l^2 \equiv c_\mathrm{s}^2\, l(l+1)/r^2$ is the Lamb frequency of degree l. Equations 1.27 and 1.31 can then be combined to yield:

$$\frac{1}{r^2}\frac{\partial}{\partial r}(r^2\xi_r) - \frac{g}{c_\mathrm{s}^2}\xi_r + \left(1 - \frac{L_l^2}{\omega^2}\right)\frac{\delta P}{\rho c_\mathrm{s}^2} = 0\,, \tag{1.33}$$

where we make use of the definition of N^2 and $\partial P/\partial r = -\rho g$ (hydrostatic equilibrium). [43] suggests to define the following variables:

$$\tilde{\xi} \equiv r^2\xi_r \exp\left(-\int_0^r \frac{g}{c_\mathrm{s}^2}\mathrm{d}r\right), \tag{1.34}$$

$$\tilde{\eta} \equiv \frac{\delta P}{\rho} \exp\left(-\int_0^r \frac{N^2}{g}\mathrm{d}r\right), \tag{1.35}$$

such that equations 1.30 and 1.33 become the following canonical form:

$$\frac{\partial \tilde{\xi}}{\partial r} = h(r)\frac{r^2}{c_s^2}\left(\frac{L_l^2}{\omega^2} - 1\right)\tilde{\eta}\,, \tag{1.36}$$

$$\frac{\partial \tilde{\eta}}{\partial r} = \frac{1}{h(r)r^2}(\omega^2 - N^2)\tilde{\xi}\,, \tag{1.37}$$

where $h(r) = \exp(\int_0^r (N^2/g - g/c_s^2)\mathrm{d}r)$. When the oscillations have small wavelengths compare to the pressure and density scale heights in the star, their radial derivatives are always much greater than the derivatives of local properties. We can hence use the Jeffreys–Wentzel–Kramers–Brillouin (JWKB) approximation to replace every $\partial/\partial r$ by ik_r, where k_r is the radial wave vector. With these notations and approximations, the above equations can be combined to yield the following dispersion relation that must be satisfied by physical oscillations:

$$k_r^2 = \frac{(\omega^2 - L_l^2)(\omega^2 - N^2)}{\omega^2 c_s^2}\,. \tag{1.38}$$

As k_r is the radial wave number with the JWKB approximation (i.e., $\boldsymbol{\xi} \propto e^{ik_r r}$), oscillations can propagate as waves if k_r is real, while they will be evanescent if k_r is purely imaginary. Therefore, for propagating waves, we require $k_r^2 > 0$, or $(\omega^2 - L_l^2)(\omega^2 - N^2) > 0$. Figure 1.4 shows the Brunt–Väisälä frequency and the $l = 2$ Lamb frequency inside a blue supergiant star model, adapted from [25]. We can see that there are two regions in the frequency space where the above relation could be satisfied. This kind of figure is called a propagation diagram, and we analyze the two scenarios below.

Sound waves (p modes)

$k_r^2 > 0$ can be satisfied if $\omega^2 > L_l^2$ and $\omega^2 > N^2$. This corresponds to the grey shaded region in Figure 1.4. If we take the limiting case $\omega^2 \gg L_l^2$ and $\omega^2 \gg N^2$, the dispersion relation 1.38 reduces to

$$k_r^2 = \frac{\omega^2}{c_s^2}\,. \tag{1.39}$$

We can see that this is the dispersion relation for sound waves with a sound speed c_s. Therefore, this scenario corresponds to sound waves inside the star, and the corresponding restoring forces are the internal pressure. For this reason, this kind of oscillations are also called p (pressure) modes.

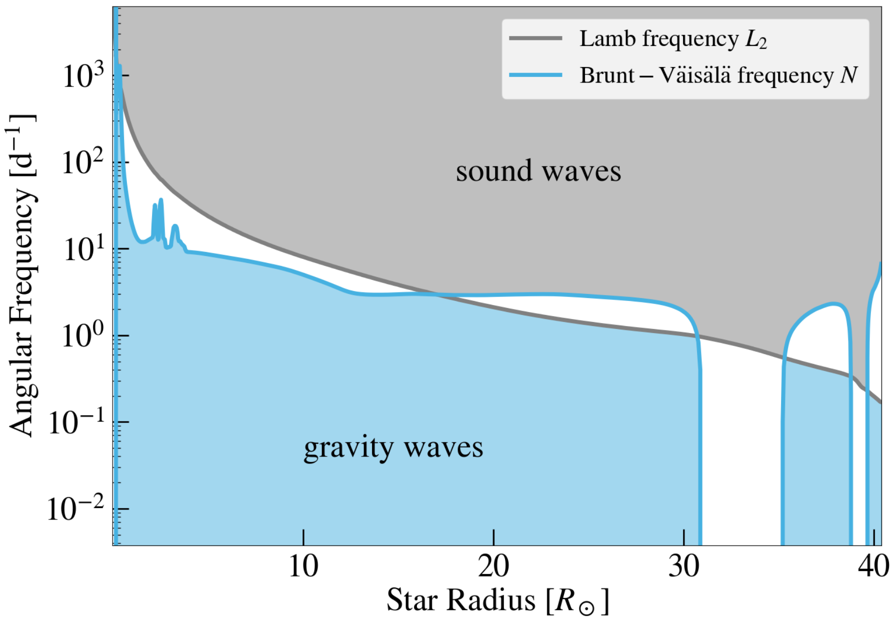

Figure 1.4: The propagation diagram for a blue supergiant model, adapted from [25]. The blue and grey lines show the Brunt–Väisälä frequency and the $l = 2$ Lamb frequency inside the star. Below both frequencies, gravity waves can propagate (shaded blue region). Above both frequencies, sound waves can propagate (shaded grey region). Both waves are evanescent in the white regions.

We note from Figure 1.4 that sound waves are often of very high frequencies. However, only oscillations with comparable frequencies to the stellar companion's orbital frequency can be tidally excited efficiently (see the driven oscillator equation 1.21). As orbits of such high frequencies typically do not exist, sound waves are almost never related to tidally excited oscillations.

Gravity waves (g modes)

$k_r^2 > 0$ can also be satisfied if both $\omega^2 < L_l^2$ and $\omega^2 < N^2$. This corresponds to the blue shaded region in Figure 1.4. If we take the limiting case $\omega^2 \ll L_l^2$ and $\omega^2 \ll N^2$, the dispersion relation 1.38 reduces to

$$k_r^2 = \frac{l(l+1)N^2}{r^2\omega^2}\,. \tag{1.40}$$

This scenario corresponds to the gravity waves (g modes) inside the star, whose restoring force is buoyancy. In convective regions of a star, buoyancy cannot restore a fluid element if its position is perturbed, and the corresponding N^2 vanishes. Gravity waves hence cannot propagate in convective regions, as shown in Figure 1.4 for the two sub-surface convective zones in the stellar model.

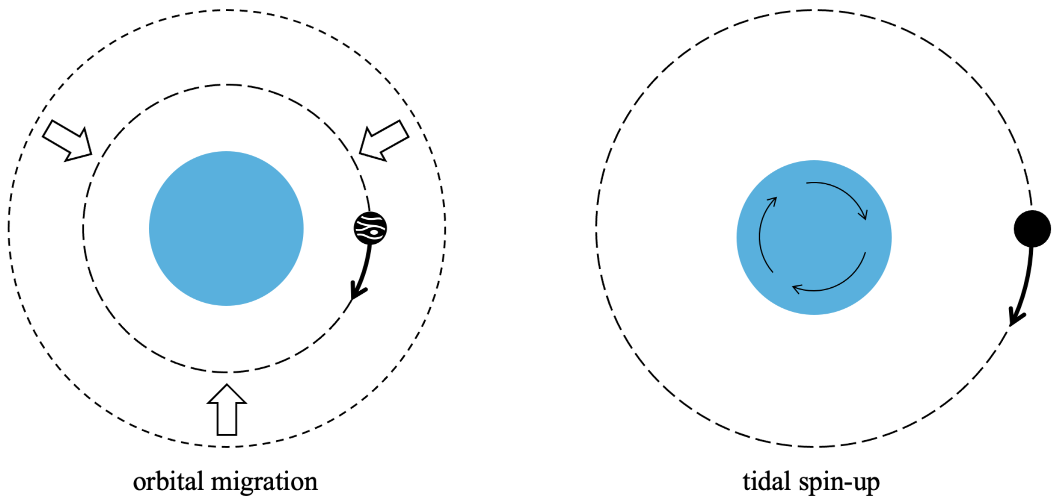

Figure 1.5: Possible dynamics of tidal dissipation: **Left**: When the companion mass is much smaller than the mass of the star where the tides are excited (e.g., for a planet around a stellar host), the loss of orbital angular momentum of the companion can cause its orbit to migrate significantly. **Right**: When the companion has comparable mass to the central star, the transfer of angular momentum between the orbit and the star can change its rotation rates significantly. If the star is initially slowly rotating, this may cause tidal spin-up of the star.

As gravity waves have lower frequencies, they can be tidally excited by the companion's orbit. As they do not propagate in convective zones, their main dissipation mechanism is radiative diffusion in the radiative zones of a star.

The above analysis is based on pure hydrodynamic analysis of non-rotating stars. For rotating stars, Rossby waves (r modes) and inertial modes (i modes), which are restored by the Coriolis force, can also be tidally excited. For stars with magnetic fields, Alfvén waves, which are restored by electro-magnetic forces, may also exist. In reality they may form mixed modes with stellar g and p modes, and the tidal excitation and dissipation of these mixed oscillations can be very complicated.

1.3 Tidal Evolution

When tides are excited, they exchange energy and angular momentum with the companion's orbit. These energy and angular momentum are transferred to/from the star when the tides dissipate. Therefore, tides can shape the dynamical evolution of the star and its orbital companion.

We summarize two typical kinds of tidal dynamical evolution in Figure 1.5. In cases where the mass of the companion object is much less than the mass of the star (e.g., for a star hosting a planet), the orbital energy and angular momentum is much less than the internal energy and angular momentum of the star itself. Therefore, the dynamics of the star will not change significantly even if tides can transfer all the orbital energy and angular momentum to the stellar interior. However, if tides are strong enough in this case, the obits may lose/acquire significant amount of energy and angular momentum. This typically cause the companion's orbit to migrate. Observations have confirmed this kind of tidal migration for the Earth-Moon system, as well as some other satellites in the solar system.

On the other hand, if the mass of the companion object is comparable to the mass of the star, tides can significantly alter the rotational evolution of the star even if only a small amount of orbital angular momentum is transferred between the star and the orbit, with negligible orbital migration. This is particularly interesting as it may explain the fast rotations of some stars which should be born slowly rotating, as they undergo this tidal spin-up process.

1.4 Questions and Existing Efforts

Many questions related to dynamical friction and tidal dissipation are still not fully solved. These questions might be of pure theoretical interests, or closely related to recent observational discoveries.

As discussed in 1.1, the process of dynamical friction originates from the gravitational interactions between celestial bodies, hence it should be fully captured if the dynamics of all particles in a system are resolved. However, this is usually not the case for galactic simulations in practice. The enormous numbers of lighter physical particles (e.g., stars and dark matter particles) in these simulations are often approximately represented by some more massive "simulation particles" with some spatial distribution and extension, rather than being resolved individually at sufficient resolution, as shown in Figure 1.1. As the individual dynamics of these lighter particles are unimportant, this method could significantly reduce the computational expense of these simulations. However, the two-body scatterings between a massive object with these simulation particles is quite different from those with the physical, less-massive particles. Therefore, a sub-grid treatment of dynamical friction is needed in these simulations.

There have been several existing efforts to implement a general sub-grid model for dynamical friction into N-body simulations. Most of these works are based on the classical Chandrasekhar's formula [7, 10, 42, 37], yet they suffer from the ambiguously defined Coulomb logarithm in the formula, and there is no consistent way to evaluate the particle mass-density ρ directly from N-body simulations. Some works make use of a zoom-in approach by resolving the individual particle dynamics around massive particles in simulations [29], yet these methods are generally complicated and may increase the computational expenses. Hence, it still remains a question to develop an accurate dynamical friction estimator that is easily implemented into N-body simulations.

The classical picture of massive black hole inspiral with dynamical friction has also been challenged by observations. Specifically, observations have confirmed the existence of super-massive black holes in $z > 7$ galaxies [14, 13, 23, 50, 31, 22, 48], which formed in less than 1 Gyr after the universe was born. The emerging data from the James Webb Space Telescope (JWST) are pushing this limit to even higher redshifts [51, 49]. It hence remains a question on whether dynamical friction could be efficient enough to sink these massive black holes in such a short period of time.

Additionally, the chaotic dynamical processes in high-redshift galaxies may further complicate the picture of black hole inspiral. The mass distribution in typical high-z galaxies is far from the isothermal density profile described in Equation 1.8, and the chaotic scattering processes can make the inspiral timescale even longer. Long inspiral processes would challenge the formation scenarios of super-massive black holes, as the existing growing mechanisms for these black holes could be very inefficient if they do not sink promptly into the galactic center [46, 47, 1, 5]. Therefore, an investigation into the detailed dynamics of these black holes in high-z galaxies is needed.

In recent years, NASA *Kepler*/K2 and TESS missions have greatly increased the number of known exoplanets around different types of stars. Due to the observational bias of transits and radial velocity measurements, many of them are discovered as short period exoplanets where tidal interactions may shape their orbital architectures through their lifetime. Ground-based follow-up observations have been trying to directly measure the orbital migration of planets (e.g., [28, 41]), and there has been at least one confirmed detection of exoplanet orbital decay directly (WASP-12b, see [27, 35]). These data provide great opportunities to study the tidal evolution of planets.

Most theoretical works on the tidal migration of planets investigate the classical picture of equilibrium tides [30, 18, 11, 45], where the tidal quality factor Q has constant dependence on the orbital frequency. Some indirect constraints based on the stellar spin measurements suggests that this may not be the case [36]. Hence, it remains a question whether the dynamical excitation of tides can explain the trend of planet migration found in data, and how it will predict the tidal evolution process of planets.

The photometric data obtained from *Kepler*/K2 and TESS not only help to identify planet transits, but also provide an opportunity to study the properties of stars. In particular, asteroseismic techniques have allowed for accurate measurements of stellar rotation rates from photometry [32, 9]. An interesting kind of system is the short-period subdwarf B (sdB) binary. Observations have shown a clear trend of spin–orbit synchronization for sdB binaries with orbital periods less than ~ 6 hours [39], which can be a result of tidal synchronization. Therefore, it remains a question about whether some tidal dissipation mechanism can explain this trend.

The evidence of tidal evolution can not only be found in living stars, but may as well be discovered in their graveyard. Gravitational wave data from LIGO/Virgo has confirmed a limited amount of binary stellar-mass black holes with non-negligible rotation [2, 15], which is inconsistent with the predictions from single stellar evolution modeling, as most of the angular momentum of the stellar core should be lost before core-collapse [24, 17]. One possible scenario to produce these rotating black holes is a prior tidal spin-up phase in massive stellar binaries consisting of a first-born black hole and a Wolf–Rayet star. If the Wolf–Rayet star can be significantly spun-up during its lifetime, it may collapse to a fast rotating black hole eventually.

A number of works have been looking at this scenario by calculating the tidal evolution with damped gravity waves inside the Wolf–Rayet star [3, 34, 16]. However, none of these works calculated the realistic tidal excitation of stellar oscillations, and they instead used a formalism developed by [52] to estimate the tidal torque. As this formalism originally applied to massive main-sequence stars, it is questionable whether they can be used for Wolf–Rayet stars. It is also a question how a realistic treatment of tidally excited gravity waves will predict about the spins of binary black holes born from Wolf–Rayet tidal spin-up.

1.5 Thesis Outline

In the remaining chapters of this thesis, I present a series of works addressing the questions mentioned in the previous section.

In Chapter 2, I develop a new sub-grid dynamical friction estimator. The estimator is based on the discrete nature of N-body simulations, and avoids the ambiguously defined quantities in Chandrasekhar's dynamical friction formula. I test this dynamical friction estimator in the GIZMO code, and prove that it is accurate, easily-implementable, and computationally efficient.

In Chapter 3, I study the dynamics of massive black hole seeds in high-redshift galaxies. I analyze the direct integration of seed black hole trajectories in high-resolution cosmological simulations, and carry out post-processing analysis of test particles with dynamical friction. I show that seed black holes less massive than $10^8\,M_\odot$ (i.e. all but the already-supermassive seeds) cannot efficiently sink in typical high-redshift galaxies.

In Chapter 4, I study the effects of tidal resonance locking for exoplanet systems. I show that the planet orbital decay timescale with resonance locking is typically comparable to the star's main-sequence lifetime, corresponding to a wide range in effective stellar quality factor ($10^3 < Q' < 10^9$). I make predictions for several individual systems and examine the orbital evolution resulting from both resonance locking and nonlinear wave dissipation.

In Chapter 5, I investigate the tidal spin-up of sdB binaries. I directly calculate the tidal excitation of internal gravity waves in realistic sdB stellar models, and integrate the coupled spin–orbit evolution of sdB binaries. I show that for canonical sdB ($M_{\rm sdB} = 0.47\,M_\odot$) binaries, the transitional orbital period below which they could reach tidal synchronization in the sdB lifetime is ~ 0.2 days, with weak dependence on the companion masses. This value is very similar to the tidal synchronization boundary evident from observations.

In Chapter 6, I investigate the scenario of Wolf–Rayet tidal spin-up to form rotating binary black holes. I show that for short-period orbits and massive Wolf–Rayet stars, the tidal interaction is mostly contributed by standing gravity modes, in contrast to Zahn's model of travelling waves which is frequently assumed in the literature. I show that tidal synchronization is rarely reached in Wolf–Rayet–black-hole binaries, and the resulting black hole spins have $a \lesssim 0.4$ for all but the shortest period ($P_{\rm orb} \lesssim 0.5$ d) binaries.

I summarize the results in Chapter 7.

References

[1] Enrico Barausse et al. "Massive Black Hole Merger Rates: The Effect of Kiloparsec Separation Wandering and Supernova Feedback". In: *The Astrophysical Journal* 904.1, 16 (Nov. 2020), p. 16. DOI: 10.3847/1538-4357/abba7f. arXiv: 2006.03065 [astro-ph.GA].

[2] K. Belczynski, C. Done, and J. -P. Lasota. "All Apples: Comparing black holes in X-ray binaries and gravitational-wave sources". In: *arXiv e-prints* (Nov. 2021), arXiv:2111.09401. arXiv: 2111.09401 [astro-ph.HE].

[3] K. Belczynski et al. "Evolutionary roads leading to low effective spins, high black hole masses, and O1/O2 rates for LIGO/Virgo binary black holes". In: *Astronomy & Astrophysics* 636, A104 (Apr. 2020), A104. DOI: 10.1051/0004-6361/201936528. arXiv: 1706.07053 [astro-ph.HE].

[4] James Binney and Scott Tremaine. *Galactic dynamics: Second Edition*. Princeton University Press, 2008.

[5] Onur Çatmabacak et al. "Black hole-galaxy scaling relations in FIRE: the importance of black hole location and mergers". In: *Monthly Notices of the Royal Astronomical Society* 511.1 (Mar. 2022), pp. 506–535. DOI: 10.1093/mnras/stac040. arXiv: 2007.12185 [astro-ph.GA].

[6] S. Chandrasekhar. "Dynamical Friction. I. General Considerations: the Coefficient of Dynamical Friction." In: *The Astrophysical Journal* 97 (Mar. 1943), p. 255. DOI: 10.1086/144517.

[7] M. Colpi et al. "On the inspiral of massive black holes in gas-rich galaxy mergers". In: *The Multicolored Landscape of Compact Objects and Their Explosive Origins; AIP, Cefalu, Sicily (Italy)*. Ed. by T. di Salvo, G. L. Israel, L. Piersant L. Burderi G. Matt A. Tornambe & M. T. Menna. Vol. 924. American Institute of Physics Conference Series. Aug. 2007, pp. 705–714. DOI: 10.1063/1.2774931. arXiv: 0706.1851.

[8] T. G. Cowling. "The non-radial oscillations of polytropic stars". In: *Monthly Notices of the Royal Astronomical Society* 101 (Jan. 1941), p. 367. DOI: 10.1093/mnras/101.8.367.

[9] S. Deheuvels et al. "Seismic evidence for a weak radial differential rotation in intermediate-mass core helium burning stars". In: *Astronomy & Astrophysics* 580, A96 (Aug. 2015), A96. DOI: 10.1051/0004-6361/201526449. arXiv: 1506.02704 [astro-ph.SR].

[10] M. Dotti et al. "Dual black holes in merger remnants - I. Linking accretion to dynamics". In: *Monthly Notices of the Royal Astronomical Society* 396 (July 2009), pp. 1640–1646. DOI: 10.1111/j.1365-2966.2009.14840.x. arXiv: 0902.1525.

[11] Craig D. Duguid, Adrian J. Barker, and C. A. Jones. “Convective turbulent viscosity acting on equilibrium tidal flows: new frequency scaling of the effective viscosity”. In: *Monthly Notices of the Royal Astronomical Society* 497.3 (July 2020), pp. 3400–3417. DOI: 10.1093/mnras/staa2216. arXiv: 2007.12624 [astro-ph.EP].

[12] Event Horizon Telescope Collaboration et al. “First M87 Event Horizon Telescope Results. I. The Shadow of the Supermassive Black Hole”. In: *The Astrophysical Journal Letters* 875.1, L1 (Apr. 2019), p. L1. DOI: 10.3847/2041-8213/ab0ec7. arXiv: 1906.11238 [astro-ph.GA].

[13] Xiaohui Fan et al. “A Survey of z>5.7 Quasars in the Sloan Digital Sky Survey. II. Discovery of Three Additional Quasars at z>6”. In: *The Astronomical Journal* 125.4 (Apr. 2003), pp. 1649–1659. DOI: 10.1086/368246. arXiv: astro-ph/0301135 [astro-ph].

[14] Xiaohui Fan et al. “A Survey of z>5.8 Quasars in the Sloan Digital Sky Survey. I. Discovery of Three New Quasars and the Spatial Density of Luminous Quasars at z~6”. In: *The Astronomical Journal* 122.6 (Dec. 2001), pp. 2833–2849. DOI: 10.1086/324111. arXiv: astro-ph/0108063 [astro-ph].

[15] Maya Fishbach and Vicky Kalogera. “Apples and Oranges: Comparing Black Holes in X-Ray Binaries and Gravitational-wave Sources”. In: *The Astrophysical Journal Letters* 929.2, L26 (Apr. 2022), p. L26. DOI: 10.3847/2041-8213/ac64a5. arXiv: 2111.02935 [astro-ph.HE].

[16] Jim Fuller and Wenbin Lu. “The spins of compact objects born from helium stars in binary systems”. In: *Monthly Notices of the Royal Astronomical Society* 511.3 (Apr. 2022), pp. 3951–3964. DOI: 10.1093/mnras/stac317. arXiv: 2201.08407 [astro-ph.HE].

[17] Jim Fuller and Linhao Ma. “Most Black Holes Are Born Very Slowly Rotating”. In: *The Astrophysical Journal Letters* 881.1, L1 (Aug. 2019), p. L1. DOI: 10.3847/2041-8213/ab339b. arXiv: 1907.03714 [astro-ph.SR].

[18] F. Gallet et al. “Tidal dissipation in rotating low-mass stars and implications for the orbital evolution of close-in planets. I. From the PMS to the RGB at solar metallicity”. In: *Astronomy & Astrophysics* 604, A112 (Aug. 2017), A112. DOI: 10.1051/0004-6361/201730661. arXiv: 1705.10164 [astro-ph.EP].

[19] A. M. Ghez et al. “Measuring Distance and Properties of the Milky Way’s Central Supermassive Black Hole with Stellar Orbits”. In: *The Astrophysical Journal* 689.2 (Dec. 2008), pp. 1044–1062. DOI: 10.1086/592738. arXiv: 0808.2870 [astro-ph].

[20] S. Gillessen et al. “Monitoring Stellar Orbits Around the Massive Black Hole in the Galactic Center”. In: *The Astrophysical Journal* 692.2 (Feb.

2009), pp. 1075–1109. DOI: 10.1088/0004-637X/692/2/1075. arXiv: 0810.4674 [astro-ph].

[21] P. Goldreich and S. Soter. "Q in the Solar System". In: *Icarus* 5 (1966), pp. 375–389. DOI: 10.1016/0019-1035(66)90051-0.

[22] Kohei Inayoshi, Eli Visbal, and Zoltán Haiman. "The Assembly of the First Massive Black Holes". In: *Annual Review of Astronomy and Astrophysics* 58 (Aug. 2020), pp. 27–97. DOI: 10.1146/annurev-astro-120419-014455. arXiv: 1911.05791 [astro-ph.GA].

[23] A. Lawrence et al. "The UKIRT Infrared Deep Sky Survey (UKIDSS)". In: *Monthly Notices of the Royal Astronomical Society* 379.4 (Aug. 2007), pp. 1599–1617. DOI: 10.1111/j.1365-2966.2007.12040.x. arXiv: astro-ph/0604426 [astro-ph].

[24] Linhao Ma and Jim Fuller. "Angular momentum transport in massive stars and natal neutron star rotation rates". In: *Monthly Notices of the Royal Astronomical Society* 488.3 (Sept. 2019), pp. 4338–4355. DOI: 10.1093/mnras/stz2009. arXiv: 1907.03713 [astro-ph.SR].

[25] Linhao Ma et al. "Variability of Blue Supergiants in the LMC with TESS". In: *The Astrophysical Journal* 966.2, 196 (May 2024), p. 196. DOI: 10.3847/1538-4357/ad38bc. arXiv: 2310.19546 [astro-ph.SR].

[26] Gordon J. F. MacDonald. "Tidal Friction". In: *Reviews of Geophysics and Space Physics* 2 (Jan. 1964), pp. 467–541. DOI: 10.1029/RG002i003p00467.

[27] G. Maciejewski et al. "Departure from the constant-period ephemeris for the transiting exoplanet WASP-12". In: *Astronomy & Astrophysics* 588, L6 (Apr. 2016), p. L6. DOI: 10.1051/0004-6361/201628312. arXiv: 1602.09055 [astro-ph.EP].

[28] Vineet Kumar Mannaday et al. "Probing Transit Timing Variation and Its Possible Origin with 12 New Transits of TrES-3b". In: *The Astronomical Journal* 160.1, 47 (July 2020), p. 47. DOI: 10.3847/1538-3881/ab9818. arXiv: 2006.00599 [astro-ph.EP].

[29] Matias Mannerkoski et al. "KETJU - resolving small-scale supermassive black hole dynamics in GADGET-4". In: *Monthly Notices of the Royal Astronomical Society* 524.3 (Sept. 2023), pp. 4062–4082. DOI: 10.1093/mnras/stad2139. arXiv: 2306.04963 [astro-ph.IM].

[30] S. Mathis et al. "The impact of rotation on turbulent tidal friction in stellar and planetary convective regions". In: *Astronomy & Astrophysics* 592, A33 (July 2016), A33. DOI: 10.1051/0004-6361/201527545. arXiv: 1604.08570 [astro-ph.SR].

[31] Eric Morganson et al. "The First High-redshift Quasar from Pan-STARRS". In: *The Astronomical Journal* 143.6, 142 (June 2012), p. 142. DOI: 10.1088/0004-6256/143/6/142. arXiv: 1109.6241 [astro-ph.CO].

[32] B. Mosser et al. "Spin down of the core rotation in red giants". In: *Astronomy & Astrophysics* 548, A10 (Dec. 2012), A10. DOI: 10.1051/0004-6361/201220106. arXiv: 1209.3336 [astro-ph.SR].

[33] Isaac Newton. *Philosophiae naturalis principia mathematica*. 1687.

[34] A. Olejak and K. Belczynski. "The Implications of High Black Hole Spins for the Origin of Binary Black Hole Mergers". In: *The Astrophysical Journal Letters* 921.1, L2 (Nov. 2021), p. L2. DOI: 10.3847/2041-8213/ac2f48. arXiv: 2109.06872 [astro-ph.HE].

[35] Kishore C. Patra et al. "The Continuing Search for Evidence of Tidal Orbital Decay of Hot Jupiters". In: *The Astronomical Journal* 159.4, 150 (Apr. 2020), p. 150. DOI: 10.3847/1538-3881/ab7374. arXiv: 2002.02606 [astro-ph.EP].

[36] Kaloyan Penev et al. "Empirical Tidal Dissipation in Exoplanet Hosts From Tidal Spin-up". In: *The Astronomical Journal* 155.4, 165 (Apr. 2018), p. 165. DOI: 10.3847/1538-3881/aaaf71. arXiv: 1802.05269 [astro-ph.SR].

[37] Hugo Pfister et al. "The erratic dynamical life of black hole seeds in high-redshift galaxies". In: *Monthly Notices of the Royal Astronomical Society* 486.1 (June 2019), pp. 101–111. DOI: 10.1093/mnras/stz822. arXiv: 1902.01297 [astro-ph.GA].

[38] A. K. Schenk et al. "Nonlinear mode coupling in rotating stars and the r-mode instability in neutron stars". In: *Physical Review D* 65.2, 024001 (Jan. 2002), p. 024001. DOI: 10.1103/PhysRevD.65.024001. eprint: gr-qc/0101092.

[39] R. Silvotti et al. "EPIC 216747137: a new HW Vir eclipsing binary with a massive sdOB primary and a low-mass M-dwarf companion". In: *Monthly Notices of the Royal Astronomical Society* 500.2 (Jan. 2021), pp. 2461–2474. DOI: 10.1093/mnras/staa3332. arXiv: 2010.13524 [astro-ph.SR].

[40] Yoshiaki Sofue and Vera Rubin. "Rotation Curves of Spiral Galaxies". In: *Annual Review of Astronomy and Astrophysics* 39 (Jan. 2001), pp. 137–174. DOI: 10.1146/annurev.astro.39.1.137. arXiv: astro-ph/0010594 [astro-ph].

[41] John Southworth et al. "A search for transit timing variations in the HATS-18 planetary system". In: *Monthly Notices of the Royal Astronomical Society* 515.3 (Sept. 2022), pp. 3212–3223. DOI: 10.1093/mnras/stac1931. arXiv: 2207.05873 [astro-ph.EP].

[42] M. Tremmel et al. "Off the beaten path: a new approach to realistically model the orbital decay of supermassive black holes in galaxy formation simulations". In: *Monthly Notices of the Royal Astronomical Society* 451.2 (Aug. 2015), pp. 1868–1874. DOI: 10.1093/mnras/stv1060. arXiv: 1501.07609 [astro-ph.GA].

[43] W. Unno et al. *Nonradial oscillations of stars.*, 1989.

[44] Vilho Väisälä. “Über die Wirkung der Windschwankungen auf die Pilotbeobachtungen”. In: *Societus Scientiarum Fennica Commentationes Physico-Mathematicae* 2 (Jan. 1925), p. 19.

[45] Jérémie Vidal and Adrian J. Barker. “Turbulent Viscosity Acting on the Equilibrium Tidal Flow in Convective Stars”. In: *The Astrophysical Journal Letters* 888.2, L31 (Jan. 2020), p. L31. DOI: 10.3847/2041-8213/ab6219. arXiv: 1912.07910 [astro-ph.SR].

[46] M. Volonteri et al. “The cosmic evolution of massive black holes in the Horizon-AGN simulation”. In: *Monthly Notices of the Royal Astronomical Society* 460.3 (Aug. 2016), pp. 2979–2996. DOI: 10.1093/mnras/stw1123. arXiv: 1602.01941 [astro-ph.GA].

[47] Marta Volonteri et al. “Black hole mergers from dwarf to massive galaxies with the NewHorizon and Horizon-AGN simulations”. In: *Monthly Notices of the Royal Astronomical Society* 498.2 (Oct. 2020), pp. 2219–2238. DOI: 10.1093/mnras/staa2384. arXiv: 2005.04902 [astro-ph.GA].

[48] Feige Wang et al. “A Luminous Quasar at Redshift 7.642”. In: *The Astrophysical Journal Letters* 907.1, L1 (Jan. 2021), p. L1. DOI: 10.3847/2041-8213/abd8c6. arXiv: 2101.03179 [astro-ph.GA].

[49] Feige Wang et al. “A SPectroscopic Survey of Biased Halos in the Reionization Era (ASPIRE): JWST Reveals a Filamentary Structure around a z = 6.61 Quasar”. In: *The Astrophysical Journal Letters* 951.1, L4 (July 2023), p. L4. DOI: 10.3847/2041-8213/accd6f. arXiv: 2304.09894 [astro-ph.GA].

[50] Chris J. Willott et al. “Four Quasars above Redshift 6 Discovered by the Canada-France High-z Quasar Survey”. In: *The Astronomical Journal* 134.6 (Dec. 2007), pp. 2435–2450. DOI: 10.1086/522962. arXiv: 0706.0914 [astro-ph].

[51] Jinyi Yang et al. “A SPectroscopic Survey of Biased Halos in the Reionization Era (ASPIRE): A First Look at the Rest-frame Optical Spectra of z > 6.5 Quasars Using JWST”. In: *The Astrophysical Journal Letters* 951.1, L5 (July 2023), p. L5. DOI: 10.3847/2041-8213/acc9c8. arXiv: 2304.09888 [astro-ph.GA].

[52] J. -P. Zahn. “The dynamical tide in close binaries.” In: *Astronomy & Astrophysics* 41 (July 1975), pp. 329–344.

Chapter 2

A NEW N-BODY DYNAMICAL FRICTION ESTIMATOR

[1] Linhao Ma et al. "A new discrete dynamical friction estimator based on N-body simulations". In: *Monthly Notices of the Royal Astronomical Society* 519.4 (2023), pp. 5543–5553. DOI: 10.1093/mnras/stad036.

Abstract

A longstanding problem in galactic simulations is to resolve the dynamical friction (DF) force acting on massive black hole particles when their masses are comparable to or less than the background simulation particles. Many sub-grid models based on the traditional Chandrasekhar DF formula have been proposed, yet they suffer from fundamental ambiguities in the definition of some terms in Chandrasekhar's formula when applied to real galaxies, as well as difficulty in evaluating continuous quantities from (spatially) discrete simulation data. In this work we present a new sub-grid dynamical friction estimator based on the discrete nature of N-body simulations, which also avoids the ambiguously-defined quantities in Chandrasekhar's formula. We test our estimator in the GIZMO code and find that it agrees well with high-resolution simulations where DF is fully captured, with negligible additional computational cost. We also compare it with a Chandrasekhar estimator and discuss its applications in real galactic simulations.

2.1 Introduction

An essential element in the study of galactic dynamics is the process of dynamical friction (DF, [12]), a statistical effect of numerous two-body scatterings which causes a massive particle to lose its momentum when it travels through a medium of much lighter background particles. DF is believed to be an important effect to drive massive black holes (BHs, from intermediate mass BHs to super-massive BHs) to galactic centers (see, e.g. [43, 56, 13]), and it plays an essential role in the evolution of globular clusters (see, e.g. [45, 23, 1, 50]). Hence the evaluation of DF is important in studying the evolution of galaxies, globular clusters, and black holes in a wide variety of contexts.

In numerical N-body simulations with sufficient resolution (such as in the limit in which all bodies such as stars, black holes, or even dark matter particles are represented by individual N-body particles), DF will be automatically captured. However, as DF is an accumulated effect of many weak encounters in the regime where the "target" mass is much larger than the mass of the "background" particles masses ($M_{\text{target particle}} \gg M_{\text{background particle}}$), it is often not possible to fully resolve this background. This is especially true in large-scale simulations of e.g. galactic scales, where a typical "N-body particle" can easily have mass much larger than intermediate and super-massive black holes ($\gg 10^4\, M_\odot$), let alone the masses of individual stars, dark matter particles, or hydrogen ions. Specifically, when the N-body particle mass becomes comparable to or larger than the "target" mass, the explicit results of an N-body solver will not return the correct DF forces. For example, in e.g. the "high-resolution" simulations of high-redshift galaxies in Ma et al. [36, 35, 34], the baryonic mass resolution is $\Delta m_i \sim 7000 m_\odot$ and the dark matter mass resolution is 5 times larger, which makes it impossible to resolve dynamical friction effects for BHs or other "sink" particles (e.g. particles which might represent unresolved massive, dense structures such as globular clusters, or hyper-dense exotic dark matter structures, etc.) less massive than $\sim 10^5 M_\odot$. Hence, in these types of simulations, an additional "sub-grid" DF force must be added to these "target" particles to attempt to recover their real dynamics, to replace the lost information of individual two-body encounters in the smoothed-out gravity potential in simulations.

Multiple sub-grid DF models have been proposed in the literature (e.g. [15, 20, 53, 44]) based on the classical Chandrasekhar's dynamical friction formula ([12], or C43 hereafter):

$$\mathbf{a}_{\text{df}}^{\text{C43}} = -4\pi G^2 M m \ln\Lambda \int d^3\mathbf{v}_m f(\mathbf{v}_m) \frac{\mathbf{v}_M - \mathbf{v}_m}{|\mathbf{v}_M - \mathbf{v}_m|^3}\,, \tag{2.1}$$

where M and m are the masses of the moving "target" particle and the background or field particles, respectively. Here $\mathbf{v}_M$ and $\mathbf{v}_m$ are their velocities, and Λ is the Coulomb logarithm defined by $\Lambda \equiv b_{\max}/b_{\min}$ where $b_{\max}$ and $b_{\min}$ are the maximum and minimum impact factors of scattered particles in weak encounters. $f(\mathbf{v}_m)$ is the velocity distribution of field particles, and, with the usual assumption of a Maxwellian velocity distribution with dispersion σ, the formula reduces to [5]:

$$\mathbf{a}_{\text{df}}^{\text{C43}} = -\frac{4\pi^2 G^2 M\rho \ln\Lambda}{V_M^3}\left[\text{erf}\left(\frac{v_m}{\sqrt{2}\sigma}\right) - \sqrt{\frac{2}{\pi\sigma}} e^{-v_m^2/2\sigma^2} v_m\right]\mathbf{v}_M\,, \tag{2.2}$$

i.e. the DF acceleration is proportional to the local field particle density ρ and is in the opposite direction of the particle velocity $\mathbf{v}_M$, effectively acting as a "friction" force. Despite its elegance and (often surprising) accuracy in estimating the DF, Chandrasekhar's formula suffers from the following shortcomings when applied as a sub-grid model:

1. In deriving the formula, C43 assumes an isotropic and homogeneous medium of field particles. This is generally not true for real galaxies. For example, it has been pointed out that high-redshift galaxies and low-redshift dwarf galaxies could be chaotic and clumpy (e.g., [55, 39, 21]). The existence of such systems makes the physical assumptions behind C43 formula questionable.

2. The Coulomb logarithm is ambiguously defined, and is often selected ad-hoc in practice, with a case-dependent selection of the minimum and maximum impact parameters (see, e.g., [53, 44]), which introduces a large systematic uncertainty in the sub-grid model.

3. The formula has an explicit dependence on the local mass density, which must be evaluated from discrete N-body data for collisionless fluid (stars or dark matter, often "blended" with gas for which the density is continuously defined, depending on the numerical hydrodynamic method). The choice of how to do so is arbitrary and has no defined "preferred" scale. Most commonly it is done with a local kernel density estimator at some multiple of the resolution scale (see, e.g. [53]), but this is known to be quite noisy, and is not consistent with the unique local gas density available from hydrodynamic calculations.

4. The velocity integral and $f(\mathbf{v}_m)$ must be estimated with some similar ad-hoc local estimator, which is also undefined, and different choices can lead to different *directions* for the dynamical friction acceleration. Usually the choice of a local kernel sampling amplifies numerical noise further here and means that $f(\mathbf{v}_m)$ must be assumed to be Maxwellian (since it cannot be fit to an arbitrary function given just a few local points).

5. There is no self-consistent way to incorporate force softening, which is necessary in N-body simulations to avoid spurious divergences in the forces, as an N-body particle does not physically represent a point-mass particle. Fail to incorporate softening can produce inconsistent results between the (often softened) gravitational acceleration and the additional dynamical friction acceleration.

6. As C43 depends on *local* continuous field parameters but represents long-range forces, there is no way to self-consistently implement it in a way that conserves momentum, while in reality dynamical friction should be exactly conservative since it is derived from an infinite superposition of pair-wise N-body encounters;

7. Evaluating C43 numerically requires operations which are not algorithmically identical to the gravity solver in N-body equations, which introduces not only additional inconsistencies, but also substantial computational expense. This also means numerical convergence for C43 applied to N-body particles is undefined: there is no formal guarantee of convergence even on idealized, smooth problems.

To tackle these problems, we develop a new sub-grid DF estimator which can be efficiently embedded into discrete N-body calculations in this work. The new estimator is based on a discrete version of the DF formula which can be applied to an arbitrary phase-space distribution of field particles, and avoids the fundamental ambiguity in the definitions of some terms in Chandrasekhar's formula. It also naturally embeds force softening and momentum conservation. It can also easily be generalized to assumptions beyond those of C43 for the nature of DF-like forces. We test our estimator in both on-the-fly simulations and in post processing, and compare our results to those from a Chandrasekhar DF estimator. The chapter is written as follows: in § 2.2 we derived our discrete DF formula. In § 2.3 we describe the methods we use to test the estimator. In § 2.4 and § 2.5 we present and discuss the results.

2.2 Derivation of the Discrete Dynamical Friction Formula

Here we present the derivation of our discrete DF formula, and general comments on its application in N-body methods.

Derivation

In C43, the classical DF formula is derived as follows: assume a test particle with mass M travels through an infinite, homogeneous and isotropic medium (filled with background particles with mass $m \ll M$), and experiences a number of individual two-body encounters. During each encounter, along the direction of relative motion, the test particle velocity in the parallel direction to the initial relative velocity is altered by (after integrating along the encounter path ds from $s \to -\infty$ to $s \to +\infty$)

$$
\begin{aligned}
\Delta \mathbf{v}_{\parallel} &= \frac{2\,m\,\mathbf{V}}{M+m}\left[1+\frac{b^2\,V^4}{G^2\,(M+m)^2}\right]^{-1} \\
&= \frac{2\,m\,\mathbf{V}}{(M+m)\,(1+\alpha^2)}\,,
\end{aligned}
\tag{2.3}
$$

where $\mathbf{V} \equiv \mathbf{v}_m - \mathbf{v}_M$ (i.e. the velocity of m in the rest frame of M), b is the impact parameter, and $\alpha \equiv b\,V^2/G\,(M+m)$ parameterizes the encounter strength. Note that the perpendicular deflection $\Delta\mathbf{v}_\perp$ will be cancelled by symmetry if the medium is homogeneous and isotropic so we neglect it for now, but we will return to this below. To account for the contributions of *all* encounters, C43 then integrates Eq. 2.3, by noting that the encounter rate in a differential time dt is the sum of encounters within a cylindrical slice, with surface area dA in the plane perpendicular to the relative motion and height $V\,dt$, over all relatively velocities and angles

$$
\begin{aligned}
\mathbf{a}_{\rm df} \equiv \frac{d\mathbf{v}_M}{dt} &= \int \Delta\mathbf{v}_{\parallel}\,V\,dA\,\mathcal{N}(\mathbf{x},\,\mathbf{v})\,d^3\mathbf{v} \\
&= \int \frac{2\,\alpha}{1+\alpha^2}\,\frac{G\,m}{b}\,\hat{\mathbf{V}}\,\mathcal{N}(\mathbf{x},\,\mathbf{v})\,dp\,dq\,d^3\mathbf{v}\,,
\end{aligned}
\tag{2.4}
$$

where $\mathcal{N}(\mathbf{x},\,\mathbf{v}) = dN/d^3\mathbf{x}\,d^3\,\mathbf{v}$ is the phase space distribution function (by number) of the background particles; $\hat{\mathbf{V}} \equiv \mathbf{V}/V$, and p and q are the two spatial coordinates perpendicular to the path length ds, i.e. characterizing the surface dA (so $ds\,dp\,dq = d^3\mathbf{x}$). The integral can be easily carried out for an isotropic and homogeneous distribution with $\mathcal{N}(\mathbf{x},\,\mathbf{v}) = n\,f_{\rm M}(\mathbf{v})$, where n is the number density (constant) and $f_{\rm M}(\mathbf{v})$ is the Maxwellian velocity distribution, leading to the classical formula.

To generalize the above formula to an arbitrary phase space distribution sampled by a discrete set of data points as in our simulations, one might naively attempt to directly insert the usual N-body approximation, replacing $\mathcal{N}(\mathbf{x},\,\mathbf{v}) \to \sum_i (\Delta m_i/m)\,\delta(\mathbf{x} - \mathbf{x}_i,\ \mathbf{v}-\mathbf{v}_i)$. This treats the distribution function as a sum of Dirac δ-functions, i.e. point particles, each with N-body particle mass Δm_i, so representing $N = \Delta m_i/m$ "background" particles of mass m. However, the integral in Eq. 2.4 only integrates over the two-dimensional surface ($dpdq$) as a slice of the full phase space, which makes it impossible to discretize directly. The missing integral parameter reflects the fundamental conceptual difficulty in deriving the DF formula for *arbitrary* phase space distribution. In deriving Eq. 2.4, we actually already performed the integral over the missing degree of freedom when calculating $\Delta\mathbf{v}_\parallel$, by integrating over path length ds in each encounter from $-\infty$ to ∞, containing the full effect of one two-body

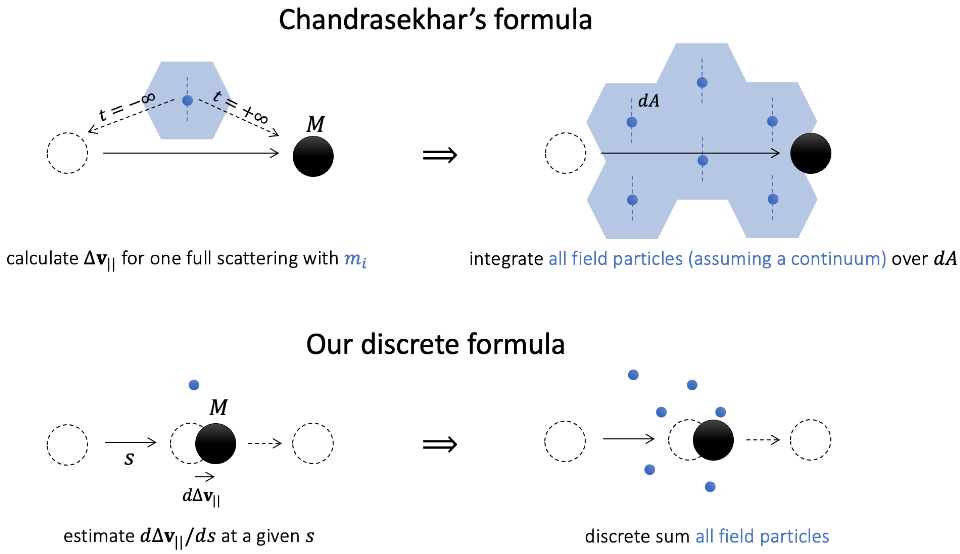

Figure 2.1: A comparison between the derivation of Chandrasekhar's DF formula (C43) and ours: in C43, Chandrasekhar calculates the change of velocity $\Delta\mathbf{v}_{||}$ for one full scattering, and integrates over the remaining two dimensions dA (perpendicular to the direction of motion) for all field particles, assuming a homogeneous and isotropic continuum such that the overall contribution is characterized by the Coulomb logarithm; in our derivation, we estimate the change of velocity $d\mathbf{v}_{||}/ds$ over the line of motion (coordinated by s) at a given point in the scattering process, which allows us to integrate all field particles over the full configuration space (as the dimension along the line of motion is now recovered), such that a discrete numerical sum is possible.

encounter before we sum them up to get the final result. This is only correct if the background distribution is isotropic and homogeneous, since in principal, the DF process cannot be evaluated in this manner for any given instant of time, without knowing all the history and future of the full dynamics, unless the background profile is static (i.e. isotropic and homogeneous). Nevertheless, it is still suggestive to consider what an inhomogeneous background particle distribution could bring (quantitatively) to this story, hence we offer an ad hoc derivation here.

The key conceptual requirement to replace Eq. 2.4 with one that can be discretized for an arbitrary N is to re-expand the integral that gave rise to $\Delta\mathbf{v}_{||}$ (Eq. 2.3) to explicitly account for the contributions of particles at different distances s along their two-body encounter trajectory, i.e. taking $\Delta\mathbf{v}_{||} \to \int \langle d\Delta\mathbf{v}_{||}/ds\rangle_{\rm deflected}\, ds$ (see comparison in Fig. 2.1). Recall that the entire point of our derivation is to develop a formula which can be applied where the *explicit* N-body evolution of the mass M was not followed. Since DF fundamentally arises from the "back-reaction" of the medium (i.e. the deflection of mass m as it feels gravity from M creating a net "drag"), we need to identify the *difference* between the contribution to $d\mathbf{v}_M/dt$ which m *would have* at a distance r along its encounter trajectory with M if it had indeed been deflected by M, relative to the acceleration M would feel if it saw m on an "un-deflected" trajectory. The latter is, of course, just the "normal" gravitational acceleration on M.[1] The full expressions for this are quite cumbersome and cannot be analytically closed; but they are still, in any case, approximate (as we still ignore many effects such as other influences on the orbit of m during each stage of its 2-body encounter), so we can safely approximate them to the same order of accuracy by noting that asymptotically $\langle d\Delta\mathbf{v}_{\parallel}/ds\rangle_{\rm deflected} \rightarrow \Delta\mathbf{v}_{\parallel}\, b^2/2\,(s^2+b^2)^{3/2}$ at large $r \gg b$ (noting $r^2 \equiv s^2+b^2$), and (for weak encounters, the only case where our derivation is meaningful) near pericenter ($r = b\,(1+\epsilon)$ with $\epsilon \ll 1$) $\langle d\Delta\mathbf{v}_{\parallel}/ds\rangle_{\rm deflected} \rightarrow \Delta\mathbf{v}_{\parallel}\,(1/2\,b)$. Together with the identity $1 = (b/2)\int_{-\infty}^{+\infty} b\,ds/(s^2+b^2)^{3/2}$, we can replace $\Delta\mathbf{v}_{\parallel}$ in Eq. 2.4 with this expression, giving:

$$\begin{aligned}
\mathbf{a}_{\rm df} &= \int \frac{2\,\alpha\,G\,m\,\mathcal{N}(\mathbf{x},\,\mathbf{v})}{b\,(1+\alpha^2)}\,\hat{\mathbf{V}}\,dp\,dq\,d^3\mathbf{v}\,\frac{b}{2}\int_s \frac{b\,ds}{(s^2+b^2)^{3/2}} \\
&\approx \int\int_s \frac{2\,\alpha\,G\,m\,\mathcal{N}(\mathbf{x},\,\mathbf{v})}{b\,(1+\alpha^2)}\,\hat{\mathbf{V}}\,dp\,dq\,d^3\mathbf{v}\,\frac{b}{2}\,\frac{b\,ds}{(s^2+b^2)^{3/2}} \\
&= \int \frac{\alpha\,b\,G\,m}{(1+\alpha^2)\,r^3}\,\hat{\mathbf{V}}\,\mathcal{N}(\mathbf{x},\,\mathbf{v})\,d^3\mathbf{x}\,d^3\mathbf{v}\,, \qquad (2.5)
\end{aligned}$$

where we used $ds\,dp\,dq \equiv d^3\mathbf{x}$, and in the $\approx$ step, where we move the integrand, we essentially make a much weaker version of the original Chandrasekhar [12] approximation, assuming that quantities such as $\mathcal{N}$ do not vary strongly over the timescale during which most of the $\Delta\mathbf{v}_{\parallel}$ is imparted by each 2-body encounter. Now, we can insert the discrete N-body form of $\mathcal{N}$ as a sum of δ functions to trivially obtain:

$$\begin{aligned}
\mathbf{a}_{\rm df} &\rightarrow \sum_i \frac{\alpha_i\,b_i\,G\,\Delta m_i}{(1+\alpha_i^2)\,r_i^3}\,\hat{\mathbf{V}}_i \\
&= \sum_i \left(\frac{\alpha_i}{1+\alpha_i^2}\right)\left(\frac{b_i}{r_i}\right)\left(\frac{G\,\Delta m_i}{r_i^2}\right)\hat{\mathbf{V}}_i\,. \qquad (2.6)
\end{aligned}$$

[1]This contribution will differ depending on the sign of s at a given r, i.e. depending on whether m is "approaching" or "receding" from M; however in our application to N-body simulations, the sign of $\mathbf{V}$ for distant m will change frequently, so there is no way to unique identify "approaching" or "receding" elements without actually performing the full time integral of every encounter (i.e. doing the full "live" N-body calculation with M, exactly what we wish to avoid). We therefore simply average between the two, giving $\langle d\Delta\mathbf{v}_{\parallel}/ds\rangle_{\rm deflected} \equiv (1/2\,|ds|)\,[\int_{-s-ds}^{-s}(\mathbf{a}'-\mathbf{a}^0)\,dt + \int_s^{s+ds}(\mathbf{a}'-\mathbf{a}^0)\,dt]$, where $\mathbf{a}' \equiv \mathbf{a}_{Mm}[\mathbf{x}_M^{\rm deflected}(t),\,\mathbf{x}_m^{\rm deflected}(t)]$ and $\mathbf{a}^0 \equiv \mathbf{a}_{Mm}[\mathbf{x}_M^{m-{\rm undeflected}}(t),\,\mathbf{x}_m^{\rm undeflected}(t)]$ are the two-body accelerations assuming m follows the deflected and un-deflected trajectories, respectively (note M still "sees" m in its un-deflected trajectory, but m does not "see" M in that case)

We have of course made a number of assumptions to derive Eq. 2.6, and our final expression is not necessarily unique. However it has many useful properties. (1) In a spatially homogeneous medium (i.e. any where we can write $\mathcal{N} = n\,f(\mathbf{v})$), then it is trivial to verify by inserting this in Eq. 2.5 that Eq. 2.6 reproduces *exactly* the expressions from Chandrasekhar [12] for any $f(\mathbf{v})$. (2) Eq. 2.6, as intended, can be easily applied to an arbitrary N-body simulation collection of particles of arbitrary types (summing different components such as dark matter, gas, or stars simply involves carrying out the sum in Eq. 2.6 with the appropriate Δm_i and m for each "species"). (3) Eq. 2.6 removes a number of ambiguities: the Coulomb logarithm is removed (it only "re-appears" if indeed the medium is infinite and homogeneous), and the $\mathbf{V}$ which appears is un-ambiguous (discussed further below). (4) Eq. 2.6 above can be trivially generalized for softened gravity (below). (5) Eq. 2.6 at least asymptotically captures the relative contributions of near versus far particles m to the DF force, i.e. the dimensional scaling with r, e.g. correctly capturing the fact that most of the effect comes from when particles are near-pericenter.

Force Softening

To apply Eq. 2.6 to numerical simulations, we must account for force softening as in the simulations (since an N-body particle of mass Δm_i represents many individual stars, collocating them at a specific $\mathbf{x}_i$, $\mathbf{v}_i$ would lead to spurious divergences in the forces). In Eq. 2.6, note that all but one term are well-behaved: $0 < \alpha_i/(1+\alpha_i^2) < 1/2$, $0 < b_i/r_i < 1$, and $|\hat{\mathbf{V}}| = 1$, so numerical divergence entirely arises from the term $G\,\Delta m_i/r_i^2$. But this is just the Newtonian gravity from a point N-body particle, i.e. *exactly* the same term that is force-softened in the simulations. Hence we insert the same softening kernel $S_i(r_i)$ as used in the actual N-body simulation (taking $G\,\Delta m_i/r_i^2 \rightarrow S_i(r_i)\,G\,\Delta m_i/r_i^2$).

For the specific simulations here, this follows from the adaptive gravitational softening scheme described in [27], corresponding to a cubic spline mass distribution:

$$S_i(r_i) = \begin{cases} \frac{32}{3}q_i^3 - \frac{192}{5}q_i^5 + 32q_i^6 & 0 \le q_i < \frac{1}{2} \\ -\frac{1}{15} + \frac{64}{3}q_i^3 - 48q_i^4 & \\ \qquad + \frac{192}{5}q_i^5 - \frac{32}{3}q_i^6 & \frac{1}{2} \le q_i < 1 \\ 1 & q_i \ge 1\,, \end{cases} \tag{2.7}$$

where $q_i \equiv r_i/H_i$ with $H_i \approx 2.8\,\epsilon_i$ the radius of compact support of the kernel and ϵ_i the equivalent Plummer softening. This removes the numerical divergence and gives the correct result for a uniform density distribution sampled by N-body particles. [2]

Perpendicular Force

In the above, we only included the parallel DF term ($\propto \hat{\mathbf{V}}_i$). However two-body encounters also produce a perpendicular deflection $\mathbf{a}_{\mathrm{df},\perp}$; this only vanishes in the C43 derivation because of the assumption of a homogeneous $\mathcal{N}$ (giving exact cancellation). Because we do not assume homogeneous $\mathcal{N}$, we can (if desired) retain these terms, giving:

$$\mathbf{a}_{\mathrm{df},\perp} = -\sum_i \left(\frac{1}{1+\alpha_i^2}\right)\left(\frac{b_i}{r_i}\right)\left(S_i(r_i)\,\frac{G\,\Delta m_i}{r_i^2}\right)\hat{\mathbf{b}}_i \tag{2.8}$$
$$\mathbf{b}_i \equiv \mathbf{r}_i - (\mathbf{r}_i \cdot \hat{\mathbf{V}}_i)\,\hat{\mathbf{V}}_i\,.$$

This differs from the parallel $\mathbf{a}_{\mathrm{df},\parallel}$ only by one power of α_i and, of course, the direction. The power of α_i means that the perpendicular deflection can be stronger (compared to the parallel term) in strong encounters (although $0 < 1/(1+\alpha_i^2) < 1$ so this term is still bounded and cannot produce spurious divergences or forces larger than the regular/external acceleration). But because the integrated force is always dominated by weak deflections (where $\alpha_i \gg 1$), then even ignoring cancellations (which further reduce $\mathbf{a}_{\mathrm{df},\perp}$ even in inhomogeneous $\mathcal{N}$), this term is generally smaller than the parallel $|\mathbf{a}_{\mathrm{df},\parallel}|$ by one power of $\sim G\,M/r\,V^2 \sim M/M_{\mathrm{total,\,galaxy}}(<r) \ll 1$.

We show in an additional set of tests that this term is completely negligible for most galaxy simulation contexts, hence we do not include them in our final expression and tests below. But we emphasize that it is trivial to include and imposes no additional cost.

Final Expression

It is straightforward to generalize the above for a spectrum of masses m, i.e. integrating over the stellar initial mass function (IMF). However for any $M \gtrsim 10\,M_\odot$, this makes a negligible difference to our results. Since we do not know the “true” dark matter particle mass, it is more straightforward to simply assume the limit $M \gg m$, in which case the species masses m completely factor out of the salient expressions.

[2] Note that in principle this softening is not exactly self-consistent with our derivation, since if Δm_i represents an extended spatial distribution of particles, each would be deflected slightly differently in Eq. 2.5. However, this *is* consistent with the simulations: N-body softening for collisionless fluids simply features this ambiguity at a fundamental level, because an individual N-body particle cannot actually deform in a fully-Lagrangian manner.

This gives the expression we will use throughout:

$$\begin{aligned} \mathbf{a}_{\rm df} &= \sum_i \Delta\mathbf{a}^i_{\rm df} \\ \Delta\mathbf{a}^i_{\rm df} &\equiv \left(\frac{\alpha_i\, b_i}{(1+\alpha_i^2)\, r_i}\right)\left(S_i(r_i)\,\frac{G\,\Delta m_i}{r_i^2}\right)\hat{\mathbf{V}}_i\,, \end{aligned} \tag{2.9}$$

with $\alpha_i \approx b_i\, V_i^2/G\,M$.

Numerical Implementation

In the form of Eq. 2.9, it is particularly straightforward to implement our estimator. First, noting that α_i and $b_i \equiv r_i\,|\hat{\mathbf{r}}_i - (\hat{\mathbf{r}}_i\cdot\hat{\mathbf{V}}_i)\,\hat{\mathbf{V}}_i|$ is a function only of $\mathbf{r}_i$ and $\mathbf{V}_i$, we see that the only piece of additional of information needed to compute Eq. 2.9, alongside the usual gravity force, in an N-body solver is the velocity $\mathbf{V}$ (already known). In other words, we do not need to construct some estimator for values in the C43 formula, like ρ, Λ, $\langle\mathbf{V}\rangle$ which are not actually computed in standard N-body simulations. Second, we also immediately see that it is completely trivial to carry out this sum over any arbitrary set of species (e.g. stars+gas+dark matter+other BHs).

Comparing the form of Eq. 2.9 and the "regular" gravitational acceleration $\mathbf{a}_{\rm ext}$:

$$\mathbf{a}_M = \mathbf{a}_{\rm ext} + \mathbf{a}_{\rm df} = \sum_i \Delta\mathbf{a}^i_{\rm ext} + \sum_i \Delta\mathbf{a}^i_{\rm df}\,, \tag{2.10}$$

$$\Delta\mathbf{a}^i_{\rm ext} \equiv \left(S_i(r_i)\,\frac{G\,\Delta m_i}{r_i^2}\right)\hat{\mathbf{r}}_i\,, \tag{2.11}$$

$$\Delta\mathbf{a}^i_{\rm df} \equiv \left(\frac{\alpha_i\, b_i}{(1+\alpha_i^2)\, r_i}\right)\left(S_i(r_i)\,\frac{G\,\Delta m_i}{r_i^2}\right)\hat{\mathbf{V}}_i\,, \tag{2.12}$$

we immediately see that the operation needed to compute $\mathbf{a}_{\rm df}$ is algorithmically identical to that needed to compute the normal gravitational forces. In Tree-gravity, Tree-PM, direct N-body, or many other methods, implementing exact evaluation of Eq. 2.9 in a manifestly-conservative manner is especially trivial. [3] In e.g. a

[3] In PM and related methods, where long-range forces are evaluated via computing the potential from a Particle-Mesh Fourier method, implementing Eq. 2.9 is less trivial: the issue is that the direction $\hat{\mathbf{V}}_i$ differs from $\hat{\mathbf{r}}_i$, so one cannot simply treat $\mathbf{a}_{\rm sf}$ as a scalar correction to the regular external gravitational potential, but must compute a separate potential/field. However in hybrid Tree-PM methods, such as (optionally) implemented in GIZMO, the less-accurate PM forces are only used at large distances; given this, we find (consistent with Fig. 2.7) that the errors from simply truncating the sum for $\mathbf{a}_{\rm df}$ by including only the contributions from the tree-walk (ignoring the PM terms in $\mathbf{a}_{\rm df}$) are entirely negligible (below normal integration-error level).

tree-walk, as one sums up to compute $\mathbf{a}_{\rm ext}$, we simply sum the additional term $\Delta\mathbf{a}^i_{\rm df}$, which scales exactly with the $|\Delta\mathbf{a}^i_{\rm ext}|$ multiplied by the numerical pre-factor $\alpha_i\,b_i/(1+\alpha_i^2)\,r_i$, and oriented in the different direction $\hat{\mathbf{V}}_i$. The gravitational force softening is also naturally embedded in Eq. 2.9.

Moreover, our Eq. 2.9 is well-behaved when applied to tree nodes/leaves, not just individual particles: one simply treats each node as a "super-particle" with the appropriate total Δm_i and mass-averaged $\mathbf{V}_i$, $\mathbf{r}_i$, in the same manner as done for the usual gravity calculation. It is trivial to verify from the form of Eq. 2.9 that the order of the errors from this approach will always be equal to or better than the order of errors in $\mathbf{a}_{\rm ext}$ in the tree (i.e. convergence is equal or faster).

To ensure manifest momentum conservation, we simply enforce equal and opposite forces, i.e. apply an acceleration $\Delta\mathbf{a}_{\rm M-to-i} = -(M/\Delta m_i)\,\Delta\mathbf{a}^i_{\rm df}$ to each particle i. The scaling of the pre-factor in Eq. 2.9 is such that it guarantees this "back-reaction" term is well behaved and does not produce any spurious numerical divergences in the accelerations of the particles i.[4]

2.3 Numerical Validation: Methodology

To study the accuracy of our DF formula, we compare it to both direct high-resolution simulations and calibrated versions of the local Chandrasekhar's DF formula, using both "on-the-fly" applications in simulations (§ 2.3) and post processing methods (§ 2.3). Here we detail those methods. In what follows, we refer to the "target" or "sinking" particle as a black hole (BH) of mass $M_{\rm BH}$, since this is a particularly relevant motivating case for our sub-grid model, but of course the "target" particle could in principle represent any sufficiently compact bound massive object.

On-the-fly Simulations

Numerical Methods

We have implemented the "discrete DF estimator" Eq. 2.9 in the GIZMO multi-physics code [27], which uses a standard Barnes-Hut tree algorithm to solve the gravity equations (an improved version of that in [51]). GIZMO is well-tested in numerous applications of N-body dynamics problems involving dynamical friction, N-body resonances and wake problems (see, e.g. [32, 14, 22, 8, 41, 7, 9]), to which we refer for more detailed descriptions of numerical methods, demonstrations of

[4]That behavior is *not* guaranteed if one attempts to conserve momentum by simply applying a C43-style formula to M and then ad-hoc "redistribute" the equal-and-opposite momentum change to the neighboring i around M.

convergence, test problems, etc. As described above we simply evaluate the DF force $\mathbf{a}_{\rm df}$ alongside the "normal" gravitational force (using the identical softening, etc.) in the tree-walk operation, imposing negligible CPU cost.

Initial Conditions

To test the estimator, we have run a series of test problems. In each, we initialize a steady-state "halo" of collisionless particles (e.g. "dark matter" or "stars") using the GALIC code [58], with a target/BH particle on an initial orbit expected to decay owing to DF. We have experimented with several different choices for the initial halo density profile, whether the halo velocity distribution is anisotropic or isotropic, and other parameters of the halo and orbit (e.g. eccentric versus circular, and initial position/energy/angular momentum). Our qualitative conclusions and comparison of methods are identical in each case (and of course, this being a pure N-body problem it is scale free), so we focus on and show plots from one example with typical cosmological units for the sake of clarity.

In our fiducial example, we adopt a Hernquist [25]-profile halo with total mass $2 \times 10^{11}\, M_{\odot}$ with the Yurin and Springel [58] concentration parameter of 4 and spin parameter 0.04 (consistent with typical dark matter halo parameters, [11], and sufficient to make the halo mildly anisotropic because of rotation), so that the Hernquist [25] scale-length $a = 30.2\,$kpc. The target/BH is placed 5 kpc away from the halo center and has a tangential velocity of 59 km/s, which is the circular velocity of the halo at that radius. The black hole mass is $10^8\, M_{\odot}$, much less than the enclosed dark matter mass inside 5 kpc ($\sim 4 \times 10^9\, M_{\odot}$), to avoid disrupting the dynamical equilibrium of the galaxy.

Sub-Grid Versus Resolved Simulations

As DF should be fully resolved when the target/BH mass $M_{\rm BH}$ is much more than the background ("dark matter" or DM) particle mass $M_{\rm DM}$, one would expect that only in a low resolution simulation (i.e., $M_{\rm BH} \lesssim M_{\rm DM}$) a sub-grid treatment of DF is necessary[5]. However, if the resolution is *too* low, the orbital semi-major axis of the BH particle will be smaller than the inter-particle spacing of the N-body simulation and the BH will have essentially "sunk to the center" already — trivially,

[5]When the resolution lies in between and DF is partially resolved, a sub-grid treatment may cause "double counting" when calculating DF. While this remains an open question in general, we find that it can be avoided by multiplying a field-mass-dependent function on the DF formula in our tests. See discussions in 2.4.

if it were just one background/DM particle inside of the initial 5 kpc, then there is no define-able smaller-scale center towards which even a "perfect" sub-grid model could migrate the target/BH. We hence choose $M_{\rm DM} = 10^7 M_\odot$ in the tests with sub-grid DF, so $\sim$ 400 dark matter particles are enclosed inside the initial 5 kpc. We further run a set of 50 simulations with the same background halo, but with the BH particles placed randomly on a 5 kpc-radius sphere with a random direction of velocity in the tangent plane. By choosing the median between these runs, we can smooth out the chaotic motions intrinsic in the problem, as well as the effects of anisotropy (both real, from the halo rotation, and numerical, from N-body noise) generating eccentric orbits which produce larger oscillations in the instantaneous BH speed (making the results more difficult to read).

To test our results, we compare a set of reference simulations at varying resolution which do not adopt any sub-grid DF, but with the same setups of black hole initial conditions. At sufficiently high resolution, these simulations satisfy $M_{\rm BH} \gg M_{\rm DM}$ and so should directly capture the salient effects of DF on the target.

Simulations with a "Fitted" C43 Sub-Grid Model

Finally, we consider a third set of simulations where we again adopt a sub-grid DF estimator, but instead adopt the local Chandrasekhar DF estimator of Eq. 2.2 as previously introduced in GADGET in e.g. Cox et al. [16] updated to be essentially identical to that in Tremmel et al. [53]. Here we assume a Maxwellian velocity distribution, estimate the mean velocity and dispersion as a kernel-and-cell-mass-weighted mean, and use the BH kernel density estimator from Wellons et al. [57] to estimate ρ.

We previously noted intrinsic difficulties this method faces: however, for this particular test problem, the background halo is (by construction) smooth and nearly isotropic and single-component and nearly-Maxwellian, so this provides a "best-case scenario" for a C43-like estimator. But this still leaves un-resolved the question of how to estimate the Coulomb logarithm. We find that common choices (e.g. the ratio of virial radius to "true" inter-particle spacing) are not only impossible to predict a-priori in a completely general simulation (they must be put in "by-hand"), but also appear to give DF forces which differ systematically from the resolved solutions by tens of percent or up to a factor of two. Therefore, to give this model the best possible chance, we explicitly *fit* the Coulomb logarithm, varying it until we find a model which best matches the BH orbital decay seen in the explicit high-resolution

set	$M_{\rm DM}/M_{\rm BH}$	sub-grid DF model	ϵ criterion	num. of runs
1	10^{-1}	this paper	$\epsilon \sim \Delta x_i$	50
2	10^{-1}	fitted C43	$\epsilon \sim \Delta x_i$	50
3	10^{0}	none	$\epsilon < b_{\rm min}$	50
4	10^{-1}	none	$\epsilon < b_{\rm min}$	50
5	10^{-2}	none	$\epsilon < b_{\rm min}$	50
6	10^{-3}	none	$\epsilon < b_{\rm min}$	1
7	10^{-4}	none	$\epsilon < b_{\rm min}$	1
8	10^{0}	none	$\epsilon \sim \Delta x_i$	50
9	10^{-1}	none	$\epsilon \sim \Delta x_i$	50
10	10^{-2}	none	$\epsilon \sim \Delta x_i$	50
11	10^{-3}	none	$\epsilon \sim \Delta x_i$	1
12	10^{-4}	none	$\epsilon \sim \Delta x_i$	1
13	10^{-5}	none	$\epsilon \sim \Delta x_i$	1

Table 2.1: Representative simulation summary for our idealized tests. Different sets share the same setup of initial conditions: a $10^8\,M_\odot$ black hole particle placed randomly at a 5 kpc radius with a velocity of 59 km/s in a random tangent direction. The background particles form an Hernquist halo with $M_{\rm halo} = 2 \times 10^{11}\,M_\odot$. The black hole speed from these tests are shown in Fig. 2.3 (when multiple runs are at present, only the median value is shown).

N-body calculation. We use this, essentially as a way of detecting how our method compares to a "best-case" C43 estimator calibrated ahead of time to the *specific* problem being simulated.

The simulation setups are summarized in Table 2.1.

Post-Processing in Multi-Physics Galaxy Simulations

While comparing our discrete estimator with the Chandrasekhar estimator in the idealized test problem above can help to test its accuracy, it is of course also important to apply it to some more "realistic" (or at least more complicated) galaxy simulations which involve multi-component (gas+star+DM) anisotropic, highly-inhomogeneous backgrounds. Full applications to such simulations on-the-fly can be used to make predictions for e.g. demographics of free-floating BHs, IMBHs, and rates of BH-BH coalescence in galaxy nuclei (e.g. predictions for LISA). However this is clearly beyond the scope of this work. Instead here we will select some snapshots of N-body information from high-redshift galaxies in the Feedback In Realistic Environments (FIRE; [29, 28]) project, and use these to make some simple post-processing comparisons in order to see how the full on-the-fly application of

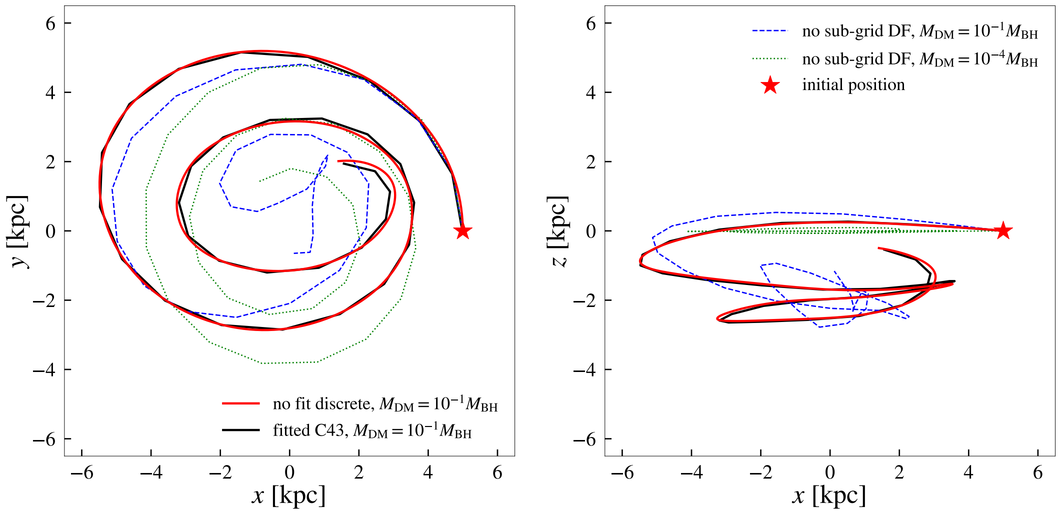

Figure 2.2: Example trajectories of a black hole particle in our simulations. The black hole is initially placed 5 kpc away from the halo center (the coordinate origin) on the x-axis and has a circular velocity of 59 km/s in the $\hat{y}$ direction. We see that in the high-resolution run (green dashed) the black hole sinks to the halo center in circular orbits as time evolves, which is partially resolved by the low-resolution runs with sub-grid DF (red and black lines, with the discrete DF and the "calibrated Chandrasekhar" estimator, respectively), but not by the run without it (blue dashed; the black hole departs significantly from the halo center in the z-direction). The low-resolution runs (with or without sub-grid DF) suffer from dynamical heating which significantly perturbs the circular orbit. In addition, our discrete estimator matches well with the calibrated Chandrasekhar estimator, though we have not calibrated our discrete DF estimator in any way (we are simply using Eq. 2.9 directly, without any input parameter other than the smoothing length ϵ).

the estimator used here might differ (or not) from other approaches to including or ignoring DF in these kinds of systems.

2.4 Results and Discussion

Validation in On-The-Fly Simulations

Figs. 2.2-2.3 show some representative results of our numerical validation tests in on-the-fly simulations, specifically focusing on an illustrative trajectory of the BHs as well as the BH velocity as a function of time.

First, we examine the behavior of pure N-body calculations (*without* sub-grid DF) as a function of resolution. Not surprisingly, when the target mass is similar to the N-body particles (e.g. $m_{DM} \gtrsim M_{BH}$), no DF is captured. Most previous studies arguing for different "sufficient" resolutions to capture DF refer to this regime [see e.g. 54, 15, 10, 28, 44, 4, 6, 33], depending on the specific problems they are

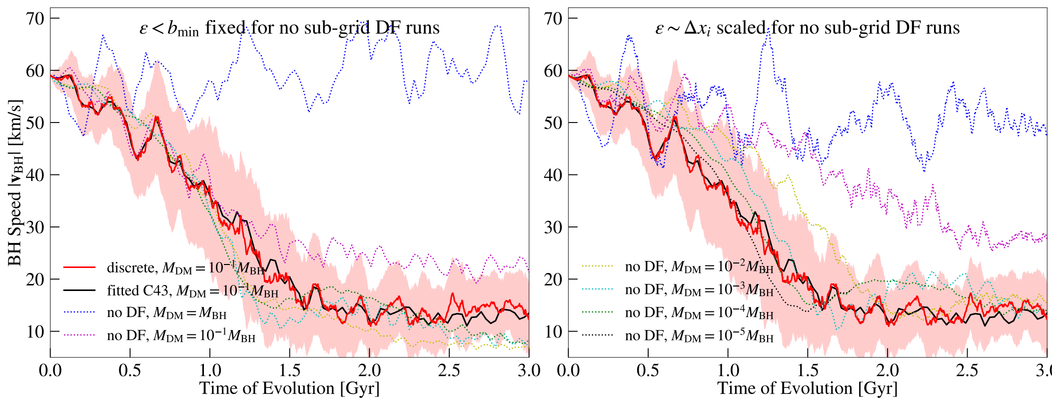

Figure 2.3: The speed of black hole particles upon time of evolution in our test problem. The thick red, thick black and dotted lines show the (median of) results from low-resolution runs with our discrete estimator, with Chandrasekhar's DF estimator (with a fitted $\ln\Lambda = 4$) and from multi-resolution runs without sub-grid DF, respectively (see Table 2.1). The red-shaded area shows the $\pm\sigma$ range for all runs with the discrete estimator. We see that the speed of black hole particles decreases significantly as the black holes sink to the halo center. The results from our discrete estimator matches well with the fitted Chandrasekhar estimator, and matches the converged results of the no sub-grid DF runs at higher resolution. The convergence is better for no sub-grid DF runs with smoothing length less than the minimum impact-parameter ($\epsilon < b_{\rm min}$, left panel) than those with (the usually chosen) length comparable to the inter-particle separation ($\epsilon \sim \Delta x_i$, right panel), as in the later case the effective Coulomb logarithm is artificially truncated, causing a logarithmic convergence behaviour (see discussions in §2.4).

choosing. In our case, at better resolution ($m_{\rm DM} \ll M_{\rm BH}$) we see DF but with an important dependence on how we treat the *spatial* force softening ϵ. If we adopt a fixed Plummer-equivalent ϵ comparable to or smaller than the canonical minimum impact parameter for strong encounters $b_{\rm min} \sim G\,M_{\rm BH}/(2\,\sigma^2 + V_{\rm bh}^2)$ (here $\sim 60\,{\rm pc}$ at the initial BH position), we see excellent convergence once $m_{\rm DM} \ll 0.1\,M_{\rm BH}$ (Fig. 2.3, left-panel). However, this is not how force softenings are typically set in N-body simulations which do not resolve the individual point masses: instead, to prevent spurious noise in *other* properties, the "optimal" softening is usually chosen to roughly match the inter-particle separation $\epsilon \sim \Delta x_i \sim (\Delta m_i/\rho_i)^{1/3}$ (Fig. 2.3, right-panel; [40, 49, 3, 17, 48]). When we do this, we see notably worse convergence: in fact, the convergence is logarithmic in $m_{\rm DM}$, because we have $\epsilon > b_{\rm min}$, the effective Coulomb logarithm is artificially truncated (i.e. we artificially suppress close encounters). This is a known challenge for DF in softened gravity (see e.g., [31] for more details and extended discussion), and it further emphasizes the importance of a sub-grid model like ours: achieving $\Delta x_i \ll b_{\rm min}$ requires $m_{\rm DM} \ll 10^{-5}\,M_{\rm BH}$, i.e. billions of N-body particles even for a simple, idealized halo like that here.

We then compare our "sub-grid" DF model (Eq. 2.9) calculated on-the-fly to an extremely low-resolution IC with $m_{\rm DM} = 0.1\,M_{\rm BH}$,[6] using $\epsilon \sim \Delta x_i$ as would be applied in typical cosmological simulations. For this low-resolution case, there is significant variation owing to different eccentric orbits and discreteness noise, so we show the median and $\pm 1\sigma$ range of BH velocities. The median agrees remarkably well with the converged solution. We stress that Eq. 2.9 contains *no other adjustable parameter* beyond the physically motivated ϵ: this is an actual prediction.

Next we compare the "fitted" C43 model Eq. 2.2: as described above, in addition to the arbitrary choice of kernel estimator size and shape (which we set to the smallest size that reduces noise acceptably), we freely vary the numerical pre-factor ("effective Coulomb log") $\ln\Lambda$ in Eq. 2.2 until we find a value which best matches our high-resolution simulations. For the best-fit value, the result is strikingly similar to our Eq. 2.9 (perhaps not surprising, given that we start from the same assumptions) — but we stress that even small, $\sim 10\%$ differences in $\ln\Lambda$ produce significant disagreement with the high-resolution simulations. Moreover, we have considered a dozen "standard" estimates of $\ln\Lambda$ widely used in the literature (see references above and [24, 30, 2, 19]), e.g. $\Lambda \sim |\rho/\nabla\rho|/b_{\rm min}$, and find that *none* of them correctly predicts the best-fit Λ (usually discrepant by factors $\sim 1.3-2$). This probably owes at least in part to the fact that the central Hernquist [25] distribution function is appreciably non-Maxwellian, as discussed in [31], so the fitted $\ln\Lambda$ is essentially compensating for this error (the "erf(...) − ..." term in Eq. 2.2).

As noted above, these conclusions are robust to the parameters of the initial halo and orbit, mass profile of the halo assumed, amount of angular momentum (anisotropy in the distribution function), and other choices of the problem setup: however, we find as expected that the C43 "effective Coulomb logarithm" must be re-calibrated in many cases to fit high-resolution simulations. We have also tested other numerical aspects of the method including e.g. the tree opening criteria [46, 51], timestep

[6] We find that the results of our sub-grid DF runs are robust and nearly independent of resolution so long as the dynamical mass of the target/BH particle is at least slightly larger (a factor of $\gtrsim 2-3$) than the mass-weighted median of the "background" N-body particles. If the BH particle has mass lighter than the background, then either sub-grid DF model (C43 or Eq. 2.9) requires additional care, or else spurious N-body heating effects can become larger than the true DF forces. So for practical applications where one wishes to evolve the dynamics of targets with very small masses, it is useful to follow standard practice [52, 18, 26] and assign a separate "true target/BH mass" used for the DF calculation and other physics to the N-body particle "carrying" the target/BH.

size/integration accuracy [28, 22], and inclusion/exclusion of the perpendicular force (Eq. 2.8): none of these has a significant effect (consistent with previous studies, see e.g., [30, 31, 42]).

Given the close agreement between the discrete DF and explicitly calibrated-Chandrasekhar DF models, it is likely that more detailed differences in orbit shape we see comparing *either* of these models and the true, high-resolution simulation owes not to anything we can simply "further calibrate" (like a Coulomb logarithm), but rather to fundamental resolution effects (e.g. more accurately recovering the shape of the background potential itself, hence the "correct" elliptical orbit structure; or the treatment of subparsec-scale physics around SMBHs, a known issue as discussed in, e.g. [47, 37, 38]), as well as assumptions of the Chandrasekhar-like derivation which our DF derivation also implicitly assumes. For example, the assumption of linearity (that the net effect on the BH can be approximated via the sum of many independent two-body encounters) or forward/backward asymmetry in the distribution function (implicit in a stronger assumption like homogeneity but present in a weaker form in our derivation as well).

Post-Processing in Multi-Physics Galaxy Simulations

While the idealized experiments above are important for validation, their simplicity means that it is difficult to gain insight into possible differences between our Eq. 2.9 and the fitted C43 model. We therefore briefly consider this in post-processing of a multi-physics galaxy formation simulation. The specific (arbitrary) simulation and time we select is the " **z5m12b**" galaxy at redshift 7.0 described in [33], illustrated in Fig. 2.4. The simulation is multi-component, containing dark matter, stars, multi-phase gas, and black holes, with complicated cooling, star formation and "feedback" physics all included on-the-fly. This particular snapshot is chosen because it is dynamically unstable, asymmetric, gas-rich and starforming, and contains several giant star clusters and molecular cloud complexes, all of which complicate the dynamics. We compare the results from the discrete estimator with the Chandrasekhar estimator and discuss their differences and implications.

In Fig. 2.5 we compare the acceleration amplitude $a_{\rm df} \equiv |\mathbf{a}_{\rm df}|$ calculated from different formulae for a test particle of mass $10^5\,M_\odot$ in the representative snapshot. The test particle is placed along an arbitrary x-axis passing through the galaxy center with a simulation-frame velocity of $\mathbf{V}_M = 200\,{\rm km\,s^{-1}}\,\hat{y}$ (Fig. 2.4, red dashed line and arrow). We compare the results from our "full" expression (Eq. 2.9),

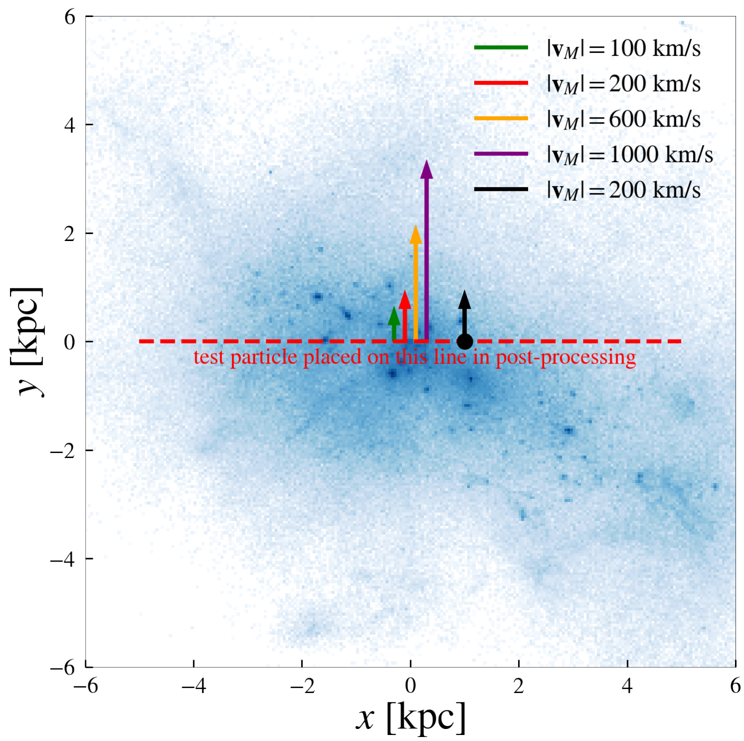

Figure 2.4: The galaxy snapshot we chose for post-processing analysis. The color scales with the projected total mass density (DM+stars+gas). It is the "**z5m12b**" galaxy at redshift 7.0 described in [33], which is clumpy and dynamically unstable. The post-processing tests are also shown: (a) a test particle of $10^5\ M_\odot$ placing on the x-axis with a velocity of $V_M = 200\,\mathrm{km/s}\,\hat{y}$; (b) the same particle but with different velocities $(100, 200, 600$ and $1000\,\mathrm{km/s})$ in the $\hat{y}$ direction; (c) a fixed particle at $(1, 0, 0)$ with $V_M = 200\,\mathrm{km/s}\,\hat{y}$. The implications of these tests are described in the main text.

our expression ignoring force softening (Eq. 2.6), and the classical C43 expression (Eq. 2.1). Eqs. 2.9 & 2.6 can be directly applied to the simulations without any processing. To apply Eq. 2.1, we estimate the continuous ρ at each position $\mathbf{x}_M$ using a kernel density estimator by averaging through the 0.4 kpc cubic box around $\mathbf{x}_M$; we calculate the local velocity integral by converting it into the usual discrete sum in this box, and we take $\ln \Lambda = 5$ to be constant, once again fitting it so that the median/mean acceleration is essentially identical.

The agreement between Eq. 2.9 and Eq. 2.1 is reasonable, but again this requires choosing Λ specific for the problem and snapshot (we note, for example, that the effective Λ here differs by almost a factor of two from the value fit to the idealized Hernquist [25] profile sphere tests in the previous section). Eq. 2.6, which ignores force softening, is also quite similar, except for occasional "spikes" arising from

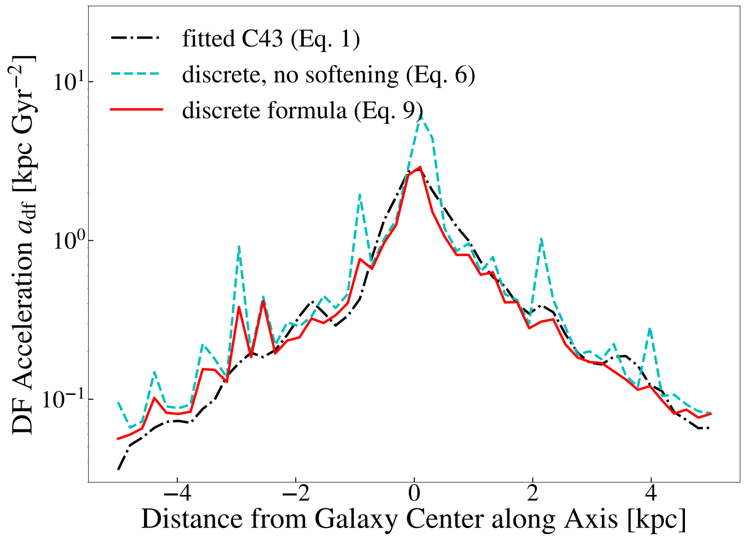

Figure 2.5: Comparison of the DF amplitude calculated from different DF formulas. The test particle is a $10^5 M_\odot$ particle with a 200 km/s velocity in the y direction, put at different positions on the x axis (Fig. 2.4, red dashed line and arrow). The black, cyan and red lines show the results from Chandrasekhar's formula (Eq. 2.1, with a (fitted) constant Coulomb logarithm $\ln \Lambda = 5$), our formula without smoothing (Eq. 2.6) and our formula with smoothing (Eq. 2.9), respectively. Our discrete formula remains very close to Chandrasekhar's approximation. The smoothing removes most of the peaks which could be caused by numerical divergence.

close proximity to N-body particles producing a spurious large force which is not actually present in the simulations (accounted for correctly in our Eq. 2.9).

Fig. 2.6 similarly compares the direction $\hat{\mathbf{a}}_{\rm df}$. Because C43 assume homogeneity, and their $\mathbf{a}_{\rm df}^{\rm C43}$ has equal contributions from all scales, a major ambiguity in Eq. 2.1 — even after we fit out the Coulomb logarithm — is where/how to evaluate $\mathbf{V} = \mathbf{V}_M - \mathbf{V}_m$. Should we interpolate to the local value at $\mathbf{x}_M$, weight by contribution to Λ, or weight by mass (dominated by distant particles)? If we follow the same procedure above to obtain a "local" $\mathbf{V}$, then we see that usually, the direction of $\hat{\mathbf{a}}_{\rm df}$ from Eq. 2.9 and from Eq. 2.1 agree, especially if we assume a test particle M with large lab-frame $|\mathbf{V}_M|$ (since then $\mathbf{V} \approx \mathbf{V}_M$, independent of the background $\mathbf{v}_m$). But when $\mathbf{V}_M$ is small (the case of interest for sinking), Eq. 2.1 can occasionally "flip" to point in an unphysical direction in a noisy velocity field.

Our Eq. 2.9 allows us to easily quantify the contributions to the total $a_{\rm df}$ from all the mass in radial shells. Fig. 2.7 shows this (specifically $da_{\rm df}/d\ln r$, integrating the contributions from all particles in logarithmically-spaced shells of distance r from M) again for a representative example (with M at $|\mathbf{x}_M| = 1$ kpc from the origin

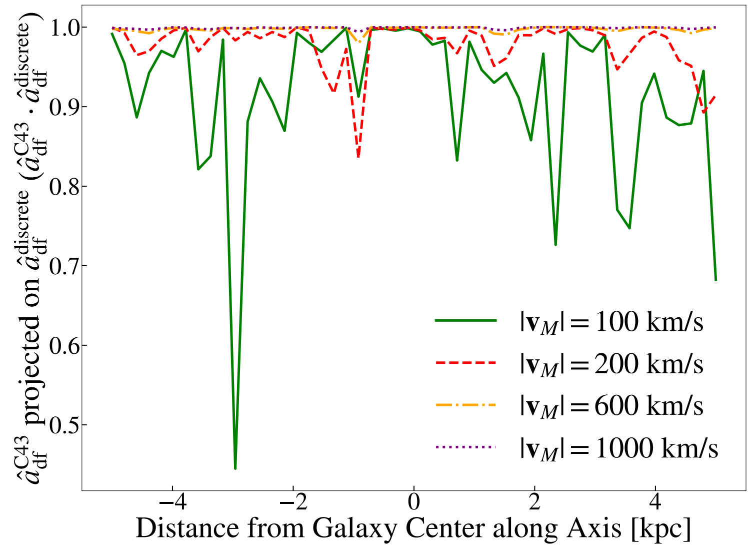

Figure 2.6: The unit direction vectors calculated from Chandrasekhar's projected on those from our DF formula. The test particle is the same as in Fig. 2.5 but with different velocities (still along the y axis). The difference of this value from 1 shows how mis-aligned the directions are. At most positions the directions are perfectly aligned for relative high velocities, yet at low velocities huge error could occur due to contributions from particles far apart.

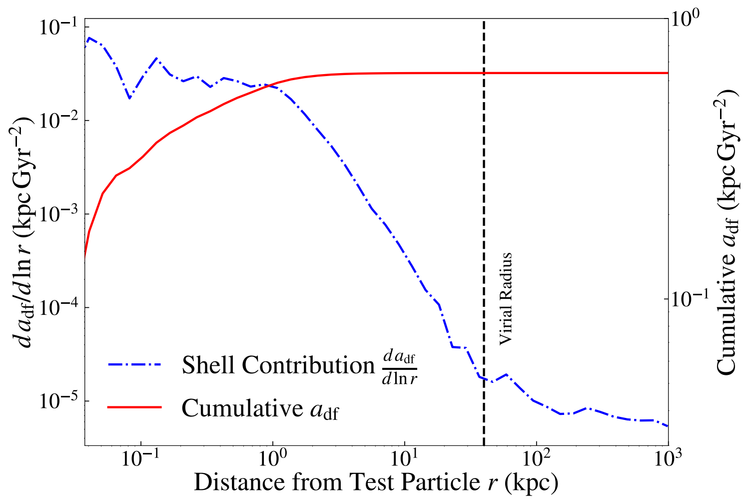

Figure 2.7: The contributions and cumulative results on DF from slices with different radius around a test particle. The test particle is a $10^5 M_\odot$ particle at $(0, 1, 0)$ with a 200 km/s velocity in the y direction. The particle's distance to the virial radius where we cutoff the sum is labelled with a black dashed line. We see that contributions are mostly from slices near the particle, while those from slices outside the virial radius are $\gtrsim$ 1000 times lower, suggesting that our cutoff makes little difference.

on the x-axis) in the same snapshot. At small scales ($r \lesssim 1\,\mathrm{kpc}$) around M, where the density field is *statistically* homogeneous (there are local fluctuations, but there is not a strong systematic dependence of density on distance r from M), we see the expected Coulomb log behavior ($da_{\rm df}/d\ln r \sim$ constant). At larger radii, the contribution falls rapidly. We can, for example, truncate the sum in Eq. 2.9 at the virial radius (labeled) with negligible loss of accuracy. This is expected if the galaxy follows a realistic density profile, as in e.g. an isothermal sphere, the density is not constant, but at $r \gg |\mathbf{x}_M|$ falls rapidly ($\propto r^{-2}$, giving rapid convergence). As expected, the behavior at larger r does motivate the value of $\ln\Lambda$ we fit: if we take $\Lambda = b_{\rm max}/b_{\rm min}$, with $b_{\rm min} \sim \max[(m/\rho)^{1/3},\, G\,M/V^2] \sim 1\,\mathrm{pc}$, and $b_{\rm max} \sim 1\,\mathrm{kpc}$, we obtain $\ln\Lambda \sim 7$, similar to our fitted value.

The above discussions are closely related to cases where the background field particles have a non-negligible physical bulk motion, like a wandering BH in a rotating disc-galaxy setup. While studying such simulations in detail is beyond the scope of this work, we comment that the rotating of star particles in the disc could largely affect the strength and direction of DF, since their phase space distribution departs significantly from homogeneity and isotropy. In an extremely dense galactic environment, we may expect the local disc particles with similar circular velocities contribute most to the BH's DF, such that the BH is boosted by the field particles around it, which is similar to the case we already studied. For a less dense setup, non-local (halo) particles with different circular velocity could be important, and their combined contribution to DF with local disc particles could make the BH dynamics more complicated. Our DF estimator, which applies to an arbitrary phase space distribution and counts the DF contribution from each individual field particle, would be ideal for studying such problems. Such topics will be studied in future work.

Briefly, one might wonder whether on sufficiently large scales, where the Universe becomes homogeneous and isotropic, $a_{\rm df}$ might begin to grow logarithmically again. However, even if we ignore finite speed-of-gravity effects (i.e. consider pure Newtonian gravity), on these scales the velocity must include the Hubble flow, so $\mathbf{v}_{\rm physical} = \mathbf{v}_{\rm peculiar} + H(z)\,\mathbf{r}$. In an isotropic pure Hubble-flow medium, the DF is identically zero, as there is always equal-and-opposite contributions to $\mathbf{a}_{\rm df}$ from the fact that $\mathbf{V} \propto \mathbf{r}$ (i.e. because $\langle \mathbf{V} \rangle = 0$ on all scales). If we consider a Hubble flow plus peculiar velocities, then expanding Eq. 2.9 appropriate for large r where $\langle \rho(r) \rangle \sim$ constant and $H\,r \gg \langle |\mathbf{v}_{\rm peculiar}(r)|^2 \rangle^{1/2}$, the contributions to the sum take the form $\sum G^2\, M\, \langle|\mathbf{v}_{\rm peculiar}(r)|^2\rangle^{1/2}\, \Delta m_i / H^3\, r^6 \;\propto\; \int \rho\, r^{-6}\, d^3\mathbf{x}$, which converges rapidly as $r \rightarrow \infty$.

Interpolating the Sub-Grid Model in Simulations With Variable Masses

Finally, one can easily imagine situations such as cosmological simulations with a range of BH masses where the DF forces are well-resolved for some targets (e.g. supermassive BHs with $M_{\rm BH} \sim 10^{10}\, M_\odot$) but not others (e.g. lower-mass BHs). In these cases applying Eq. 2.9 to all BHs would "double count" for some. A simple (albeit ad-hoc) approach to avoid double-counting is to multiply $\Delta\mathbf{a}^i_{\rm df}$ by a sigmoid or "switch"-like function $g(\Delta m_i/M_j, ...)$ which has the property $g(x, ...) \rightarrow 0$ for $x \rightarrow 0$ and $g(x, ...) \rightarrow 1$ for $x \rightarrow \infty$. It is beyond the scope of our paper here to develop and test such models, and from Fig. 2.3 we see one complication is that this should depend on how one treats the force softening (not just particle masses Δm_i), but a quick examination of the idealized tests in § 2.4 with different $M_{\rm BH}$ suggests (if we assume $\epsilon \sim \Delta x$, as usually adopted in such simulations) a simple function like $g = \min(1.0, \max(0, (3/\log(M_{{\rm BH},\,j}/\Delta m_i) - 1)/1.6))$ works reasonably well. Another advantage of our Eq. 2.9 is that because it operates in pairwise fashion, it can naturally deal with simulations with a wide range of Δm_i (a common situation), while attempting to apply such a correction factor "locally" to Eq. 2.1 leaves it ill-defined which value of Δm_i to use.

2.5 Conclusion

In numerical simulations, especially of star and galaxy formation, it is common to encounter the limit where DF *should* be experienced ($M \gtrsim m$) by some explicitly-evolved objects M (e.g. black holes, massive stars), but it cannot be *numerically* resolved ($\Delta m_i \gtrsim M$). As a result, there have been several attempts to develop and apply "on the fly" sub-grid DF models. Almost all of these amount to some attempt to calculate and apply the traditional C43 formula (Eq. 2.1) to the masses M at each time (see, e.g., [15, 20, 53, 44]). However, this can introduce a number of problems in practice, namely the ambiguity of kernel-dependent locally-defined quantities, inconsistency in applying force softening and momentum conservation, the semi-arbitrary choice of Coulomb logarithm, the necessity of assuming Maxwellian velocity distribution functions, and additional computational expenses for kernel estimates.

In this manuscript, we derive a new discrete expression for the DF force, $\mathbf{a}_{\rm df}$, given in Eq. 2.9. This formula is specifically designed for application to numerical simulations, either in post-processing, or "on the fly" when the DF forces cannot be resolved (e.g. when N-body particle masses are comparable to the BH mass M, as a "sub-grid" DF model). While still approximate, this has a large number of advantages compared to the traditional Chandrasekhar [12] (C43) analytic expression, including (1) it allows for an arbitrary distribution function, without requiring an infinite homogeneous time-invariant medium with constant density, Maxwellian velocity distribution, etc. (but it does reduce *identically* to a discrete form of the C43 expression, when these assumptions are actually satisfied); (2) it is designed specifically for simulations so it is represented only as a sum over quantities which are always well-defined in the simulation for all N-body particles (e.g. positions, velocities, masses), and does not require the expensive and fundamentally ill-defined evaluation of quantities like a "smoothed" density, background mean velocity/dispersion/distribution function, Coulomb logarithm, etc.; (3) it trivially incorporates force softening exactly consistent with how it is treated in-code, and generalizes to arbitrary multi-component N-body simulations with different species and an arbitrary range of particle masses; (4) it manifestly conserves total momentum, unlike N-body implementations of C43; and (5) it can be evaluated directly alongside the normal gravitational forces with negligible cost, and automatically inherits all of the desired convergence and accuracy properties of the N-body solver. We have implemented this "live" evaluation of Eq. 2.9 in GIZMO, and verified that all of the properties above apply, that it agrees well with our N-body simulations, and that the computational overhead of evaluating it alongside gravity in the tree is immeasurably small.

There are still uncertainties in our work. In our derivation of the discrete formula, we inserted an approximate integral kernel, which is not necessarily unique or best-behaved. We found that even if our discrete estimator closely agrees with the calibrated-Chandrasekhar DF estimator in our test problems, it still differs from the the high-resolution simulation results in terms of the detailed particle trajectories, which might be related to the fundamental Chandrasekhar-like assumptions we have made in our formula. We also note that it remains an open question how to accurately avoid "double counting" when some of the DF may be captured self-consistently by the N-body code while additional DF is modeled using our sub-grid model. This is especially the case when the system evolves (such as when supermassive black holes grow) and the fraction of "resolved" dynamical friction changes with time. Future work will be needed to make improvements on these points.

Acknowledgements

We thank Sophia Taylor for early contributions to the development of the discrete dynamical friction estimator, and Daniel Anglés-Alcázar for useful discussions. Support for LM & PFH was provided by NSF Collaborative Research Grants 1715847 & 1911233, NSF CAREER grant 1455342, NASA grants 80NSSC18K0562, JPL 1589742. LZK was supported by NSF-AAG-1910209, and by the Research Corporation for Science Advancement through a Cottrell Fellowship Award. CAFG was supported by NSF through grants AST-1715216, AST-2108230, and CAREER award AST-1652522; by NASA through grants 17-ATP17-0067 and 21-ATP21-0036; by STScI through grants HST-AR-16124.001-A and HST-GO-16730.016-A; by CXO through grant TM2-23005X; and by the Research Corporation for Science Advancement through a Cottrell Scholar Award. Numerical calculations were run on the Caltech compute cluster "Wheeler," allocations FTA-Hopkins supported by the NSF and TACC, and NASA HEC SMD-16-7592.

Data Availability

The data and source code supporting the plots within this article are available on reasonable request to the corresponding author.

References

[1] Emiliano Alessandrini et al. "Dynamical Friction in Multi-component Evolving Globular Clusters". In: *The Astrophysical Journal* 795.2, 169 (Nov. 2014), p. 169. DOI: 10.1088/0004-637X/795/2/169. arXiv: 1409.4987 [astro-ph.SR].

[2] Fabio Antonini and David Merritt. "Dynamical Friction around Supermassive Black Holes". In: *The Astrophysical Journal* 745.1, 83 (Jan. 2012), p. 83. DOI: 10.1088/0004-637X/745/1/83. arXiv: 1108.1163 [astro-ph.GA].

[3] E. Athanassoula et al. "Optimal softening for force calculations in collisionless N-body simulations". In: *Monthly Notices of the Royal Astronomical Society* 314 (May 2000), pp. 475–488. DOI: 10.1046/j.1365-8711.2000.03316.x. eprint: astro-ph/9912467.

[4] Enrico Barausse et al. "Massive Black Hole Merger Rates: The Effect of Kiloparsec Separation Wandering and Supernova Feedback". In: *The Astrophysical Journal* 904.1, 16 (Nov. 2020), p. 16. DOI: 10.3847/1538-4357/abba7f. arXiv: 2006.03065 [astro-ph.GA].

[5] James Binney and Scott Tremaine. *Galactic dynamics: Second Edition*. Princeton University Press, 2008.

[6] Pierre Boldrini, Roya Mohayaee, and Joseph Silk. "Subhalo sinking and off-centre massive black holes in dwarf galaxies". In: *Monthly Notices of the Royal Astronomical Society* 495.1 (Mar. 2020), pp. L12–L16. DOI: 10.1093/mnrasl/slaa043. arXiv: 2003.02611 [astro-ph.GA].

[7] Matteo Bonetti et al. "Dynamical evolution of massive perturbers in realistic multicomponent galaxy models I: implementation and validation". In: *Monthly Notices of the Royal Astronomical Society* 502.3 (Apr. 2021), pp. 3554–3568. DOI: 10.1093/mnras/stab222. arXiv: 2010.08555 [astro-ph.GA].

[8] Matteo Bonetti et al. "Dynamical friction-driven orbital circularization in rotating discs: a semi-analytical description". In: *Monthly Notices of the Royal Astronomical Society* 494.2 (Apr. 2020), pp. 3053–3059. DOI: 10.1093/mnras/staa964. arXiv: 2002.04621 [astro-ph.GA].

[9] Elisa Bortolas et al. "The role of bars on the dynamical-friction-driven inspiral of massive objects". In: *Monthly Notices of the Royal Astronomical Society* 512.3 (May 2022), pp. 3365–3382. DOI: 10.1093/mnras/stac645. arXiv: 2103.07486 [astro-ph.GA].

[10] M. Boylan-Kolchin, C.-P. Ma, and E. Quataert. "Dynamical friction and galaxy merging time-scales". In: *Monthly Notices of the Royal Astronomical Society* 383 (Jan. 2008), pp. 93–101. DOI: 10.1111/j.1365-2966.2007.12530.x. eprint: arXiv:0707.2960.

[11] J. S. Bullock et al. "A Universal Angular Momentum Profile for Galactic Halos". In: *The Astrophysical Journal* 555.1 (July 2001), pp. 240–257. DOI: 10.1086/321477. arXiv: astro-ph/0011001 [astro-ph].

[12] S. Chandrasekhar. "Dynamical Friction. I. General Considerations: the Coefficient of Dynamical Friction." In: *The Astrophysical Journal* 97 (Mar. 1943), p. 255. DOI: 10.1086/144517.

[13] Nianyi Chen et al. "Dynamical friction modelling of massive black holes in cosmological simulations and effects on merger rate predictions". In: *Monthly Notices of the Royal Astronomical Society* 510.1 (Feb. 2022), pp. 531–550. DOI: 10.1093/mnras/stab3411. arXiv: 2104.00021 [astro-ph.GA].

[14] Angela Collier. "Violent buckling benefits galactic bars". In: *Monthly Notices of the Royal Astronomical Society* 492.2 (Feb. 2020), pp. 2241–2249. DOI: 10.1093/mnras/stz3625. arXiv: 1912.08190 [astro-ph.GA].

[15] M. Colpi et al. "On the inspiral of massive black holes in gas-rich galaxy mergers". In: *The Multicolored Landscape of Compact Objects and Their Explosive Origins; AIP, Cefalu, Sicily (Italy)*. Ed. by T. di Salvo, G. L. Israel, L. Piersant L. Burderi G. Matt A. Tornambe & M. T. Menna. Vol. 924. American Institute of Physics Conference Series. Aug. 2007, pp. 705–714. DOI: 10.1063/1.2774931. arXiv: 0706.1851.

[16] T. J. Cox et al. "X-Ray Emission from Hot Gas in Galaxy Mergers". In: *The Astrophysical Journal* 643 (June 2006), pp. 692–706. DOI: 10.1086/503284. eprint: astro-ph/0504156.

[17] W. Dehnen. "Towards optimal softening in three-dimensional N-body codes - I. Minimizing the force error". In: *Monthly Notices of the Royal Astronomical Society* 324 (June 2001), pp. 273–291. DOI: 10.1046/j.1365-8711.2001.04237.x. eprint: astro-ph/0011568.

[18] T. Di Matteo et al. "Black Hole Growth and Activity in a Λ Cold Dark Matter Universe". In: *The Astrophysical Journal* 593 (Aug. 2003), pp. 56–68. DOI: 10.1086/376501. eprint: arXiv:astro-ph/0301586.

[19] Fani Dosopoulou and Fabio Antonini. "Dynamical Friction and the Evolution of Supermassive Black Hole Binaries: The Final Hundred-parsec Problem". In: *The Astrophysical Journal* 840.1, 31 (May 2017), p. 31. DOI: 10.3847/1538-4357/aa6b58. arXiv: 1611.06573 [astro-ph.GA].

[20] M. Dotti et al. "Dual black holes in merger remnants - I. Linking accretion to dynamics". In: *Monthly Notices of the Royal Astronomical Society* 396 (July 2009), pp. 1640–1646. DOI: 10.1111/j.1365-2966.2009.14840.x. arXiv: 0902.1525.

[21] José A. Flores Velázquez et al. "The time-scales probed by star formation rate indicators for realistic, bursty star formation histories from the FIRE simulations". In: *Monthly Notices of the Royal Astronomical Society* 501.4 (Mar. 2021), pp. 4812–4824. DOI: 10.1093/mnras/staa3893. arXiv: 2008.08582 [astro-ph.GA].

[22] Michael Y. Grudić and Philip F. Hopkins. "A general-purpose time-step criterion for simulations with gravity". In: *Monthly Notices of the Royal Astronomical Society* 495.4 (July 2020), pp. 4306–4313. DOI: 10.1093/mnras/staa1453. arXiv: 1910.06349 [astro-ph.IM].

[23] M. Atakan Gürkan, Marc Freitag, and Frederic A. Rasio. "Formation of Massive Black Holes in Dense Star Clusters. I. Mass Segregation and Core Collapse". In: *The Astrophysical Journal* 604.2 (Apr. 2004), pp. 632–652. DOI: 10.1086/381968. arXiv: astro-ph/0308449 [astro-ph].

[24] Y. Hashimoto, Y. Funato, and J. Makino. "To Circularize or Not To Circularize?-Orbital Evolution of Satellite Galaxies". In: *The Astrophysical Journal* 582 (Jan. 2003), pp. 196–201. DOI: 10.1086/344260. eprint: arXiv:astro-ph/0208452.

[25] Lars Hernquist. "An Analytical Model for Spherical Galaxies and Bulges". In: *The Astrophysical Journal* 356 (June 1990), p. 359. DOI: 10.1086/168845.

[26] P. F. Hopkins et al. "A Physical Model for the Origin of Quasar Lifetimes". In: *The Astrophysical Journal Letters* 625 (June 2005), pp. L71–L74. DOI: 10.1086/431146. eprint: astro-ph/0502241.

[27] Philip F. Hopkins. "A new class of accurate, mesh-free hydrodynamic simulation methods". In: *Monthly Notices of the Royal Astronomical Society* 450.1 (June 2015), pp. 53–110. DOI: 10.1093/mnras/stv195. arXiv: 1409.7395 [astro-ph.CO].

[28] Philip F. Hopkins et al. "FIRE-2 simulations: physics versus numerics in galaxy formation". In: *Monthly Notices of the Royal Astronomical Society* 480.1 (Oct. 2018), pp. 800–863. DOI: 10.1093/mnras/sty1690. arXiv: 1702.06148 [astro-ph.GA].

[29] Philip F. Hopkins et al. "Galaxies on FIRE (Feedback In Realistic Environments): stellar feedback explains cosmologically inefficient star formation". In: *Monthly Notices of the Royal Astronomical Society* 445.1 (Nov. 2014), pp. 581–603. DOI: 10.1093/mnras/stu1738. arXiv: 1311.2073 [astro-ph.CO].

[30] A. Just et al. "Dynamical friction of massive objects in galactic centres". In: *Monthly Notices of the Royal Astronomical Society* 411.1 (Feb. 2011), pp. 653–674. DOI: 10.1111/j.1365-2966.2010.17711.x. arXiv: 1009.2455 [astro-ph.CO].

[31] Simon J. Karl et al. "Dynamical evolution of massive black holes in galactic-scale N-body simulations - introducing the regularized tree code 'rVINE'". In: *Monthly Notices of the Royal Astronomical Society* 452.3 (Sept. 2015), pp. 2337–2352. DOI: 10.1093/mnras/stv1453. arXiv: 1507.01009 [astro-ph.GA].

[32] Ewa L. Łokas. "Anatomy of a buckling galactic bar". In: *Astronomy & Astrophysics* 629, A52 (Sept. 2019), A52. DOI: 10.1051/0004-6361/201936056. arXiv: 1906.03916 [astro-ph.GA].

[33] Linhao Ma et al. "Seeds don't sink: even massive black hole 'seeds' cannot migrate to galaxy centres efficiently". In: *Monthly Notices of the Royal Astronomical Society* 508.2 (Dec. 2021), pp. 1973–1985. DOI: 10.1093/mnras/stab2713. arXiv: 2101.02727 [astro-ph.GA].

[34] Xiangcheng Ma et al. "Dust attenuation, dust emission, and dust temperature in galaxies at z ≥ 5: a view from the FIRE-2 simulations". In: *Monthly Notices of the Royal Astronomical Society* 487.2 (Aug. 2019), pp. 1844–1864. DOI: 10.1093/mnras/stz1324. arXiv: 1902.10152 [astro-ph.GA].

[35] Xiangcheng Ma et al. "Simulating galaxies in the reionization era with FIRE-2: galaxy scaling relations, stellar mass functions, and luminosity functions". In: *Monthly Notices of the Royal Astronomical Society* 478.2 (Aug. 2018), pp. 1694–1715. DOI: 10.1093/mnras/sty1024. arXiv: 1706.06605 [astro-ph.GA].

[36] Xiangcheng Ma et al. "Simulating galaxies in the reionization era with FIRE-2: morphologies and sizes". In: *Monthly Notices of the Royal Astronomical

Society 477.1 (June 2018), pp. 219–229. DOI: 10.1093/mnras/sty684. arXiv: 1710.00008 [astro-ph.GA].

[37] Matias Mannerkoski et al. "Resolving the Complex Evolution of a Supermassive Black Hole Triplet in a Cosmological Simulation". In: *The Astrophysical Journal Letters* 912.2, L20 (May 2021), p. L20. DOI: 10.3847/2041-8213/abf9a5. arXiv: 2103.16254 [astro-ph.GA].

[38] Matias Mannerkoski et al. "Signatures of the Many Supermassive Black Hole Mergers in a Cosmologically Forming Massive Early-type Galaxy". In: *The Astrophysical Journal* 929.2, 167 (Apr. 2022), p. 167. DOI: 10.3847/1538-4357/ac5f0b. arXiv: 2112.03576 [astro-ph.GA].

[39] Xi Meng and Oleg Y. Gnedin. "Origin of giant stellar clumps in high-redshift galaxies". In: *Monthly Notices of the Royal Astronomical Society* 494.1 (May 2020), pp. 1263–1275. DOI: 10.1093/mnras/staa776. arXiv: 1910.03443 [astro-ph.GA].

[40] D. Merritt. "Optimal Smoothing for N-Body Codes". In: *The Astronomical Journal* 111 (June 1996), p. 2462. DOI: 10.1086/117980. eprint: astro-ph/9511146.

[41] Ben Morton, Sadegh Khochfar, and Jose Oñorbe. "Gaseous Dynamical Friction: A Challenge to Modern Hydrodynamical Schemes". In: *arXiv e-prints*, arXiv:2103.15848 (Mar. 2021), arXiv:2103.15848. arXiv: 2103.15848 [astro-ph.GA].

[42] Diptajyoti Mukherjee et al. "Fast Multipole Methods for N-body Simulations of Collisional Star Systems". In: *The Astrophysical Journal* 916.1, 9 (July 2021), p. 9. DOI: 10.3847/1538-4357/ac03b2. arXiv: 2012.02207 [astro-ph.GA].

[43] Eve C. Ostriker. "Dynamical Friction in a Gaseous Medium". In: *The Astrophysical Journal* 513.1 (Mar. 1999), pp. 252–258. DOI: 10.1086/306858. arXiv: astro-ph/9810324 [astro-ph].

[44] Hugo Pfister et al. "The erratic dynamical life of black hole seeds in high-redshift galaxies". In: *Monthly Notices of the Royal Astronomical Society* 486.1 (June 2019), pp. 101–111. DOI: 10.1093/mnras/stz822. arXiv: 1902.01297 [astro-ph.GA].

[45] Simon F. Portegies Zwart and Stephen L. W. McMillan. "The Runaway Growth of Intermediate-Mass Black Holes in Dense Star Clusters". In: *The Astrophysical Journal* 576.2 (Sept. 2002), pp. 899–907. DOI: 10.1086/341798. arXiv: astro-ph/0201055 [astro-ph].

[46] C. Power et al. "The inner structure of ΛCDM haloes - I. A numerical convergence study". In: *Monthly Notices of the Royal Astronomical Society* 338 (Jan. 2003), pp. 14–34. DOI: 10.1046/j.1365-8711.2003.05925.x. eprint: arXiv:astro-ph/0201544.

[47] Antti Rantala et al. "Post-Newtonian Dynamical Modeling of Supermassive Black Holes in Galactic-scale Simulations". In: *The Astrophysical Journal* 840.1, 53 (May 2017), p. 53. DOI: 10.3847/1538-4357/aa6d65. arXiv: 1611.07028 [astro-ph.GA].

[48] S. A. Rodionov and N. Y. Sotnikova. "Optimal Choice of the Softening Length and Time Step in N-body Simulations". In: *Astronomy Reports* 49 (June 2005), pp. 470–476. DOI: 10.1134/1.1941489. eprint: astro-ph/0504573.

[49] A. B. Romeo. "Modelling gravity in N-body simulations of disc galaxies. Optimal types of softening for given dynamical requirements". In: *Astronomy & Astrophysics* 335 (July 1998), pp. 922–928. eprint: astro-ph/9804276.

[50] Yanlong Shi, Michael Y. Grudić, and Philip F. Hopkins. "The mass budget for intermediate-mass black holes in dense star clusters". In: *Monthly Notices of the Royal Astronomical Society* 505.2 (Aug. 2021), pp. 2753–2763. DOI: 10.1093/mnras/stab1470. arXiv: 2008.12290 [astro-ph.GA].

[51] V. Springel. "The cosmological simulation code GADGET-2". In: *Monthly Notices of the Royal Astronomical Society* 364 (Dec. 2005), pp. 1105–1134. DOI: 10.1111/j.1365-2966.2005.09655.x. eprint: astro-ph/0505010.

[52] V. Springel and L. Hernquist. "Cosmological smoothed particle hydrodynamics simulations: a hybrid multiphase model for star formation". In: *Monthly Notices of the Royal Astronomical Society* 339 (Feb. 2003), pp. 289–311. DOI: 10.1046/j.1365-8711.2003.06206.x. eprint: astro-ph/0206393.

[53] M. Tremmel et al. "Off the beaten path: a new approach to realistically model the orbital decay of supermassive black holes in galaxy formation simulations". In: *Monthly Notices of the Royal Astronomical Society* 451.2 (Aug. 2015), pp. 1868–1874. DOI: 10.1093/mnras/stv1060. arXiv: 1501.07609 [astro-ph.GA].

[54] F. C. van den Bosch et al. "Substructure in Dark Halos: Orbital Eccentricities and Dynamical Friction". In: *The Astrophysical Journal* 515 (Apr. 1999), pp. 50–68. DOI: 10.1086/307023. eprint: arXiv:astro-ph/9811229.

[55] Daniel R. Weisz et al. "The Star Formation Histories of Local Group Dwarf Galaxies. I. Hubble Space Telescope/Wide Field Planetary Camera 2 Observations". In: *The Astrophysical Journal* 789.2, 147 (July 2014), p. 147. DOI: 10.1088/0004-637X/789/2/147. arXiv: 1404.7144 [astro-ph.GA].

[56] Emma Jane Weller et al. "Dynamics of intermediate-mass black holes wandering in the milky way galaxy using the illustris TNG50 simulation". In: *Monthly Notices of the Royal Astronomical Society* 511.2 (Apr. 2022),

pp. 2229–2238. DOI: 10.1093/mnras/stac179. arXiv: 2201.07234 [astro-ph.GA].

[57] Sarah Wellons et al. “Exploring supermassive black hole physics and galaxy quenching across halo mass in FIRE cosmological zoom simulations”. In: *Monthly Notices of the Royal Astronomical Society* 520.4 (Apr. 2023), pp. 5394–5412. DOI: 10.1093/mnras/stad511. arXiv: 2203.06201 [astro-ph.GA].

[58] Denis Yurin and Volker Springel. “An iterative method for the construction of N-body galaxy models in collisionless equilibrium”. In: *Monthly Notices of the Royal Astronomical Society* 444.1 (Oct. 2014), pp. 62–79. DOI: 10.1093/mnras/stu1421. arXiv: 1402.1623 [astro-ph.CO].

Chapter 3

NON-SINKING OF MASSIVE BLACK HOLES IN HIGH REDSHIFT GALAXIES

[1] Linhao Ma et al. "Seeds don't sink: even massive black hole 'seeds' cannot migrate to galaxy centres efficiently". In: *Monthly Notices of the Royal Astronomical Society* 508.2 (2021), pp. 1973–1985. DOI: 10.1093/mnras/stab2713.

Abstract

Possible formation scenarios of supermassive black holes in the early universe include rapid growth from less massive seed black holes (BHs) via super-Eddington accretion or runaway mergers, yet both of these scenarios would require seed BHs to efficiently sink to and be trapped in the galactic center via dynamical friction. This may not be true for their complicated dynamics in clumpy high-z galaxies. In this work we study this "sinking problem" with state-of-the-art high-resolution cosmological simulations, combined with both direct N-body integration of seed BH trajectories and post-processing of randomly generated test particles with a newly developed dynamical friction estimator. We find that seed BHs less massive than $10^8\,M_\odot$ (i.e., all but the already-supermassive seeds) cannot efficiently sink in typical high-z galaxies. We also discuss two possible solutions: dramatically increasing the number of seeds such that one seed can end up trapped in the galactic center by chance, or seed BHs being embedded in dense structures (e.g. star clusters) with effective masses above the mass threshold. We discuss the limitations of both solutions.

3.1 Introduction

Supermassive black holes (SMBHs) are of crucial importance in understanding galaxy formation and evolution. Observations of high-redshift quasars have confirmed the existence of SMBHs in the first billion years after the Big Bang ([34, 33, 76, 144, 96], see Figure 1 of [67] for a summary of observations). One of the long standing problems with models of SMBHs regards how they could possibly grow to such an enormous mass in a relatively short time period [132]. Recent discoveries have found both extremely massive SMBHs in the early universe (e.g. SDSS

J010013.02+280225.8 as a $1.2 \times 10^{10}\, M_\odot$ SMBH at $z = 6.3$, see [145]) and massive SMBHs in the extremely early universe (e.g. ULAS J1342+0928 as a $7.8 \times 10^{8}\, M_\odot$ SMBH at $z = 7.54$, see [7]). Continued discoveries of SMBHs at higher redshifts and masses naturally makes the problem even more intriguing [50, 99].

The existence of such massive black holes (BHs) at such early times poses many unsolved theoretical challenges. The most well-known is the "timescale problem": if seeds begin life as much less massive BHs, they would have to accrete at $\sim 100\%$ of the Eddington limit, for $\gtrsim 100\%$ of the age of the universe to reach their observed masses at $z > 7$. But observations at all lower redshifts, and theoretical estimates of the effect of SNe and BH feedback and BH dynamics all argue for much lower duty cycles (see, e.g., [68, 143, 2, 95, 48]). An obvious possible solution is to form more massive seeds: it has been proposed that primordial gas at high-z could experience inefficient cooling and fragmentation, producing massive Population III stars [19] which could collapse to BH seeds as large as $\sim 100\, M_\odot$ (e.g., [92, 78, 137, 51]) or even hyper-massive quasi-stars which could leave seeds as large as $\sim 10^4 - 10^5\, M_\odot$ (e.g., [20, 62, 63, 52, 66]), or directly collapsing to BHs as massive as $10^5\, M_\odot$ [79, 80]. Yet several authors argue that this requires vanishingly improbable conditions (see, e.g. [26] and discussions in § 5.2 and § 5.3 from [67]). But even these most-optimistic models only reduce the timescales by a logarithmic factor (as timescales scale as $\log(M_{\rm SMBH}/M_{\rm seed})$): even in these models, a phase of highly super-Eddington accretion – either resulting from runaway gas capture in high-gas-density regions (e.g. [91, 1, 82, 104, 109, 98]), or runaway mergers of massive stars (e.g. [108, 30, 71, 111]) or of other seed BHs (e.g. [27, 81]) at the center of a common potential minimum undergoing dynamical relaxation – is likely needed to explain SMBHs at $z > 7$ [49, 72, 103, 65, 114, 123].

However, in the past two decades, many independent studies (e.g., focused on galaxy mergers [42, 139, 22, 13, 131], dwarf galaxy evolution [125, 12, 16] and/or BH growth/dynamics [21, 138, 140, 3, 14, 105, 9, 23]) have pointed out that *all* of these models face a different and potentially even more severe challenge: what we refer to as the "sinking problem." In brief: essentially all of the rapid/efficient accretion models require that BHs sink "efficiently" and remain tightly bound to the galaxy center or potential minimum, where densities are on average highest. This usually requires a well-defined and stable dense central region in a relatively massive galaxy at lower redshift ($z \lesssim 4$) [130, 129, 112], but it may not be possible *dynamically* for even "high" mass seeds in realistic turbulent, clumpy, high-redshift

($z \gtrsim 7$) galaxies which undergo frequent dynamical perturbations (from e.g. mergers and "bursty" star formation and stellar feedback) and lack such central regions, especially in the short timescales available. Observationally, SMBHs are seen in the galactic center for most massive quasi-stellar objects (QSOs) (including those at high-z where imaging is possible, e.g. [136, 8, 28, 100, 141], and almost *all* massive galaxies comparable to QSO hosts at low redshifts, see e.g. [37, 39, 127, 43, 10]). But in spatially-resolvable low-z dwarf galaxies where star formation is known to be "bursty" [142, 118, 35, 134] and there is no well-defined dynamical center (see e.g. [69]), AGNs are extremely rare and those identified are randomly-scattered in position around the galaxy [110, 94]. As numerical simulations of high-z galaxies have improved in both numerical resolution and incorporating the physics of star formation and stellar feedback in a turbulent, multi-phase ISM [5, 3, 74], most models have converged toward the prediction that high-z galaxies are clumpy, bursty, chaotic, and dynamically-unrelaxed systems (even more so than most local dwarfs, e.g. [125, 97, 101, 89, 73, 93]), in agreement with deep observations with the *Hubble Space Telescope* (HST) [31, 102, 120]. Although there is some evidence for rotation in some hosts as noted by, e.g. [29, 135], they usually exhibit very large dispersion with $\sigma \sim v$, consistent with the simulations analyzed in [90], which does not challenge the conclusion. But in almost all models for rapid BH growth at near-Eddington or super-Eddington rates at $z \gtrsim 7$, the most optimistic assumption possible is usually made: namely that the BH remains "anchored" to the local potential minimum at the center of some well-ordered galaxy (e.g. [78]). To accrete gas, the BH must first capture it from the surroundings, and dimensional estimates for the "capture rate" drop highly super-linearly and extremely rapidly if the BH or background medium are moving relative to one another and/or if the BH lies outside of the galactic density maximum [64]. Models like runaway stellar mergers or BH-BH seed mergers for rapid growth fundamentally *depend* on the idea that both the "main seed" BH and all other stars/seeds are anchored to and sinking rapidly towards a common dynamical center [107, 46, 116, 41].

Historically, the "sinking" of BH seeds in high-z galaxies has largely been studied by assuming (1) seeds form at the centers of their proto-galaxies (rather than where stars form or at local density maxima), (2) galaxies are smooth objects with well-defined dynamical centers and centrally-peaked density profiles (i.e. bulge+disk or isothermal sphere models, rather than messy, non-relaxed systems), and (3) that BH and merging galaxy orbits decay according to dynamical friction (DF), which is a statistical accumulative effect caused by successive two-body gravity encounters, effectively acting like a "drag force" proportional to the BH/merging galaxy mass, in which the traditional [24] (C43) DF formula (assuming a homogeneous, infinite, idealized background medium) is applied. In this paper, we therefore revisit the "sinking" and "retention" problems for seed BHs in early galaxies. We use high-resolution cosmological simulations which include the crucial physics described above, combined with both direct ("live") N-body integration of seed BH trajectories and semi-analytic orbit integration in post processing, to follow a wide range of possible BH seed populations with different formation properties and locations. In post processing, we apply a modified DF estimator developed in a companion paper (Ma et al. in prep.), which is more flexible, accurate, and computationally efficient. In § 3.2 we describe our numerical simulations and the semi-analytic post-processing method.

The plan of this chapter is as follows: in § 3.3 we present the results from simulations and semi-analytical integration of sample orbits, and show that seed BHs are generally not able to sink efficiently or be retained even at high seed masses. In § 3.4, we discuss possible solutions to this problem, but also use our simulations to highlight how these solutions encounter still other problems. We summarize in § 3.5.

Throughout, we assume a standard flat ΛCDM cosmology with $\Omega_{\rm m} = 0.31$, $\Omega_\Lambda = 1 - \Omega_{\rm m}$, $\Omega_{\rm b} = 0.046$, and $H_0 = 68\,{\rm km\,s^{-1}Mpc^{-1}}$ (e.g. [106]).

3.2 Methods

Direct Simulations

Simulation Details

The simulations we study are re-simulations of the high-redshift ($z > 5$) galaxies presented in [89, 88, 86] based on the Feedback In Realistic Environments (FIRE; [54, 61]) project[1]. Specifically, we re-simulate the cosmological zoom-in simulations centered around the galaxies "z9m12a" and "z5m12b". Each of these represents a galaxy which has reached a halo mass $\gtrsim 10^{12}\,M_\odot$, a stellar mass $> 10^{10}\,M_\odot$, and a star formation rate $\gtrsim 150\,M_\odot\,{\rm yr}^{-1}$ by redshifts $z \sim 9$ and 5, respectively. As discussed in [86], these are chosen to be plausible analogues to the observed hosts of the highest-redshift, brightest QSOs. We note that while there are many other well-resolved galaxies in each cosmological zoom-in volume, we follow the most massive galaxy as it is the best candidate for a QSO host (but our conclusions about

[1] See the FIRE project website: `http://fire.northwestern.edu`.

failure of BHs to "sink" are even stronger in lower-mass galaxies).

The simulations are run with an identical version of the GIZMO[2] code [56] to their original versions in [88]. We use the mesh-less finite-mass (MFM) mode for solving hydrodynamic equations, with the identical FIRE-2 implementation of star formation and stellar feedback. The detailed baryonic physics included are all described extensively in [61], but briefly summarized here. Gas cooling includes a variety of processes (molecular, atomic, fine structure, recombination, dust, free-free, Compton, etc.) accounting for 11 separately tracked species (H, He, C, N, O, Ne, Mg, Si, S, Ca, and Fe), following the meta-galactic UV background from [36] with self-shielding. Stars are formed on the free-fall time from gas which is locally self-gravitating, molecular/self-shielded, denser than $n > 1000\,\mathrm{cm}^{-3}$, and Jeans-unstable following [57]. Each star particle, once-formed, represents an IMF-sampled population of known mass, age, and metallicity, and we explicitly account for stellar mass-loss (from OB and AGB outflows), core-collapse and Ia supernovae, and radiative feedback (in the forms of photo-ionization and photo-electric heating, and single and multiple-scattering radiation pressure), with rates tabulated from standard stellar evolution models [77].

The only difference between our simulations and those in [88] is that we re-run them including a "live" model for the formation of a broad spectrum of BH seeds, which are allowed to follow the full N-body dynamics. We emphasize that we do not artificially "force" BHs to follow the potential minimum or decay their orbits via any prescriptions of sub-grid DF, as in some cosmological simulations (e.g. [119, 60, 59, 58, 117, 6]).

We form BH seeds as follows: whenever gas meets all the star formation criteria above and is about to be transformed into a star particle, it is assigned a probability of instead becoming a BH seed. Instead of setting the probability as an adjustable constant as in, e.g. [11], it is weighted so that BH seeds form preferentially at the lowest metallicities [130] and highest surface densities/gravitational acceleration scales: specifically, we adopt $p \propto \exp(-Z/0.01\,Z_\odot)\,[1-\exp(-\Sigma/\Sigma_0)]$ where $\Sigma \sim M/R^2$ is integrated to infinity with the Sobolev estimator from [61] and $\Sigma_0 = 1\,\mathrm{g\,cm}^{-2}$, with $0.01\,Z_\odot = 1.4\times10^{-4}$. The metallicity weighting is motivated to be consistent with our current understanding of seed BH formation models, all requiring low-metallicities. For instance, Pop III stars and direct collapse models require

[2] A public version of GIZMO is available at `http://www.tapir.caltech.edu/~phopkins/Site/GIZMO.html`

low-metallicity primordial gas, while models of runaway mergers in star clusters strongly favor low-metallicity due to the lower mass-loss of massive stars in such environments [41]. The value of Σ_0 is specifically chosen because it is the density where analytic models [32] and numerical simulations [40, 44, 73] of individual star formation and BH growth have shown robustly that stellar feedback fails to "blow out" gas from the region efficiently, leading to runaway collapse/accretion. Exceeding this limit is required in many (but not all) models for massive BH seeds, either to prevent extended accretion disks from being destroyed by radiation from the accreting proto-quasi-star in direct collapse models, or as a necessary requirement to form super-dense star clusters, which are the essential prerequisite for star cluster-based IMBH formation models (e.g. runaway merging) to initiate rapid growth (see e.g. [116, 44]). The normalization of p is chosen to form the maximum number of seeds before they begin to represent an appreciable fraction of the total galaxy mass and therefore perturb the dynamics. If the particle is selected to become a BH seed, then we draw a BH seed mass uniformly in $\log M$ from $M = 10^3 - 10^7\, M_\odot$.

Because we wish to *only* study the dynamics of BH seeds, we ignore BH accretion or feedback. These will be studied in future work.

Resolution and Treatments of (Un)Resolved DF

Our "default" simulations have an approximately constant baryonic mass resolution of $\Delta m_i \sim 7000\, M_\odot$ and a 5 times higher DM resolution. This is sufficient to explicitly resolve N-body DF and other effects on the more massive seeds ($\gtrsim 10^5\, M_\odot$) we simulate: depending on the details of the gravity scheme, one generally achieves this for seed masses $M \gtrsim (10 - 100)\, \Delta m_i$.[3] To assess the effects of resolution on the dynamics of lower-mass BH seeds, we briefly re-simulate one of our galaxies after applying a super-Lagrangian (AMR-like) refinement step (e.g. [4]), to run with $800\, M_\odot$ baryonic resolution [4] , and measure whether there is any significant

[3]We enable the additional improvements to the gravitational timestep criteria, tidal force treatment, tree-opening, and integration accuracy detailed in [47, 45] where they were developed for simulations of star formation which require accurate evolution of stellar binaries and multiples, and set the force softening of the BH seeds to a very small value (10^{-3} pc) to represent real sink particles while using adaptive force softening for all other types to represent a smooth background. Detailed studies have shown that using adaptive softening as we do to ensure a smooth background force and with the more strict timestep and integration accuracy criteria used here, DF-like forces can be accurately captured for BHs with masses $\gtrsim$ 10 times the background particle mass, while with less accurate integration often used in cosmological simulations which do not intend to resolve few-body effects, the pre-factor is more like ~ 100 [133, 25, 18, 61, 105, 9, 16].

[4]Since the gravitational acceleration for BHs we study is strongly dominated by baryonic masses near the galactic center (we confirm the N-body forces from dark matter are sub-dominant by order-of-

difference in the "sinking rate" of seeds at any BH mass after 100 Myr. We find no measurable difference. There is a simple reason why the detailed numerical accuracy of the DF forces on such low mass seeds has little effect: the actual DF time for low-mass seeds (with e.g. $M \ll 10^5\,M_\odot$) is far longer than the Hubble time at these (high) redshifts, so DF plays an essentially negligible role in their dynamics on a *galactic* scale.

Semi-Analytic Orbital Evolution

Several authors who have implemented DF as a sub-grid routine (e.g., [105]) pointed out that sub-grid corrections could make a difference in the seed BH orbits. This may also be an issue for the accuracy of direct simulations, especially for low-mass seed dynamics. It is therefore useful to check the validity of our simulations with some alternative approach. Hence, we implement a semi-analytic analysis for the dynamics of BH seeds in post-processing, both as a check of our direct numerical simulations, and a way to gain analytic insight and explore even larger parameter spaces prohibited by the resolution and computational expense of our simulations. In post-processing, we can create an arbitrary sample of BH seeds at any desired time, and evolve them in time-independent potentials taken directly from the numerical simulations, allowing us to map the dynamics in detail.

To do so, we re-calculate the trajectories of 100 BH "test particles," taking background potentials from the simulations and adding an analytic DF force explicitly in post-processing, during which we apply a newly developed DF estimator that is discussed in a companion paper [85]. We approximate the N-body dynamics of a seed of mass M with an acceleration $\mathbf{a}_M = \mathbf{a}_{\rm ext} + \mathbf{a}_{\rm df}$, where $\mathbf{a}_{\rm ext}$ is the "normal" external gravitational acceleration on a test particle (computed identically to how the forces are computed in-code, for the adaptively force-softened potential from all N-body particles in the simulation). Then $\mathbf{a}_{\rm df}$ is the "DF force" — the next-order (non-linear) term which represents the drag force arising from deflection of bodies by M. Specifically, we adopt the following expressions which can be *directly* computed from the simulation data (either on the fly or in post-processing):

$$
\begin{aligned}
\mathbf{a}_{\rm ext} &= -\sum_i \left(S_i(r_i)\,\frac{G\,\Delta m_i}{r_i^2} \right) \hat{\mathbf{r}}_i \\
\mathbf{a}_{\rm df} &= \sum_i \left(\frac{\alpha_i\, b_i}{(1+\alpha_i^2)\, r_i} \right) \left(S_i(r_i)\,\frac{G\,\Delta m_i}{r_i^2} \right) \hat{\mathbf{V}}_i\,.
\end{aligned} \tag{3.1}
$$

magnitude or more), we did not refine the dark matter mass/force resolution in these re-simulations, as it is largely irrelevant to our conclusions.

Here $\mathbf{a}_{\rm ext}$ and $\mathbf{a}_{\rm df}$ are defined as a sum over all N-body particles i, with N-body masses Δm_i, relative position $\mathbf{r}_i \equiv \mathbf{x}_i - \mathbf{x}_M$, relative velocity $\mathbf{V}_i \equiv \mathbf{v}_i - \mathbf{v}_M$, $v \equiv |\mathbf{v}|$ and $\hat{\mathbf{v}} = \mathbf{v}/v$, with G the gravitational constant, $\alpha_i \equiv b_i\, V_i^2 / G\, M$ dimensionlessly parameterizing encounter strength, and $b_i \equiv r_i\, |\hat{\mathbf{r}}_i - (\hat{\mathbf{r}}_i \cdot \hat{\mathbf{V}}_i)\, \hat{\mathbf{V}}_i|$ the impact parameter. $S_i(r_i)$ is the usual dimensionless force-softening kernel to prevent numerical divergences, defined as

$$S_i(r_i) = \begin{cases} \frac{32}{3} q_i^3 - \frac{192}{5} q_i^5 + 32 q_i^6 & 0 \le q_i < \frac{1}{2} \\ -\frac{1}{15} + \frac{64}{3} q_i^3 - 48 q_i^4 + \frac{192}{5} q_i^5 - \frac{32}{3} q_i^6 & \frac{1}{2} \le q_i < 1 \\ 1 & q_i \ge 1\,. \end{cases} \tag{3.2}$$

We refer interested readers in our expression for $\mathbf{a}_{\rm df}$ to the companion paper [85]. But briefly, our expression reproduces exactly the classical [24] (C43) expression $\mathbf{a}_{\rm df}^{\rm C43} = 4\pi\, G^2\, M\, \rho\, \ln(\Lambda)\, V^{-2}\, [{\rm erf}(V/\sqrt{2}\sigma) - (2/\pi)^{1/2}\, (V/\sigma)\, \exp(-V^2/2\,\sigma^2)]\, \hat{\mathbf{V}}$ in cases consistent with the assumptions of C43, i.e. when the background distribution function is spatially homogeneous (constant density and velocity), time-invariant, Maxwellian, and single-component. But it allows more naturally for cases which violate these conditions. Our expression also removes the ambiguity of the C43 expression in estimating a number of ill-defined continuum quantities, when applied to discrete simulation N-body data (e.g. how and on what scales to evaluate ρ, σ, V, and what value of Λ to use). Usually, $\alpha_i \gg 1$ such that $\mathbf{a}_{\rm df} \propto \sum \alpha_i^{-1} \propto M$, which means as expected that the DF acceleration is the largest for the most massive BHs, and potentially negligible for small BHs.

3.3 Results

Direct Simulations

Here we present the results from direct simulations, focusing on the clustering behaviour of BH particles. In Figure 3.1 we show a projected image of the galaxy "z9m12a" at redshift $z = 10.4$, as a typical high redshift snapshot in our simulations. The left panel shows the total non-BH mass (i.e., including dark matter, gas, and stars) density distribution, with the galactic center located at the origin. The image shows the extremely clumpy appearance of typical high-z galaxies, with multiple local density maxima near the galactic center, consistent with both other simulations and observations. In the right panel, we over-plot the positions of BH particles near the galactic center. The color labels their masses, ranging from $10^3 - 10^7\, M_\odot$, which cover a wide range of seed BH masses from different formation scenarios. There is no significant position dependence upon mass for BH particles in the galaxy, with

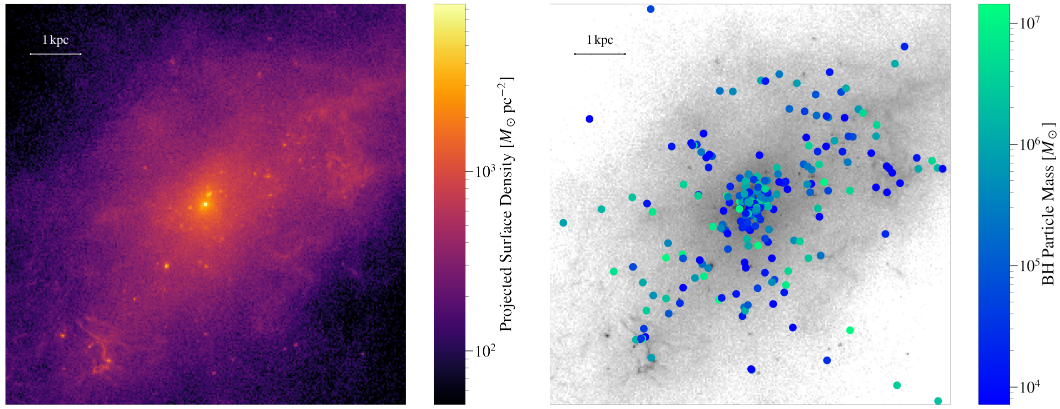

Figure 3.1: **Left:** Projected total non-BH mass (including dark matter, gas, and stars) density distribution of one of our simulations ("z9m12a") at redshift $z = 10.4$, as a typical simulation snapshot we analyze. The image shows the clumpy structure of high redshift galaxies. **Right:** The BH particles in this simulation at this particular snapshot, ranging from $10^3 - 10^7\ M_\odot$, covering a wide range of possible masses from different seed BH formation scenarios. BHs appear mostly randomly distributed in the galaxy, but with enhanced clustering near the galactic center. However we do not see significant seed-BH mass dependence, and the apparent galactic-center clustering simply reflects the overall concentration of mass (the galaxy effective radius here is $\sim$ kpc).

some mild clustering near the galactic center. No significant mass dependence is observed.

To analyse the sinking problem of seed BHs, we show the magnitudes of galacto-centric distance $\mathbf{r}$ and velocity $\mathbf{v}$ of BH particles selected from 9 different snapshots in Figure 3.2. Specifically, the BH particles are selected from snapshots in "z5m12b" at $z = 9.0, 7.7, 7.0, 5.9$, and 5.0, and snapshots from "z9m12a" at $z = 10.9, 10.4, 9.9$ and 9.5. Although snapshots at later redshifts contain BH particles that are already present at earlier redshifts in the same galaxy, the different snapshots are well separated in time such that the positions and velocities of these BH particles can be considered to be statistically independent. If a BH particle is located within 0.5 kpc from the galactic center with a (relative) velocity less than 10 km/s (Figure 3.2 shaded area), we consider it to have "efficiently" undergone sinking and trapping in the galactic center. Figure 3.2 suggests that none of our BH particles in the mass range of $10^3 - 10^7\ M_\odot$ has achieved this at the redshift they are observed. There is also no clear dependence of BH positions and velocities on their masses, indicating their dynamics is basically independent of their masses if BH masses are below $10^7\ M_\odot$, i.e. the dynamics is dominated by the mass-independent external gravity,

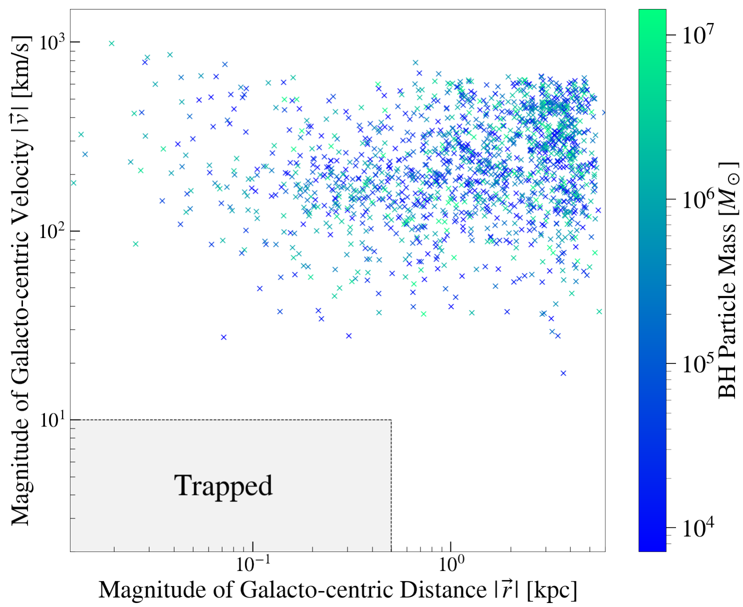

Figure 3.2: The magnitudes of velocities and galacto-centric distances of simulated BH particles for a general selection of snapshots in our simulations. We define a BH particle being trapped and efficiently sinking if it is located within < 0.5 kpc from the galactic center with a speed less than $10\,\mathrm{km\,s^{-1}}$ (shaded area). The colors label the mass of each BH particle. From our simulations there are no BH particles trapped in this manner, nor any significant dependence on their masses of their positions and velocities.

while the mass-dependent DF plays a negligible role.

Semi-Analytic Orbital Evolution

Here we present the results from semi-analytic post processing, with our new DF estimator, to cover a wider range of BH masses. Specifically, we select snapshots from "z5m12b" at $z = 5.0, 7.0, 9.0$ and "z9m12a" at $z = 9.5$. In each snapshot, we place 100 test particles to integrate their dynamics, whose initial parameters are generated in the following way: the masses are randomly selected from 100–$10^{10}\,M_\odot$ (uniformly sampling log of mass), while the initial positions and velocities are chosen randomly from star particles in the corresponding snapshot, which is not only a convenient sampling method, but physically motivated since we would expect seed BHs are mostly born in similar locations to star clusters. With such sampling, are also able to study the effects of initial galacto-centric distances/velocities on sinking (so we stress that our conclusions are completely independent of how we perform this sampling). In post processing, we ignore the dynamics of background particles, i.e. we apply a time-independent gravity potential, as we would expect the static background to represent random sample of typical chaotic high-z galaxies, not an accurate reflection of some certain galaxy. The assumption of a static but realistically clumpy mass distribution allows us to gain insight into the effects of spatial inhomogeneities in the gravitational potential expected in typical, chaotic high-z galaxies. However, the orbits that we calculate in this way are not necessarily fully realistic since they neglect the time dependence of the potential. We note, though, that time dependence of the potential seems unlikely to accelerate sinking relative to a static-potential calculation; if anything time-dependence of the potential could further contribute to keeping seeds away from the galactic center. The external gravity and DF are calculated by Equation 3.1. Essentially, the difference between our "live" dynamics simulations and these post-processing calculations allows us to see how the time-dependence of the potential alters (in aggregate) the dynamics of sinking BH seeds.

To further see how the "clumpiness" of the potential alters the BH dynamics, we re-run our semi-analytic orbit integration in a "spherically-smoothed" version of the potential. In these calculations, we take the exact same spherically-averaged mass profile from the full simulation snapshot studied above, $\rho(r) \equiv dM_{\rm enc}(< r)/4\pi\, r^2\, dr$ in narrow radial annuli dr, and then use this as the background potential for our orbit integration. So, by definition, this has the same spherically-averaged $M_{\rm enc}(< r)$ and circular velocity profile, but no substructure.

In Figure 3.3 we show several sample orbits for test particles of different masses in the $z = 7.0$ snapshot of "z5m12b" overlaid on its mass density distribution. The orbits in the original snapshots are shown in the upper panel, while in the lower panel we show the trajectories integrated from the spherically smoothed version of this snapshot, with the same test-particle initial conditions. The thin lines show the trajectories and the black cross shows the final positions of test particles. The test particles follow chaotic orbits in the clumpy snapshot with no significant dynamical center (as we would expect for a high-z galaxy). It appears that for the most massive test particles $M \gtrsim 10^8\, M_\odot$, their velocities significantly decrease within a Hubble time at $z = 7$ ($\sim 1\,$Gyr), and their final positions lie within the very central region of the galaxy. But there is no significant sinking for low-mass test particles. In the smooth galaxy the particles behave similarly, yet it takes a shorter interaction time for the most massive test particles to sink. The velocity evolution of one particular test particle of $8.7 \times 10^7 M_\odot$ is shown in Figure 3.4, and it is shown that the velocity decay timescale is about one order of magnitude shorter in the

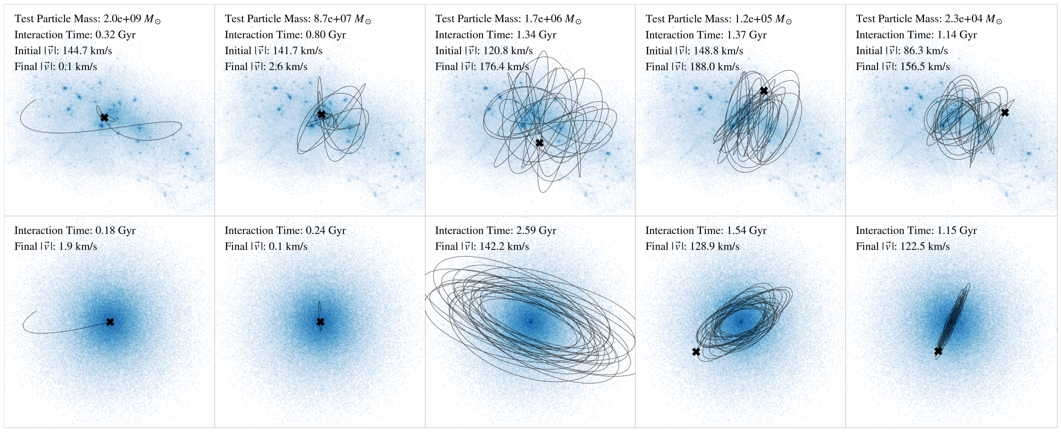

Figure 3.3: Sample orbits of several test particles (overlaid on top of the mass density distribution, shown in the blue colorscale) in the $z = 7$ snapshot of "z5m12b" (**upper**) and its "spherically smoothed equivalent" (**lower**) where we take the identical enclosed mass profile $M_{\rm enc}(< r)$ and re-distribute the mass to be a perfectly-spherically-symmetric potential. The thin lines show the trajectories and the black cross shows the final positions of test particles. Each panel is 8 kpc across in spatial scale. We find that in the high-z galaxy, the most massive test particles do sink to the galactic center within a Hubble time at $z = 7$ (~ 1 Gyr), while the low-mass seeds are simply experiencing chaotic orbits. In the smooth galaxy, the sinking behaviour is not very different for these five samples, yet for the massive seeds which are able to sink, their sinking time reduces drastically. This suggests that clumpy galactic backgrounds generally inhibit the sinking of massive seeds.

smooth galaxy compared to the clumpy galaxy. This suggests that the clumpy nature of early galaxies may increase the sinking time of seed BHs by an order of magnitude, by introducing chaotic dynamics to their orbits. In Figure 3.5 we show the initial and final positions of all test particles we integrate in this particular snapshot, and its spherically smoothed version. We also show their initial and final velocity magnitudes as a function of mass in the lower panel. In the clumpy galaxy, while the test particles are randomly distributed in the galaxy initially, those with $M \gtrsim 10^8\,M_\odot$ show clustering behaviour near the center after the integration, and their speeds decay to less than a few kilometers per second, indicating that they sink to the galactic center after the integration. The remaining low-mass particles remain scattered around, with no significant decay of their speeds. The smooth potential reduces the minimum sinking mass to $\sim 10^7\,M_\odot$, when test particles are integrated over an order of the Hubble time at $z = 7$ [5].

[5]There is a trend of increasing final speed with test particle mass in Figure 3.5 for the smooth galaxy. This turns out to be a reflection of the different integration time of these particles: we apply a timestep control proportional to $|v/a|$ to avoid numerical errors. The massive particles, with

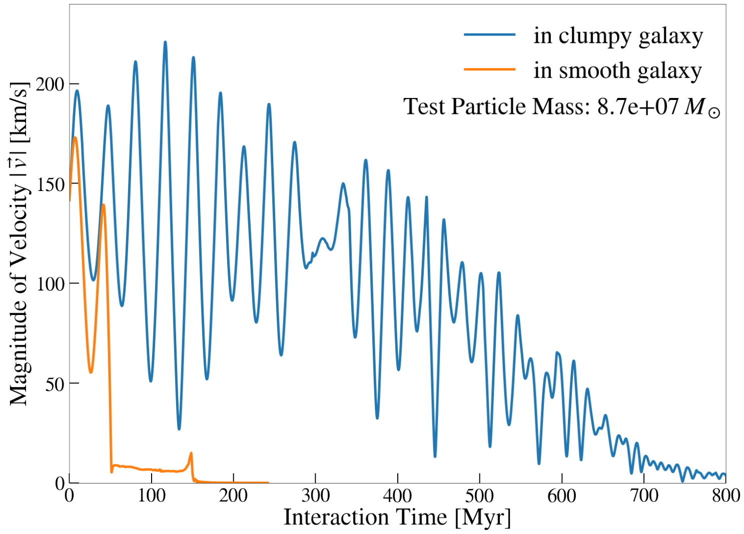

Figure 3.4: The evolution of the magnitude of the BH velocity as a function of interaction time for our integration of a $8.7 \times 10^7\, M_\odot$ test particle. We see that in both the clumpy and spherical smoothed galaxy, the velocity decays within 1 Gyr. But in the smooth galaxy the decay time is lower by about one order of magnitude than the clumpy case, suggesting again the clumpy and chaotic nature of early galaxies may drastically increase the sinking time of seed BHs.

It appears that the clumpy nature of early galaxies may increase the "minimum sinking mass" by one order of magnitude. It is worth noting that the sinking massive particles in the clumpy galaxy also do not sink exactly to the same place near the center (as they do in the smooth galaxy). This implies that a clear definition of galactic center with resolution of a few hundred pc is still ambiguous for these galaxies, and has potentially major implications for the demographics of BH-BH mergers at high redshift.

In Figure 3.6 we show the initial and final magnitudes of galacto-centric distance **r** and velocity **v** of all our test particles across different snapshots. The colored points show the final velocities and distances of test particles while the thin grey lines connect their final values with initial values. We define the "sinking" region in phase space as in § 3.3. Since we are covering a larger mass range of test particles than what we did in direct simulations for BH particles, some of the most massive particles do efficiently sink to the "trapped region" this time. Specifically, particles

larger DF (larger a), hence have smaller timesteps and shorter integration time compared to the less massive ones (see also the "interaction time" label in Figure 3.3), experiencing less deceleration in the integration. This effect does not appear in the clumpy galaxy, since the lack of dynamical centers of these galaxies makes the particle dynamics chaotic, and the gravity and DF for these particles balance each other when they reach the center, making the interaction time less important.

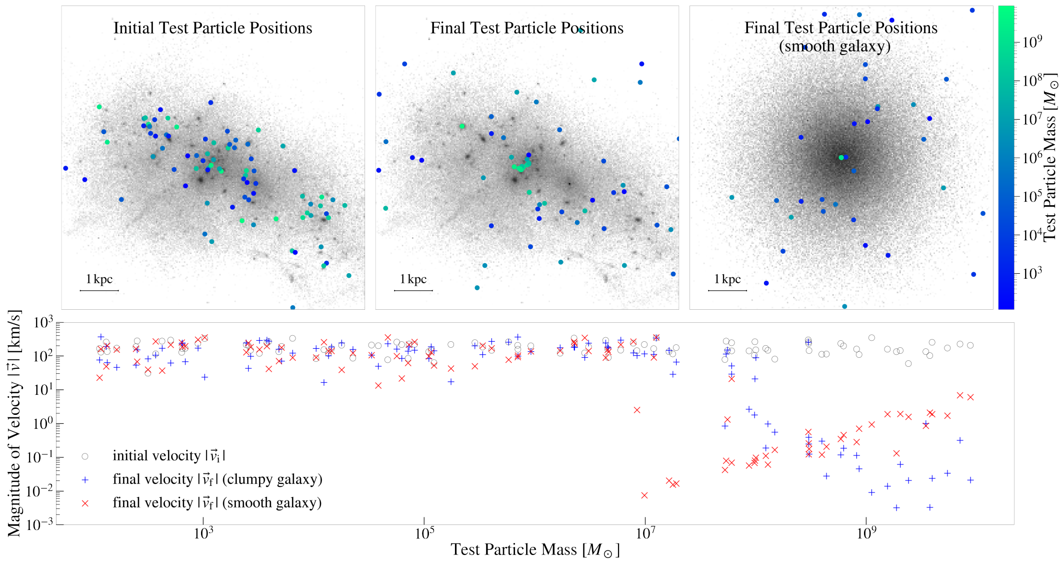

Figure 3.5: **Upper left:** The initial positions of test particles which we semi-analytically integrate, overlaid on the mass density distribution (grey) for "z5m12b" at redshift $z = 7$; **Upper middle:** The final positions of these test particles. **Upper right:** The final positions of these test particles integrated in the spherically smoothed galaxy. The colors label the test particle masses. **Lower:** The magnitude of initial velocities and final velocities as a function of the BH mass. We see that for the clumpy galaxy, the high mass ($M \gtrsim 10^8\,M_\odot$) test particles sink to the galactic center after the integration, while the low mass particles remain randomly distributed. For the smooth galaxy the minimum mass for sinking reduces to $M \gtrsim 10^7\,M_\odot$, about one order of magnitude lower. DF and sinking are negligible for the lower-mass seeds in both cases [5].

with $M \gtrsim 10^8 M_\odot$ sink to the center region of the galaxy after the integration, regardless of their initial positions and velocities. For low-mass ($M \lesssim 10^8 M_\odot$) particles, their final position and velocity distributions appear to be statistically similar to their initial configurations. This confirms the robustness of our results from direct simulations, in which all BH particles are less than $10^8\,M_\odot$ and are therefore not experiencing significant sinking.

It is also worth noting that the sinking criterion almost depends *entirely* on the particle mass, not on initial velocities/distances to galactic center. This is in contrast to what one would naively infer from the simplest DF-time calculations which assume a smooth potential with a constant circular velocity and BHs on slowly-decaying nearly-circular orbits, in which case the sinking time depends explicitly on the initial distances $t_{\rm sink} \propto r^2$ [15]. Physically, this can be explained by three factors: (1) for highly-eccentric or radial orbits, the dependence on initial radius is much

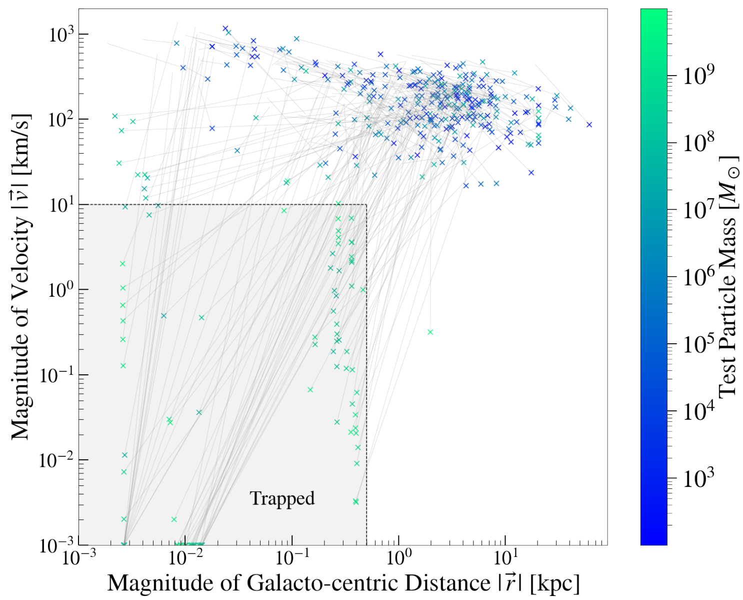

Figure 3.6: The initial and final magnitudes of velocities and galacto-centric distances of all our test particles across different snapshots. The colored points show the final velocities and distances (with any final velocities less than 10^{-3} km/s interpreted as 10^{-3} km/s for clarity). We define a BH particle as "trapped" as in Fig. 3.2. The thin grey line connects the final properties with initial properties of each particle. The colors label the mass of each particle. We can see that after our integration nearly all particles with masses $\gtrsim 10^8 M_\odot$ sink to the galactic center (with a significant decline of velocity and distance), yet lower-mass particles are still randomly distributed.

weaker, independent of the assumed density profile or details of the DF scaling [55]; (2) the chaotic dynamics of seed BHs in clumpy (i.e. non-smooth) galaxies effective erase the memories of their previous orbits, which makes the initial positions less important to their orbital decay; and (3) the traditional r^2 dependence of $t_{\rm sink}$ depends explicitly on the implicitly-assumed isothermal mass density profile of the galaxy – but more generally the DF acceleration scales as $a_{\rm DF} \propto \rho(r)/v_{\rm c}^2$. In a clumpy high-$z$ galaxy, however, the density ρ is not necessarily falling rapidly as in an isothermal sphere (and is not a trivial smooth monotonic function of galacto-centric radius), again wiping out the naively-predicted r-dependence of $t_{\rm sink}$.

3.4 Discussion

Possible Solutions

From both direct simulations and semi-analytic post-processing calculations, we have found that seed BHs less massive than $10^8\ M_\odot$ generally cannot sink to galactic centers via DF in high-z galaxies. To have at least one seed BH positioned in the galactic center so that it could accrete to $\sim 10^9\,M_\odot$ and provide a plausible origin for luminous high-redshift quasars, we discuss two categories of possible solutions.

Solution 1: A Large Number of Seeds, Forming Continuously

The first option is to use numbers as a trade off for efficiency: although one low-mass seed BH is not likely to sink and accrete, a large number (which we estimate quantitatively below) of low-mass seeds could possibly give an opportunity for a "lucky one" to sink and grow. Since the dynamics of BH particles and star particles are identically solved in our simulations (both as collisionless dynamics with external gravity), and the masses of star particles are around $10^3 M_\odot$, below the low-mass end where DF drag is significant, we can use the star particles in our simulation as an ensemble of test particles to estimate the fraction of stars and therefore relics (ignoring processes like kicks) which can be trapped in local clustering structures ("clumps"). We apply such analysis to two particular snapshots, namely, "z5m12b" at $z = 7.0$ and "z9m12a" at $z = 10.4$.

We are only interested in clumps broadly near the galactic center, hence we identify the four densest clumps within 1.6 kpc near the galactic center for each snapshot respectively, as shown in the upper panels of Figure 3.7. The center of the clumps are identified as the local density maxima, and their geometrical shapes are treated as spherically-symmetric with radius 100 pc enclosing almost all of the clump mass, a fair approximation as shown in Figure 3.7.

The lower left panel of Figure 3.7 shows the enclosed stellar mass and trapped stellar mass as a function of radius around each clump. If a star particle at radius r has a maximum possible apocentric radius r_{max} from the clump center (using the energy and angular momentum of each to evaluate its orbit, assuming the clump is static over its orbital timescale), we then say it is instantaneously enclosed within r and "trapped" within r_{max}. The gravity potential is calculated assuming a static potential around each clump with spherical symmetry (the clumps themselves, by definition, do not have substantial substructure). We see that the stellar masses in each clump ($M_{\mathrm{enclosed}}(|\mathbf{r}| < 100\,\mathrm{pc})$) range from 10^7 to $10^8\,M_\odot$. The mass fractions of trapped stars differ for different clumps and around 30%-50% of stellar mass could be trapped in a ~ 0.1 kpc radius of the clumps, yet this value decreases as we go deeper into the clump center, and the clumps could eventually trap only a few percent of enclosed star particles within ~ 50 pc. For all clumps, $\gtrsim 90\%$ of their

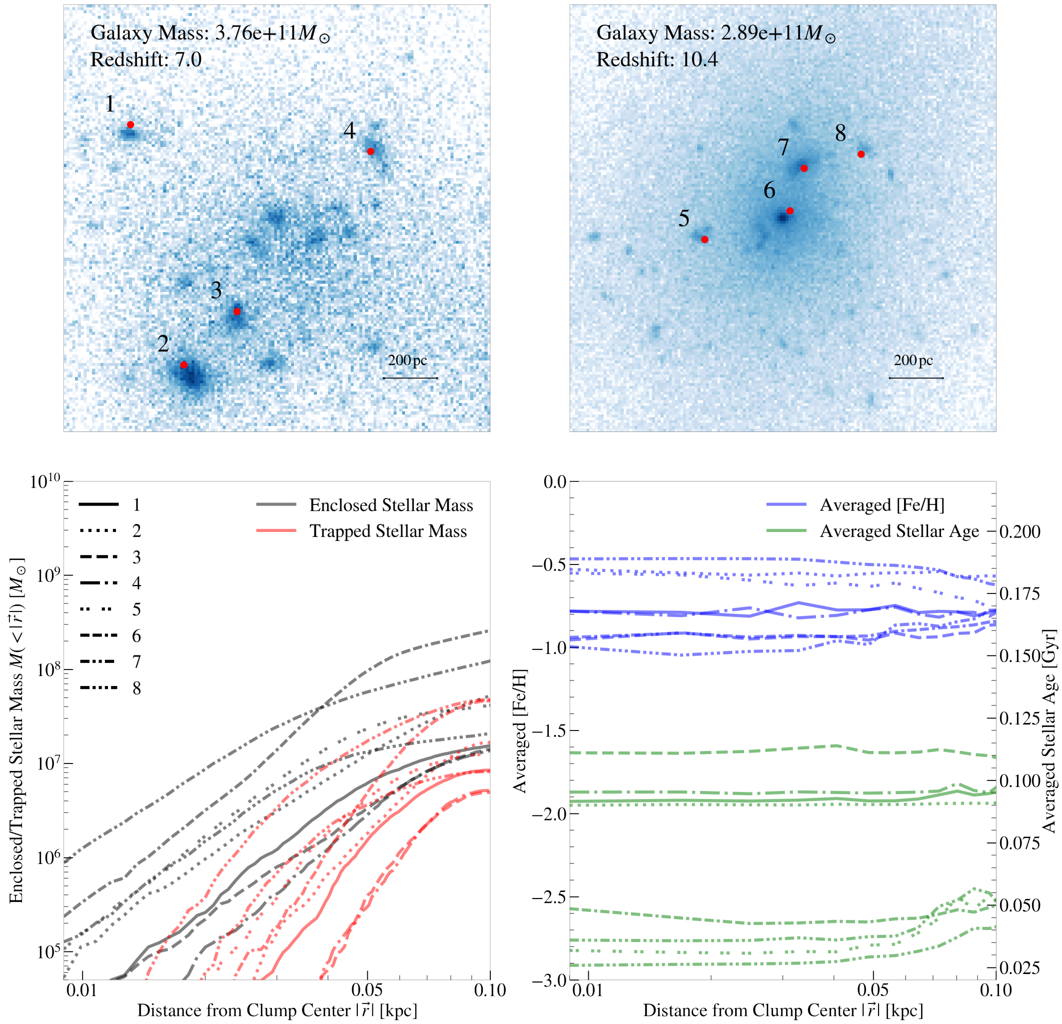

Figure 3.7: Behavior of low-mass test particles (e.g. stars) in individual high-density clumps (the "proto-bulge") within our simulations. **Upper Left:** Mass density distribution of a $z = 7$ galaxy with a total matter mass of $3.8 \times 10^{11}\, M_\odot$, where clumps 1-4 (the most massive bound sub-structures) are identified. **Upper Right:** Same for a $z = 10.4$ galaxy with a total matter mass of $2.9 \times 10^{11}\, M_\odot$, where clumps 5-8 are identified. **Lower Left:** Enclosed stellar mass inside each clump as a function of clump-centric distance, and the "trapped" mass (defined as the mass which is bound with apocentric radii inside this radius, as opposed to e.g. stars on "plunging" or unbound orbits; see text). **Lower Right:** Mean stellar metallicity and age for star particles inside each clump. We see that only a few percent of the enclosed stellar particles could be trapped well inside ($|\mathbf{r}| \lesssim 50\,$pc) the clumps. The metallicity and age also indicate that most star particles (hence the clump) are formed recently, which leads to new problems for some scenarios for seed BH growth.

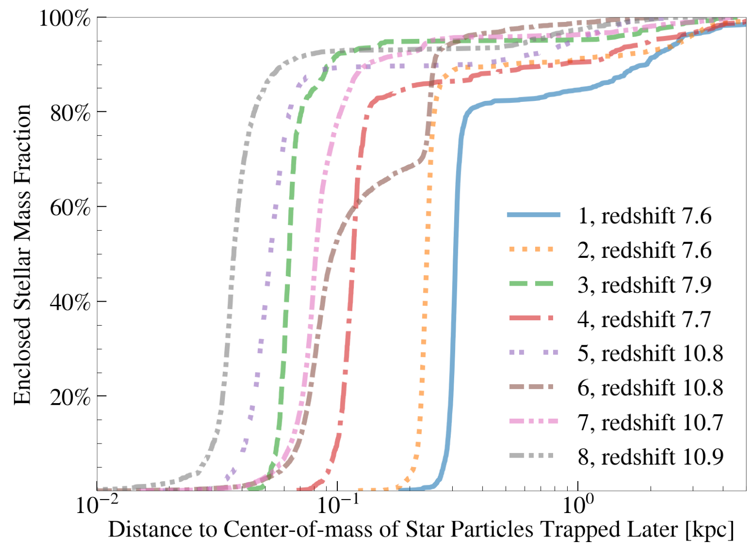

Figure 3.8: Distribution of "formation distances" for stars identified as enclosed in clumps in Fig. 3.7. We plot the cumulative distribution of distances between the center-of-mass of the main clump progenitor and the newly-formed star particle, at the time each star particle formed. We see that at least $> 80-90\%$ of star particles in these clumps form "in situ," at distances $\ll 1$ kpc from the clump center. Only a small fraction are formed outside the clump and later captured. Of those, almost all form in the same galaxy at distances < 5 kpc (as opposed to in satellites or different progenitor galaxies).

mass is in stars (as opposed to gas or dark matter).

Some low-mass objects are trapped in the dense clumps that represent the proto-bulge of these galaxies. But do they actually "sink" or get trapped dynamically, or did they simply form in-situ? To track the formation history of these star particles, we show their distances to their center-of-mass at the particular redshift when most of them are just formed [6] in Figure 3.8. It turns out for almost all clumps, $> 80-90\%$ of the star particles which we defined as "trapped" in these clumps are formed within $\ll 1$ kpc from the clump-progenitor center-of-mass, which means most trapped star particles are formed in-situ. The only seemingly exception is clump 6, where at first glance it appears that only about $\sim 70\%$ of the trapped star particles are in situ particles, but a detailed analysis shows that the remaining particles are actually formed in another clump which merges with clump 6, which does not challenge the conclusion (though it does relate to the hypothesis discussed in § 3.4). Taken together, this means that while it is possible in principle for "lucky" low-mass

[6] The simulations we use generate one snapshot per 0.01 scalefactor, which is sufficient for this exercise.

objects to be "trapped," it is quite rare: comparing the total stellar mass of the galaxy to the mass of stars which form ex-situ and are trapped near clump centers yields a probability of about $\sim 10^{-5} - 10^{-3}$ (depending on how generously we define "trapped") for a low-mass seed formed randomly in the galaxy to migrate to being "trapped" in the central $< 100\,\mathrm{pc}$ of a clump by $z \sim 7$.

Even if this occurs, the metallicity of the star particles which undergo this processes may create new problems for seed models. While the first Pop III stars or "direct collapse primordial clouds," which are candidates for forming massive seed BHs, could form very early at metallicities $Z \ll 10^{-5}\,Z_{\odot}$, the metallicity of star particles enclosed/trapped in clumps (even restricting to the "ex situ" stars) is generally much higher, and turns out to be the highest for the most massive clump, as shown in the lower right panel of Figure 3.7. This indicates that the trapped star particles in these clumps may not represent a fair sample of the ex-situ seed BH particles which are formed before the clumps themselves are formed. The earliest-forming stars are actually the *least* likely to be trapped in such clumps: they tend to form in mini-halos at much earlier times and therefore across many different progenitors and thus have to migrate in from the furthest distances, while the "ex situ but trapped" stars primarily still form in situ (*in the same galaxy*) just at distances of $\sim 1\,\mathrm{kpc}$ from the clump.

For all seed BHs, either in-situ or ex-situ, a related problem is related to the tension between the required clump masses and their ages. In many SMBH formation mechanisms, seed BHs have a higher probability both to be initially trapped and to subsequently accrete gas rapidly in the most dense/massive clumps, but these clumps are preferentially formed later, hence providing less time for BHs to migrate and to accrete. The average age of star particles inside clumps, as shown in the lower right panel of Figure 3.7, is far less than the Hubble time at the redshift we examined, providing a strict constraint on duty cycle if seed BHs are indeed hyper-Eddington accreting to become SMBHs in these clumps. Nevertheless, it is worth noting that SMBH seeding prescriptions are still highly uncertain, and other mechanisms may be able to circumvent these constraints.

Solution 2: High "Effective Masses" for Seeds

From the semi-analytic calculations in section 3.3 we have found that only seed particles as massive as $\gtrsim 10^{8}\,M_{\odot}$ can efficiently or reliably sink to galactic centers in a Hubble time. Such a large mass, however, is already a SMBH. On the other hand, our analysis in the previous section has shown that dense young star clusters as massive as $10^7 - 10^8\, M_\odot$ *are* present near the galactic center. In the previous section we also show that most trapped star particles within those clumps are already formed in situ. This suggests another possibility: while randomly formed seed BHs are generally not massive enough to decelerate individually via DF, their preferential formation in tightly bound structures with large "effective mass" is more realistic, as clusters could scatter with other components in the galaxy and sink effectively to the galactic center. Indeed, in [87] we show that the most-massive clumps do merge efficiently as these simulations are run to lower redshift and form the "proto-bulge" of the galaxy.

There have been numerous papers arguing that runaway mergers in dense globular (star) clusters are a potential way to produce intermediate mass black holes (IMBHs, with typical masses $10^2 - 10^5\, M_\odot$, see, e.g. [107, 46, 116, 41]), which naturally becomes a preferential way to embed massive BH seeds in dense clusters as described above. Such channels, however, suffer from other problems like large gravitational recoils that can remove the formed IMBHs from the cluster (e.g. [53]). There are also works arguing that gas accretion in nuclear star clusters (NSCs) and starburst clusters can also build up the mass of IMBHs rapidly [75, 98], which could be another way to apply this solution here. Yet observations have put upper limits on IMBHs masses (e.g. [83, 84, 70, 146]), which introduce additional constraints on these channels. It should also be noted that, while globular clusters are usually assumed to be mainly pristine clusters that formed at very high redshift in mini-halos, hence define an "old" population for astrophysicists in the local universe, they are not so much older than the stars at $z \gtrsim 7$. In fact, the overwhelming majority of the clusters form *in-situ* in the galaxy as it evolves from in-situ gas, not from mini-halos merging in. This means that the metallicity and timing problems discussed in § 3.4 apply to this scenario, as well.

Comparisons to Other Works

Our conclusions are consistent with other recent works focusing on slightly different aspects of this problem. For instance, [113] and [124] study the co-evolution of SMBH pairs, finding that galactic clumps (originated either from high-z star forming regions or a clumpy interstellar medium created by galaxy mergers) significantly perturb their orbital evolution, which potentially delay the decay process. [124] and [125] also point out that SMBH/IMBH pairs are still separated by $0.1 - 2\,\mathrm{kpc}$ after $\sim 1\,\mathrm{Gyr}$ in their simulations, which is consistent with our findings that no well-defined galactic centers can be identified on sub-kpc scales under these conditions. [17] simulate a $10^6\,M_\odot$ BH in a *non-clumpy* galaxy embedded in a cosmological environment at $z = 6 - 7$ and they show that DF torques are usually unimportant compared to the large-scale stochastic gravitational torques in determining the BH decay, even if no clumpy structures are considered. These works support our conclusion that the chaotic structures of high-z galaxies could drastically change the sinking timescale (hence the minimum sinking mass), if only DF is considered.

[105] presented a complementary study to ours, focusing on more idealized simulations analogous to lower-redshift systems, and a smaller number of test cases, but considering in more detail many of the numerical details of "live" sub-grid BH DF treatments (e.g. explicitly adding an analytic DF force term in low-resolution simulations). They concluded that *even in* idealized galaxies designed by construction with a well-defined dynamical center and a single, massive, centrally-peaked bulge (e.g., an exponential-disk and an Hernquist bulge), lower-level clumpiness in the gas (e.g., GMCs with typical masses $\sim 10^5 - 10^6\,M_\odot$) would drive wandering or ejection of BHs with seeds less massive than $\sim 10^5\,M_\odot$. They hence concluded that $10^5\,M_\odot$ is the minimum required mass for a BH to be well stabilized in the center of its host. Since observed star-forming clumps or complexes are much more massive at high redshifts (e.g., [122, 38, 121]), this criterion should only move to higher masses at high-z, consistent with our findings. Further, from post-processing cosmological simulations of massive galaxies with well-defined dynamical centers merging at $z < 6$, [105] also concluded that it was crucial that BHs are already well-anchored to the galaxy centers before and throughout mergers, and that the centers are well-defined and dense enough to avoid tidal disruption, in order for BHs to "sink." They specifically concluded that it was crucial that BHs be embedded either in a dense satellite nucleus or a massive nuclear star cluster. This is essentially identical to our "solution 2" above. [105] also noted that in the cosmologically simulated galaxies at earlier times, when the universe is < 1 Gyr old, even with their most massive ($\sim 10^5\,M_\odot$) seeds, the model for DF does not help in keeping BHs in the center, as the galaxy is so chaotic that BHs wander no matter the implementation of DF. This is again in good agreement with our conclusion.

A recent study by [126] provides another excellent illustration of our key conclusions, in a single case-study of a galaxy simulation with "live" AGN accretion and feedback. While the authors found that they could produce rapid BH growth by $z \sim 6$, they (1) had to impose a sub-grid DF model with an artificial superlinear density dependence ($\propto \rho^3$ at high densities) designed to "anchor" BHs into high-density regions (essentially our solution 2, again); (2) still found almost no BH growth until $z \lesssim 8$, after the galaxy reaches $M_* \gg 10^9\,M_\odot$ and forms a dense, strongly-peaked and well-defined central "proto-bulge" structure, very much like the late-time-forming structures we argue are necessary for BH capture and retention; and (3) still only reach peak luminosities $\ll 10^{43}\,\mathrm{erg\,s^{-1}}$ in X-rays, about a factor of $\sim 10^3 - 10^4$ less-luminous than the most luminous QSOs observed at these redshifts [115], which makes them still challenging to form.

There are some recent studies which might appear to be in contrast to our results at first glance. For instance, [128] has shown that host galaxies could aid SMBHs to shorter sinking timescales, and the ROMULUS simulations [130, 129, 112] argue that it is possible to grow massive black holes by intermediate redshifts. But a closer comparison shows these simulations are consistent with all of our key conclusions. In these studies, the BHs are, as the authors note [128], embedded in nuclear regions of the host galaxy, which are dense enough to avoid tidal disruption and much more massive than the BHs. The nuclear regions, with high "effective mass", hence sink as a whole — again following our "solution 2" above. This is effective because these studies focus on cases where the galaxies are already massive, with unambiguous massive central peaks in their density profiles at relatively low redshift (with $z \lesssim 2 - 4$, cf. Fig 4 in [128]). Moreover, in e.g. ROMULUS, the simulations have an effective seed mass $\sim 10^6 - 10^7\,M_\odot$[7], close to our sinking mass threshold in a smooth galaxy. These demonstrate that, given enough time and a pre-existing massive density peak to "anchor" a SMBH, BHs can indeed grow following e.g. our solution 2 as speculated above. Our focus here is essentially on how the "initial conditions" of these simulations (at earlier times and smaller mass and spatial scales) could arise. We focus on galaxies at much higher redshifts, where those dense central regions either do not exist, or have formed relatively recently (e.g. $z < 9$) and one wishes to form an extremely-massive SMBH by $z > 7$, significantly shortening the available time for BH growth, especially from extremely low-mass seeds.

3.5 Conclusion

In this study, we explore high-resolution cosmological galaxy formation simulations to understand the dynamics of BH seeds at high-z and their implications for SMBH formation and growth. Our simulations and semi-analytic DF calculations show

[7] The authors note that their seed criterion often produces multiple seeds in the same kernel which are instantly merged, producing a range of effective initial seed masses.

that BH seeds cannot efficiently "sink" to galaxy centers and/or be retained at high redshifts unless they are extremely massive already, $M > 10^8\,M_\odot$, i.e. already SMBHs. We show that this threshold is at least an order-of-magnitude higher than what one would expect in a spherically-symmetric smooth galaxy potential, as commonly adopted in analytic or older simulation calculations which could not resolve the complex, clumpy, time-dependent sub-structure of these galaxies. For smoother galaxies, this mass threshold reduces to $10^7\,M_\odot$, which does not change the key conclusion.

We therefore join the growing number of recent studies by different groups which have reached similar conclusions [see e.g. 3, 14, 131, 105, 12, 9, 16]. All of these studies, like ours, have concluded that this "sinking problem" for BH seeds may, in fact, be even more challenging than even other well-known challenges for explaining the formation and growth of the first SMBHs with masses $\gg 10^9\,M_\odot$ in galaxy centers at redshifts $z > 7$. Our contributions to extending this previous work include: (a) studying fully-cosmological simulations with higher resolution, a broader range of redshifts, a much broader spectrum of BH seed masses, and different (sometimes more detailed) explicit models for stellar feedback; (b) comparing direct cosmological simulations which only resolved N-body dynamics to semi-analytic post-processing models for DF, to verify that these conclusions are robust; and (c) extending our comparisons to the "test particle limit" by treating all stars as possible BH seeds.

Like these other studies, we qualitatively conclude that the chaotic, rapidly time-evolving, clumpy, bursty/dynamical nature of high-redshift galaxies, coupled to the very short Hubble times ($\lesssim 1$ Gyr) make it nearly impossible for any lower-mass seeds to efficiently "migrate" from $\gtrsim 1$ kpc scales to galaxy centers, and is far more likely to eject seeds than to retain them. Like these authors concluded, the clumpy, bursty nature of the ISM is crucial for these conclusions: so this can only been seen in simulations which resolve the cold phases of the ISM and explicitly model stellar feedback. It is also worth noting that for low-mass galaxies (the progenitors where, in most models, seeds are supposed to have formed), even at $z \sim 0$, clumpiness and burstiness are ubiquitous, and it is not simply a question of dynamical perturbations but even more basically of the fact that *dwarf and high-redshift galaxies do not have well-defined dynamical centers* to which anything *could* "sink." This is true even for well-evolved galaxies such as the LMC today.

In fact, we show that even the extremely massive BHs ($\gtrsim 10^8\,M_\odot$) which do "sink" actually do not sink to the same location at sub-kpc scales, where their migration stalls. This has potentially profound implications for LISA detections of SMBH-SMBH mergers in high-redshift galaxies. Essentially, the "last parsec problem" so well-studied in the extremely dense, smooth, well-defined bulges of $z = 0$ galaxies (where the Hubble time is long) becomes a "last kiloparsec problem" in these galaxies.

Solutions to the "sinking problem" for SMBH growth/formation generically fall into one of two categories which we discuss in detail. (1) Either seeds form "in situ" when the massive bulge finally forms and creates a deep central potential, or a large number of seeds form so that even the infinitesimally small fraction which have just the right orbital parameters to be "captured" by this bulge can exist. In either case, the problem is that we show this deep central potential well does not form until quite "late," at redshift $z \lesssim 9$, from gas and stars which are already highly metal-enriched (metallicities $\gtrsim 0.1\,Z_{\odot}$). This would mean popular speculative BH seed formation channels like Pop III relics or "direct collapse" from hyper-massive quasi-stars could not provide the origin of the SMBHs. Moreover, the combination of the fact that this occurs late, and that the stellar IMF is "normal" at these metallicities, means that the "timescale" problem is much more serious: stellar-relic BHs, if primarily growing by accretion in such massive bulges, must grow from $\sim 10\,M_{\odot}$ to $\gg 10^{9}\,M_{\odot}$ in $\lesssim 200\,\mathrm{Myr}$ — requiring sustained highly super-Eddington accretion. Alternatively (2) "seed" BHs must have enormous "effective" masses to form early and remain "trapped" and/or sink efficiently to the growing galaxy center. Of course, BHs "born" with $M_{\mathrm{BH}} \gg 10^{7}\,M_{\odot}$ would solve this, but only by bypassing any stage that could be called a "seed" (moreover, no serious models involving standard-model physics can produce seeds of such large mass). However, models where seeds preferentially form tightly-bound in dense star cluster centers owing to physics not modeled here (for example, runaway stellar mergers in the center of dense, high-z massive star clusters; see [116]) could (if the cluster is sufficiently dense) have an "effective" dynamical mass for our purposes of roughly the cluster itself, which could reach such large values. This suggests these regions may be promising sites for SMBH seed formation.

In future work, we will explore the role of BH accretion and feedback, and more explicitly consider models where BH seeds form in resolved star clusters, as well as a wider range of galaxy simulations. It is likely that *all* of the scenarios above require a sustained period of super-Eddington accretion, so we will also explore whether this requires seed BHs residing (or avoiding) certain regions within high-z galaxies. We have also neglected models where non-standard model physics (e.g. dissipative dark matter, primordial BHs) allows for new formation channels and test-body dynamics. We will also explore new applications of our numerical DF approximator, in a variety of other interesting contexts (e.g. pairing of SMBHs in massive galaxy mergers at low redshifts).

Acknowledgements

We thank Zuyi Chen and Alessandro Lupi for useful discussions. Support for LM & PFH was provided by NSF Research Grants 1911233 & 20009234, NSF CAREER grant 1455342, NASA grants 80NSSC18K0562, HST-AR-15800.001-A. DAA acknowledges support by NSF grant AST-2009687 and by the Flatiron Institute, which is supported by the Simons Foundation. CAFG was supported by NSF through grants AST-1715216 and CAREER award AST-1652522; by NASA through grant 17-ATP17-0067; and by a Cottrell Scholar Award and a Scialog Award from the Research Corporation for Science Advancement. Numerical calculations were run on the Caltech compute cluster "Wheeler," allocations FTA-Hopkins supported by the NSF and TACC, and NASA HEC SMD-16-7592.

Data Availability

The data and source code supporting the plots within this article are available on reasonable request to the corresponding author.

References

[1] Tal Alexander and Priyamvada Natarajan. "Rapid growth of seed black holes in the early universe by supra-exponential accretion". In: *Science* 345.6202 (Sept. 2014), pp. 1330–1333. DOI: 10.1126/science.1251053. arXiv: 1408.1718 [astro-ph.GA].

[2] Marcelo A. Alvarez, John H. Wise, and Tom Abel. "Accretion onto the First Stellar-Mass Black Holes". In: *The Astrophysical Journal Letters* 701.2 (Aug. 2009), pp. L133–L137. DOI: 10.1088/0004-637X/701/2/L133. arXiv: 0811.0820 [astro-ph].

[3] D. Anglés-Alcázar et al. "Black holes on FIRE: stellar feedback limits early feeding of galactic nuclei". In: *Monthly Notices of the Royal Astronomical Society* 472 (Nov. 2017), pp. L109–L114. DOI: 10.1093/mnrasl/slx161. arXiv: 1707.03832.

[4] Daniel Anglés-Alcázar et al. "Cosmological Simulations of Quasar Fueling to Subparsec Scales Using Lagrangian Hyper-refinement". In: *The Astro-*

physical Journal 917.2, 53 (Aug. 2021), p. 53. DOI: 10.3847/1538-4357/ac09e8. arXiv: 2008.12303 [astro-ph.GA].

[5] Daniel Anglés-Alcázar et al. "Cosmological Zoom Simulations of z = 2 Galaxies: The Impact of Galactic Outflows". In: *The Astrophysical Journal* 782.2, 84 (Feb. 2014), p. 84. DOI: 10.1088/0004-637X/782/2/84. arXiv: 1303.6959 [astro-ph.CO].

[6] Daniel Anglés-Alcázar et al. "Gravitational torque-driven black hole growth and feedback in cosmological simulations". In: *Monthly Notices of the Royal Astronomical Society* 464.3 (Jan. 2017), pp. 2840–2853. DOI: 10.1093/mnras/stw2565. arXiv: 1603.08007 [astro-ph.GA].

[7] Eduardo Bañados et al. "An 800-million-solar-mass black hole in a significantly neutral Universe at a redshift of 7.5". In: *Nature* 553.7689 (Jan. 2018), pp. 473–476. DOI: 10.1038/nature25180. arXiv: 1712.01860 [astro-ph.GA].

[8] Eduardo Bañados et al. "The z = 7.54 Quasar ULAS J1342+0928 Is Hosted by a Galaxy Merger". In: *The Astrophysical Journal Letters* 881.1, L23 (Aug. 2019), p. L23. DOI: 10.3847/2041-8213/ab3659. arXiv: 1909.00027 [astro-ph.GA].

[9] Enrico Barausse et al. "Massive Black Hole Merger Rates: The Effect of Kiloparsec Separation Wandering and Supernova Feedback". In: *The Astrophysical Journal* 904.1, 16 (Nov. 2020), p. 16. DOI: 10.3847/1538-4357/abba7f. arXiv: 2006.03065 [astro-ph.GA].

[10] A. Beifiori et al. "On the correlations between galaxy properties and supermassive black hole mass". In: *Monthly Notices of the Royal Astronomical Society* 419.3 (Jan. 2012), pp. 2497–2528. DOI: 10.1111/j.1365-2966.2011.19903.x. arXiv: 1109.6265 [astro-ph.CO].

[11] Jillian Bellovary et al. "The First Massive Black Hole Seeds and Their Hosts". In: *The Astrophysical Journal* 742.1, 13 (Nov. 2011), p. 13. DOI: 10.1088/0004-637X/742/1/13. arXiv: 1104.3858 [astro-ph.CO].

[12] Jillian M. Bellovary et al. "Multimessenger signatures of massive black holes in dwarf galaxies". In: *Monthly Notices of the Royal Astronomical Society* 482.3 (Jan. 2019), pp. 2913–2923. DOI: 10.1093/mnras/sty2842. arXiv: 1806.00471 [astro-ph.GA].

[13] Jillian M. Bellovary et al. "Wandering Black Holes in Bright Disk Galaxy Halos". In: *The Astrophysical Journal Letters* 721.2 (Oct. 2010), pp. L148–L152. DOI: 10.1088/2041-8205/721/2/L148. arXiv: 1008.5147 [astro-ph.CO].

[14] Pawel Biernacki, Romain Teyssier, and Andreas Bleuler. "On the dynamics of supermassive black holes in gas-rich, star-forming galaxies: the case for nuclear star cluster co-evolution". In: *Monthly Notices of the Royal*

Astronomical Society 469.1 (July 2017), pp. 295–313. DOI: 10.1093/mnras/stx845. arXiv: 1701.05190 [astro-ph.GA].

[15] James Binney and Scott Tremaine. *Galactic dynamics: Second Edition*. Princeton University Press, 2008.

[16] Pierre Boldrini, Roya Mohayaee, and Joseph Silk. “Subhalo sinking and off-centre massive black holes in dwarf galaxies”. In: *Monthly Notices of the Royal Astronomical Society* 495.1 (Mar. 2020), pp. L12–L16. DOI: 10.1093/mnrasl/slaa043. arXiv: 2003.02611 [astro-ph.GA].

[17] Elisa Bortolas et al. “Global torques and stochasticity as the drivers of massive black hole pairing in the young Universe”. In: *Monthly Notices of the Royal Astronomical Society* 498.3 (Nov. 2020), pp. 3601–3615. DOI: 10.1093/mnras/staa2628. arXiv: 2005.02409 [astro-ph.GA].

[18] M. Boylan-Kolchin, C.-P. Ma, and E. Quataert. “Dynamical friction and galaxy merging time-scales”. In: *Monthly Notices of the Royal Astronomical Society* 383 (Jan. 2008), pp. 93–101. DOI: 10.1111/j.1365-2966.2007.12530.x. eprint: arXiv:0707.2960.

[19] Volker Bromm and Richard B. Larson. “The First Stars”. In: *Annual Review of Astronomy and Astrophysics* 42.1 (Sept. 2004), pp. 79–118. DOI: 10.1146/annurev.astro.42.053102.134034. arXiv: astro-ph/0311019 [astro-ph].

[20] Volker Bromm and Abraham Loeb. “Formation of the First Supermassive Black Holes”. In: *The Astrophysical Journal* 596.1 (Oct. 2003), pp. 34–46. DOI: 10.1086/377529. arXiv: astro-ph/0212400 [astro-ph].

[21] Simone Callegari et al. “Growing Massive Black Hole Pairs in Minor Mergers of Disk Galaxies”. In: *The Astrophysical Journal* 729.2, 85 (Mar. 2011), p. 85. DOI: 10.1088/0004-637X/729/2/85. arXiv: 1002.1712 [astro-ph.CO].

[22] Simone Callegari et al. “Pairing of Supermassive Black Holes in Unequal-Mass Galaxy Mergers”. In: *The Astrophysical Journal Letters* 696.1 (May 2009), pp. L89–L92. DOI: 10.1088/0004-637X/696/1/L89. arXiv: 0811.0615 [astro-ph].

[23] Onur Çatmabacak et al. “Black hole-galaxy scaling relations in FIRE: the importance of black hole location and mergers”. In: *Monthly Notices of the Royal Astronomical Society* 511.1 (Mar. 2022), pp. 506–535. DOI: 10.1093/mnras/stac040. arXiv: 2007.12185 [astro-ph.GA].

[24] S. Chandrasekhar. “Dynamical Friction. I. General Considerations: the Coefficient of Dynamical Friction.” In: *The Astrophysical Journal* 97 (Mar. 1943), p. 255. DOI: 10.1086/144517.

[25] M. Colpi et al. “On the inspiral of massive black holes in gas-rich galaxy mergers”. In: *The Multicolored Landscape of Compact Objects and Their Explosive Origins; AIP, Cefalu, Sicily (Italy)*. Ed. by T. di Salvo, G. L. Israel, L. Piersant L. Burderi G. Matt A. Tornambe & M. T. Menna. Vol. 924. American Institute of Physics Conference Series. Aug. 2007, pp. 705–714. DOI: 10.1063/1.2774931. arXiv: 0706.1851.

[26] C. Corbett Moran, M. Y. Grudić, and P. F. Hopkins. “The effects of metallicity and cooling physics on fragmentation: implications on direct-collapse black hole formation”. In: *arXiv e-prints* (Mar. 2018), arXiv:1803.06430. arXiv: 1803.06430 [astro-ph.GA].

[27] Melvyn B. Davies, M. Coleman Miller, and Jillian M. Bellovary. “Supermassive Black Hole Formation Via Gas Accretion in Nuclear Stellar Clusters”. In: *The Astrophysical Journal Letters* 740.2, L42 (Oct. 2011), p. L42. DOI: 10.1088/2041-8205/740/2/L42. arXiv: 1106.5943 [astro-ph.CO].

[28] Roberto Decarli et al. “ALMA and HST Kiloparsec-scale Imaging of a Quasar-galaxy Merger at $Z \approx 6.2$”. In: *The Astrophysical Journal* 880.2, 157 (Aug. 2019), p. 157. DOI: 10.3847/1538-4357/ab297f. arXiv: 1906.05308 [astro-ph.GA].

[29] Roberto Decarli et al. “An ALMA [C II] Survey of 27 Quasars at $z > 5.94$”. In: *The Astrophysical Journal* 854.2, 97 (Feb. 2018), p. 97. DOI: 10.3847/1538-4357/aaa5aa. arXiv: 1801.02641 [astro-ph.GA].

[30] B. Devecchi and M. Volonteri. “Formation of the First Nuclear Clusters and Massive Black Holes at High Redshift”. In: *The Astrophysical Journal* 694.1 (Mar. 2009), pp. 302–313. DOI: 10.1088/0004-637X/694/1/302. arXiv: 0810.1057 [astro-ph].

[31] Debra Meloy Elmegreen et al. “Resolved Galaxies in the Hubble Ultra Deep Field: Star Formation in Disks at High Redshift”. In: *The Astrophysical Journal* 658.2 (Apr. 2007), pp. 763–777. DOI: 10.1086/511667. arXiv: astro-ph/0701121 [astro-ph].

[32] S. Michael Fall, Mark R. Krumholz, and Christopher D. Matzner. “Stellar Feedback in Molecular Clouds and its Influence on the Mass Function of Young Star Clusters”. In: *The Astrophysical Journal Letters* 710.2 (Feb. 2010), pp. L142–L146. DOI: 10.1088/2041-8205/710/2/L142. arXiv: 0910.2238 [astro-ph.SR].

[33] Xiaohui Fan et al. “A Survey of z>5.7 Quasars in the Sloan Digital Sky Survey. II. Discovery of Three Additional Quasars at z>6”. In: *The Astronomical Journal* 125.4 (Apr. 2003), pp. 1649–1659. DOI: 10.1086/368246. arXiv: astro-ph/0301135 [astro-ph].

[34] Xiaohui Fan et al. “A Survey of z>5.8 Quasars in the Sloan Digital Sky Survey. I. Discovery of Three New Quasars and the Spatial Density of Luminous Quasars at z~6”. In: *The Astronomical Journal* 122.6 (Dec.

2001), pp. 2833–2849. DOI: 10.1086/324111. arXiv: astro-ph/0108063 [astro-ph].

[35] Claude-André Faucher-Giguère. “A model for the origin of bursty star formation in galaxies”. In: *Monthly Notices of the Royal Astronomical Society* 473.3 (Jan. 2018), pp. 3717–3731. DOI: 10.1093/mnras/stx2595. arXiv: 1701.04824 [astro-ph.GA].

[36] Claude-André Faucher-Giguère et al. “A New Calculation of the Ionizing Background Spectrum and the Effects of He II Reionization”. In: *The Astrophysical Journal* 703.2 (Oct. 2009), pp. 1416–1443. DOI: 10.1088/0004-637X/703/2/1416. arXiv: 0901.4554 [astro-ph.CO].

[37] Laura Ferrarese and David Merritt. “A Fundamental Relation between Supermassive Black Holes and Their Host Galaxies”. In: *The Astrophysical Journal Letters* 539.1 (Aug. 2000), pp. L9–L12. DOI: 10.1086/312838. arXiv: astro-ph/0006053 [astro-ph].

[38] N. M. Förster Schreiber et al. “Constraints on the Assembly and Dynamics of Galaxies. II. Properties of Kiloparsec-scale Clumps in Rest-frame Optical Emission of z ~2 Star-forming Galaxies”. In: *The Astrophysical Journal* 739.1, 45 (Sept. 2011), p. 45. DOI: 10.1088/0004-637X/739/1/45. arXiv: 1104.0248 [astro-ph.CO].

[39] Karl Gebhardt et al. “A Relationship between Nuclear Black Hole Mass and Galaxy Velocity Dispersion”. In: *The Astrophysical Journal Letters* 539.1 (Aug. 2000), pp. L13–L16. DOI: 10.1086/312840. arXiv: astro-ph/0006289 [astro-ph].

[40] Sam Geen, Juan D. Soler, and Patrick Hennebelle. “Interpreting the star formation efficiency of nearby molecular clouds with ionizing radiation”. In: *Monthly Notices of the Royal Astronomical Society* 471.4 (Nov. 2017), pp. 4844–4855. DOI: 10.1093/mnras/stx1765. arXiv: 1703.10071 [astro-ph.GA].

[41] Elena González et al. “Intermediate-mass Black Holes from High Massive-star Binary Fractions in Young Star Clusters”. In: *The Astrophysical Journal Letters* 908.2, L29 (Feb. 2021), p. L29. DOI: 10.3847/2041-8213/abdf5b. arXiv: 2012.10497 [astro-ph.HE].

[42] F. Governato, M. Colpi, and L. Maraschi. “The fate of central black holes in merging galaxies”. In: *Monthly Notices of the Royal Astronomical Society* 271 (Nov. 1994), p. 317. DOI: 10.1093/mnras/271.2.317. arXiv: astro-ph/9407018 [astro-ph].

[43] Alister W. Graham et al. “An expanded M_{bh}-σ diagram, and a new calibration of active galactic nuclei masses”. In: *Monthly Notices of the Royal Astronomical Society* 412.4 (Apr. 2011), pp. 2211–2228. DOI: 10.1111/j.1365-2966.2010.18045.x. arXiv: 1007.3834 [astro-ph.CO].

[44] M. Y. Grudić et al. "When feedback fails: the scaling and saturation of star formation efficiency". In: *Monthly Notices of the Royal Astronomical Society* 475 (Apr. 2018), pp. 3511–3528. DOI: 10.1093/mnras/sty035. arXiv: 1612.05635.

[45] Michael Y. Grudić and Philip F. Hopkins. "A general-purpose time-step criterion for simulations with gravity". In: *Monthly Notices of the Royal Astronomical Society* 495.4 (May 2020), pp. 4306–4313. DOI: 10.1093/mnras/staa1453. arXiv: 1910.06349 [astro-ph.IM].

[46] M. Atakan Gürkan, Marc Freitag, and Frederic A. Rasio. "Formation of Massive Black Holes in Dense Star Clusters. I. Mass Segregation and Core Collapse". In: *The Astrophysical Journal* 604.2 (Apr. 2004), pp. 632–652. DOI: 10.1086/381968. arXiv: astro-ph/0308449 [astro-ph].

[47] Dávid Guszejnov et al. "Can magnetized turbulence set the mass scale of stars?" In: *Monthly Notices of the Royal Astronomical Society* 496.4 (Aug. 2020), pp. 5072–5088. DOI: 10.1093/mnras/staa1883. arXiv: 2002.01421 [astro-ph.GA].

[48] Mélanie Habouzit, Marta Volonteri, and Yohan Dubois. "Blossoms from black hole seeds: properties and early growth regulated by supernova feedback". In: *Monthly Notices of the Royal Astronomical Society* 468.4 (July 2017), pp. 3935–3948. DOI: 10.1093/mnras/stx666. arXiv: 1605.09394 [astro-ph.GA].

[49] Zoltán Haiman. "Constraints from Gravitational Recoil on the Growth of Supermassive Black Holes at High Redshift". In: *The Astrophysical Journal* 613.1 (Sept. 2004), pp. 36–40. DOI: 10.1086/422910. arXiv: astro-ph/0404196 [astro-ph].

[50] Zoltán Haiman and Abraham Loeb. "What Is the Highest Plausible Redshift of Luminous Quasars?" In: *The Astrophysical Journal* 552.2 (May 2001), pp. 459–463. DOI: 10.1086/320586. arXiv: astro-ph/0011529 [astro-ph].

[51] Shingo Hirano et al. "One Hundred First Stars: Protostellar Evolution and the Final Masses". In: *The Astrophysical Journal* 781.2, 60 (Feb. 2014), p. 60. DOI: 10.1088/0004-637X/781/2/60. arXiv: 1308.4456 [astro-ph.CO].

[52] Shingo Hirano et al. "Supersonic gas streams enhance the formation of massive black holes in the early universe". In: *Science* 357.6358 (Sept. 2017), pp. 1375–1378. DOI: 10.1126/science.aai9119. arXiv: 1709.09863 [astro-ph.CO].

[53] Kelly Holley-Bockelmann et al. "Gravitational Wave Recoil and the Retention of Intermediate-Mass Black Holes". In: *The Astrophysical Journal* 686.2 (Oct. 2008), pp. 829–837. DOI: 10.1086/591218. arXiv: 0707.1334 [astro-ph].

[54] P. F. Hopkins et al. “Galaxies on FIRE (Feedback In Realistic Environments): Stellar Feedback Explains Cosmologically Inefficient Star Formation”. In: *Monthly Notices of the Royal Astronomical Society* 445 (Nov. 2014), pp. 581–603. DOI: 10.1093/mnras/stu1738. arXiv: 1311.2073 [astro-ph.CO].

[55] P. F. Hopkins et al. “The Radical Consequences of Realistic Satellite Orbits for the Heating and Implied Merger Histories of Galactic Disks”. In: *The Astrophysical Journal* 688 (Dec. 2008), pp. 757–769. DOI: 10.1086/592087. arXiv: 0806.2861.

[56] Philip F. Hopkins. “A new class of accurate, mesh-free hydrodynamic simulation methods”. In: *Monthly Notices of the Royal Astronomical Society* 450.1 (June 2015), pp. 53–110. DOI: 10.1093/mnras/stv195. arXiv: 1409.7395 [astro-ph.CO].

[57] Philip F. Hopkins, Desika Narayanan, and Norman Murray. “The meaning and consequences of star formation criteria in galaxy models with resolved stellar feedback”. In: *Monthly Notices of the Royal Astronomical Society* 432.4 (July 2013), pp. 2647–2653. DOI: 10.1093/mnras/stt723. arXiv: 1303.0285 [astro-ph.CO].

[58] Philip F. Hopkins et al. “A Cosmological Framework for the Co-Evolution of Quasars, Supermassive Black Holes, and Elliptical Galaxies. I. Galaxy Mergers and Quasar Activity”. In: *The Astrophysical Journal Supplement Series* 175.2 (Apr. 2008), pp. 356–389. DOI: 10.1086/524362. arXiv: 0706.1243 [astro-ph].

[59] Philip F. Hopkins et al. “A Unified, Merger-driven Model of the Origin of Starbursts, Quasars, the Cosmic X-Ray Background, Supermassive Black Holes, and Galaxy Spheroids”. In: *The Astrophysical Journal Supplement Series* 163.1 (Mar. 2006), pp. 1–49. DOI: 10.1086/499298. arXiv: astro-ph/0506398 [astro-ph].

[60] Philip F. Hopkins et al. “Black Holes in Galaxy Mergers: Evolution of Quasars”. In: *The Astrophysical Journal* 630.2 (Sept. 2005), pp. 705–715. DOI: 10.1086/432438. arXiv: astro-ph/0504190 [astro-ph].

[61] Philip F. Hopkins et al. “FIRE-2 simulations: physics versus numerics in galaxy formation”. In: *Monthly Notices of the Royal Astronomical Society* 480.1 (Oct. 2018), pp. 800–863. DOI: 10.1093/mnras/sty1690. arXiv: 1702.06148 [astro-ph.GA].

[62] Takashi Hosokawa, Kazuyuki Omukai, and Harold W. Yorke. “Rapidly Accreting Supergiant Protostars: Embryos of Supermassive Black Holes?” In: *The Astrophysical Journal* 756.1, 93 (Sept. 2012), p. 93. DOI: 10.1088/0004-637X/756/1/93. arXiv: 1203.2613 [astro-ph.CO].

[63] Takashi Hosokawa et al. “Formation of Primordial Supermassive Stars by Rapid Mass Accretion”. In: *The Astrophysical Journal* 778.2, 178 (Dec.

2013), p. 178. DOI: 10.1088/0004-637X/778/2/178. arXiv: 1308.4457 [astro-ph.SR].

[64] F. Hoyle and R. A. Lyttleton. "The effect of interstellar matter on climatic variation". In: *Proceedings of the Cambridge Philosophical Society* 35.3 (Jan. 1939), p. 405. DOI: 10.1017/S0305004100021150.

[65] Kohei Inayoshi, Zoltán Haiman, and Jeremiah P. Ostriker. "Hyper-Eddington accretion flows on to massive black holes". In: *Monthly Notices of the Royal Astronomical Society* 459.4 (July 2016), pp. 3738–3755. DOI: 10.1093/mnras/stw836. arXiv: 1511.02116 [astro-ph.HE].

[66] Kohei Inayoshi, Miao Li, and Zoltán Haiman. "Massive black hole and Population III galaxy formation in overmassive dark-matter haloes with violent merger histories". In: *Monthly Notices of the Royal Astronomical Society* 479.3 (Sept. 2018), pp. 4017–4027. DOI: 10.1093/mnras/sty1720. arXiv: 1804.03143 [astro-ph.GA].

[67] Kohei Inayoshi, Eli Visbal, and Zoltán Haiman. "The Assembly of the First Massive Black Holes". In: *Annual Review of Astronomy and Astrophysics* 58 (Aug. 2020), pp. 27–97. DOI: 10.1146/annurev-astro-120419-014455. arXiv: 1911.05791 [astro-ph.GA].

[68] Jarrett L. Johnson and Volker Bromm. "The aftermath of the first stars: massive black holes". In: *Monthly Notices of the Royal Astronomical Society* 374.4 (Feb. 2007), pp. 1557–1568. DOI: 10.1111/j.1365-2966.2006.11275.x. arXiv: astro-ph/0605691 [astro-ph].

[69] Nitya Kallivayalil et al. "Third-epoch Magellanic Cloud Proper Motions. I. Hubble Space Telescope/WFC3 Data and Orbit Implications". In: *The Astrophysical Journal* 764.2, 161 (Feb. 2013), p. 161. DOI: 10.1088/0004-637X/764/2/161. arXiv: 1301.0832 [astro-ph.CO].

[70] S. Kamann et al. "MUSE crowded field 3D spectroscopy of over 12 000 stars in the globular cluster NGC 6397. II. Probing the internal dynamics and the presence of a central black hole". In: *Astronomy & Astrophysics* 588, A149 (Apr. 2016), A149. DOI: 10.1051/0004-6361/201527065. arXiv: 1602.01643 [astro-ph.SR].

[71] Harley Katz, Debora Sijacki, and Martin G. Haehnelt. "Seeding high-redshift QSOs by collisional runaway in primordial star clusters". In: *Monthly Notices of the Royal Astronomical Society* 451.3 (Aug. 2015), pp. 2352–2369. DOI: 10.1093/mnras/stv1048. arXiv: 1502.03448 [astro-ph.GA].

[72] T. Kawashima et al. "Comptonized Photon Spectra of Supercritical Black Hole Accretion Flows with Application to Ultraluminous X-Ray Sources". In: *The Astrophysical Journal* 752.1, 18 (June 2012), p. 18. DOI: 10.1088/0004-637X/752/1/18.

[73] Ji-hoon Kim et al. "High-redshift Galaxy Formation with Self-consistently Modeled Stars and Massive Black Holes: Stellar Feedback and Quasar Growth". In: *The Astrophysical Journal* 887.2, 120 (Dec. 2019), p. 120. doi: 10.3847/1538-4357/ab510b. arXiv: 1910.12888 [astro-ph.GA].

[74] Michael Kretschmer and Romain Teyssier. "Forming early-type galaxies without AGN feedback: a combination of merger-driven outflows and inefficient star formation". In: *Monthly Notices of the Royal Astronomical Society* 492.1 (Feb. 2020), pp. 1385–1398. doi: 10.1093/mnras/stz3495. arXiv: 1906.11836 [astro-ph.GA].

[75] Pavel Kroupa et al. "Very high redshift quasars and the rapid emergence of supermassive black holes". In: *Monthly Notices of the Royal Astronomical Society* 498.4 (Nov. 2020), pp. 5652–5683. doi: 10.1093/mnras/staa2276. arXiv: 2007.14402 [astro-ph.GA].

[76] A. Lawrence et al. "The UKIRT Infrared Deep Sky Survey (UKIDSS)". In: *Monthly Notices of the Royal Astronomical Society* 379.4 (Aug. 2007), pp. 1599–1617. doi: 10.1111/j.1365-2966.2007.12040.x. arXiv: astro-ph/0604426 [astro-ph].

[77] Claus Leitherer et al. "Starburst99: Synthesis Models for Galaxies with Active Star Formation". In: *The Astrophysical Journal Supplement Series* 123.1 (July 1999), pp. 3–40. doi: 10.1086/313233. arXiv: astro-ph/9902334 [astro-ph].

[78] Yuexing Li et al. "Formation of z~6 Quasars from Hierarchical Galaxy Mergers". In: *The Astrophysical Journal* 665.1 (Aug. 2007), pp. 187–208. doi: 10.1086/519297. arXiv: astro-ph/0608190 [astro-ph].

[79] Giuseppe Lodato and Priyamvada Natarajan. "Supermassive black hole formation during the assembly of pre-galactic discs". In: *Monthly Notices of the Royal Astronomical Society* 371.4 (Oct. 2006), pp. 1813–1823. doi: 10.1111/j.1365-2966.2006.10801.x. arXiv: astro-ph/0606159 [astro-ph].

[80] Giuseppe Lodato and Priyamvada Natarajan. "The mass function of high-redshift seed black holes". In: *Monthly Notices of the Royal Astronomical Society* 377.1 (May 2007), pp. L64–L68. doi: 10.1111/j.1745-3933.2007.00304.x. arXiv: astro-ph/0702340 [astro-ph].

[81] A. Lupi et al. "Constraining the high-redshift formation of black hole seeds in nuclear star clusters with gas inflows". In: *Monthly Notices of the Royal Astronomical Society* 442.4 (Aug. 2014), pp. 3616–3626. doi: 10.1093/mnras/stu1120. arXiv: 1406.2325 [astro-ph.GA].

[82] A. Lupi et al. "Growing massive black holes through supercritical accretion of stellar-mass seeds". In: *Monthly Notices of the Royal Astronomical Society* 456.3 (Mar. 2016), pp. 2993–3003. doi: 10.1093/mnras/stv2877. arXiv: 1512.02651 [astro-ph.GA].

[83] N. Lützgendorf et al. "Limits on intermediate-mass black holes in six Galactic globular clusters with integral-field spectroscopy". In: *Astronomy & Astrophysics* 552, A49 (Apr. 2013), A49. DOI: 10.1051/0004-6361/201220307. arXiv: 1212.3475 [astro-ph.GA].

[84] Nora Lützgendorf et al. "Re-evaluation of the central velocity-dispersion profile in NGC 6388". In: *Astronomy & Astrophysics* 581, A1 (Sept. 2015), A1. DOI: 10.1051/0004-6361/201425524. arXiv: 1507.02813 [astro-ph.GA].

[85] Linhao Ma et al. "A new discrete dynamical friction estimator based on N-body simulations". In: *Monthly Notices of the Royal Astronomical Society* 519.4 (2023), pp. 5543–5553. DOI: 10.1093/mnras/stad036.

[86] Xiangcheng Ma et al. "Dust attenuation, dust emission, and dust temperature in galaxies at z ≥ 5: a view from the FIRE-2 simulations". In: *Monthly Notices of the Royal Astronomical Society* 487.2 (Aug. 2019), pp. 1844–1864. DOI: 10.1093/mnras/stz1324. arXiv: 1902.10152 [astro-ph.GA].

[87] Xiangcheng Ma et al. "Self-consistent proto-globular cluster formation in cosmological simulations of high-redshift galaxies". In: *Monthly Notices of the Royal Astronomical Society* 493.3 (Apr. 2020), pp. 4315–4332. DOI: 10.1093/mnras/staa527. arXiv: 1906.11261 [astro-ph.GA].

[88] Xiangcheng Ma et al. "Simulating galaxies in the reionization era with FIRE-2: galaxy scaling relations, stellar mass functions, and luminosity functions". In: *Monthly Notices of the Royal Astronomical Society* 478.2 (Aug. 2018), pp. 1694–1715. DOI: 10.1093/mnras/sty1024. arXiv: 1706.06605 [astro-ph.GA].

[89] Xiangcheng Ma et al. "Simulating galaxies in the reionization era with FIRE-2: morphologies and sizes". In: *Monthly Notices of the Royal Astronomical Society* 477.1 (June 2018), pp. 219–229. DOI: 10.1093/mnras/sty684. arXiv: 1710.00008 [astro-ph.GA].

[90] Xiangcheng Ma et al. "Why do high-redshift galaxies show diverse gas-phase metallicity gradients?" In: *Monthly Notices of the Royal Astronomical Society* 466.4 (Apr. 2017), pp. 4780–4794. DOI: 10.1093/mnras/stx034. arXiv: 1610.03498 [astro-ph.GA].

[91] Piero Madau, Francesco Haardt, and Massimo Dotti. "Super-critical Growth of Massive Black Holes from Stellar-mass Seeds". In: *The Astrophysical Journal Letters* 784.2, L38 (Apr. 2014), p. L38. DOI: 10.1088/2041-8205/784/2/L38. arXiv: 1402.6995 [astro-ph.CO].

[92] Piero Madau and Martin J. Rees. "Massive Black Holes as Population III Remnants". In: *The Astrophysical Journal Letters* 551.1 (Apr. 2001), pp. L27–L30. DOI: 10.1086/319848. arXiv: astro-ph/0101223 [astro-ph].

[93] Xi Meng and Oleg Y. Gnedin. "Origin of giant stellar clumps in high-redshift galaxies". In: *Monthly Notices of the Royal Astronomical Society* 494.1 (May 2020), pp. 1263–1275. DOI: 10.1093/mnras/staa776. arXiv: 1910.03443 [astro-ph.GA].

[94] Mar Mezcua and Helena Domínguez Sánchez. "Hidden AGNs in Dwarf Galaxies Revealed by MaNGA: Light Echoes, Off-nuclear Wanderers, and a New Broad-line AGN". In: *The Astrophysical Journal Letters* 898.2, L30 (Aug. 2020), p. L30. DOI: 10.3847/2041-8213/aba199. arXiv: 2007.08527 [astro-ph.GA].

[95] Miloš Milosavljević, Sean M. Couch, and Volker Bromm. "Accretion Onto Intermediate-Mass Black Holes in Dense Protogalactic Clouds". In: *The Astrophysical Journal Letters* 696.2 (May 2009), pp. L146–L149. DOI: 10.1088/0004-637X/696/2/L146. arXiv: 0812.2516 [astro-ph].

[96] Eric Morganson et al. "The First High-redshift Quasar from Pan-STARRS". In: *The Astronomical Journal* 143.6, 142 (June 2012), p. 142. DOI: 10.1088/0004-6256/143/6/142. arXiv: 1109.6241 [astro-ph.CO].

[97] Alexander L. Muratov et al. "Gusty, gaseous flows of FIRE: galactic winds in cosmological simulations with explicit stellar feedback". In: *Monthly Notices of the Royal Astronomical Society* 454.3 (Dec. 2015), pp. 2691–2713. DOI: 10.1093/mnras/stv2126. arXiv: 1501.03155 [astro-ph.GA].

[98] Priyamvada Natarajan. "A new channel to form IMBHs throughout cosmic time". In: *Monthly Notices of the Royal Astronomical Society* 501.1 (Feb. 2021), pp. 1413–1425. DOI: 10.1093/mnras/staa3724. arXiv: 2009.09156 [astro-ph.GA].

[99] Priyamvada Natarajan. "Seeds to monsters: tracing the growth of black holes in the universe". In: *General Relativity and Gravitation* 46, 1702 (May 2014), p. 1702. DOI: 10.1007/s10714-014-1702-6.

[100] Mladen Novak et al. "An ALMA Multiline Survey of the Interstellar Medium of the Redshift 7.5 Quasar Host Galaxy J1342+0928". In: *The Astrophysical Journal* 881.1, 63 (Aug. 2019), p. 63. DOI: 10.3847/1538-4357/ab2beb. arXiv: 1906.08569 [astro-ph.GA].

[101] Antonija Oklopčić et al. "Giant clumps in the FIRE simulations: a case study of a massive high-redshift galaxy". In: *Monthly Notices of the Royal Astronomical Society* 465.1 (Feb. 2017), pp. 952–969. DOI: 10.1093/mnras/stw2754. arXiv: 1603.03778 [astro-ph.GA].

[102] R. A. Overzier et al. "Morphologies of Local Lyman Break Galaxy Analogs. II. A Comparison with Galaxies at z $\simeq$ 2-4 in ACS and WFC3 Images of the Hubble Ultra Deep Field". In: *The Astrophysical Journal* 710.2 (Feb. 2010), pp. 979–991. DOI: 10.1088/0004-637X/710/2/979. arXiv: 0911.1279 [astro-ph.CO].

[103] Fabio Pacucci, Marta Volonteri, and Andrea Ferrara. “The growth efficiency of high-redshift black holes”. In: *Monthly Notices of the Royal Astronomical Society* 452.2 (Sept. 2015), pp. 1922–1933. DOI: 10.1093/mnras/stv1465. arXiv: 1506.04750 [astro-ph.GA].

[104] Edwige Pezzulli, Rosa Valiante, and Raffaella Schneider. “Super-Eddington growth of the first black holes”. In: *Monthly Notices of the Royal Astronomical Society* 458.3 (May 2016), pp. 3047–3059. DOI: 10.1093/mnras/stw505. arXiv: 1603.00475 [astro-ph.GA].

[105] Hugo Pfister et al. “The erratic dynamical life of black hole seeds in high-redshift galaxies”. In: *Monthly Notices of the Royal Astronomical Society* 486.1 (June 2019), pp. 101–111. DOI: 10.1093/mnras/stz822. arXiv: 1902.01297 [astro-ph.GA].

[106] Planck Collaboration et al. “Planck 2018 results. VI. Cosmological parameters”. In: *Astronomy & Astrophysics* 641, A6 (Sept. 2020), A6. DOI: 10.1051/0004-6361/201833910. arXiv: 1807.06209 [astro-ph.CO].

[107] Simon F. Portegies Zwart and Stephen L. W. McMillan. “The Runaway Growth of Intermediate-Mass Black Holes in Dense Star Clusters”. In: *The Astrophysical Journal* 576.2 (Sept. 2002), pp. 899–907. DOI: 10.1086/341798. arXiv: astro-ph/0201055 [astro-ph].

[108] Simon F. Portegies Zwart et al. “Formation of massive black holes through runaway collisions in dense young star clusters”. In: *Nature* 428.6984 (Apr. 2004), pp. 724–726. DOI: 10.1038/nature02448. arXiv: astro-ph/0402622 [astro-ph].

[109] John A. Regan et al. “Super-Eddington accretion and feedback from the first massive seed black holes”. In: *Monthly Notices of the Royal Astronomical Society* 486.3 (July 2019), pp. 3892–3906. DOI: 10.1093/mnras/stz1045. arXiv: 1811.04953 [astro-ph.GA].

[110] Amy E. Reines et al. “A New Sample of (Wandering) Massive Black Holes in Dwarf Galaxies from High-resolution Radio Observations”. In: *The Astrophysical Journal* 888.1, 36 (Jan. 2020), p. 36. DOI: 10.3847/1538-4357/ab4999. arXiv: 1909.04670 [astro-ph.GA].

[111] B. Reinoso et al. “Collisions in primordial star clusters. Formation pathway for intermediate mass black holes”. In: *Astronomy & Astrophysics* 614, A14 (June 2018), A14. DOI: 10.1051/0004-6361/201732224. arXiv: 1801.05891 [astro-ph.GA].

[112] Angelo Ricarte et al. “Tracing black hole and galaxy co-evolution in the ROMULUS simulations”. In: *Monthly Notices of the Royal Astronomical Society* 489.1 (Oct. 2019), pp. 802–819. DOI: 10.1093/mnras/stz2161. arXiv: 1904.10116 [astro-ph.GA].

[113] Rok Roškar et al. "Orbital decay of supermassive black hole binaries in clumpy multiphase merger remnants". In: *Monthly Notices of the Royal Astronomical Society* 449.1 (May 2015), pp. 494–505. DOI: 10.1093/mnras/stv312. arXiv: 1406.4505 [astro-ph.GA].

[114] Taeho Ryu et al. "Intermediate-mass black holes from Population III remnants in the first galactic nuclei". In: *Monthly Notices of the Royal Astronomical Society* 460.4 (Aug. 2016), pp. 4122–4134. DOI: 10.1093/mnras/stw1241. arXiv: 1603.08513 [astro-ph.GA].

[115] Yue Shen et al. "Gemini GNIRS Near-infrared Spectroscopy of 50 Quasars at z $\gtrsim$ 5.7". In: *The Astrophysical Journal* 873.1, 35 (Mar. 2019), p. 35. DOI: 10.3847/1538-4357/ab03d9. arXiv: 1809.05584 [astro-ph.GA].

[116] Yanlong Shi, Michael Y. Grudić, and Philip F. Hopkins. "The mass budget for intermediate-mass black holes in dense star clusters". In: *Monthly Notices of the Royal Astronomical Society* 505.2 (Aug. 2021), pp. 2753–2763. DOI: 10.1093/mnras/stab1470. arXiv: 2008.12290 [astro-ph.GA].

[117] Debora Sijacki et al. "The Illustris simulation: the evolving population of black holes across cosmic time". In: *Monthly Notices of the Royal Astronomical Society* 452.1 (Sept. 2015), pp. 575–596. DOI: 10.1093/mnras/stv1340. arXiv: 1408.6842 [astro-ph.GA].

[118] Martin Sparre et al. "(Star)bursts of FIRE: observational signatures of bursty star formation in galaxies". In: *Monthly Notices of the Royal Astronomical Society* 466.1 (Apr. 2017), pp. 88–104. DOI: 10.1093/mnras/stw3011. arXiv: 1510.03869 [astro-ph.GA].

[119] Volker Springel, Tiziana Di Matteo, and Lars Hernquist. "Modelling feedback from stars and black holes in galaxy mergers". In: *Monthly Notices of the Royal Astronomical Society* 361.3 (Aug. 2005), pp. 776–794. DOI: 10.1111/j.1365-2966.2005.09238.x. arXiv: astro-ph/0411108 [astro-ph].

[120] A. M. Swinbank et al. "A Hubble Space Telescope NICMOS and ACS morphological study of z $\sim$2 submillimetre galaxies". In: *Monthly Notices of the Royal Astronomical Society* 405.1 (June 2010), pp. 234–244. DOI: 10.1111/j.1365-2966.2010.16485.x. arXiv: 1002.2518 [astro-ph.CO].

[121] A. M. Swinbank et al. "The Interstellar Medium in Distant Star-forming Galaxies: Turbulent Pressure, Fragmentation, and Cloud Scaling Relations in a Dense Gas Disk at z = 2.3". In: *The Astrophysical Journal* 742.1, 11 (Nov. 2011), p. 11. DOI: 10.1088/0004-637X/742/1/11. arXiv: 1110.2780 [astro-ph.CO].

[122] L. J. Tacconi et al. "High molecular gas fractions in normal massive star-forming galaxies in the young Universe". In: *Nature* 463.7282 (Feb.

2010), pp. 781–784. DOI: 10.1038/nature08773. arXiv: 1002.2149 [astro-ph.CO].

[123] Eishun Takeo et al. “Super-Eddington growth of black holes in the early universe: effects of disc radiation spectra”. In: *Monthly Notices of the Royal Astronomical Society* 488.2 (Sept. 2019), pp. 2689–2700. DOI: 10.1093/mnras/stz1899. arXiv: 1901.04514 [astro-ph.HE].

[124] Valentina Tamburello et al. “Supermassive black hole pairs in clumpy galaxies at high redshift: delayed binary formation and concurrent mass growth”. In: *Monthly Notices of the Royal Astronomical Society* 464.3 (Jan. 2017), pp. 2952–2962. DOI: 10.1093/mnras/stw2561. arXiv: 1603.00021 [astro-ph.GA].

[125] Tomas Tamfal et al. “Formation of LISA Black Hole Binaries in Merging Dwarf Galaxies: The Imprint of Dark Matter”. In: *The Astrophysical Journal Letters* 864.1, L19 (Sept. 2018), p. L19. DOI: 10.3847/2041-8213/aada4b. arXiv: 1806.11112 [astro-ph.GA].

[126] Maxime Trebitsch, Marta Volonteri, and Yohan Dubois. “Modelling a bright z = 6 galaxy at the faint end of the AGN luminosity function”. In: *Monthly Notices of the Royal Astronomical Society* 494.3 (May 2020), pp. 3453–3463. DOI: 10.1093/mnras/staa1012. arXiv: 2004.03611 [astro-ph.GA].

[127] Scott Tremaine et al. “The Slope of the Black Hole Mass versus Velocity Dispersion Correlation”. In: *The Astrophysical Journal* 574.2 (Aug. 2002), pp. 740–753. DOI: 10.1086/341002. arXiv: astro-ph/0203468 [astro-ph].

[128] M. Tremmel et al. “Dancing to CHANGA: a self-consistent prediction for close SMBH pair formation time-scales following galaxy mergers”. In: *Monthly Notices of the Royal Astronomical Society* 475.4 (Apr. 2018), pp. 4967–4977. DOI: 10.1093/mnras/sty139. arXiv: 1708.07126 [astro-ph.GA].

[129] M. Tremmel et al. “Introducing ROMULUSC: a cosmological simulation of a galaxy cluster with an unprecedented resolution”. In: *Monthly Notices of the Royal Astronomical Society* 483.3 (Mar. 2019), pp. 3336–3362. DOI: 10.1093/mnras/sty3336. arXiv: 1806.01282 [astro-ph.GA].

[130] M. Tremmel et al. “The Romulus cosmological simulations: a physical approach to the formation, dynamics and accretion models of SMBHs”. In: *Monthly Notices of the Royal Astronomical Society* 470.1 (Sept. 2017), pp. 1121–1139. DOI: 10.1093/mnras/stx1160. arXiv: 1607.02151 [astro-ph.GA].

[131] Michael Tremmel et al. “Wandering Supermassive Black Holes in Milky-Way-mass Halos”. In: *The Astrophysical Journal Letters* 857.2, L22 (Apr. 2018), p. L22. DOI: 10.3847/2041-8213/aabc0a. arXiv: 1802.06783 [astro-ph.GA].

[132] Edwin L. Turner. "Quasars and Galaxy Formation. I. The Z > 4 Objects". In: *The Astronomical Journal* 101 (Jan. 1991), p. 5. DOI: 10.1086/115663.

[133] F. C. van den Bosch et al. "Substructure in Dark Halos: Orbital Eccentricities and Dynamical Friction". In: *The Astrophysical Journal* 515 (Apr. 1999), pp. 50–68. DOI: 10.1086/307023. eprint: arXiv:astro-ph/9811229.

[134] José A. Flores Velázquez et al. "The time-scales probed by star formation rate indicators for realistic, bursty star formation histories from the FIRE simulations". In: *Monthly Notices of the Royal Astronomical Society* (Dec. 2020). DOI: 10.1093/mnras/staa3893.

[135] Bram P. Venemans et al. "400 pc Imaging of a Massive Quasar Host Galaxy at a Redshift of 6.6". In: *The Astrophysical Journal Letters* 874.2, L30 (Apr. 2019), p. L30. DOI: 10.3847/2041-8213/ab11cc. arXiv: 1903.09202 [astro-ph.GA].

[136] Bram P. Venemans et al. "The Compact, ~1 kpc Host Galaxy of a Quasar at a Redshift of 7.1". In: *The Astrophysical Journal* 837.2, 146 (Mar. 2017), p. 146. DOI: 10.3847/1538-4357/aa62ac. arXiv: 1702.03852 [astro-ph.GA].

[137] M. Volonteri. "The Formation and Evolution of Massive Black Holes". In: *Science* 337.6094 (Aug. 2012), p. 544. DOI: 10.1126/science.1220843. arXiv: 1208.1106 [astro-ph.CO].

[138] M. Volonteri et al. "The cosmic evolution of massive black holes in the Horizon-AGN simulation". In: *Monthly Notices of the Royal Astronomical Society* 460.3 (Aug. 2016), pp. 2979–2996. DOI: 10.1093/mnras/stw1123. arXiv: 1602.01941 [astro-ph.GA].

[139] Marta Volonteri and Rosalba Perna. "Dynamical evolution of intermediate-mass black holes and their observable signatures in the nearby Universe". In: *Monthly Notices of the Royal Astronomical Society* 358.3 (Apr. 2005), pp. 913–922. DOI: 10.1111/j.1365-2966.2005.08832.x. arXiv: astro-ph/0501345 [astro-ph].

[140] Marta Volonteri et al. "Black hole mergers from dwarf to massive galaxies with the NewHorizon and Horizon-AGN simulations". In: *Monthly Notices of the Royal Astronomical Society* 498.2 (Oct. 2020), pp. 2219–2238. DOI: 10.1093/mnras/staa2384. arXiv: 2005.04902 [astro-ph.GA].

[141] Feige Wang et al. "Spatially Resolved Interstellar Medium and Highly Excited Dense Molecular Gas in the Most Luminous Quasar at z = 6.327". In: *The Astrophysical Journal* 880.1, 2 (July 2019), p. 2. DOI: 10.3847/1538-4357/ab2717. arXiv: 1906.06801 [astro-ph.GA].

[142] Daniel R. Weisz et al. "The Star Formation Histories of Local Group Dwarf Galaxies. I. Hubble Space Telescope/Wide Field Planetary Camera 2 Observations". In: *The Astrophysical Journal* 789.2, 147 (July 2014), p. 147. DOI: 10.1088/0004-637X/789/2/147. arXiv: 1404.7144 [astro-ph.GA].

[143] Daniel Whalen et al. “The Destruction of Cosmological Minihalos by Primordial Supernovae”. In: *The Astrophysical Journal* 682.1 (July 2008), pp. 49–67. DOI: 10.1086/589643. arXiv: 0801.3698 [astro-ph].

[144] Chris J. Willott et al. “Four Quasars above Redshift 6 Discovered by the Canada-France High-z Quasar Survey”. In: *The Astronomical Journal* 134.6 (Dec. 2007), pp. 2435–2450. DOI: 10.1086/522962. arXiv: 0706.0914 [astro-ph].

[145] Xue-Bing Wu et al. “An ultraluminous quasar with a twelve-billion-solar-mass black hole at redshift 6.30”. In: *Nature* 518.7540 (Feb. 2015), pp. 512–515. DOI: 10.1038/nature14241. arXiv: 1502.07418 [astro-ph.GA].

[146] Alice Zocchi, Mark Gieles, and Vincent Hénault-Brunet. “Radial anisotropy in ω Cen limiting the room for an intermediate-mass black hole”. In: *Monthly Notices of the Royal Astronomical Society* 468.4 (July 2017), pp. 4429–4440. DOI: 10.1093/mnras/stx316. arXiv: 1702.00725 [astro-ph.GA].

Chapter 4

ORBITAL DECAY OF EXOPLANETS VIA TIDAL RESONANCE LOCKING

[1] Linhao Ma and Jim Fuller. "Orbital Decay of Short-period Exoplanets via Tidal Resonance Locking". In: *The Astrophysical Journal* 918.1 (2021), p. 16. DOI: 10.3847/1538-4357/ac088e.

Abstract

A large fraction of known exoplanets have short orbital periods where tidal excitation of gravity waves within the host star causes the planets' orbits to decay. We study the effects of tidal resonance locking, in which the planet locks into resonance with a tidally excited stellar gravity mode. Because a star's gravity mode frequencies typically increase as the star evolves, the planet's orbital frequency increases in lockstep, potentially causing much faster orbital decay than predicted by other tidal theories. Due to nonlinear mode damping, resonance locking in Sun-like stars likely only operates for low-mass planets ($M \lesssim 0.1\, M_{\rm Jup}$), but in stars with convective cores it can likely operate for all planetary masses. The orbital decay timescale with resonance locking is typically comparable to the star's main-sequence lifetime, corresponding to a wide range in effective stellar quality factor ($10^3 \lesssim Q' \lesssim 10^9$), depending on the planet's mass and orbital period. We make predictions for several individual systems and examine the orbital evolution resulting from both resonance locking and nonlinear wave dissipation. Our models demonstrate how short-period massive planets can be quickly destroyed by nonlinear mode damping, while short-period low-mass planets can survive, even though they undergo substantial inward tidal migration via resonance locking.

4.1 Introduction

Historically, exoplanets have been easiest to detect at short orbital periods through transits or radial velocity measurements. Consequently, many known exoplanets orbit at small distances where gravitational forces are strong, allowing the ensuing tidal effects to shape the planetary architectures we observe today. In most cases, the orbits of short-period exoplanets are expected to quickly circularize due to tidal dissipation within the exoplanet, with the spin of the exoplanet aligning and synchronizing with its orbit (though see [48] for an exception). Subsequent orbital migration is then driven by tidal dissipation within the star, and it is this case we study here.

Traditionally, tidal dissipation within the star is parameterized by the effective tidal quality factor $Q' = Q/k_2$, where Q is the inverse of the phase lag between the tidal potential and the tidal bulge [26] and k_2 is the tidal Love number. In this model, the value of Q' is related to the orbital decay rate by

$$Q' \equiv \frac{3M_\mathrm{p}}{M_*}\left(\frac{R_*}{a}\right)^5 t_\mathrm{tide}(\Omega_\mathrm{orb} - \Omega_\mathrm{s}) \,, \tag{4.1}$$

where M_p and M_* are the masses of the planet and the star, respectively. R_* the radius of the star, a the orbital semi-major axis, Ω_orb the angular orbital frequency, Ω_s the stellar spin frequency, and t_tide the tidal migration timescale, defined as

$$t_\mathrm{tide} = -\frac{a}{\dot{a}_\mathrm{tide}} = \frac{E_\mathrm{orb}}{\dot{E}_\mathrm{orb}} \,. \tag{4.2}$$

Although widely discussed in the literature, Q' is difficult to calculate from first principles and a number of theoretical models have been proposed. Tidal dissipation in exoplanet host stars is believed to result from a combination of a few dissipation mechanisms: (1) damping of the equilibrium tidal distortion of the star via turbulent viscosity in the convective envelope (recent work includes [47, 21, 15, 72]), (2) damping of dynamically excited inertial waves in the convective envelope (e.g., [53, 51, 1, 46, 29]), and (3) thermal and nonlinear dissipation of tidally excited gravity waves in the radiative interior of the star [28, 73, 38, 16, 19]. Throughout this paper we will be focusing on gravity wave damping, which is likely to be most effective for planets on circular, short-period orbits aligned with the host star's spin [4].

Most prior theoretical investigations have overlooked an essential aspect of the tidal migration problem: the coupled evolution of the stellar structure and the planetary orbit. Even sophisticated models rarely perform full orbital evolution simulations that solve for tidal dissipation at each time step. Instead, they typically invoke a constant tidal quality factor Q', or at best recompute a frequency-averaged Q' at different timesteps. Such averaging is problematic because the effective Q' for gravity waves or inertial waves is a sensitive function of forcing frequency, such that it has sharp minima over narrow frequency ranges surrounding resonances with stellar oscillations.

In this work, we examine the possibility of tidal migration driven by “resonance locking" with stellar oscillation modes, in which a planet can become trapped in a resonance with a star's oscillation mode, often allowing for large amounts of tidal dissipation and faster orbital migration. Resonance locking has previously been discussed for binary stars [75, 76, 17, 11, 10, 79], with direct evidence arising from large-amplitude tidally excited oscillations in eccentric heartbeat stars [30, 18, 12]. Resonance locking within Saturn also appears to drive the orbital expansion of its outer moons Rhea and Titan [20, 41, 42] at rates 10-100 times faster than most prior expectations. Resonance locking could have similarly dramatic effects for the inward or outward migration of short-period exoplanets, and we examine this possibility for the first time.

In Section 4.2 we discuss the tidal dissipation mechanisms, where in Section 4.2 we focus on resonance locking, and in Section 4.2 we discuss complications introduced by nonlinear damping effects. We compare our results with observational constraints in Section 4.3. In Section 4.4, we discuss the observational implications of resonance locking and other nonlinear tidal theories for exoplanet systems, focusing on individual systems and statistical distributions. We summarize in Section 4.5.

4.2 Tidal Dissipation Mechanisms

Here we describe the basic idea of resonance locking and the tidal migration time scales it predicts. We also contrast this against tidal migration induced by nonlinear gravity wave dissipation, and we discuss the corresponding tidal Q's and domains of validity of these theories.

Resonance Locking

Resonances between tidal forcing frequencies and stellar oscillation mode frequencies can greatly enhance tidal dissipation rates. Specifically, the orbital energy loss rate due to a tidally forced mode with angular frequency ω_α excited by the tidal potential of a circularly orbiting planet with forcing frequency ω_f (each measured in a frame corotating with the star) is given by [19]

$$\dot{E}_\mathrm{orb,tide} = \frac{m\omega_\alpha \Omega_\mathrm{orb} |\gamma_\alpha| M_* R_*^2 |Q_\alpha|^2 \omega_\mathrm{f}^2}{(\omega_\alpha - \omega_\mathrm{f})^2 + \gamma_\alpha^2} \left(\frac{M_\mathrm{p}}{M_*}\right)^2 \left(\frac{R_*}{a}\right)^6 , \tag{4.3}$$

where γ_α is the mode growth rate and m is the mode's azimuthal index ($m = 2$ corresponds to the strongest tidal forcing for aligned orbits). Q_α is a dimensionless number describing the spatial coupling between oscillations and the tidal potential defined in [19]. The denominator is smallest near resonance, when $\omega_\alpha \simeq \omega_\mathrm{f}$, leading to the greatest tidal dissipation and the smallest tidal migration timescale, as shown in the left panel of Figure 4.1.

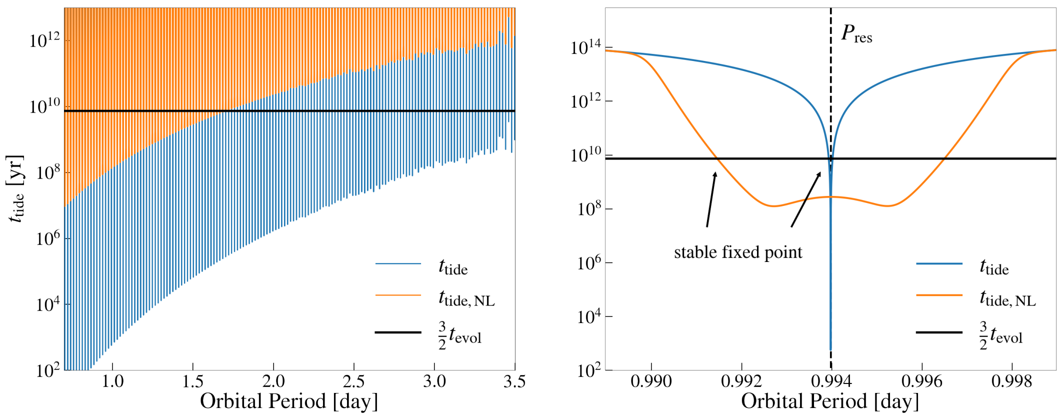

Figure 4.1: **Left**: tidal migration timescale of a $10\,M_\oplus$ exoplanet as a function of orbital period for a Sun-like star (blue line) due to linear g mode damping, along with a typical mode evolution time scale (black line). The orange line represents a possible modification due to nonlinear damping that saturates g mode resonances. **Right**: zoom-in around the g mode resonance at $P_{\rm orb} \approx 1$ days, showing the stable fixed point where $1.5t_{\rm evol} = t_{\rm tide}$, corresponding to inward migration via resonance locking. Nonlinear damping makes the resonances shallower, preventing resonance locking at longer periods (see discussion in Section 4.2 and Appendix 4.6)

The thick radiative zones in main-sequence stars cause internal gravity modes (g modes) to have a dense spectrum in frequency space (see Figure 4.2, left panel). Because the star's internal Brunt-Väisälä frequency typically increases on a stellar evolution timescale, the g mode frequencies increase on a similar time scale, which we define as the mode evolution timescale $t_\alpha \equiv \omega_\alpha/\dot{\omega}_\alpha$. A planet at angular orbital frequency $\Omega_{\rm orb}$ produces tidal forcing at the frequency $\omega_{\rm f} = m(\Omega_{\rm orb} - \Omega_{\rm s})$, where $\Omega_{\rm s}$ is the stellar spin frequency. As the stellar oscillation mode frequencies increase, one of them will quickly encounter a resonance with the tidal forcing frequency, i.e., $\omega_\alpha \to \omega_{\rm f}$ (see Figure 4.2, right panel).

As the planet falls into resonance, it can become "trapped" in resonance (resonantly locked) in the following manner, as shown in Figure 4.1. If the orbit is perturbed outward such that $\omega_{\rm f}$ decreases, it falls deeper into resonance, which increases the tidal dissipation, such that the planet migrates inward and away from exact resonance. If the orbit is perturbed inward such that $\omega_{\rm f}$ increases, it moves further from resonance, which decreases the tidal dissipation, allowing the increasing mode frequency to catch up with the planet and sustain the resonant lock. The planet is thus forced to "ride the mode" and evolve inwards at the same pace as the mode's resonant location (i.e., a resonance lock), and the planet's orbital frequency increases as the star's oscillation mode frequency increases (see Figure 4.2, right panel). The mode

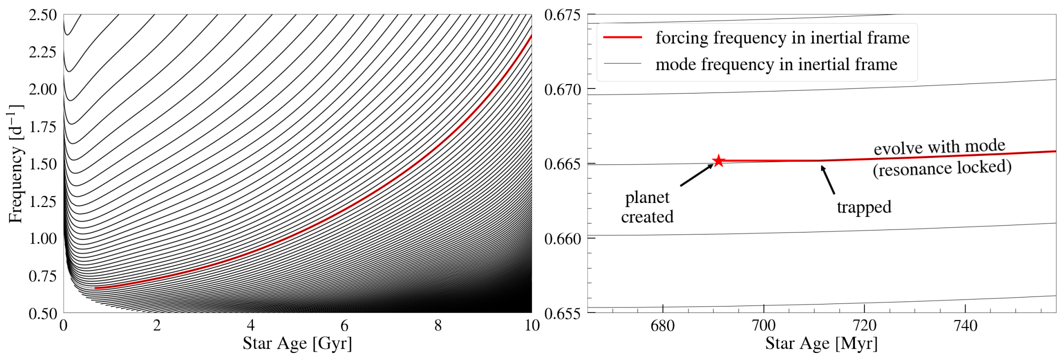

Figure 4.2: The life of a planet undergoing resonance locking with a 1 $M_\odot$ star. **Left**: each line marks the frequency of a stellar g mode in the inertial frame, while the red line is the planet's tidal forcing frequency, which equals twice the orbital frequency in the inertial frame. We only plot one out of three g modes for clarity. A planet born at ~ 700 Myr in a 3-day orbit will soon get trapped in resonance with one of the modes, causing it to migrate inward via resonance locking. **Right**: zoom-in on the moment where resonance locking is first established.

evolution timescale $t_\alpha \equiv \omega_\alpha/\dot{\omega}_\alpha$ hence determines the tidal migration timescale $t_{\rm tide}$, which is directly related to Q' by Equation 4.1.

Stellar Models

To make quantitative predictions, we construct solar-metallicity stellar models with the MESA stellar evolution code [56, 59, 57, 58, 60], and we compute their non-adiabatic oscillation modes with the GYRE pulsation code [70, 69, 27]. Example inlists are given in the supplementary materials. The models start at zero-age main sequence (ZAMS) with a spin period of 3 days, though we do not include rotational effects within the MESA model. The nontidal angular momentum loss rate is assumed to be similar to Skumanich's law and is calculated via [65, 39]

$$\dot{J}_{*,\rm ex} = K_w I_* \Omega_{\rm s}^3 \left(\frac{M}{M_\odot}\right)^{-1/2} \left(\frac{R}{R_\odot}\right)^{1/2}, \tag{4.4}$$

where $K_w \approx -6 \times 10^{-12}$ day is a constant fitted by the Sun's spin period and age.

In Figure 4.3 we plot mode evolution timescales t_α for g modes in stellar models with different masses. The example g modes we plot have periods of 1.5 days in the inertial frame (i.e., they would be resonant with a planet at $P_{\rm orb} = 3$ days) at a stellar age of 700 Myr. We see that t_α is usually comparable to the star's main-sequence lifetime $t_{\rm MS}$. The evolution time scale is slightly shorter near the beginning and end of the main sequence when the star's structure changes more rapidly. For the

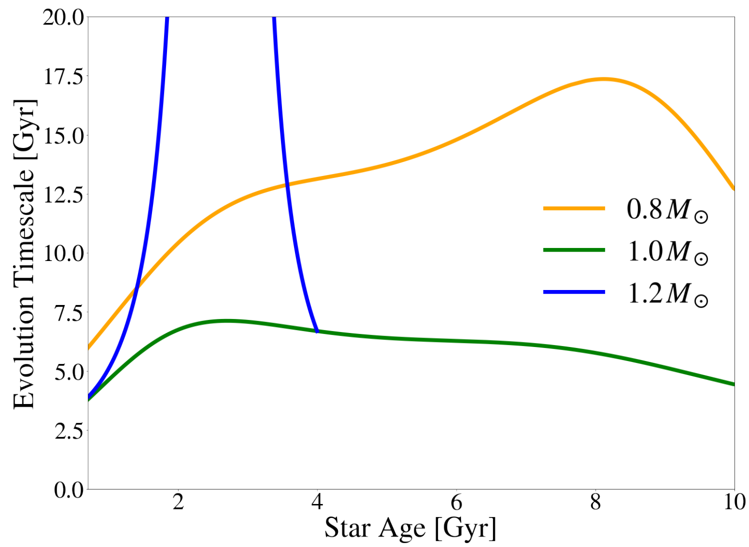

Figure 4.3: Mode evolution timescales $t_\alpha \equiv \omega_\alpha/\dot{\omega}_\alpha$ of example g modes in 0.8, 1.0 and 1.2 $M_\odot$ models. The selected g modes have periods of 1.5 days in the inertial frame at 700 Myr. The mode frequencies typically increase with the star's Brunt-Väisälä frequency as the star evolves. Less massive models have longer mode evolution timescales due to their longer main-sequence lifetime $t_{\rm MS}$. The 1.2 $M_\odot$ model has a negative t_α from about 1.7 to 3.7 Gyr, during which time inward migration via resonance locking cannot occur.

1.2 $M_\odot$ model, the g mode frequencies first increase and then decrease with time due to a growing convective core, causing the value of t_α to diverge and then become negative. During that time, inward migration via resonance locking cannot occur because the resonance locations move away from the star rather than toward it.

Tidal Migration Timescale and Quality Factor

As discussed above, during resonance locking a star's mode frequency remains nearly equal to the tidal forcing frequency [20]: [1]

$$\omega_\alpha \simeq \omega_{\rm f} = m(\Omega_{\rm orb} - \Omega_{\rm s}) \tag{4.5}$$

at all times. Differentiating this equation over time leads to the locking criterion

$$\dot{\omega}_\alpha \simeq \dot{\omega}_{\rm f} = m(\dot{\Omega}_{\rm orb} - \dot{\Omega}_{\rm s}) \,. \tag{4.6}$$

[1] In [20] $\omega_\alpha = m(\Omega_{\rm s} - \Omega_{\rm orb})$ during resonance locking. Here we flip the sign for convenience since the stellar spin frequency is usually much smaller than the orbital frequency for short-period exoplanet systems.

Combining the above equations and defining the spin evolution timescale $t_\mathrm{s} \equiv \Omega_\mathrm{s}/\dot{\Omega}_\mathrm{s}$, we immediately arrive at the (inverse of) the tidal migration timescale

$$t_\mathrm{tide}^{-1} \equiv -\frac{\dot{a}_\mathrm{tide}}{a} = \frac{2}{3}\frac{\dot{\Omega}_\mathrm{orb}}{\Omega_\mathrm{orb}} = \frac{2}{3}\left(t_\alpha^{-1} - \frac{\Omega_\mathrm{s}}{\Omega_\mathrm{orb}}(t_\alpha^{-1} - t_\mathrm{s}^{-1})\right). \tag{4.7}$$

However, when tidal migration occurs, the planet adds angular momentum to the stellar spin, which means t_s and t_tide are related. This is especially important for systems with massive planets, as shown in [42]. Additionally, the system may lose angular momentum due to magnetic braking of the host star. To account for these factors, recall that the total angular momentum J_tot of the star-planet system is

$$J_\mathrm{tot} = J_* + J_\mathrm{p} = I_*\Omega_\mathrm{s} + M_\mathrm{p}\sqrt{GM_*a}\,, \tag{4.8}$$

where I_* is the moment of inertia of the star. Defining the system's change in total angular momentum as $\dot{J}_{*,\mathrm{ex}}$, we have

$$\dot{J}_{*,\mathrm{ex}} = \dot{I}_*\Omega_\mathrm{s} + I_*\dot{\Omega}_\mathrm{s} - \frac{1}{2}J_\mathrm{p}t_\mathrm{tide}^{-1}\,, \tag{4.9}$$

assuming constant stellar/planetary masses as appropriate in most exoplanet systems. If we define evolution timescale for the moment of inertia $t_I = I_*/\dot{I}_*$ and the external stellar spin evolution timescale $t_\mathrm{s,ex} = J_*/\dot{J}_{*,\mathrm{ex}}$, this leads us to the relation

$$t_\mathrm{s}^{-1} = t_\mathrm{s,ex}^{-1} - t_I^{-1} + \frac{J_\mathrm{p}}{2J_*}t_\mathrm{tide}^{-1}\,. \tag{4.10}$$

Substituting Equation 4.10 into Equation 4.7, we get the final expression for t_tide

$$\begin{aligned} t_\mathrm{tide} &= \frac{3}{2}\frac{\Omega_\mathrm{orb}}{\dot{\Omega}_\mathrm{orb}} \\ &= \frac{3}{2}\left(1 - \frac{I_\mathrm{p}}{3I_*}\right)\left[\frac{1}{t_\alpha} - \frac{\Omega_\mathrm{s}}{\Omega_\mathrm{orb}}\left(\frac{1}{t_\alpha} - \frac{1}{t_\mathrm{s,ex}} + \frac{1}{t_I}\right)\right]^{-1}, \end{aligned} \tag{4.11}$$

where $I_\mathrm{p} = M_\mathrm{p}a^2$ is the moment of inertia of the planet's orbit. The pre-factor $1 - I_\mathrm{p}/3I_*$ accounts for the angular momentum transport from the planet's orbit to the stellar spin, indicating that the tidal migration timescale becomes very short for massive planets as I_p approaches $3I_*$, and resonance locking cannot occur if $I_\mathrm{p} > 3I_*$. In practice, one can combine Equation 4.9 and Equation 4.11 to get a set of coupled differential equations for $\Omega_\mathrm{s}(t)$ and $\Omega_\mathrm{orb}(t)$, and hence solve the full evolution of the spin and orbit numerically. For most short-period exoplanet systems, Ω_s is usually negligible compared to Ω_orb. I_p is usually negligible compared to I_*, except for high-mass or long-period planets.

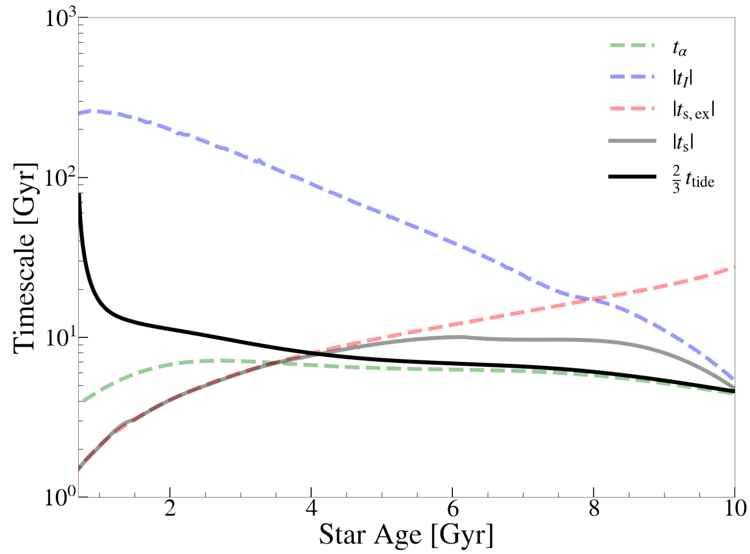

Figure 4.4: Several related timescales in the expression of $t_{\rm tide}$ (Equation 4.11) for our $1\,M_\odot - 10\,M_\oplus$ model. Absolute values of negative quantities are plotted. At later ages ($t \gtrsim 3\,$Gyr), stellar rotation is negligible and the shortest timescale is the mode evolution timescale t_α, such that $2t_{\rm tide}/3 \simeq t_\alpha$ and the planet undergoes orbital decay on a structural evolution time scale. At early ages, rapid stellar spin creates competition between the two terms inside the square bracket of Equation 4.11, raising $t_{\rm tide}$.

In Figure 4.4, we plot the relevant evolution timescales for a $1\,M_\odot$ star with a $10\,M_\oplus$ planet. The external spin evolution timescale $t_{s,\rm ex}$ is usually comparable to the stellar age, and t_I is always long during the main sequence. At early times when the star is rapidly rotating, the second term in brackets in equation 4.11 contributes, increasing the value of $t_{\rm tide}$. The star quickly spins down such that $\Omega_s \ll \Omega_{\rm orb}$, at which point $t_{\rm tide} \sim \frac{3}{2}t_\alpha$ until the end of the main sequence. Hence, the tidal migration timescale is primarily determined by the evolution timescale of the stellar oscillation mode in resonance with the orbit.

The corresponding effective tidal quality factor during resonance locking is

$$\begin{aligned} Q'_{\rm RL} &= \frac{9}{2}\frac{M_{\rm p}}{M_*}\left(\frac{R_*}{a}\right)^5\left(1-\frac{I_{\rm p}}{3I_*}\right) \\ &\times\left[\frac{1}{t_\alpha}-\frac{\Omega_{\rm s}}{\Omega_{\rm orb}}\left(\frac{1}{t_\alpha}-\frac{1}{t_{\rm s,ex}}+\frac{1}{t_I}\right)\right]^{-1}(\Omega_{\rm orb}-\Omega_{\rm s})\,. \end{aligned} \tag{4.12}$$

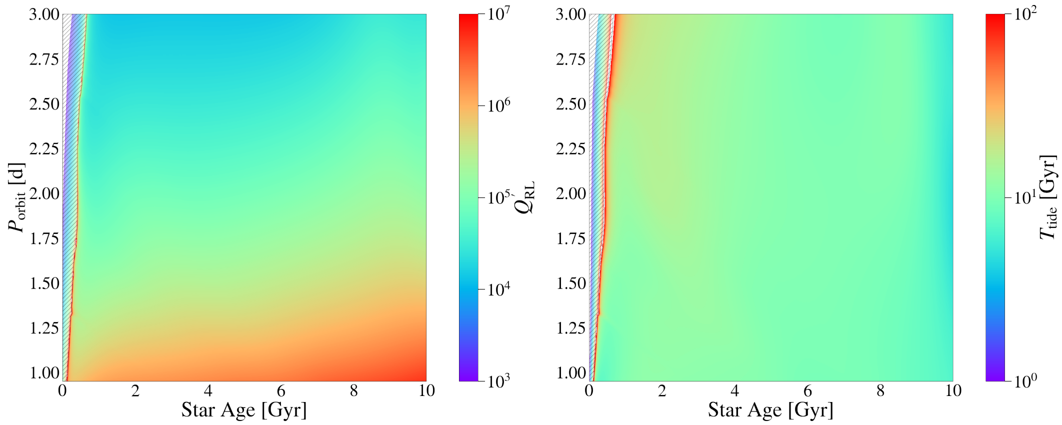

Figure 4.5: Effective tidal quality factor Q'_{RL} (**left**) and tidal migration timescale t_{tide} (**right**) due to resonance locking between a 1 $M_{\odot}$ star with a 10 $M_{\oplus}$ planet. Q'_{RL} decreases sharply as the orbital period increases (see Equation 4.12), and increases slowly with time due to the expansion of the star. In contrast, t_{tide} remains nearly constant within this parameter space. The primary exception is the red feature at very early ages, which is caused by rapid stellar rotation that creates a divergence in t_{tide} (Equation 4.11) and Q'_{RL}. To the left of that feature (hatched regions), t_{tide} is negative and inward migration via resonance locking cannot occur.

When $\Omega_s \ll \Omega_{\mathrm{orb}}$ as appropriate at most stellar ages, this reduces to

$$\begin{aligned} Q'_{\mathrm{RL}} &\simeq \frac{9}{2}\frac{M_{\mathrm{p}}}{M_*}\left(\frac{R_*}{a}\right)^5 t_\alpha \Omega_{\mathrm{orb}} \\ &\approx \frac{9}{2}\frac{(2\pi)^{13/3} M_{\mathrm{p}} R_*^5}{G^{5/3} M_*^{8/3}} t_\alpha P_{\mathrm{orb}}^{-13/3} \,. \end{aligned} \tag{4.13}$$

By solving for the evolution of internal oscillation mode frequencies in stellar models, we can quickly compute the corresponding tidal quality factor resulting from resonance locking. Equation 4.13 evaluates to

$$\begin{aligned} &Q'_{\mathrm{RL}} \simeq 2\times 10^6 \times \\ &\left(\frac{M_{\mathrm{p}}}{M_{\mathrm{J}}}\right)\left(\frac{M_*}{M_{\odot}}\right)^{-8/3}\left(\frac{R_*}{R_{\odot}}\right)^5\left(\frac{t_\alpha}{5\,\mathrm{Gyr}}\right)\left(\frac{P_{\mathrm{orb}}}{2\,\mathrm{days}}\right)^{-13/3} \,. \end{aligned} \tag{4.14}$$

That is, Q'_{RL} is proportional to the planet mass, and it has a $-13/3$ power-law dependence on the orbital period. This is very different from the prescription of constant Q' that is often assumed in the literature.

Figure 4.5 shows the value of Q'_{RL} for a 1 $M_{\odot}$ star with a 10 $M_{\oplus}$ planet as a function of orbital period and stellar age. Q'_{RL} decreases sharply as the orbital period increases, and it increases somewhat as a function of age primarily because the stellar radius increases slightly, as we would expect from Equation 4.12. In contrast, the value of $t_{\rm tide} \simeq \frac{3}{2} t_\alpha$ remains nearly constant within this parameter space.

An exception is at early ages, where the stellar spin is larger than a critical frequency such that the second term in the square bracket of Equation 4.11 is larger than the first, which occurs at approximately

$$\Omega_{\rm s} = \Omega_{\rm s,crit} \simeq \frac{|t_{\rm s,ex}|}{|t_{\rm s,ex}| + t_\alpha} \Omega_{\rm orb} \, , \tag{4.15}$$

where we assumed $t_{\rm s} < 0$ for main-sequence magnetic braking (spin-down). This would lead to a divergence of $t_{\rm tide}$ and $Q'_{\rm RL}$. Physically, the divergence signals the boundary where tidal migration due to resonance locking no longer occurs: for a higher spin frequency (or lower orbital frequency) the resonant locations move outward rather than inward. Since $\Omega_{\rm s}$ is still less than $\Omega_{\rm orb}$ according to Equation 4.15, tidal dissipation would still push the planet inward, and the planet would evolve through the resonances rather than becoming locked in resonance. The colored hatched regions of Figure 4.5 indicate these regions where resonance locking cannot occur.

At even higher spin frequencies where $\Omega_s > \Omega_{\rm orb}$ (gray regions of Figure 4.5), the planet would migrate outward, in the same direction as the resonant locations, such that outward migration via resonance locking could occur. This effect could potentially drive rapid outward migration of short-period planets at very young ages, but we do not study that process in this paper.

Nonlinear Wave Dissipation

Validity of linear theory

The whole theory of resonance locking is based on a linear analysis of dynamical tides [19]. After the waves get excited at the radiative/convective interface inside a star, they propagate toward the center and are geometrically focused such that their amplitudes increase. We thus expect that resonance locking may not occur if the waves become sufficiently nonlinear near the star's center. Specifically, the dominant nonlinear term in the fluid momentum equation is $\xi \cdot \nabla \xi \sim \xi |d\xi_r/dr|$ for g modes. Hence, the quantity $|d\xi_r/dr|$ naturally serves as a measure of nonlinearity: if $|d\xi_r/dr| \gtrsim 1$, then nonlinear effects become very strong, typically causing wave breaking near the center of the star [6] such that standing g modes no longer exist, and resonance locking cannot occur. In fact, nonlinear g mode damping occurs at smaller g mode amplitudes (see Section 4.2), further limiting the situations in which resonance locking can operate.

When resonance locking does occur, the amplitude of oscillating modes can be calculated as follows: the energy and angular momentum dissipation rates are determined by the tidal migration rate of the planet (Equation 4.11). Since energy and angular momentum are conserved, this allows us to compute the corresponding wave amplitude, given a wave damping rate (see [19]).[2] The result is

$$|a_\alpha|_{\rm RL} = \frac{1}{2}\left|\frac{m\Omega_{\rm orb}}{\chi_\alpha \omega_\alpha \gamma_\alpha t_{\alpha,\rm in}}\right|^{1/2}, \tag{4.16}$$

where $\chi_\alpha \equiv 12(M_* + M_{\rm p})R^2/(M_{\rm p}a^2) - 10/(3\kappa)$ for $l = m = 2$ modes and $\kappa \equiv I_*/(M_* R_*^2)$ is the dimensionless moment of inertia of the star. Above, $t_{\alpha,\rm in} \equiv \sigma_\alpha/\dot{\sigma}_\alpha$ is the mode evolution timescale in the inertial frame, with $\sigma_\alpha = \omega_\alpha + m\Omega_{\rm s} \simeq m\Omega_{\rm orb}$.

To test the linear approximation for resonantly locked modes in our models, we evaluate the magnitude of $|d\xi_r/dr|$. Figure 4.6 shows $|d\xi_r/dr|$ as a function of radius for a $1.0\,M_\odot$ model at 3.2 Gyr and a $1.2\,M_\odot$ model [3] at 1.1 Gyr. For each model we include the mode excited by an off-resonance 1 $M_{\rm J}$ hot Jupiter and an on-resonance $10\,M_\oplus$ mini-Neptune (with amplitude calculated via equation 4.16), both of which are put in a 2-day orbit. We find that for all models, the g mode nonlinearity indeed increases near the center of the star due to geometrical focusing. However, in the model with a convective core ($1.2\,M_\odot$ model), gravity waves do not propagate into the stellar core, and the g mode always remains linear ($|d\xi/dr| \lesssim 10^{-3}$). For the model with a radiative core ($1.0\,M_\odot$ model), the resonantly locked mode excited by a mini-Neptune comes close to the wave-breaking threshold ($|d\xi/dr| \sim 1$) but does not exceed it. Interestingly, this mode has a larger amplitude than the non-resonant mode excited by a hot Jupiter, demonstrating the great enhancement in amplitude produced by the resonant forcing.

We note that the resonant locking amplitude computed above depends on the damping rate γ_α in equation 4.16. Weak nonlinear damping may increase the effective value of γ_α, decreasing the necessary mode amplitude for resonance locking. We revisit this issue in Section 4.2.

[2] Equation 4.16 follows from [19] for $N = m = 2$ as appropriate for nearly circular orbits.

[3] In the $1.2\,M_\odot$ model, there is a "jumping core boundary" issue that prevents us from directly solving the mode evolution timescale. We hence smooth the mode frequency solution by fifth-order polynomials. This is discussed in detail in Appendix 4.6.

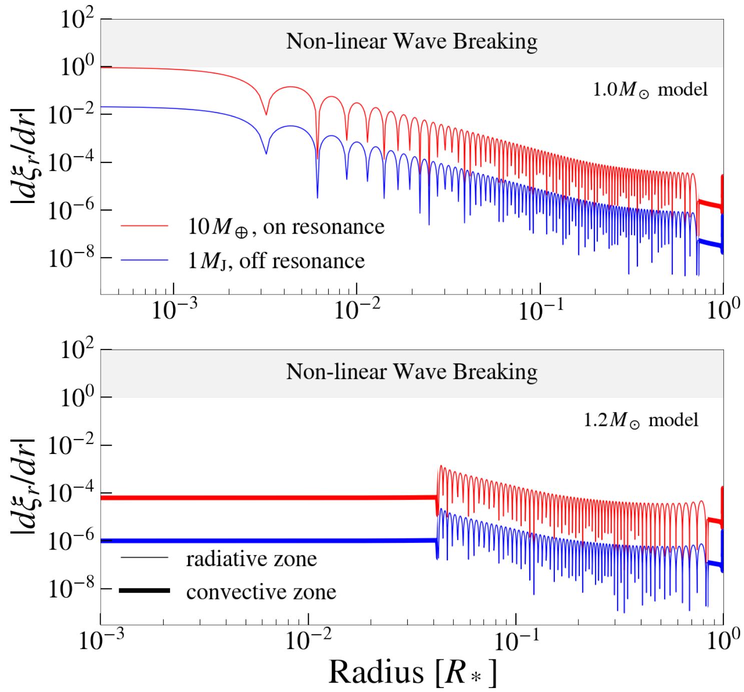

Figure 4.6: Linearity tests for tidally excited g modes in our $1.0\, M_\odot$ (top panel) and $1.2\, M_\odot$ (bottom panel) models. For each model we compute the value of $|d\xi_r/dr|$ for an off-resonance $1\, M_J$ hot Jupiter (blue line) and an on-resonance $10\, M_\oplus$ mini-Neptune (red line), both of which are put in a 2-day orbit. We see that g modes in the $1.2\, M_\odot$ model are generally far from wave breaking due to their convective cores (thick lines) which prevent the g modes from propagating near the stellar center. For the $1\, M_\odot$ model with a radiative core, g modes near the stellar center are much more nonlinear but do not reach wave-breaking amplitudes (gray shaded region).

Wave Breaking

When nonlinear wave breaking occurs near the stellar center, the waves overturn the stratification and are efficiently absorbed [5, 6]. The tidally excited gravity waves can then be treated as traveling waves rather than standing g modes, and the corresponding energy dissipation rates have been closely examined in several works [78, 25, 28, 4]. Specifically, [5] compute the corresponding tidal quality factor for wave breaking:

$$Q'_{\rm WB} = 10^5 \left(\frac{\mathcal{G}_\odot}{\mathcal{G}}\right)\left(\frac{M}{M_\odot}\right)^2\left(\frac{R_\odot}{R}\right)\left(\frac{P_{\rm tide}}{0.5\ {\rm days}}\right)^{8/3}, \tag{4.17}$$

where $P_{\rm tide} = 2\pi/\omega_{\rm f}$ is the tidal forcing period and $\mathcal{G}$ is a parameter that depends on the stellar structure and is defined in [4].

Nonlinear wave breaking in Sun-like stars only occurs for planets with $M \gtrsim$

$3\,M_{\rm J}(P/1\,{\rm d})^{-1/6}$, according to [5]. This appears roughly consistent with the calculation of linear mode amplitude in Figure 4.6. Hence, in our calculations of planetary evolution in Section 4.4, we only use equation 4.17 for the most massive exoplanets.

Weakly Nonlinear Damping

[16] have examined the nonlinear damping of g modes tidally excited by hot Jupiters with periods $P \lesssim 4$ days in Sun-like stars. They examined the weakly nonlinear case where the g waves do not break, but they are sufficiently nonlinear to excite daughter and granddaughter modes that dissipate their energy. They found that even for off-resonance hot Jupiters (like the model shown in Figure 4.6), nonlinear damping is sufficient to wipe out resonances, i.e., the energy dissipation rate is the same for resonant and non-resonant modes. Our on-resonance mini-Neptune in Figure 4.6 excites even larger oscillations than an off-resonance hot Jupiter, meaning that nonlinear damping will dominate over linear damping before the resonant amplitude of equation 4.16 is reached.

However, [16] also found that nonlinear energy dissipation is much smaller for off-resonance planets with $M_p \lesssim 0.3\,M_{\rm J}$. For a $10\,M_\oplus$ planet, this implies that the nonlinear energy dissipation rate is small away from resonance and will greatly increase as the planet moves toward a resonance such that the mode amplitude increases and nonlinear dissipation ramps up. In essence, the total damping rate γ in the expression for the mode amplitude is itself a function of the mode amplitude in this situation. If γ becomes too large near resonance, the resonance will be “saturated" (i.e., the blue curve in Figure 4.1 will be moved upward near resonance) such that the resonance locking fixed point does not exist.

To address this possibility, in Appendix 4.6 we attempt to extrapolate the results of [16] to low-mass planets below $\simeq 0.3\,M_{\rm J}$. Using the resulting nonlinear damping rate in place of the linear damping rate in equation 4.3 results in the orange curve in Figure 4.1, in which the nonlinear damping makes the resonance wells much shallower and wider. The planet may become trapped in resonance if its orbital period is short enough ($P_{\rm orb} \lesssim 1.7$ days in Figure 4.1), though we emphasize that more detailed nonlinear coupling calculations are needed for reliable results. This suggests that resonance locking may occur for sufficiently low-mass planets at sufficiently short periods, though the exact mass threshold requires a more accurate calculation of nonlinear damping.

[16] finds that the following quality factor provides a good fit to their calculations

for sufficiently massive planets around Sun-like stars:

$$Q'_{\mathrm{EW}} = 2 \times 10^5 \left(\frac{M_{\mathrm{p}}}{M_{\mathrm{J}}}\right)^{1/2} \left(\frac{P_{\mathrm{tide}}}{0.5\,\mathrm{days}}\right)^{2.4}. \tag{4.18}$$

Based on their results, equation 4.18 breaks down for planet masses with $M \lesssim 0.3\,M_{\mathrm{J}}$, so we only use this formula for planets in the range $0.3\,M_{\mathrm{J}} \leq M_p \leq 3\,M_{\mathrm{J}}$ in our calculations of orbital evolution in Section 4.4.

We see that in both Equation 4.17 and Equation 4.18, the effective tidal quality factor increases with the orbital period, in stark contrast to the prediction of resonance locking where Q' *decreases* with orbital period. This entails that resonance locking may be more important at longer orbital periods (so long as it can operate), while nonlinear dissipation is likely to dominate at short orbital periods, with important differences in long-term behavior of real systems (see Section 4.4).

We conclude that resonance locking will not be prevented by nonlinear effects in stars with convective cores, but nonlinear damping will prevent resonance locking from occurring for hot Jupiters around Sun-like stars. It is unclear whether nonlinear damping will prevent resonance locking of low-mass ($M \lesssim 0.3\,M_{\mathrm{J}}$) planets, and this should be studied in future work.

4.3 Comparison with Observations

Comparison with Penev et al. 2018

[63] analyzed 188 known hot Jupiter systems to constrain their effect tidal factors based on an improved method from [62]. They managed to constrain two-sided limits on Q' for 35 systems, and to derive lower bounds on Q' for another 40 systems, while the remaining systems in their sample did not lead to meaningful constraints. Of the 75 systems they studied, they found a clear trend toward lower Q' for larger P_{tide}, where $P_{\mathrm{tide}} \equiv (P_{\mathrm{orb}}^{-1} - P_{\mathrm{spin}}^{-1})^{-1}/m$. The trend is then fitted by the following power-law formula (see Figure 4.7 or Figure 2 in [63]):

$$Q' = \max\left[10^{6.0}\left(\frac{P_{\mathrm{tide}}}{1\mathrm{days}}\right)^{-3.1}, 10^5\right]. \tag{4.19}$$

When resonance locking occurs and stellar spin is negligible compared to the orbit, Equation 4.14 predicts $Q' \approx 2 \times 10^6\,(P_{\mathrm{tide}}/1\,\mathrm{day})^{-13/3}$ for fiducial hot Jupiter parameters. This simple analysis immediately leads to a similar power-law trend to the fitted formula 4.19, but with no free parameters. In reality, we expect significant scatter due to the variation of other factors in equation 4.14 away from fiducial parameters (e.g., variations in R_* and M_{p} translate to variations in Q').

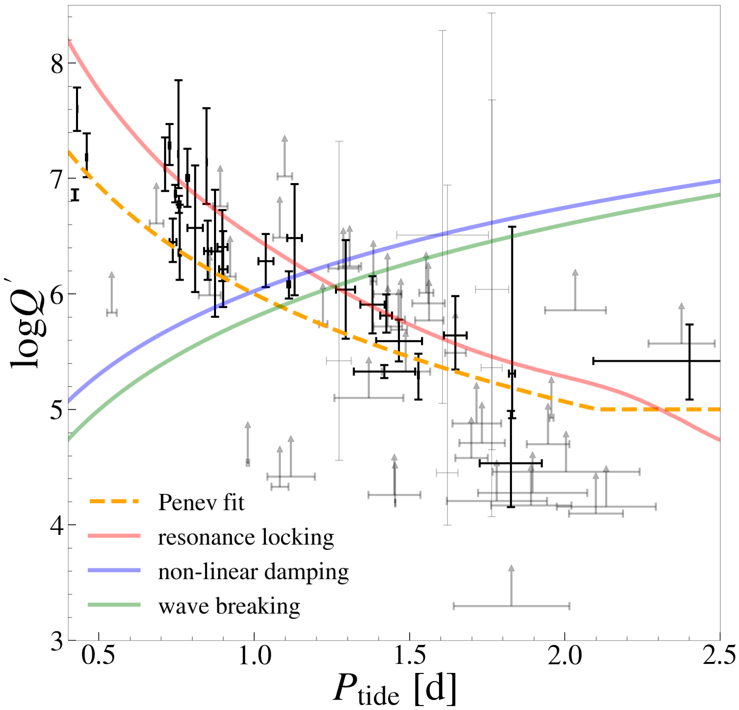

Figure 4.7: Dependence of Q' on tidal period as predicted by resonance locking (red line), nonlinear damping (blue line) and wave breaking (green line) for models of a Sun-like star with a $1\,M_{\rm J}$ planet. We also plot the inferred values of Q' for individual systems from [63], and their power-law fit (orange dashed line). Black points are cases for which Q' was bounded within two orders of magnitude, while thinner gray symbols are cases with weaker constraints. While the prediction of resonance locking is very similar to the trend from [63], other explanations for this trend may be possible (see text).

To compute the exact value of Q' as a function of $P_{\rm tide}$ for resonance locking, we construct a $1\,M_\odot$ stellar model with MESA and compute non-adiabatic oscillation modes. Assuming a stellar rotational evolution based on the modified Skumanich law (Equation 4.4), we track the run of Q' upon $P_{\rm tide}$ for a typical $1\,M_{\rm J}$ planet at the stellar age of 5 Gyr, using equation 4.12. The results are shown in Figure 4.7. We find that the predicted trend is remarkably similar to the power-law fit by [63], though slightly offset to higher values of Q'. Overall, the resonance locking prediction fits the data very well. We also plot the predicted relations from wave breaking (Equation 4.17) and weakly nonlinear dissipation (Equation 4.18). Those models predict that Q' increases as $P_{\rm orb}$ increases, opposite to the trend inferred by [63].

While these results at first glance appear to provide compelling evidence for the operation of resonance locking in hot Jupiter systems, we caution that other explanations for the trend in Q' from [63] should be examined. From a theoretical perspective, resonance locking likely cannot operate for Jupiter-mass planets around Sun-like stars due to the nonlinear damping discussed in Section 4.2. Hence, we are hesitant to ascribe the trend in Q' from [63] to resonance locking, though resonance locking could provide a nice explanation if nonlinear mode dissipation is much less efficient than found by [16].

Another possibility worth considering is that the inferred trend in Q' from [63] does not arise from tidal spin-up of the host stars. [63] infer the value of the host stars' Q' by combining age estimates with measurements of spin period. Rapidly rotating host stars (compared to typical field stars) are often inferred to have been tidally spun up by their hot Jupiter companions, entailing that the tidal spin-up time scale is comparable to the main-sequence life time of the host star. This can be seen because much shorter tidal spin-up times would result in the synchronization of the star or the destruction of the hot Jupiter, while much longer ones would not increase the star's rotation significantly. Assuming $t_s = \Omega_{\rm s}/\dot{\Omega}_{\rm s} = 10\,{\rm Gyr}$, some algebra shows that this requires a scaling $Q' \sim 2 \times 10^6 (P_{\rm tide}/1\,{\rm day})^{-4} (P_{\rm spin}/10{\rm days}) (M_{\rm p}/M_{\rm J})^2$, almost identical to the trend shown in Figure 4.7. Hence, if one does not have accurate age estimates and assumes that hot Jupiter hosts have similar ages to typical field stars, it could yield a spurious scaling of Q' that is very similar to the trend found by [63].

Instead, we speculate that moderately rotating host stars of hot Jupiters are (in some cases) simply young stars that are still spinning down, and that they have not been substantially spun up by tides. This may be consistent with the young average ages of hot Jupiter host stars found by [31]. In this case, it is very difficult to observationally constrain the host star's Q', except perhaps to place a lower limit. For massive planets where nonlinear effects prevent resonance locking, we expect a trend in Q' similar to that predicted by [16] and [4]. Future work could aim to more accurately constrain the ages of the hot Jupiter host stars in [63] to determine whether their rapid rotation arises from youth or tidal spin-up.

Individual Hot Jupiter Systems

Here we summarize our prediction for the effective tidal Q's of 15 real systems based on resonance locking. Most of the systems are chosen from [55], who argue that the orbital decay of these systems should be the easiest to observe. We also study TRES-3b and WASP-4b which have new observational constraints [9, 45], and we include WASP-128b, a system with a very massive hot Jupiter.

The observational properties of these systems are summarized in Table 4.2. For each system, we construct a number of stellar models to fit their host stars with different initial masses and metallicities within the observational errors and locate the model that matches the other observed properties of the star. We are able to fit the masses, radii, metallicities, ages, and effective temperatures within the observational error (see Table 4.2 for a summary) for all the host stars except KELT-16b. A typical inlist file is given in the supplementary material.

For each stellar model, we compute $\ell = 2$ non-adiabatic oscillation modes with GYRE, with typical inlist files given in the supplementary material. For each system, we assume a negligible spin of the host star and identify the oscillation mode resonant with the tidal forcing, and we calculate the value of t_α for that mode. The effective tidal Q's are then calculated via Equation 4.12 using our model properties. We summarize the predictions for resonance locking in Table 4.1, along with predictions for tidal migration rates due to wave breaking [4] and nonlinear dissipation by Equation 4.18 [16]. Below are detailed discussions for each system.

Name	$Q'_{\rm obs}$	$Q'_{\rm RL}$	$Q'_{\rm WB}$	$Q'_{\rm EW}$	Core Status	$t_{\rm tide,\,RL}$ (Gyr)
HAT-P-23b	$> (3.6 \pm 1.1) \times 10^5$	6.0×10^7	$\mathbf{3 \times 10^5}$	$\mathbf{4.6 \times 10^5}$	radiative?	5.6
HATS-18b		2.1×10^8	$\mathbf{7 \times 10^4}$	$\mathbf{1.9 \times 10^5}$	radiative	9.7
KELT-16b	$> (0.5 \pm 0.1) \times 10^5$	$\mathbf{5.1 \times 10^8}$	5×10^5	3.1×10^5	convective	9.8
OGLE-TR-56b	$> (4.4 \pm 1.3) \times 10^5$	$\mathbf{1.1 \times 10^8}$	10^6	3.7×10^5	convective	12.9
TRES-3b	$(5.5 \pm 4.2) \times 10^4$	1.2×10^7	$\mathbf{4.3 \times 10^5}$	$\mathbf{5.3 \times 10^5}$	radiative	8.0
WASP-4b	$(1.8 \pm 0.2) \times 10^4$	1.1×10^7	$\mathbf{2 - 3 \times 10^5}$	$\mathbf{4.4 \times 10^5}$	radiative	9.9
WASP-12b	$(1.1 \pm 0.1) \times 10^5$	1.9×10^8	$\mathbf{0.18 - 3 \times 10^6}$	$\mathbf{3.0 \times 10^5}$	convective?	7.2
WASP-18b	$> (1.0 \pm 0.2) \times 10^6$	$\mathbf{3.3 \times 10^8}$	2×10^6	5.8×10^5	convective	4.7
WASP-19b	$(3.1 \pm 0.9) \times 10^5$	2.2×10^8	$\mathbf{0.4 - 0.5 \times 10^5}$	$\mathbf{1.2 \times 10^5}$	radiative	9.7
WASP-43b	$> (2.5 \pm 0.2) \times 10^5$	2.3×10^8	$\mathbf{1 \times 10^5}$	$\mathbf{1.7 \times 10^5}$	radiative	26.6
WASP-72b	$> (1.2 \pm 0.8) \times 10^3$	4.5×10^6	$> 2 \times 10^{12}$	$\mathbf{1.7 \times 10^6}$	radiative	0.8
WASP-103b	$> (6.4 \pm 0.6) \times 10^4$	$\mathbf{4.0 \times 10^8}$	2×10^5	2.1×10^5	convective	9.7
WASP-114b		$\mathbf{4.5 \times 10^7}$	2×10^6	7.6×10^5	convective	7.9
WASP-122b		$\mathbf{6.4 \times 10^6}$	2.3×10^5	8.2×10^5	convective	2.4
WASP-128b		(no RL)	$\mathbf{0.03 - 1.3 \times 10^8}$	$\mathbf{8.2 \times 10^6}$	radiative	20.9

Table 4.1: Observed/calculated tidal quality factor Q', core status and resonance locking induced $t_{\rm tide,\,RL}$ of the systems we study. $Q'_{\rm obs}$ shows the observed constraints from [55, 9] and [45]. $Q'_{\rm RL}$ is the predicted tidal factor from the best-fit resonance locking model. $Q'_{\rm WB}$ is the predicted tidal factor from gravity wave breaking [4], and $Q'_{\rm EW}$ is the predicted tidal factor from nonlinear g mode dissipation [16]. We also show the convective/radiative core status of our models. We emphasize that for massive planets like these, resonance locking is only expected to occur in stars with convective cores, and wave breaking/nonlinear dissipation is expected to dominate stars with radiative cores. We bold the Q' values of our inference of the appropriate tidal theory for each system, while the other values are left for reference. The $t_{\rm tide,\,RL}$ values show that most system have long tidal migration timescales if they experience resonance locking. **Note**: some authors use a different definition of Q' from ours. We have corrected their results to make them consistent with our definition, so the numbers here may appear different from the original literature.

1. **HAT-P-23b**: A planet of 2.09 M_J in a 1.21-day orbit around a G-type dwarf [3]. Our best-fit model is a 1.10 $M_\odot$ star with a radiative core. Lack of detected orbital decay requires $Q' > (3.6 \pm 1.1) \times 10^5$ [55]. Our resonance locking calculation predicts $Q'_{\rm RL} = 6.0 \times 10^7$, with $t_{\rm tide} = 5.6\,$Gyr, but resonance locking is not expected due to nonlinear effects in the radiative core. [4] predicts $Q'_{\rm WB} = 3 \times 10^5$ from calculations of wave breaking, but the best-fit model in that work has a convective core. Weak nonlinear mode damping gives $Q'_{\rm EW} = 4.6 \times 10^5$. This is a promising system in which to observe tidal decay if the core is indeed radiative.

2. **HATS-18b**: A planet of 1.98 M_J in a 0.84-day orbit around a G-type star [61]. Our best-fit model is a 1.03 $M_\odot$ star with a radiative core. No reliable constraint on Q' could be found due to the lack of data [55]. Our resonance locking calculation predicts $Q'_{\rm RL} = 2.1 \times 10^8$, with $t_{\rm tide} = 9.7\,$Gyr, but resonance locking is not expected due to nonlinear effects since the star has a radiative core and a massive planet. [4] predicts $Q'_{\rm WB} \approx 7 \times 10^4$ from calculations of wave breaking, weak nonlinear mode damping predicts $Q'_{\rm EW} = 1.9 \times 10^5$. The results make HATS-18b a very promising candidate in which to observe orbital decay.

3. **KELT-16b**: A planet of 2.75 M_J in a 0.97-day orbit around an F-type star [50]. Our best-fit model is a 1.18 $M_\odot$ star with a convective core. Lack of detected orbital decay requires $Q' > (0.5 \pm 0.1) \times 10^5$ [55]. Our resonance locking calculation predicts $Q'_{\rm RL} = 5.1 \times 10^8$, with $t_{\rm tide} = 9.8\,$Gyr, which is consistent with the observed lower limit, indicating no tidal decay should have been observed.

4. **OGLE-TR-56b**: A planet of 1.39 M_J in a 1.21-day orbit around an F-type star [64, 68]. Our best-fit model is a 1.23 $M_\odot$ star with a convective core. Lack of detected orbital decay requires $Q' > (4.4 \pm 1.3) \times 10^5$ [55]. Our resonance locking calculation predicts $Q'_{\rm RL} = 1.1 \times 10^8$, with $t_{\rm tide} = 12.9\,$Gyr, which is consistent with the observed lower limit, indicating no tidal decay should be observed.

5. **TRES-3b**: A planet of 1.92 M_J in a 1.306-day orbit around an G-type dwarf [49]. Our best-fit model is a 0.89 $M_\odot$ star with a radiative core. Observations indicate $Q' \approx (5.5 \pm 4.2) \times 10^4$ [45], potentially detecting rapid orbital decay. Our resonance locking calculation predicts $Q'_{\rm RL} = 1.2 \times 10^7$, with $t_{\rm tide} =$

8.0 Gyr, but resonance locking is not expected due to nonlinear damping in the radiative core. [4] predicts $Q'_{\rm WB} = 4.3 \times 10^5$ from calculations of wave breaking, slightly larger than the measured value. Weak nonlinear mode damping predicts $Q'_{\rm EW} = 5.3 \times 10^5$. Further observations should attempt to verify the result of [45] and will help calibrate models of orbital decay via nonlinear g mode damping in the core.

6. **WASP-4b**: A planet of 1.186 $M_{\rm J}$ in a 1.338-day orbit around a main-sequence star [9, 66]. Our best-fit model is a 0.83 $M_\odot$ star with a radiative core. Observations suggest $Q' = (1.8 \pm 0.2) \times 10^4$ [9], but [8] recently discovered a third massive companion that might cause the shift in transit times. Our resonance locking calculation predicts $Q'_{\rm RL} = 1.1 \times 10^7$, with $t_{\rm tide} = 9.9$ Gyr, but resonance locking is not expected due nonlinear damping in the radiative core. [4] predicts $Q'_{\rm WB} = 2-3 \times 10^5$ from calculations of wave breaking. Weak nonlinear mode damping predicts $Q'_{\rm EW} = 4.4 \times 10^5$. Further observations will shed more light on the system and have a good chance of confirming the detection of orbital decay.

7. **WASP-12b**: A planet of 1.47 $M_{\rm J}$ in a 1.09-day orbit around a late F-type main-sequence star or a subgiant [33, 74, 13]. Our best-fit model is a 1.44 $M_\odot$ star with a convective core, but sub-giant models without convective cores are also compatible with the data [2]. Observations indicate orbital decay with a quality factor $Q' = (1.1 \pm 0.1) \times 10^5$ [54, 55]. Our resonance locking calculation predicts $Q'_{\rm RL} = 1.9 \times 10^8$, three orders of magnitude too high, with $t_{\rm tide} = 7.2$ Gyr. [4] finds $Q'_{\rm WB}$ ranging from 1.8×10^5 to 3×10^6 assuming that gravity waves break near a radiative core, based on different stellar models they choose. Weak nonlinear mode damping predicts $Q'_{\rm EW} = 3.0 \times 10^5$. The measured decay rate thus indicates that the star is indeed a sub-giant undergoing orbital decay via nonlinear gravity wave damping.

   We speculate that WASP-12b was previously migrating inward slowly via resonance locking when the host star was on the main sequence and had a convective core. When the core became radiative at the end of the main sequence, nonlinear damping became effective, driving the much faster orbital decay we see today. This may help alleviate fine-tuning problems in formation models for WASP-12b, allowing the planet to survive until the end of the main sequence, while also explaining the rapid inward migration at the start of the subgiant phase.

8. **WASP-18b**: A massive planet of $11.4\,M_J$ in a 0.94-day orbit around a relatively hot ($T_{\rm eff} = 6431$ K) F-type star [36, 67]. The mass of the host star is a bit uncertain, with a measurement of $1.46 \pm 0.29\,M_\odot$ reported. Our best-fit model falls at the low end of the mass measurement, with a mass of $1.17\,M_\odot$ and a convective core. Lack of detected orbital decay requires $Q' > (1.0 \pm 0.2) \times 10^6$ [55]. Our resonance locking calculation predicts $Q'_{\rm RL} = 3.3 \times 10^8$, with $t_{\rm tide} = 4.7$ Gyr, which is consistent with the observed lower limit, indicating no tidal decay should have been observed.

9. **WASP-19b**: A planet of $1.139\,M_J$ in a 0.79-day orbit around a Sun-like star, making it the hot Jupiter system with the shortest period yet observed [34, 44]. Our best-fit model is a $0.91\,M_\odot$ star with a radiative core. Observations indicate $Q' = (3.1 \pm 0.9) \times 10^5$, but the authors encourage caution due to the scanty data [55]. Our resonance locking calculation predicts $Q'_{\rm RL} = 2.2 \times 10^8$, with $t_{\rm tide} = 9.7$ Gyr, but resonance locking is not expected due to nonlinear effects in the radiative core. [4] predicts $Q'_{\rm WB} \approx 4 - 5 \times 10^4$ from calculations of wave breaking, smaller than the observational constraint. Weak nonlinear mode damping predicts $Q'_{\rm EW} = 1.2 \times 10^5$. Further observations of this system will hence be very useful to constrain tidal theories.

10. **WASP-43b**: A planet of $2.034\,M_J$ in a 0.81-day orbit around a K-type dwarf [35, 22]. Our best-fit model is a $0.70\,M_\odot$ star with a radiative core. Lack of detected orbital decay requires $Q' > (2.5 \pm 0.2) \times 10^5$ [55]. Our resonance locking calculation predicts $Q'_{\rm RL} = 2.3 \times 10^8$, with $t_{\rm tide} = 26.6$ Gyr, but resonance locking is not expected due to nonlinear effects in the radiative core. [4] predicts $Q'_{\rm WB} \approx 10^5$ from calculations of wave breaking, comparable to the lower limit from observations. Weak nonlinear mode damping predicts $Q'_{\rm EW} = 1.7 \times 10^5$. This is another good candidate for orbital decay to be detected in the near future.

11. **WASP-72b**: A planet of $1.546\,M_J$ in a 2.22-day orbit around an F-type star [24]. Our best-fit model is a $1.33\,M_\odot$ subgiant with a radiative core. Lack of detected orbital decay requires $Q' > (1.2 \pm 0.8) \times 10^3$ [55]. Our resonance locking calculation predicts $Q'_{\rm RL} = 4.5 \times 10^6$, with $t_{\rm tide} = 0.8$ Gyr, but resonance locking is not expected due to nonlinear damping in the radiative core. [4] predicts a very large $Q'_{\rm WB} > 10^{12}$ from calculations of wave breaking. However, that work appears to use a stellar model with surface temperature much higher than the observed temperature of $T = 6250 \pm 100$ K from [24],

likely translating to a predicted value of Q' that is far too high. Weak nonlinear mode damping predicts $Q'_{\rm EW} = 1.7 \times 10^6$. Future models should re-examine the theoretical predictions.

12. **WASP-103b**: A planet of 1.51 $M_{\rm J}$ in a 0.93-day orbit around a late F-type star [23, 14]. Our best-fit model is a 1.18 $M_\odot$ star with a convective core. Lack of detected orbital decay requires $Q' > (6.4 \pm 0.6) \times 10^4$ [55]. Our resonance locking calculation predicts $Q'_{\rm RL} = 4.0 \times 10^8$, with $t_{\rm tide} = 9.7$ Gyr, which is consistent with the observed lower limit, indicating no tidal decay should have been observed.

13. **WASP-114b**: A planet of 1.769 $M_{\rm J}$ in a 1.55-day orbit around an early G-type star [7]. Our best-fit model is a 1.24 $M_\odot$ star with a convective core. Being a newly discovered system, no reliable constraint on Q' could be found due to its lack of data [55]. Our resonance locking calculation predicts $Q'_{\rm RL} = 4.5 \times 10^7$, with $t_{\rm tide} = 7.9$ Gyr, and the linearity of resonant modes shows resonance locking could occur. Orbital decay is unlikely to be detected for this system unless the star is less massive and contains a radiative core.

14. **WASP-122b**: A planet of 1.284 $M_{\rm J}$ in a 1.71-day orbit around a G-type star [71]. Our best-fit model is a 1.25 $M_\odot$ star with a convective core. Being a newly discovered system, no reliable constraint on Q' could be found due to its lack of data [55]. Our resonance locking calculation predicts $Q'_{\rm RL} = 6.3 \times 10^6$, with $t_{\rm tide} = 2.4$ Gyr, and the linearity of resonant modes shows resonance locking could occur. Orbital decay is unlikely to be detected for this system unless the star is less massive and contains a radiative core.

15. **WASP-128b**: A brown dwarf of 37.19 $M_{\rm J}$ in a 2.209-day orbit around an G-type dwarf [37]. Our best-fit model is a 1.13 $M_\odot$ star with a radiative core. No observational constraint on Q' is available at current time. The large companion mass makes the tidal stellar spin-up important, and we do not expect resonance locking in this system because $I_{\rm p} > 3I_*$ in Equation 4.11 such that resonance cannot be maintained. [4] predicts $Q'_{\rm WB}$ from 3×10^6 to 1.3×10^8 from calculations of wave breaking, based on the different rotation periods in the stellar models in that work. Weak nonlinear mode damping predicts $Q'_{\rm EW} = 8.2 \times 10^6$. Further observations should attempt to measure the stellar spin rate and could potentially detect orbital decay.

To summarize, for the hot Jupiter systems above, we predict orbital decay timescales of a few gigayears for host stars with convective cores in which resonance locking can operate. Orbital decay via nonlinear mode damping [16] or wave breaking [4] is likely to operate in stars with radiative cores, causing shorter tidal decay time scales that can be more easily observed. Future observations can help confirm our prediction of more rapid orbital decay of hot Jupiters in stars with radiative cores.

4.4 Discussion

System Evolution: The Big Picture

We have argued that resonance locking, nonlinear g mode dissipation, and gravity wave breaking can all operate in short-period exoplanet systems. In general, one must solve for the angular momentum evolution (equation 4.9) with appropriate tidal dissipation physics (i.e. the appropriate value of Q' from equation 4.1) to track the full orbital evolution of the system. We expect that resonance locking is the dominant tidal dissipation mechanism for stars massive enough to have convective cores ($M \gtrsim 1.1\, M_\odot$), where nonlinear damping is weak and g modes can be resonantly excited. In these stars, equation 4.11 can be used to estimate the tidal dissipation rate. Heartbeat stars with large-amplitude, tidally excited g modes (e.g., [19]) are proof that nonlinear damping does not prevent resonant mode excitation in these stars, even for stellar-mass companions.

For stars with radiative cores, a planet more massive than a few Jupiter masses causes gravity wave breaking near the core [5] such that tidal dissipation is determined by equation 4.17. For Jupiter-mass exoplanets approximately in the range $0.3\, M_\mathrm{J} \lesssim M_p \lesssim 3\, M_\mathrm{J}$, wave breaking does not occur, but nonlinear mode damping prevents resonant excitation and produces tidal dissipation according to equation 4.18 [16]. Resonance locking is likely to be the dominant dissipation mechanism for less massive planets with $M \lesssim 0.3\, M_\mathrm{J}$, though future work is needed to quantify this number more accurately (see Section 4.2).

We hence study the orbital evolution of three fiducial exoplanet systems with masses of $10\, M_\oplus$, $1\, M_\mathrm{J}$ and $5\, M_\mathrm{J}$, in which resonance locking, nonlinear damping, and wave breaking apply, respectively. We initialize calculations of orbital evolution for planets in 3-day orbits around a $1\, M_\odot$ star at an age of 700 Myr. We integrate the combined equations of orbital decay (equation 4.2), spin evolution (equation 4.10) and tidal theories (equation 4.12, 4.17 or 4.18) to track the full evolution of the systems. We also integrate a system without planets (i.e. a star spinning down

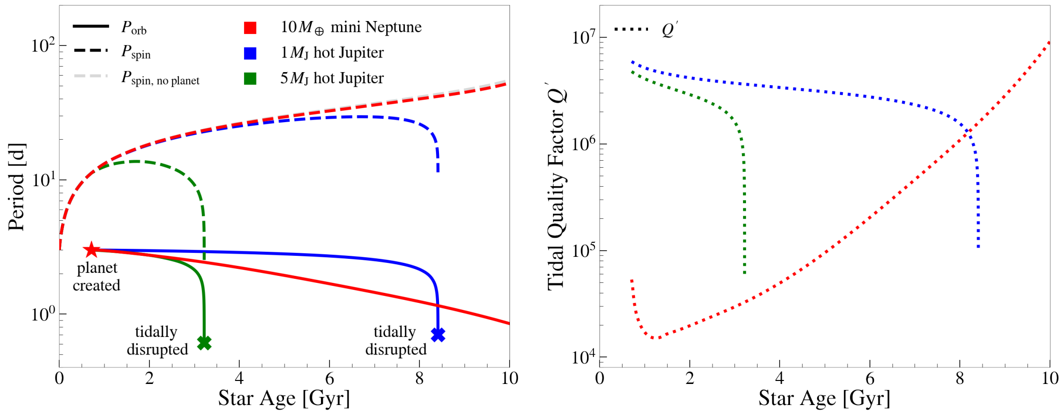

Figure 4.8: **Left:** the evolution of planetary orbital period (solid lines) and stellar spin period (dashed lines) for a $1M_\odot$ host star with a $10M_\oplus$ mini-Neptune model (red lines), along with $1M_{\rm J}$ (blue lines) and $5M_{\rm J}$ (green lines) hot Jupiter models. In the mini-Neptune model, resonance locking is at work, leading to a significant decrease in orbital period during the evolution. Nonlinear mode damping for the 1 $M_{\rm J}$ planet and wave breaking for the 5 $M_{\rm J}$ planet lead to tidal disruption on timescales of a few gigayears. **Right:** the corresponding effective stellar tidal quality factor, Q', over the course of each evolution.

purely by magnetic braking) for comparison. The results are shown in Figure 4.8.

For the $10\,M_\oplus$ mini-Neptune, resonance locking causes significant orbital decay during the main sequence, with $t_{\rm tide} \sim t_{\rm MS}$ as typically expected from resonance locking. We note that the effective tidal quality factor driving this planet's inward migration is initially quite small, with $Q' < 10^5$. Consequently, the planet migrates much farther than typical parameterized tidal models with $Q' \sim 10^5$–10^6. Compared to prior work, resonance locking typically predicts substantially more tidal migration for low-mass planets at orbital periods $P \gtrsim 2$ days. In this example, the planet has migrated to ultrashort periods by the end of the main sequence, but it does not plunge into its host star because the value of Q' increases at short periods in order to maintain $t_{\rm tide} \sim t_\alpha$. Due to the relatively low mass of the planet, the stellar spin is hardly influenced by the angular momentum input from the planet's orbit.

For the 1 $M_{\rm J}$ hot Jupiter where nonlinear mode damping dominates the dissipation, the orbit initially decays more slowly than what resonance locking would predict during the first $\sim$ 7 Gyr, because resonance locking would predict a path very similar to that of the $10\,M_\oplus$ planet above. The slow initial migration is due to the strong period dependence of Q' from equation 4.18, producing an initially large value of Q'. However, the orbit decays very rapidly after the planet migrates to a critical period

$P \lesssim 2$ days, after which the planet is quickly tidally disrupted. Hence, nonlinear mode coupling predicts rapid orbital decay for hot Jupiters with the shortest periods of $P_{\rm orb} \lesssim 2$ days, so that such systems are expected to be rare around Sun-like stars with radiative cores. The final plunge also spins up the host star by a factor of ≈ 3.

A similar evolution occurs for the $5\,M_{\rm J}$ planet, which is massive enough to trigger wave breaking. The mass dependence of this mechanism (equation 4.17) entails shorter migration times for more massive planets, so it takes less time (~ 3.5 Gyr) for tidal disruption to occur. The host star is highly spun up during the final plunge.

Hence, we conclude that hot Jupiters on short-period orbits around Sun-like stars are likely to be destroyed during the main sequence. Short-period super-Earths and mini-Neptunes are more likely to survive, though their orbits are expected to decay significantly due to resonance locking.

Compatibility with Host Star Populations

Our main predictions appear to be consistent with the recent finding that hot Jupiter host stars are on average slightly younger than field stars [31], implying that a substantial fraction of hot Jupiters are destroyed before their host star evolves off the main sequence. More detailed population modeling will be required to predict an exact number, but we also predict that host stars of short-period (e.g., $P_{\rm orb} \lesssim 3$ d) hot Jupiters will be younger than host stars of long-period (e.g., $P_{\rm orb} \gtrsim 4$ d) hot Jupiters. Noting also the well-known trend that higher-mass hot Jupiters have shorter orbital periods on average (e.g., [52]), we predict that host stars of high-mass hot Jupiters will be younger than host stars of low-mass hot Jupiters, for host stars of nearly the same mass.

In stars with radiative cores, we predict that orbital decay for massive planets ($M \gtrsim 0.3\,M_{\rm J}$) at short periods ($P \lesssim 2$ days) proceeds much more rapidly due to nonlinear damping processes. Tidal destruction takes much longer if these processes do not operate (Figure 4.8). Our resonance locking models indicate that wave breaking rarely occurs in stars with convective cores, and the damping produced by nonlinear mode coupling is also likely to be strongly reduced relative to Sun-like stars. Hence, we predict slower orbital decay at short orbital periods and a higher main-sequence survival fraction of hot Jupiters in stars with $M \gtrsim 1.2\,M_\odot$ than of their lower-mass counterparts.

For mini-Neptunes or less massive planets ($M \lesssim 0.1\,M_{\rm J}$), resonance locking is probably the dominant tidal dissipation mechanism for stars both with and without convective cores. Resonance locking predicts $t_{\rm tide} \approx 10\,{\rm Gyr}$ for Sun-like stars regardless of planet mass and orbital period, corresponding to an effective quality factor of

$$Q' \sim 8\times10^{6}\frac{M_p}{3M_\oplus}\left(\frac{P_{\rm orb}}{0.5\,{\rm day}}\right)^{-13/3} . \tag{4.20}$$

This is very close to the inferred constraint from [32] for ultrashort-period planets (USPs), though we caution against comparing Q' values because they are very sensitive to the stellar radius. Our predicted tidal migration time scale is comparable to the main-sequence lifetime, consistent with the old ages of USP host stars, but also allowing tidal orbital decay to have significantly shortened the period without destroying the planet.

We can also rule out a naive extrapolation of the nonlinear damping model of [16] to ultrashort-period planets, which predicts a tidal migration time scale of only $t_{\rm tide} \simeq 4\,{\rm Myr}\left(M_p/3M_\oplus\right)^{-0.5}\left(P_{\rm orb}/0.5\,{\rm d}\right)^{6.7}$, corresponding to a tidal quality factor of $Q' \simeq 6\times10^{3}\left(M_p/3M_\oplus\right)^{0.5}\left(P_{\rm orb}/0.5\,{\rm day}\right)^{2.4}$. This is inconsistent with the old ages of host stars from [32], and corresponding inferred lower limits of $Q' \gtrsim 10^{7}$ for most USPs. Hence, the scaling of the nonlinear migration rate (Equation 4.18) must break down for lower-mass planets as predicted by [16], likely because the tidally excited gravity modes do not reach sufficient amplitude to transfer energy to daughter modes.

System Evolution: Statistical Distributions

Resonance locking makes unique predictions for the statistical distributions of exoplanet orbits. Consider exoplanets born at a given orbital period $P_{\rm i}$ at a constant rate $R = dN(P_{\rm i})/dt$, and then migrating inward due to resonance locking/nonlinear dissipation. For a steady-state distribution, the rate of planets migrating through shorter periods is constant, i.e.

$$\frac{dN(P)}{dt} = \frac{dN(P_{\rm i})}{dt} = R \tag{4.21}$$

or

$$\begin{aligned}\frac{dN(P)}{da} &= \frac{dN(P)}{dt}\frac{dt}{da} = \frac{R}{\dot a}\\ \Rightarrow\ \frac{dN(P)}{d\ln P} &= \frac{2}{3}Rt_{\rm tide} .\end{aligned} \tag{4.22}$$

For low-mass planets migrating inward via resonance locking, we expect $t_{\rm tide}$ is roughly constant, which entails $dN/d\ln P$ = constant, i.e., a uniform distribution over $\log P$. For more massive planets migrating inward via nonlinear wave damping, $t_{\rm tide}$ becomes strongly dependent on P. For nonlinear mode coupling, this implies

$$\frac{dN(P)}{d\ln P} \propto t_{\rm tide} \propto P^{6.7}\,, \tag{4.23}$$

such that the number of planets should fall very sharply with decreasing orbital period.

However, there are many uncertainties that complicate this simple picture. First, the observed distribution of exoplanets is not necessarily in a steady state. The number of short-period exoplanets may be growing as more numerous exoplanets born at longer periods migrate inward. Second, the birth-period distribution is also likely to be a strong function of period [43], which complicates interpretation. To first order, we expect resonance locking to shift the birth-period distribution to shorter periods without changing its shape. We therefore expect a flatter distribution of exoplanets at short periods when resonance locking operates, compared to nonlinear dissipation or models with a constant stellar Q' which destroy short-period planets more rapidly.

Recent studies may provide evidence for a distribution of *Kepler* planets sculpted by resonance locking migration. For instance, Figures 2 and 3 of [80] show a relatively uniform occurrence rate of planets with $R_{\rm p} \lesssim 2R_\oplus$ within the orbital period range $0.6\,\text{days} \lesssim P_{\rm orb} \lesssim 2\,\text{days}$, which agrees with the basic prediction of resonance locking. In contrast, the occurrence rate of hot Jupiters falls steeply toward short orbital periods, as expected from nonlinear g mode damping for massive planets. A prediction of resonance locking is that the occurrence rate of hot Jupiters should show a flatter trend with orbital period around slightly more massive stars with convective cores. Since resonance locking in individual hot Jupiter systems is generally hard to detect due to the long tidal migration timescale, this may serve as the best prospect to justify whether resonance locking is occurring in these systems. Future population modeling should examine the short-period exoplanetary distribution resulting from resonance locking in more detail.

As resonance locking typically predicts tidal migration timescales $2-3$ orders of magnitudes longer than nonlinear g mode dissipation for hot Jupiters at orbital periods of ~ 1 day (Table 4.1), we might expect short-period hot Jupiters orbiting stars with convective cores (where resonance locking is operating) to be more common than those orbiting Sun-like stars with radiative cores (where nonlinear dissipation dominates). However, several additional factors may complicate this picture: if the hot Jupiters are born at some minimum period (e.g., 3 days), the slow tidal migration induced by resonance locking might prevent them from reaching short orbital periods before the massive star evolves off the main sequence. The observed hot Jupiter population may also suffer from observational biases that preferentially detect systems with certain types of host stars. While disentangling these effects is beyond the scope of this paper, future population analyses may shed more light on this issue.

Early and Late-time evolution

We have avoided modeling the early evolution ($t \lesssim 500\,\mathrm{Myr}$) and post-main-sequence evolution of exoplanet systems in this work. At early times, it is often the case that inward migration via resonance locking cannot occur because resonant locations move outward, as discussed in Section 4.2. However, in this case, rapidly rotating young stars with $P_\mathrm{s} < P_\mathrm{orb}$ could instead drive outward migration via resonance locking. It is not clear how far planets could be driven outward, but this possibility should be investigated in future work. For example, resonance locking via $m = 0$ modes during the pre-main sequence evolution of stellar binaries likely helps to circularize their orbits [79].

After the main sequence, the timescales for stellar evolution and those for mode frequency evolution, t_α, decrease dramatically, naively resulting in much faster migration via resonance locking. However, post-main-sequence stars contain strongly stratified radiative cores, likely making nonlinear damping in the core even more efficient than in Sun-like stars. Hence, it is not clear whether resonance locking can ever occur in subgiants or stars ascending the red giant branch.

Nonlinear damping and the maximum period for resonance locking

For massive planets, nonlinear damping likely dominates over linear mode damping processes. This causes the resonances to saturate at lower mode amplitudes, decreasing the maximum period P_max above which resonance locking cannot operate. The orange line in Figure 4.1 demonstrates this qualitatively, but the crudeness of our approximation of nonlinear damping prevents a quantitative prediction for P_max. Realistic calculations of nonlinear mode damping rates are needed to reliably predict P_max. These calculations should be performed for planets of different masses and orbital periods, as well as for stars of different masses and ages. This would allow for better predictions of the statistical distribution of exoplanets as a function of planet mass, orbital period, stellar mass, and stellar age.

4.5 Conclusion

In this work, we study the orbital decay of short-period exoplanets via tidal resonance locking, where planets fall into resonance with stellar oscillation modes and migrate along with the resonant locations (Figure 4.2). When resonance locking between planets and stellar gravity modes (g modes) operates, planetary orbits typically decay on a mode evolution timescale, which is usually similar to the star's main-sequence lifetime. The tidal migration time scale is nearly independent of planet mass and orbital period, such that the effective tidal quality factor Q' decreases toward longer orbital periods and lower-mass planets (equation 4.14).

Resonance locking can be prevented by nonlinear damping that saturates (or eliminates) resonant mode excitation. Both the stellar structure and the planet mass influence the nonlinearity of the tidally excited g modes. For solar-type host stars with radiative cores, nonlinear effects become very important near the center of the star, wiping out resonances. Hot Jupiters of $M \gtrsim 0.3\,M_{\rm J}$ trigger efficient nonlinear dissipation of gravity modes [16], and more massive planets ($M \gtrsim 3\,M_{\rm J}$) cause wave breaking [4]. In either case, energy dissipation has a very strong power-law dependence on orbital frequency, with the tidal migration timescale increasing sharply with orbital period. Resonance locking may operate for low-mass planets ($M \lesssim 0.1\,M_{\rm J}$) around solar-type hosts, and future work should examine this regime. Additionally, resonance locking can likely operate for planets of any mass that orbit massive host stars with convective cores, which prevent gravity waves from reaching the stellar center.

Based on stellar spin measurements, [63] recently inferred a strong period dependence of the tidal quality factor Q' of hot Jupiter host stars (Figure 4.7). If resonance locking occurs in hot Jupiter systems, it produces a remarkably similar power-law dependence of Q', which could provide evidence in favor of resonance locking. However, since nonlinear dissipation likely prevents resonance locking from occurring in these systems, other potential explanations should be explored. We have suggested that many moderately rotating hot Jupiter hosts (which were inferred to have been tidally spun up, thereby placing a constraint on Q') are instead simply younger than average [31]. In this scenario, their more rapid rotation stems primarily from their youth, and only a lower limit of Q' can be inferred. Future age constraints for those systems may determine which explanation is more likely.

We apply resonance locking to 15 observed hot Jupiter systems and predict that these systems generally have Q's in the range 10^6 – 10^9, which is typically 2 – 3 orders of magnitude higher than observed lower limits. This means their orbital decay will be hard to measure if resonance locking is operating, as we expect for stars with convective cores. However, nonlinear damping likely operates in host stars possessing radiative cores, leading to much smaller Q's, like that measured for WASP-12b [55]. Further observations of these systems can thus help to improve our understanding of which tidal process operates.

We examine the long-term orbital evolution of exoplanets, combining theories based on resonance locking and nonlinear dissipation/wave breaking (Figure 4.8). We predict that hot Jupiters migrate inwards via nonlinear wave damping and are frequently destroyed during the main sequence for solar-type host stars. This may help to explain the recent finding that hot Jupiter host stars are on average slightly younger than field stars [31]. For hot Neptunes and super-Earths, we predict that resonance locking can operate, driving inward migration on a stellar evolution time scale. This can result in a tidal quality factor of $Q' \lesssim 10^5$, causing much more orbital decay than prior expectations. However, the corresponding quality factor at short orbital periods can exceed $Q' \gtrsim 10^7$, allowing the planets to survive at ultrashort periods for extended lengths of time, consistent with the observed old ages of ultrashort-period planet hosts [32].

Since nonlinear dissipation occurs for massive planets orbiting stars with radiative cores, we predict a sharp decline in the population of short-period ($P_{\rm orb} \lesssim 2$ days) hot Jupiters orbiting solar-type host stars. We predict a more gradual decline for low-mass planets and host stars with convective cores, where resonance locking is at work, producing a much smoother distribution with orbital period. Future observations will help test this prediction, provided that effects of tidal migration can be distinguished from the birth-period distribution (e.g., [43]).

Acknowledgements

We thank Hang Yu, Rich Townsend, and Josh Winn for very helpful discussion and feedback. This work is partially supported by NASA through grant 20-XRP20 2-0147. JF is thankful for support through an Innovator Grant from The Rose Hills Foundation, and the Sloan Foundation through grant FG-2018-10515.

4.6 Appendix

Table of observed and modelled system properties

See Table 4.2 for details. References for observations as labeled in the table: 1. [3], 2. [61], 3. [50] , 4. [68], 5. [49], 6. [9], 7. [13], 8. [36], 9. [44], 10. [22], 11. [24],

12. [14], 13. [7], 14. [71], 15. [37].

Name	$M_*/M_\odot$	$R_*/R_\odot$	$T_{\mathrm{eff}}/\mathrm{K}$	age/Gyr	[Fe/H]	$M_{\mathrm{p}}/M_{\mathrm{J}}$	P/day
HAT-P-23b[1]	1.13(4)	1.20(7)	5905(80)	4.0(1.0)	0.15(4)	2.09(11)	1.21
(model)	1.102	1.25	5985	4.74	0.176		
HATS-18b[2]	1.04(5)	1.02(6)	5600(120)	4.2(2.2)	0.28(8)	1.980(77)	0.84
(model)	1.032	1.02	5627	5.6	0.337		
KELT-16b[3]	1.21(5)	1.36(6)	6236(54)	3.1(3)	-0.002(90)	2.75(16)	0.97
(model)	1.183	1.42	6197	2.7	0.074		
OGLE-TR-56b[4]	1.23(8)	1.36(9)	6050(100)	3.1(1.2)	0.22(10)	1.39(18)	1.21
(model)	1.227	1.38	6032	3.0	0.283		
TRES-3b[5]	0.90(15)	0.80(5)	5720(150)			1.92(23)	1.306
(model)	0.889	0.82	5570	1.52	0.0		
WASP-4b[6]	0.86(18)	0.89(7)	5400(180)	7.0(2.0)	-0.07(38)	1.19(20)	1.338
(model)	0.825	0.83	5573	7.23	-0.078		
WASP-12b[7]	1.43(1)	1.66(5)	6360(140)	2.0(1.0)	0.33(17)	1.470(76)	1.09
(model)	1.435	1.70	6238	1.8	0.337		
WASP-18b[8]	1.46(29)	1.29(5)	6431(48)	1.0(5)	0.00(9)	11.4(1.4)	0.94
(model)	1.172	1.25	6408	1.0	-0.027		
WASP-19b[9]	0.94(4)	1.02(1)	5460(90)	10.2(3.8)	0.14(11)	1.139(36)	0.79
(model)	0.906	1.02	5510	13.2	0.237		
WASP-43b[10]	0.72(3)	0.67(1)	4520(120)		-0.01(12)	2.034(52)	0.81
(model)	0.696	0.67	4560	6.75	0.085		
WASP-72b[11]	1.39(6)	1.98(24)	6250(100)	3.2(6)	-0.06(9)	1.546(59)	2.22
(model)	1.331	2.19	6347	2.78	0.028		
WASP-103b[12]	1.21(11)	1.42(4)	6110(160)	4.0(1.0)	0.06(13)	1.51(11)	0.93
(model)	1.179	1.46	6163	3.0	0.063		
WASP-114b[13]	1.29(5)	1.43(60)	5940(140)	4.0(2.0)	0.14(7)	1.769(64)	1.55
(model)	1.244	1.54	6079	3.08	0.178		
WASP-122b[14]	1.24(4)	1.52(3)	5720(130)	5.11(80)	0.32(9)	1.284(32)	1.71
(model)	1.252	1.53	5713	5.03	0.406		
WASP-128b[15]	1.16(8)	1.15(4)	5950(100)	2.2(1.8)	0.01(24)	37.19(1.70)	2.209
(model)	1.127	1.15	6019	2.52	0.207		

Table 4.2: Properties of the systems we study. For each system, the first line shows the values inferred from observational literature, with numbers in brackets corresponding to 95% confidence intervals. The second line shows the parameters of our best-fit MESA models. Planetary parameters (M_{p} and P) are taken directly from the literature.

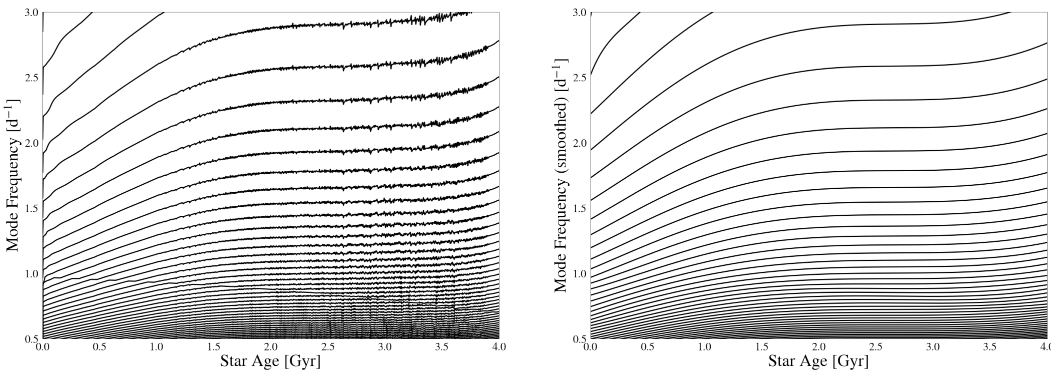

Figure 4.9: Mode frequencies of a 1.2 $M_\odot$ MESA model. For models with convective cores, it is generally difficult for MESA to accurately determine the boundary of the convective core. This can cause unphysical jumping in the computed mode frequencies (left panel). We smooth the mode frequencies in time by fitting fifth-order polynomials (right panel), giving a more accurate estimate of mode evolution timescales.

Solving Modes for MESA Models with Convective Cores

Throughout the paper, we have constructed MESA models to track the evolution of the stellar structure. We then use GYRE to solve the stellar oscillation modes for individual profiles generated by MESA and study the evolution of the modes by tracking the same mode across different profiles at different stellar ages. While this process is straightforward for models of Sun-like stars, it frequently fails for models of massive stars with convective cores.

In Figure 4.9 we describe what we refer to the “jumping core boundary” issue for models with convective cores. It is generally difficult for MESA to accurately determine the position of convective core boundaries in the presence of composition gradients. As a result, the mode frequencies solved by GYRE exhibit unphysical jumping, due to the discontinuous jumps in the core boundary. We find that turning on predictive mixing and element diffusion in MESA, as well as choosing smaller time steps and mesh spacing, helps to decrease the unphysical jumping (as shown in Figure 4.9, left panel). However, this is still not satisfactory when solving for mode evolution timescales, which is related to the derivatives of the frequency, so that even small jumps in the frequencies result in large errors.

Therefore, we choose an alternative approach to determine the mode evolution timescale. Instead of solving the derivatives directly, we fit the frequency solutions with fifth-order polynomials (as shown in Figure 4.9, right panel). This enables us to compute smoothly varying mode evolution time scales t_α, as shown in Figure 4.3.

Estimate of nonlinear damping rate

Nonlinear mode damping can be modeled as an additional amplitude-dependent damping term $\gamma_{\rm NL}$. The increased damping will cause the Lorentzian dips in $t_{\rm tide}$ in Figure 4.1 to become broader and shallower, altering where resonance locking can operate.

To estimate the nonlinear damping rate, we first realize that the maximum damping rate achievable is the rate at which waves propagate from the convective envelope (where they are excited) to the center of the star (where they are dissipated). This damping rate is the inverse group travel time, $\gamma_{\rm NL,max} \sim -1/\tau_2$, where

$$\begin{aligned} \tau_2 &= \int_{r_0}^{r_c} \frac{dr}{v_g} \\ &= \frac{\sqrt{6}}{\omega^2} \int_{r_0}^{r_c} \frac{dr}{r} N \,, \end{aligned} \tag{4.24}$$

where we have used the g mode dispersion relation $\omega^2 = N^2 \ell(\ell+1)/k^2 r^2$ where $\ell = 2$ is the mode's spherical harmonic index for tidally excited gravity waves. $r_0 \simeq 0$ is the inner turning point, r_c is the outer turning point at the base of the convective envelope. We note that $\tau_2 = \int_{r_0}^{r_c} k dr/\omega = n\pi$, hence τ_2 scales with the frequency spacing $\Delta\omega_g$ as $\tau_2 = \pi/\Delta\omega_g$.

The maximum damping rate $\gamma_{\rm NL,max} \sim -1/\tau_2$ will be achieved for modes with large enough amplitude, which dissipate efficiently after one wave crossing time. Nonlinear wave breaking can be approximated by this damping rate, but sufficiently strong three-mode coupling could produce the same effective damping rate. Modes at smaller amplitudes a will be damped at smaller rates. In Sun-like stars, nonlinear g mode damping is caused by a nonlinear instability in which daughter modes are driven to larger amplitude by the tidally excited parent mode [40, 73]. The instability only occurs above a threshold amplitude $a_{\rm NL}$, hence we expect very little nonlinear damping below this threshold. The nonlinear damping rate should fall sharply for $|a| \lesssim |a_{\rm NL}|$, hence we model the nonlinear damping via an ad hoc relation

$$\gamma_{\rm NL} \sim -\frac{1}{\tau_2} \exp\left(- \left(\frac{a_{\rm NL}}{a} \right)^2 \right). \tag{4.25}$$

Defining the dimensionless parameter $\bar{\gamma} = -\tau_2 \gamma_{\rm NL} > 0$. we have $(a_{\rm NL}/a)^2 = -\ln(\bar{\gamma})$.

To estimate the value of $a_{\rm NL}$, we examine the results of [16] for Sun-like stars. They find that the orbital decay rate for off-resonance modes is weakly dependent on planet mass (and hence mode amplitude) for planets with mass $M_\mathrm{p} \gtrsim 0.3\, M_\mathrm{J}$, while the energy dissipation rate is strongly amplitude-dependent for $M_\mathrm{p} \lesssim 0.3\, M_\mathrm{J}$. There appears to be a very weak dependence of this cutoff on orbital period, as we might expect since the g mode nonlinearity scales as $|k_r \xi_r| \propto P^{1/6}$. Therefore, their results suggest that $a \simeq a_\mathrm{NL}$ for planets with $M \simeq 0.3\, M_\mathrm{J}$ and resonant detuning $|(\omega_\alpha - \omega_\mathrm{f})| = \Delta\omega \simeq \Delta\omega_g/2$. Since the tidally excited mode amplitude scales as $a \propto M_p$ and $a \propto (\Delta\omega^2 + \gamma^2)^{-1/2}$, we expect at low amplitudes that

$$\ln(\bar{\gamma}) \sim -\left(\frac{0.3\, M_\mathrm{J}}{M_\mathrm{p}}\right)^2 \left(\frac{\Delta\omega^2 + (\gamma_\mathrm{rad} + \gamma_\mathrm{NL})^2}{(\Delta\omega_g/2)^2 + (\gamma_\mathrm{rad} + 1/\tau_2)^2}\right). \tag{4.26}$$

Near resonance, the nonlinear damping is expected to be strong such that γ_rad can be neglected. With $\Delta\omega_g \tau_2 = \pi$ we have

$$\bar{\gamma}^2 + (1 + (\pi/2)^2)\left(\frac{M_\mathrm{p}}{0.3\, M_\mathrm{J}}\right)^2 \ln(\bar{\gamma}) + \tau_2^2 \Delta\omega^2 = 0\,. \tag{4.27}$$

When $M_\mathrm{p} \ll 0.3\,\mathrm{M_J}$, we expect $\bar{\gamma}^2 = \exp(-2(a_\mathrm{NL}/a)^2)$ to be exponentially smaller than $(M_\mathrm{p}/0.3\, M_\mathrm{J})^2 \ln(\bar{\gamma}) \sim (M_\mathrm{p}/0.3\, M_\mathrm{J})^2 (a_\mathrm{NL}/a)^2$, such that we can neglect the first term, yielding

$$\gamma_\mathrm{NL} \simeq -\frac{1}{\tau_2} \exp\left(-\frac{\tau_2^2 \Delta\omega^2}{(\pi/2)^2 + 1}\left(\frac{0.3\, M_\mathrm{J}}{M_\mathrm{p}}\right)^2\right). \tag{4.28}$$

We note that the threshold amplitude a_NL inferred above is not necessarily the actual threshold amplitude for a nonlinear instability, because Figure 1 of [16] shows that even an off-resonance $0.1\, M_\mathrm{J}$ planet excites a parent mode above the nonlinear threshold energy. However, the growth rate of the instability (and hence the amount of nonlinear damping) does apparently change rapidly with planet mass in this regime. A more accurate (but more complicated) model of nonlinear damping should incorporate the rapid increase in $|\gamma_\mathrm{NL}|$ at small mode amplitudes, the more gradual dependence $|\gamma_\mathrm{NL}| \propto |a|$ at intermediate amplitudes [40, 77], and the saturation $|\gamma_\mathrm{NL}| \sim 1/\tau_2$ at wave-breaking amplitudes. While such a model is beyond the scope of this work, it could significantly change both the width and depth of the resonant dips in Figure 4.1.

References

[1] P. Auclair Desrotour, S. Mathis, and C. Le Poncin-Lafitte. "Scaling laws to understand tidal dissipation in fluid planetary regions and stars I. Rotation, stratification and thermal diffusivity". In: *Astronomy & Astrophysics* 581, A118 (Sept. 2015), A118. DOI: 10.1051/0004-6361/201526246. arXiv: 1506.07705 [astro-ph.EP].

[2] Avery Bailey and Jeremy Goodman. "Understanding WASP-12b". In: *Monthly Notices of the Royal Astronomical Society* 482.2 (Jan. 2019), pp. 1872–1882. DOI: 10.1093/mnras/sty2805. arXiv: 1808.00052 [astro-ph.EP].

[3] G. Á. Bakos et al. "HAT-P-20b-HAT-P-23b: Four Massive Transiting Extrasolar Planets". In: *The Astrophysical Journal* 742.2, 116 (Dec. 2011), p. 116. DOI: 10.1088/0004-637X/742/2/116. arXiv: 1008.3388 [astro-ph.EP].

[4] A. J. Barker. "Tidal dissipation in evolving low-mass and solar-type stars with predictions for planetary orbital decay". In: *Monthly Notices of the Royal Astronomical Society* 498.2 (Sept. 2020), pp. 2270–2294. DOI: 10.1093/mnras/staa2405. arXiv: 2008.03262 [astro-ph.EP].

[5] A. J. Barker and G. I. Ogilvie. "On internal wave breaking and tidal dissipation near the centre of a solar-type star". In: *Monthly Notices of the Royal Astronomical Society* 404 (June 2010), pp. 1849–1868. DOI: 10.1111/j.1365-2966.2010.16400.x. arXiv: 1001.4009 [astro-ph.EP].

[6] A. J. Barker and G. I. Ogilvie. "Stability analysis of a tidally excited internal gravity wave near the centre of a solar-type star". In: *Monthly Notices of the Royal Astronomical Society* 417 (Oct. 2011), pp. 745–761. DOI: 10.1111/j.1365-2966.2011.19322.x. arXiv: 1106.5001 [astro-ph.EP].

[7] S. C. C. Barros et al. "WASP-113b and WASP-114b, two inflated hot Jupiters with contrasting densities". In: *Astronomy & Astrophysics* 593, A113 (Oct. 2016), A113. DOI: 10.1051/0004-6361/201526517. arXiv: 1607.02341 [astro-ph.EP].

[8] L. G. Bouma et al. "WASP-4 Is Accelerating toward the Earth". In: *The Astrophysical Journal Letters* 893.2, L29 (Apr. 2020), p. L29. DOI: 10.3847/2041-8213/ab8563. arXiv: 2004.00637 [astro-ph.EP].

[9] L. G. Bouma et al. "WASP-4b Arrived Early for the TESS Mission". In: *The Astronomical Journal* 157.6, 217 (June 2019), p. 217. DOI: 10.3847/1538-3881/ab189f. arXiv: 1903.02573 [astro-ph.EP].

[10] J. Burkart, E. Quataert, and P. Arras. "Dynamical resonance locking in tidally interacting binary systems". In: *Monthly Notices of the Royal Astronomical Society* 443 (Oct. 2014), pp. 2957–2973. DOI: 10.1093/mnras/stu1366. arXiv: 1312.4966 [astro-ph.SR].

[11] J. Burkart et al. "Tidal resonance locks in inspiraling white dwarf binaries". In: *Monthly Notices of the Royal Astronomical Society* 433 (July 2013), pp. 332–352. DOI: 10.1093/mnras/stt726. arXiv: 1211.1393 [astro-ph.SR].

[12] Shelley J. Cheng et al. "Detailed Characterization of Heartbeat Stars and Their Tidally Excited Oscillations". In: *The Astrophysical Journal* 903.2, 122 (Nov. 2020), p. 122. DOI: 10.3847/1538-4357/abb46d. arXiv: 2009.01851 [astro-ph.SR].

[13] Karen A. Collins, John F. Kielkopf, and Keivan G. Stassun. "Transit Timing Variation Measurements of WASP-12b and Qatar-1b: No Evidence Of Additional Planets". In: *The Astronomical Journal* 153.2, 78 (Feb. 2017), p. 78. DOI: 10.3847/1538-3881/153/2/78.

[14] L. Delrez et al. "High-precision multiwavelength eclipse photometry of the ultra-hot gas giant exoplanet WASP-103 b". In: *Monthly Notices of the Royal Astronomical Society* 474.2 (Feb. 2018), pp. 2334–2351. DOI: 10.1093/mnras/stx2896. arXiv: 1711.02566 [astro-ph.EP].

[15] Craig D. Duguid, Adrian J. Barker, and C. A. Jones. "Convective turbulent viscosity acting on equilibrium tidal flows: new frequency scaling of the effective viscosity". In: *Monthly Notices of the Royal Astronomical Society* 497.3 (July 2020), pp. 3400–3417. DOI: 10.1093/mnras/staa2216. arXiv: 2007.12624 [astro-ph.EP].

[16] R. Essick and N. N. Weinberg. "Orbital Decay of Hot Jupiters Due to Nonlinear Tidal Dissipation within Solar-type Hosts". In: *The Astrophysical Journal* 816, 18 (Jan. 2016), p. 18. DOI: 10.3847/0004-637X/816/1/18. arXiv: 1508.02763 [astro-ph.EP].

[17] J. Fuller and D. Lai. "Dynamical tides in eccentric binaries and tidally excited stellar pulsations in Kepler KOI-54". In: *Monthly Notices of the Royal Astronomical Society* 420 (Mar. 2012), pp. 3126–3138. DOI: 10.1111/j.1365-2966.2011.20237.x. arXiv: 1107.4594 [astro-ph.SR].

[18] J. Fuller et al. "Accelerated tidal circularization via resonance locking in KIC 8164262". In: *Monthly Notices of the Royal Astronomical Society* 472 (Nov. 2017), pp. L25–L29. DOI: 10.1093/mnrasl/slx130. arXiv: 1706.05053 [astro-ph.SR].

[19] Jim Fuller. "Heartbeat stars, tidally excited oscillations and resonance locking". In: *Monthly Notices of the Royal Astronomical Society* 472.2 (Dec. 2017), pp. 1538–1564. DOI: 10.1093/mnras/stx2135. arXiv: 1706.05054 [astro-ph.SR].

[20] Jim Fuller, Jing Luan, and Eliot Quataert. "Resonance locking as the source of rapid tidal migration in the Jupiter and Saturn moon systems". In: *Monthly Notices of the Royal Astronomical Society* 458.4 (June 2016), pp. 3867–3879. DOI: 10.1093/mnras/stw609. arXiv: 1601.05804 [astro-ph.EP].

[21] F. Gallet et al. "Tidal dissipation in rotating low-mass stars and implications for the orbital evolution of close-in planets. I. From the PMS to the RGB at solar metallicity". In: *Astronomy & Astrophysics* 604, A112 (Aug.

2017), A112. DOI: 10.1051/0004-6361/201730661. arXiv: 1705.10164 [astro-ph.EP].

[22] M. Gillon et al. “The TRAPPIST survey of southern transiting planets. I. Thirty eclipses of the ultra-short period planet WASP-43 b”. In: *Astronomy & Astrophysics* 542, A4 (June 2012), A4. DOI: 10.1051/0004-6361/201218817. arXiv: 1201.2789 [astro-ph.EP].

[23] M. Gillon et al. “WASP-103 b: a new planet at the edge of tidal disruption”. In: *Astronomy & Astrophysics* 562, L3 (Feb. 2014), p. L3. DOI: 10.1051/0004-6361/201323014. arXiv: 1401.2784 [astro-ph.EP].

[24] M. Gillon et al. “WASP-64 b and WASP-72 b: two new transiting highly irradiated giant planets”. In: *Astronomy & Astrophysics* 552, A82 (Apr. 2013), A82. DOI: 10.1051/0004-6361/201220561. arXiv: 1210.4257 [astro-ph.EP].

[25] P. Goldreich and P. D. Nicholson. “Tidal friction in early-type stars”. In: *The Astrophysical Journal* 342 (July 1989), pp. 1079–1084. DOI: 10.1086/167665.

[26] Peter Goldreich and Steven Soter. “Q in the Solar System”. In: *Icarus* 5.1 (Jan. 1966), pp. 375–389. DOI: 10.1016/0019-1035(66)90051-0.

[27] J. Goldstein and R. H. D. Townsend. “The Contour Method: a New Approach to Finding Modes of Nonadiabatic Stellar Pulsations”. In: *The Astrophysical Journal* 899.2, 116 (Aug. 2020), p. 116. DOI: 10.3847/1538-4357/aba748. arXiv: 2006.13223 [astro-ph.SR].

[28] J. Goodman and E. S. Dickson. “Dynamical Tide in Solar-Type Binaries”. In: *The Astrophysical Journal* 507 (Nov. 1998), pp. 938–944. DOI: 10.1086/306348. eprint: astro-ph/9801289.

[29] M. Guenel et al. “Tidal inertial waves in differentially rotating convective envelopes of low-mass stars. I. Free oscillation modes”. In: *Astronomy & Astrophysics* 589, A22 (May 2016), A22. DOI: 10.1051/0004-6361/201527621. arXiv: 1601.04617 [astro-ph.SR].

[30] K. Hambleton et al. “KIC 8164262: a heartbeat star showing tidally induced pulsations with resonant locking”. In: *Monthly Notices of the Royal Astronomical Society* 473.4 (Feb. 2018), pp. 5165–5176. DOI: 10.1093/mnras/stx2673. arXiv: 1706.05051 [astro-ph.SR].

[31] Jacob H. Hamer and Kevin C. Schlaufman. “Hot Jupiters Are Destroyed by Tides While Their Host Stars Are on the Main Sequence”. In: *The Astronomical Journal* 158.5, 190 (Nov. 2019), p. 190. DOI: 10.3847/1538-3881/ab3c56. arXiv: 1908.06998 [astro-ph.EP].

[32] Jacob H. Hamer and Kevin C. Schlaufman. “Ultra-short-period Planets Are Stable against Tidal Inspiral”. In: *The Astronomical Journal* 160.3, 138 (Sept. 2020), p. 138. DOI: 10.3847/1538-3881/aba74f. arXiv: 2007.10944 [astro-ph.EP].

[33] L. Hebb et al. “WASP-12b: The Hottest Transiting Extrasolar Planet Yet Discovered”. In: *The Astrophysical Journal* 693.2 (Mar. 2009), pp. 1920–1928. DOI: 10.1088/0004-637X/693/2/1920. arXiv: 0812.3240 [astro-ph].

[34] L. Hebb et al. “WASP-19b: The Shortest Period Transiting Exoplanet Yet Discovered”. In: *The Astrophysical Journal* 708.1 (Jan. 2010), pp. 224–231. DOI: 10.1088/0004-637X/708/1/224. arXiv: 1001.0403 [astro-ph.EP].

[35] C. Hellier et al. “WASP-43b: the closest-orbiting hot Jupiter”. In: *Astronomy & Astrophysics* 535, L7 (Nov. 2011), p. L7. DOI: 10.1051/0004-6361/201117081. arXiv: 1104.2823 [astro-ph.EP].

[36] Coel Hellier et al. “An orbital period of 0.94days for the hot-Jupiter planet WASP-18b”. In: *Nature* 460.7259 (Aug. 2009), pp. 1098–1100. DOI: 10.1038/nature08245.

[37] Vedad Hodžić et al. “WASP-128b: a transiting brown dwarf in the dynamical-tide regime”. In: *Monthly Notices of the Royal Astronomical Society* 481.4 (Dec. 2018), pp. 5091–5097. DOI: 10.1093/mnras/sty2512. arXiv: 1807.07557 [astro-ph.EP].

[38] P. B. Ivanov, J. C. B. Papaloizou, and S. V. Chernov. “A unified normal mode approach to dynamic tides and its application to rotating Sun-like stars”. In: *Monthly Notices of the Royal Astronomical Society* 432 (July 2013), pp. 2339–2365. DOI: 10.1093/mnras/stt595. arXiv: 1304.2027 [astro-ph.SR].

[39] Anita Krishnamurthi et al. “Theoretical Models of the Angular Momentum Evolution of Solar-Type Stars”. In: *The Astrophysical Journal* 480.1 (May 1997), pp. 303–323. DOI: 10.1086/303958.

[40] P. Kumar and J. Goodman. “Nonlinear Damping of Oscillations in Tidal-Capture Binaries”. In: *The Astrophysical Journal* 466 (Aug. 1996), p. 946. DOI: 10.1086/177565. eprint: astro-ph/9509112.

[41] V. Lainey et al. “New constraints on Saturn’s interior from Cassini astrometric data”. In: *Icarus* 281 (Jan. 2017), pp. 286–296. DOI: 10.1016/j.icarus.2016.07.014. arXiv: 1510.05870 [astro-ph.EP].

[42] V. Lainey et al. “Resonance locking in giant planets indicated by therapid orbital expansion of Titan”. In: *Nature Astronomy* (2020).

[43] E. J. Lee and E. Chiang. "Magnetospheric Truncation, Tidal Inspiral, and the Creation of Short-period and Ultra-short-period Planets". In: *The Astrophysical Journal* 842, 40 (June 2017), p. 40. DOI: 10.3847/1538-4357/aa6fb3. arXiv: 1702.08461 [astro-ph.EP].

[44] L. Mancini et al. "Physical properties, transmission and emission spectra of the WASP-19 planetary system from multi-colour photometry". In: *Monthly Notices of the Royal Astronomical Society* 436.1 (Nov. 2013), pp. 2–18. DOI: 10.1093/mnras/stt1394. arXiv: 1306.6384 [astro-ph.EP].

[45] Vineet Kumar Mannaday et al. "Probing Transit Timing Variation and Its Possible Origin with 12 New Transits of TrES-3b". In: *The Astronomical Journal* 160.1, 47 (July 2020), p. 47. DOI: 10.3847/1538-3881/ab9818. arXiv: 2006.00599 [astro-ph.EP].

[46] S. Mathis. "Variation of tidal dissipation in the convective envelope of low-mass stars along their evolution". In: *Astronomy & Astrophysics* 580, L3 (Aug. 2015), p. L3. DOI: 10.1051/0004-6361/201526472. arXiv: 1507.00165 [astro-ph.SR].

[47] S. Mathis et al. "The impact of rotation on turbulent tidal friction in stellar and planetary convective regions". In: *Astronomy & Astrophysics* 592, A33 (July 2016), A33. DOI: 10.1051/0004-6361/201527545. arXiv: 1604.08570 [astro-ph.SR].

[48] Sarah C. Millholland and Christopher Spalding. "Formation of Ultra-short-period Planets by Obliquity-driven Tidal Runaway". In: *The Astrophysical Journal* 905.1, 71 (Dec. 2020), p. 71. DOI: 10.3847/1538-4357/abc4e5. arXiv: 2010.15087 [astro-ph.EP].

[49] Francis T. O'Donovan et al. "TrES-3: A Nearby, Massive, Transiting Hot Jupiter in a 31 Hour Orbit". In: *The Astrophysical Journal Letters* 663.1 (July 2007), pp. L37–L40. DOI: 10.1086/519793. arXiv: 0705.2004 [astro-ph].

[50] Thomas E. Oberst et al. "KELT-16b: A Highly Irradiated, Ultra-short Period Hot Jupiter Nearing Tidal Disruption". In: *The Astronomical Journal* 153.3, 97 (Mar. 2017), p. 97. DOI: 10.3847/1538-3881/153/3/97. arXiv: 1608.00618 [astro-ph.EP].

[51] G. I. Ogilvie. "Tides in rotating barotropic fluid bodies: the contribution of inertial waves and the role of internal structure". In: *Monthly Notices of the Royal Astronomical Society* 429 (Feb. 2013), pp. 613–632. DOI: 10.1093/mnras/sts362. arXiv: 1211.0837 [astro-ph.EP].

[52] J. E. Owen and D. Lai. "Photoevaporation and high-eccentricity migration created the sub-Jovian desert". In: *Monthly Notices of the Royal Astronomical Society* 479 (Oct. 2018), pp. 5012–5021. DOI: 10.1093/mnras/sty1760. arXiv: 1807.00012 [astro-ph.EP].

[53] J. C. B. Papaloizou and P. B. Ivanov. "Dynamic tides in rotating objects: a numerical investigation of inertial waves in fully convective or barotropic stars and planets". In: *Monthly Notices of the Royal Astronomical Society* 407 (Sept. 2010), pp. 1631–1656. DOI: 10.1111/j.1365-2966.2010.17011.x. arXiv: 1005.2397 [astro-ph.SR].

[54] Kishore C. Patra et al. "The Apparently Decaying Orbit of WASP-12b". In: *The Astronomical Journal* 154.1, 4 (July 2017), p. 4. DOI: 10.3847/1538-3881/aa6d75. arXiv: 1703.06582 [astro-ph.EP].

[55] Kishore C. Patra et al. "The Continuing Search for Evidence of Tidal Orbital Decay of Hot Jupiters". In: *The Astronomical Journal* 159.4, 150 (Apr. 2020), p. 150. DOI: 10.3847/1538-3881/ab7374. arXiv: 2002.02606 [astro-ph.EP].

[56] Bill Paxton et al. "Modules for Experiments in Stellar Astrophysics (MESA)". In: *The Astrophysical Journal Supplement Series* 192.1, 3 (Jan. 2011), p. 3. DOI: 10.1088/0067-0049/192/1/3. arXiv: 1009.1622 [astro-ph.SR].

[57] Bill Paxton et al. "Modules for Experiments in Stellar Astrophysics (MESA): Binaries, Pulsations, and Explosions". In: *The Astrophysical Journal Supplement Series* 220.1, 15 (Sept. 2015), p. 15. DOI: 10.1088/0067-0049/220/1/15. arXiv: 1506.03146 [astro-ph.SR].

[58] Bill Paxton et al. "Modules for Experiments in Stellar Astrophysics (MESA): Convective Boundaries, Element Diffusion, and Massive Star Explosions". In: *The Astrophysical Journal Supplement Series* 234.2, 34 (Feb. 2018), p. 34. DOI: 10.3847/1538-4365/aaa5a8. arXiv: 1710.08424 [astro-ph.SR].

[59] Bill Paxton et al. "Modules for Experiments in Stellar Astrophysics (MESA): Planets, Oscillations, Rotation, and Massive Stars". In: *The Astrophysical Journal Supplement Series* 208.1, 4 (Sept. 2013), p. 4. DOI: 10.1088/0067-0049/208/1/4. arXiv: 1301.0319 [astro-ph.SR].

[60] Bill Paxton et al. "Modules for Experiments in Stellar Astrophysics (MESA): Pulsating Variable Stars, Rotation, Convective Boundaries, and Energy Conservation". In: *The Astrophysical Journal Supplement Series* 243.1, 10 (July 2019), p. 10. DOI: 10.3847/1538-4365/ab2241. arXiv: 1903.01426 [astro-ph.SR].

[61] K. Penev et al. "HATS-18b: An Extreme Short-period Massive Transiting Planet Spinning Up Its Star". In: *The Astronomical Journal* 152.5, 127 (Nov. 2016), p. 127. DOI: 10.3847/0004-6256/152/5/127. arXiv: 1606.00848 [astro-ph.EP].

[62] Kaloyan Penev, Michael Zhang, and Brian Jackson. "POET: A Model for Planetary Orbital Evolution Due to Tides on Evolving Stars". In: *Publica-*

tions of the Astronomical Society of the Pacific 126.940 (June 2014), p. 553. DOI: 10.1086/677042. arXiv: 1405.1050 [astro-ph.EP].

[63] Kaloyan Penev et al. “Empirical Tidal Dissipation in Exoplanet Hosts From Tidal Spin-up”. In: *The Astronomical Journal* 155.4, 165 (Apr. 2018), p. 165. DOI: 10.3847/1538-3881/aaaf71. arXiv: 1802.05269 [astro-ph.SR].

[64] Dimitar D. Sasselov. “The New Transiting Planet OGLE-TR-56b: Orbit and Atmosphere”. In: *The Astrophysical Journal* 596.2 (Oct. 2003), pp. 1327–1331. DOI: 10.1086/378145. arXiv: astro-ph/0303403 [astro-ph].

[65] A. Skumanich. “Time Scales for Ca II Emission Decay, Rotational Braking, and Lithium Depletion”. In: *The Astrophysical Journal* 171 (Feb. 1972), p. 565. DOI: 10.1086/151310.

[66] John Southworth et al. “Transit timing variations in the WASP-4 planetary system”. In: *Monthly Notices of the Royal Astronomical Society* 490.3 (Dec. 2019), pp. 4230–4236. DOI: 10.1093/mnras/stz2602. arXiv: 1907.08269 [astro-ph.EP].

[67] Keivan G. Stassun, Karen A. Collins, and B. Scott Gaudi. “Accurate Empirical Radii and Masses of Planets and Their Host Stars with Gaia Parallaxes”. In: *The Astronomical Journal* 153.3, 136 (Mar. 2017), p. 136. DOI: 10.3847/1538-3881/aa5df3. arXiv: 1609.04389 [astro-ph.EP].

[68] Guillermo Torres, Joshua N. Winn, and Matthew J. Holman. “Improved Parameters for Extrasolar Transiting Planets”. In: *The Astrophysical Journal* 677.2 (Apr. 2008), pp. 1324–1342. DOI: 10.1086/529429. arXiv: 0801.1841 [astro-ph].

[69] R. H. D. Townsend, J. Goldstein, and E. G. Zweibel. “Angular momentum transport by heat-driven g-modes in slowly pulsating B stars”. In: *Monthly Notices of the Royal Astronomical Society* 475.1 (Mar. 2018), pp. 879–893. DOI: 10.1093/mnras/stx3142. arXiv: 1712.02420 [astro-ph.SR].

[70] R. H. D. Townsend and S. A. Teitler. “GYRE: an open-source stellar oscillation code based on a new Magnus Multiple Shooting scheme”. In: *Monthly Notices of the Royal Astronomical Society* 435.4 (Nov. 2013), pp. 3406–3418. DOI: 10.1093/mnras/stt1533. arXiv: 1308.2965 [astro-ph.SR].

[71] O. D. Turner et al. “WASP-120 b, WASP-122 b, AND WASP-123 b: Three Newly Discovered Planets from the WASP-South Survey”. In: *Publications of the Astronomical Society of the Pacific* 128.964 (June 2016), p. 064401. DOI: 10.1088/1538-3873/128/964/064401. arXiv: 1509.02210 [astro-ph.EP].

[72] Jérémie Vidal and Adrian J. Barker. “Turbulent Viscosity Acting on the Equilibrium Tidal Flow in Convective Stars”. In: *The Astrophysical Journal Letters* 888.2, L31 (Jan. 2020), p. L31. DOI: 10.3847/2041-8213/ab6219. arXiv: 1912.07910 [astro-ph.SR].

[73] N. N. Weinberg et al. “Nonlinear Tides in Close Binary Systems”. In: *The Astrophysical Journal* 751, 136 (June 2012), p. 136. DOI: 10.1088/0004-637X/751/2/136. arXiv: 1107.0946 [astro-ph.SR].

[74] Nevin N. Weinberg et al. “Tidal Dissipation in WASP-12”. In: *The Astrophysical Journal Letters* 849.1, L11 (Nov. 2017), p. L11. DOI: 10.3847/2041-8213/aa9113. arXiv: 1710.00858 [astro-ph.EP].

[75] M. G. Witte and G. J. Savonije. “Tidal evolution of eccentric orbits in massive binary systems. A study of resonance locking”. In: *Astronomy & Astrophysics* 350 (Oct. 1999), pp. 129–147. eprint: astro-ph/9909073.

[76] M. G. Witte and G. J. Savonije. “Tidal evolution of eccentric orbits in massive binary systems. II. Coupled resonance locking for two rotating main sequence stars”. In: *Astronomy & Astrophysics* 366 (Feb. 2001), pp. 840–857. DOI: 10.1051/0004-6361:20000245.

[77] Hang Yu, Nevin N. Weinberg, and Jim Fuller. “Non-linear dynamical tides in white dwarf binaries”. In: *Monthly Notices of the Royal Astronomical Society* 496.4 (Aug. 2020), pp. 5482–5502. DOI: 10.1093/mnras/staa1858. arXiv: 2005.03058 [astro-ph.SR].

[78] J.-P. Zahn. “The dynamical tide in close binaries”. In: *Astronomy & Astrophysics* 41 (July 1975), pp. 329–344.

[79] J. J. Zanazzi and Yanqin Wu. “Tidal Circularization of Binaries by Resonance Locking. I. The Importance of the Pre-main Sequence”. In: *The Astronomical Journal* 161.6, 263 (June 2021), p. 263. DOI: 10.3847/1538-3881/abf097. arXiv: 2102.05668 [astro-ph.SR].

[80] Wei Zhu and Subo Dong. “Exoplanet Statistics and Theoretical Implications”. In: *arXiv e-prints*, arXiv:2103.02127 (Mar. 2021), arXiv:2103.02127. arXiv: 2103.02127 [astro-ph.EP].

Chapter 5

TIDAL SPIN-UP OF SUBDWARF B STARS

Abstract

Hot subdwarf B (sdB) stars are stripped helium-burning stars that are often found in close binaries, where they experience strong tidal interactions. The dissipation of tidally excited gravity waves alter their rotational evolution throughout the sdB lifetime. While many sdB binaries have well-measured rotational and orbital frequencies, here have been few theoretical efforts to accurately calculate the tidal torque produced by gravity waves. In this work, we directly calculate the tidal excitation of internal gravity waves in realistic sdB stellar models, and integrate the coupled spin–orbit evolution of sdB binaries. We find that for canonical sdB ($M_{\rm sdB} = 0.47\,M_\odot$) binaries, the transitional orbital period below which they could reach tidal synchronization in the sdB lifetime is ~ 0.2 days, with weak dependence on the companion masses. For low-mass sdBs ($M_{\rm sdB} = 0.37\,M_\odot$) formed from more massive progenitor stars, the transitional orbital period becomes ~ 0.15 days. These values are very similar to the tidal synchronization boundary (~ 0.2 days) evident from observations. We discuss the dependence of tidal torques on stellar radii, and we make predictions for the rapidly rotating white dwarfs formed from synchronized sdB binaries.

5.1 Introduction

Hot subdwarf B (sdB) stars, first observed by [33], are compact and faint stars with surface temperatures between 20,000 and 40,000 K and masses below $0.5\,M_\odot$ [32, 31, 86]. These stars have helium-burning cores and thin envelopes [28], and they are thought to be stripped cores of helium-burning red giants, whose envelopes are previously lost due to some binary interactions [29, 30, 57]. About half of the observed sdB systems are found in binaries [46, 48, 26, 14], with many of them in close ($P_{\rm orb} \lesssim 10\,{\rm d}$) orbits. This suggests that a prior common envelope phase might be responsible for the the ejection of their envelopes, as well as the inspirals of their companions to their current orbital configuration [36].

For binaries with short orbital periods, tidal interactions can shape both the migration of their orbits and the spin evolution of individual stars. Historically, sdB binaries are sometimes assumed to have reached tidal synchronization, such that their orbital parameters can be derived from measurements of sdB rotation rates (see, e.g., [37, 25]), even if the companions (typically white dwarfs or M dwarfs) are too faint to be seen. However, this assumption has been seriously challenged by observations from the past decade, especially those with high-precision measurements with TESS and *Kepler*/K2, where both spin and orbital frequencies are available (see the summary of observation results in Figure 5.3). These studies have found that sdB binaries with orbital periods as short as ~ 7 hours are not always synchronized [69]. Nevertheless, these emerging new data provide an excellent opportunity to test theoretical modelling of tidal interactions in sdB binaries.

For stars with convective cores and radiative envelopes like sdBs, tidally excited gravity waves in their envelopes are thought to be the most efficient form of tidal interaction [85]. These waves are excited by the tidal potential from the companion, and when they propagate through the stellar interior, the fluid damp via radiative diffusion, exerting effective tidal torques that transfer the angular momentum from the orbit to the stellar spin [84]. This classical theory of dynamical tides was originally proposed for massive stars, and several works have calculated the tidal evolution of sdB binaries with this model or its adaptions [25, 50, 60].

However, [43] recently pointed out that an assumption in Zahn's model may not be true for stripped helium-burning stars, like Wolf-Rayet stars in the case of massive stars, and sdBs in the case of low-mass stars. While [84] assumed that the waves are all efficiently damped when they propagate to the stellar surface, in these stripped stars they may be otherwise reflected and form standing waves. This is particularly true for high-frequency gravity waves excited by short-period orbits, with less efficient radiative damping in stellar envelopes. By direct calculations of tidally excited oscillations with radiative damping, [43] showed that real tidal torques should have more complicated frequency dependence than the simple power-law relation derived from Zahn's model. This new approach brings concerns to the existing predictions of sdB rotation rates based on Zahn's tidal calculation.

In this paper, we build sdB models and calculated their tidal evolution with the method in [43]. We carry out direct calculations of stellar oscillations and their tidal response, and we find that standing waves indeed exist in these sdBs. The tidal torques are hence different from Zahn's, and our results for sdB rotation rates are consistent with the observed trends of tidal synchronization for these systems. The manuscript is organized as follows: in Section 5.2 we describe the physics of sdB spin-up from tidally excited g-mode oscillations; in Section 5.3 we describe our

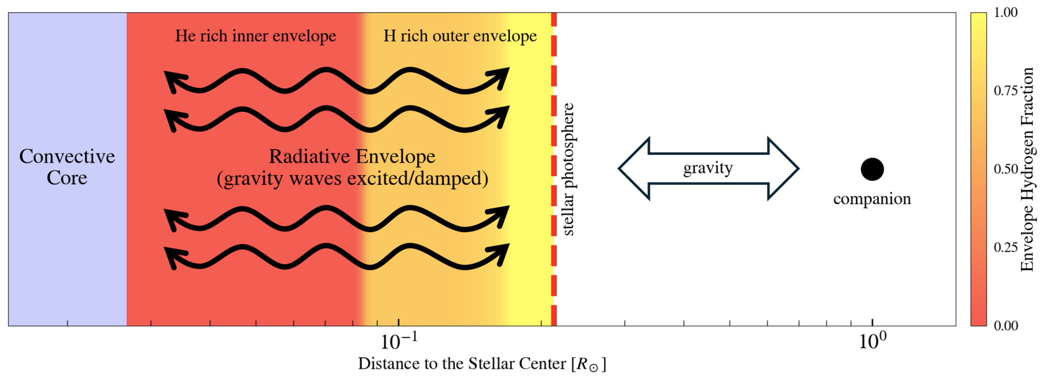

Figure 5.1: A sketch of the physics of sdB tidal spin-up. Gravity waves, propagating in the radiative envelope, can be tidally excited by the gravity from the orbiting companion. In the hydrogen-rich outer envelope, the waves damp (either partially or fully) and deposit their angular momentum into the star, transferring angular momentum from the orbit to the stellar spin. The color scale shows the hydrogen fraction in the radiative envelope.

model setup and in 5.3 and 5.3 we describe how we calculate the oscillation modes and the binary evolution. We show the results for tidal torque calculations and the spin–orbit evolution of sdB binaries in Section 5.4. We discuss the limitations of our models and the various related physical processes in Section 5.5. We finally conclude in Section 5.6.

5.2 Tidal Physics

For subdwarf B binaries, the tidal dissipation inside the sdB star is thought to be responsible for its tidal evolution. In this picture, the tides are excited by the tidal gravity potential from the companion star, which is usually an M–dwarf (dM) or a white dwarf (WD). When the binary orbit is faster than the stellar spin, the tidal dissipation transfers energy and angular momentum from the orbit to the star. For sdB stars with convective cores and radiative envelopes, two possible tidal dissipation mechanisms could be at work: namely the turbulent viscous dissipation of equilibrium tidal bulges in the stellar core [18, 17], and the radiative damping of tidally excited gravity waves in the envelope [84, 85]. Studies have found that the former is usually inefficient for close-in subdwarf binaries, as the orbital periods might be shorter than the convective turnover time in the core, such that convective viscous dissipation is suppressed [59]. We hence focus on the latter scenario to be the dominant process for tidal evolution.

We sketch the physics picture of radiative dissipation of tidally excited gravity waves in Figure 5.1. Gravity waves, propagating in the radiative envelope of the star, can be tidally excited by the orbit of the companion. In the outer envelope with large thermal diffusion, these waves damp partially or fully by radiative diffusion, releasing their energy and angular momentum, and hence exert a tidal torque on the star. The orbital angular momentum is thus transferred to the stellar spin. In previous studies, radiative dissipation is often assumed to be efficient so that these gravity waves damp completely in the radiative envelope [84], while in principle they might reflect back and instead forming standing waves, i.e. oscillation modes [43]. Hence, a realistic estimate of tidal torques requires calculation of individual stellar oscillation modes.

For an aligned and circular orbit, the tidal torque for a tidally-excited oscillation mode α is given by [43]:

$$\tau_\alpha = -\frac{m\omega_\alpha\gamma_\alpha q^2 M_1 R_1^2 |W_{lm}Q_\alpha|^2 \omega_{\rm f}^2}{(\omega_\alpha - \omega_{\rm f})^2 + \gamma_\alpha^2}\left(\frac{R_1}{a}\right)^{2(l+1)}, \tag{5.1}$$

where ω_α and γ_α are the mode frequency and growth rate (with $\gamma_\alpha < 0$ for damped modes, and the corresponding $\tau_\alpha > 0$), and $\omega_{\rm f} = m(\Omega_{\rm orb} - \Omega_{\rm spin})$ is the tidal forcing frequency (measured in the frame co-rotating with the sdB), and $\Omega_{\rm spin}$ is the sdB's angular rotation frequency. M_1 and R_1 are the mass and radius of the sdB, $q = M_2/M_1$ is the mass ratio of the companion to the sdB, a and $\Omega_{\rm orb}$ are the semi-major axis and the angular frequency of the orbit. l and m are the mode's angular and azimuthal wave numbers and W_{lm} is an expansion coefficient of the tidal potential. $Q_\alpha \equiv \langle \xi_\alpha | \nabla(r^l Y_{lm})\rangle / \omega_\alpha^2$ is the dimensionless overlap integral describing the spatial coupling between the mode and the tidal potential, which is calculated by the relation $Q_\alpha = -(2l+1)\delta\Phi_\alpha/(4\pi\omega_\alpha^2)$ [21], where $\delta\Phi_\alpha$ is the surface gravity potential perturbation. For weak damping ($\gamma_\alpha < \omega_\alpha$), the excitation of individual oscillation modes is independent from each other, such that the total tidal torque can be expressed as

$$\tau_{\rm tide} = \sum_\alpha \tau_\alpha \,. \tag{5.2}$$

Hence, by solving for the internal oscillation modes (with ω_α, γ_α and Q_α) inside the sdB, we are able to calculate the torque and the angular-momentum transfer rate, given a companion mass and orbit. We stress that there are *no* free parameters in estimating the strength of tidal torques with this method.

5.3 Methods

We calculate the tidal evolution of sdB binaries with the similar method developed for Wolf—Rayet—Black–hole binaries in [43]. We first build realistic single evolving sdB models throughout their helium-burning lifetime (Section 5.3). We then solve for stellar oscillations based on these models to estimate the tidal torques (Section 5.3). Finally, we numerically integrate the coupled spin–orbit evolution of sdB binaries with interpolation between the previously calculated sdB models and tidal torques, with different choices of initial binary parameters, i.e. the initial orbital periods and companion masses (Section 5.3).

Stellar Models

We build single sdB models with the MESA stellar evolution code (r12778; [51, 53, 52, 54, 55, 34]). We build two sdB models to represent the two types of sdBs formed from progenitors of different masses, summarized in Sections 5.3 and 5.3. We turn on element diffusion for ^{1}H, ^{4}He, ^{12}C, ^{14}N and ^{16}O in the MESA models, to account for correct treatments of gravitational settling and radiative acceleration for these atoms.

0.47 Solar-mass Canonical SdB Model

This model represents the most abundant sdBs ("canonical" sdBs) that are formed from low-mass ($M \lesssim 2\,M_{\odot}$) main-sequence progenitor stars. When these stars evolve off main-sequence, they start hydrogen shell burning which deposits helium into their helium core, until they reach the tip of the red giant branch (TRGB) when the helium core exceeds $0.46\,M_{\odot}$. At this moment, an off-center helium flash is triggered and the helium burning propagates to the center of the core, while the star loses most of its envelope through binary processes (e.g., a common envelope event), leaving a core helium-burning sdB star with a little of its envelope ($\sim 0.01\,M_{\odot}$) retained. SdB stars formed this way are insensitive to the masses of their progenitors, and have universal masses of $\approx 0.47\,M_{\odot}$. We establish this sdB model by evolving a $1.2\,M_{\odot}$ star from zero-age main-sequence (ZAMS) to TRGB, and then apply an artificial stellar wind to remove its envelope, until the off-center helium burning propagates to the stellar center. This happens at the moment when the envelope mass reaches the desired mass (see details in 5.3), due to the specific wind scaling factor we chose. The model then becomes a zero-age canonical sdB model and we evolve it until core helium depletion.

0.37 Solar-mass Low-mass SdB Model

For stars of $\sim 2-3\,M_{\odot}$, they can also ignite core helium burning without forming a fully degenerate core, at helium core masses less than $0.46\,M_{\odot}$. Hence, they usually form sdBs of lower masses compared to canonical sdBs. To simulate this scenario, we evolve a $2.7\,M_{\odot}$ star from ZAMS to TRGB, and then remove its envelope by a similar artificial wind until its envelope mass reaches the desired mass (see details in 5.3). The model then triggers central helium burning as a zero-age sdB star. The sdB model we build this way has a mass of $0.37\,M_{\odot}$.

Envelope Mass Setup

SdBs are known to retain a small amount of hydrogen envelope above their helium cores. The amount of hydrogen can be constrained from their spectroscopic properties, and are found to be between $0.001 - 0.005\,M_{\odot}$ (see, e.g., Figure 10 of [38]). We hence adjust the artificial winds such that the stellar models start core helium burning (zero-age sdB) when they have $10^{-3}\,M_{\odot}$ hydrogen left. After that moment, we turn off stellar winds as the envelope-stripping phase is considered completed. We note that, real sdB stars can possibly retain more hydrogen than $10^{-3}\,M_{\odot}$. However, we found many unstable stellar oscillations in sdB models with more massive envelopes, and we are not able to calculate the tidal dissipation of these modes with our current method. We discuss the influence of envelope masses and these unstable modes in more detail in Section 5.5.

Convective Core Boundary Setup

The excitation of gravity waves is sensitive to the size of the convective core, which in turn can be sensitive to how its boundary is treated in stellar evolution models. Unlike the standard convective-overshooting paradigm which has been established for main-sequence stars (see, e.g., the MIST project; [12]), overshooting parameters for stars with a helium-burning convective core, like sdBs, are poorly constrained. Nevertheless, asteroseismic measurements of core helium-burning stars suggest the existence of bigger cores compared to theoretical modeling [13, 8, 49]. We hence turn off overshooting for our stellar models in the core helium-burning phase, instead applying the "predictive mixing" scheme for convection [54]. This allows for a steady growth of the convective core during core helium-burning, more consistent with asteroseismic observations than other choices for convective mixing. Furthermore, the predictive mixing scheme helps prevent "breathing pulses" at late stages of the core helium-burning phase, which may split the convective core to create small radiative zones, in which very high-order gravity waves can be trapped. Breathing pulses have been argued to be numerical artifacts [7], and we aim to avoid the associated difficulties in computing gravity modes.

Rotation Setup

When stars evolve off main-sequence, their core contracts and spins up, while their envelope expands and spins down. The shear created between the core and the envelope could trigger hydrodynamical and magneto-hydrodynamical instabilities, which transfer some of the core angular momentum to the envelope, forming slowly rotating stellar cores [24, 74]. Asteroseismic measurements of red clump stars have shown that their core rotation periods are typically ~ 100 days [47]. Therefore, if these stellar cores form sdBs, they should also be slowly rotating.

We applied the modified Taylor-Spruit torque as described in [24] in our stellar models, and we found that the stellar models at the end of the envelope-stripping phase rotate slowly, with rotation rates insensitive to the initial rotation at ZAMS. The slow rotation rates are consistent with the slow sdB rotation rates measured in wide binaries, where tidal effects are not important (see, e.g., Figure 5.3). We hence set the sdB models to be non-rotating at the start of their helium burning phase. Since we only compute our spin–orbit evolution by post-processing of the stellar models, without actually updating their rotation rates in MESA (see details in 5.3), the single sdB models remain non-rotating throughout their lifetime.

Calculation of Oscillation Modes

We calculate the internal oscillation modes for the individual snapshots of our sdB models with the GYRE stellar oscillation code [73, 71, 27]. We solve for non-adiabatic oscillations which account for radiative damping in the oscillation equations. We use the second order Magnus differential scheme, as it proves to be the most reliable when dealing with low-frequency oscillations. We specify our search to $l = m = 2$ modes as this is the dominant part of the tidal potential in aligned and circular orbits, with the corresponding $W_{22} = \sqrt{3\pi/10}$. When solving for modes, we find that the Brunt-Väisälä frequency [76] profiles solved from MESA are sometimes not consistent with the density and pressure profiles from the same model, which may lead to inaccurate mode solutions. We hence slightly adjust the stellar profiles with the process described in Appendix 5.7 for our stellar models.

We checked that the change of stellar structure due to this process is negligible.

In principle, we need to sum over *all* modes to get the total tidal torque through Equation 5.2. This is practically not possible as there are infinite number of modes which could be excited at all frequencies. Nevertheless, we note from Equation 5.1 that for a given tidal forcing frequency ω_f, typically only the few nearly resonant modes with ω_α close to ω_f contribute significant torques. Torques from other non-resonant modes are usually negligible due to the $(\omega_\alpha - \omega_f)^2$ term in the denominator of Equation 5.1. We hence restricted our mode solutions to a finite period range, namely from 0.005 days to 0.5 days, and we hence found a finite number of modes. We can then calculate the total tidal torques as long as the forcing frequency ω_f is between $2\pi/(0.5\,\mathrm{d}) = 12.57\,\mathrm{d}^{-1}$ and $2\pi/(0.005\,\mathrm{d}) = 1257\,\mathrm{d}^{-1}$. The ω_f calculated from our spin–orbit evolution usually lies well within this range, except for some systems that reach tidal synchronization, whose ω_f should approach zero. We hence stop the evolution when ω_f reaches the minimum mode frequency $12.57\,\mathrm{d}^{-1}$. We checked that our binary models reaching this condition are at least at 80% synchronization, so we *define* all systems with $\Omega_{\rm spin} \geq 0.8\,\Omega_{\rm orb}$ as tidally synchronized.

Spin–Orbit Evolution

We integrate the spin–orbit evolution of the sdB binaries from the stellar models and tidal torques we computed. As the tidal dissipation in the companion star is negligible, the companion is assumed a point mass and its spin evolution is not coupled. We also assume the orbits are circular. Throughout the evolution, the orbital angular momentum of the system is lost due to gravitational wave (GW) radiation and tides, while the sdB receives spin from the tidal torque:

$$\dot{J}_{\rm orb} = -\tau_{\rm GW} - \tau_{\rm tide}\,, \tag{5.3}$$

$$\dot{J}_{\rm spin} = \tau_{\rm tide}\,, \tag{5.4}$$

where $\tau_{\rm GW} = (32/5)(G/a)^{7/2}c^{-5}M_1^2M_2^2\sqrt{M_1+M_2}$ is the effective torque by GW radiation [58]. The GW orbital decay timescale is then given by

$$\begin{aligned} T_{\rm GW} &= 5c^5(1+q)^{1/3}P_{\rm orb}^{8/3}/(64(4\pi^2)^{4/3}G^{5/3}M_1^{5/3}q) \\ &\approx 180\,\mathrm{Myr}\,(P_{\rm orb}/1\,\mathrm{h})^{8/3} \end{aligned} \tag{5.5}$$

for an equal mass sdB binary ($q = 1$), with a $0.46\,M_\odot$ canonical sdB star, comparable to the sdB lifetime of $\sim 150\,\mathrm{Myr}$ for very short-period systems. This means GW orbital decay needs to be included in the spin–orbit evolution.

As we expect efficient angular momentum transport during the core-helium burning phase ([24, 23]; see discussions in 5.3), we assume rigid rotation for the sdB star, with a uniform rotational frequency $\Omega_{\rm spin}$. We discuss the case of differential rotation in Section 5.5. The coupled spin–orbit evolution can then be integrated by:

$$\dot{\Omega}_{\rm spin} = \frac{\dot{J}_{\rm spin}}{I_{\rm spin}} - \Omega_{\rm spin}\frac{\dot{I}_{\rm spin}}{I_{\rm spin}}\,, \tag{5.6}$$

$$\dot{\Omega}_{\rm orb} = \frac{\dot{J}_{\rm orb}}{I_{\rm orb}} - \Omega_{\rm orb}\frac{\dot{I}_{\rm orb}}{I_{\rm orb}} = -3\frac{\dot{J}_{\rm orb}}{I_{\rm orb}}\,, \tag{5.7}$$

where $I_{\rm spin}$ is the moment of inertia of the sdB star, $I_{\rm orb} = \mu a^2$ is the moment of inertia of the orbit and we made use of Kepler's Third Law to simplify Equation 5.7. This means the spin of the sdB star may also change due to the changes of its internal structure and hence moment of inertia.

We make use of the integration machinery constructed in [43], with the same interpolation method. As sdB lifetime is typically longer than the Wolf–Rayet stars in [43], we choose the integration timestep to be 0.1 times the values derived from the timestep control method described in [43]. We integrate the evolution from 1 year after the start of the sdB helium-burning phase, and we stop when the model depletes its core helium (defined by the time when the core helium fraction drops below 1%) or when the system reaches $\omega_{\rm f} \lesssim 12.57\,{\rm d}^{-1}$ (see Section 5.3). The initial rotational period of sdBs is set to be 60 days, to match the observed values from single sdB stars [69]. While single sdBs may not represent a fair sample of binary sdBs at birth, this assumed initial rotational frequency is very low and never important for systems that reach synchronization. We vary the companion masses between $0.1\,M_\odot$ and $0.8\,M_\odot$, and choose the initial orbital periods to be between 1 to 18 hours, covering the observed parameter space of close-in sdB binaries [66]. We checked our results are robust against different choices of timestep resolution.

5.4 Results

In this section, we show the results of our tidal torque calculation and spin–orbit evolution.

Tidal Torque

In Figure 5.2, we show our calculated tidal torque magnitude with its dependence on the period of tidal forcing ($P_{\rm f} \equiv 2\pi/\omega_{\rm f}$). The calculation is based on the $0.47\,M_\odot$ sdB model with a companion of $0.4\,M_\odot$, when its central helium fraction drops to 60%, and we assume the sdB is non-rotating such that $\omega_f = m\Omega_{\rm orb}$. The torque

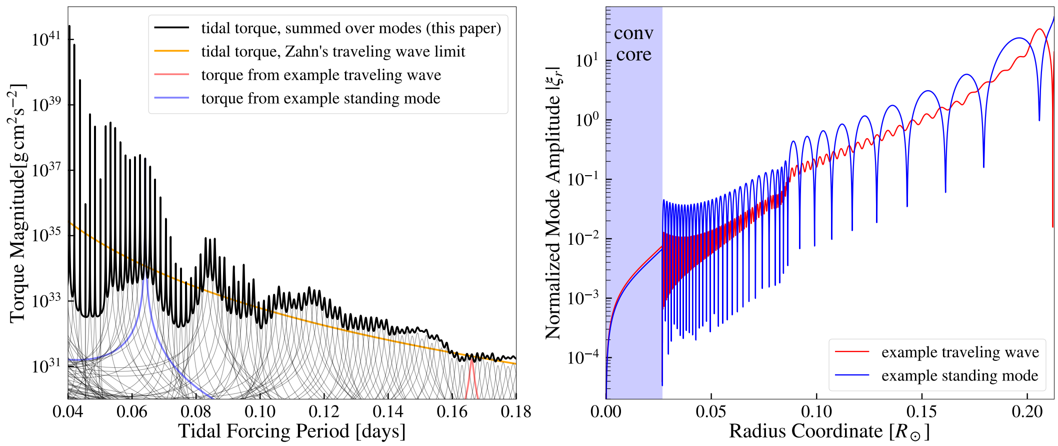

Figure 5.2: **Left**: The tidal torque calculated for a $0.47\,M_\odot$ sdB model with a companion of $0.4\,M_\odot$, when the central helium fraction is 60%, assuming the sdB is non-rotating. The thick black line shows the total torque calculated by summing over contributions from individual tidally excited g modes (thin lines). We also show the torque calculated from Zahn's formalism for comparison. At short periods, the total tidal torque is dominated by resonance peaks from individual standing g modes, different from the power-law dependence on forcing period of Zahn's formalism. At longer periods, g modes are more efficiently damped and the torque agrees better with Zahn's model. **Right**: the mode eigenfunctions for an example standing mode (blue line) and an example traveling wave (red line) in the left panel. The standing mode has nodes in its eigenfunction, while the traveling wave efficiently damps near the surface.

generally has a complicated dependence on the forcing period. By plotting the torque contributions from each individual oscillation mode J_α, we see that this dependence is caused by summing over the resonance peaks of many modes with different frequencies. When the tidal forcing frequency gets close to one of the mode frequencies, the $(\omega_\alpha - \omega_f)^2$ term in Equation 5.1 vanishes, and the total torque becomes dominated by the strong resonance peak of that mode. Therefore, the frequencies/periods of these peaks are the frequencies/periods of individual oscillation modes inside the star. These peaks have a nearly uniform period spacing, a feature expected for gravity (g) modes. In the right panel of Figure 5.2, we show some example eigenfunctions of these modes, and we can see that they are indeed g modes that propagate inside the radiative envelope of the star.

Previous studies involving the tidal dissipation of gravity waves in sdBs usually use Zahn's model for dynamical tides [25, 50, 60], which assumes these waves are efficiently damped as they reach the stellar surface ("traveling-wave limit"). We see from the right panel of Figure 5.2 that this is clearly not always the case for individual resolved stellar oscillations. The blue line shows the eigenfunction of an example oscillation at short ($P_\alpha \lesssim 0.14$ days) period. We see that instead of efficiently damping near the stellar surface, the wave reflects back at the stellar surface and forms a standing wave with nodes. This means Zahn's picture may overestimate the mode damping rate, hence the tidal dissipation.

For comparison, we show the tidal torques calculated based on Zahn's formalism with a modified formula given by [42]:

$$\tau_{\rm Zahn} = \beta_2 \frac{GM_2^2}{r_{\rm c}} \left(\frac{r_{\rm c}}{a}\right)^6 s_{\rm c}^{8/3} \frac{\rho_{\rm c}}{\bar{\rho}_{\rm c}} \left(1 - \frac{\rho_{\rm c}}{\bar{\rho}_{\rm c}}\right)^2 , \tag{5.8}$$

where $s_{\rm c} = \sqrt{3/(\pi G \bar{\rho}_{\rm c})} |\Omega_{\rm orb} - \Omega_{\rm spin}|$, while $r_{\rm c}, \rho_{\rm c}$ and $\bar{\rho}_{\rm c}$ are the convective core radius, the density at the core boundary, and the average density of the core, respectively. β_2 is a dimensionless coefficient solved from stellar structures, and different main-sequence and Wolf–Rayet stellar models have $\beta_2 \approx 1$ [42]. Its dependence on the tidal forcing period is mostly the power-law term in $s_c^{8/3} a^{-6}$, as seen in Figure 5.2. This is clearly different from the resonance peak dependence we find from realistic mode calculations. We see that at short periods, if the binary orbit has an off-resonance tidal forcing period (i.e., not close to any stellar oscillation modes), the real tidal torque can be orders of magnitude lower than Zahn's prediction. On the other hand, if the orbit is on resonance, the torque can be significantly larger than Zahn's prediction.

However, as the star and the orbit evolves, both the oscillation mode period (hence the location of the resonance peaks) and the tidal forcing period change over time, so the system can quickly pass through resonances (as long as resonance locking does not happen, see discussions in Section 5.5). Since the resonances are narrow, the system spends more time out of resonance than in resonance (i.e., with torques much weaker than Zahn's prediction), the accumulated angular momentum received by the sdB star should be less than the predictions from Zahn's theory.

At longer periods, gravity waves have larger wave numbers, and are expected to damp more efficiently with radiative damping. With larger γ_α, the γ_α^2 term becomes more important in the denominator of Equation 5.1, smoothing out the resonance peaks. We see in Figure 5.2 that this is exactly the case for the tidal torques at long period ($P_{\rm f} > 0.14$ d), when the individual modes damp so much that the resonance structure gets smoothed out. In addition, the example eigenfunction (red line) shown in the right panel of Figure 5.2 becomes a traveling wave that efficiently damps near the stellar surface, as Zahn's formalism assumes. The tidal torque's dependence on tidal forcing period also gets closer to Zahn's power-law dependence as expected. This further shows that Zahn's traveling wave picture is a limit case of realistic tidal torques at long periods.

Tidal Synchronization

With the tidal torques calculated, we are able to integrate the coupled spin–orbit evolution of our models. In Figure 5.3, we show the calculation for our $0.47\,M_\odot$ canonical sdB model and $0.37\,M_\odot$ low-mass sdB model with a fixed companion mass of $0.4\,M_\odot$, with different initial orbital periods. The rotational and orbital periods are evaluated at the end of the spin–orbit evolution (defined in Section) 5.3, and some ultra-short-orbit synchronized systems that reaches $P_{\rm orb} < 0.02\,{\rm d}$ due to gravitational wave orbital decay are not shown. We see that for the $0.47\,M_\odot$ sdB model, all systems with orbital periods less than ~ 0.2 days reach tidal synchronization, while for the $0.37\,M_\odot$ sdB model, the synchronization period becomes ~ 0.15 days.

To compare with observations, we plot the measured rotational and orbital periods for short-period sdB binaries on top of Figure 5.3. The different colors show the sdB rotation rates derived from spectral line measurements (HS 0705+6700, [16]; CD-30 11223, [78]; SDSS J162256.66+473051.1, [65]; PTF1 J0823+0819, [40]; PTF1 J011339.09+225739.1, [83]; ZTF J2130+4420, [41]; ZTF J2055+4651, [39]; SDSS J082053.53+000843.4, [64]; HW Vir, [19]; and EPIC 216747137, [68]), asteroseismic p-mode frequency splitting (NY Vir, [10]; Feige 48, [77]; V1405 Ori, [62]; and HD 265435, [56]), or g-mode frequency splitting (KIC 11179657 and KIC 2991403, [50]; FBS 1903+432, [70]; KIC 7664467, [2]; EQ Psc and PHL 457, [3]; KIC 2438324, [63]; TYC1 4544-2658-1, [69]; and PG 0101+039, [45]), respectively.

We see that all the observed systems with $P_{\rm orb} \lesssim 0.2\,{\rm d}$ are close to tidal synchronization, while all but two systems[1] above this period are not synchronized. This matches strikingly well with the theoretical prediction from our sdB models. In addition, the models with $0.3\,{\rm d} \lesssim P_{\rm orb} \lesssim 0.6\,{\rm d}$ are tidally spun-up to a rotational period of a few days, also consistent with the observed partially-synchronized systems

[1] The two exceptional systems are Feige 48 and V1405 Ori. For Feige 48, there are some discrepancies on its orbital and rotational periods measured (see, e.g., [20, 60, 4]). For V1405 Ori, there are some evidences that it might a differentially rotating sdB [62], such that its envelope can be synchronized at longer periods while its interior is not (see discussions in Section 5.5).

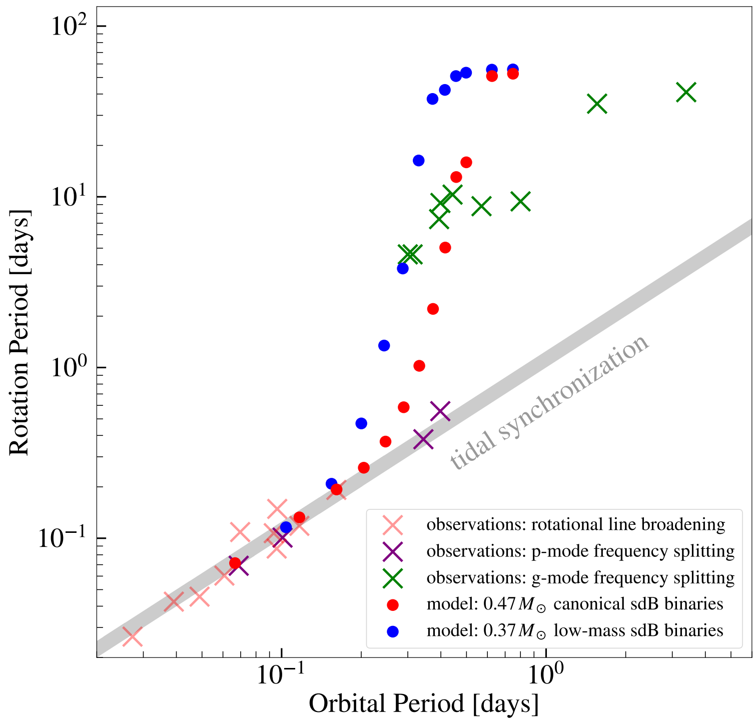

Figure 5.3: The observed trend of tidal synchronization (defined by $0.8 \leq \Omega_{\rm spin}/\Omega_{\rm orb} \leq 1$, shaded grey region) for short-period sdB binaries (crosses) versus the calculation results from binary spin–orbit evolution (dots). The red, purple and green crosses indicate rotational measurements from spectral line broadening, p-mode frequency splitting and g-mode frequency splitting. The red and blue dots indicate the modeled sdB binaries with the $0.47\,M_\odot$ and the $0.37\,M_\odot$ sdB primary, respectively. All modeled binaries have a $0.4\,M_\odot$ companion and initial orbital periods ranging from 1 to 18 hours. For $0.47\,M_\odot$ sdB binaries, we see that all systems with orbital periods less than ~ 0.2 days reach tidal synchronization, while for $0.37\,M_\odot$ sdB binaries, this synchronization period becomes ~ 0.15 days due to weaker torques on these smaller sdBs. These results match the observed trends of sdB tidal synchronization. In addition, most systems with $0.3\,\mathrm{d} \lesssim P_{\rm orb} \lesssim 0.6\,\mathrm{d}$ are spun-up to rotational periods of a few days, which also agree with the observed period range of partially synchronized binaries.

in that period range. Hence, our theoretical calculations agree with the observation data. Note that in Figure 5.3 the spin and orbital frequencies are shown at the end of the spin–orbit evolution, while measurements for realistic systems usually occur when the sdB still undergoes core-helium burning. Therefore, it is illustrative to show the tidal synchronization timescales calculated for our models, and to compare them with the sdB lifetime $T_{\rm EHB}$. If the synchronization time is shorter, then we expect those systems are likely to reach tidal synchronization to be observed. As we consider systems with 80% synchronization as synchronized (see discussions in Section 5.3), we define the tidal synchronization timescale throughout the whole evolution as:

$$\bar{T}_{\rm sync} \equiv \begin{cases} t_{\Omega_{\rm spin}/\Omega_{\rm orb}=0.8} & \text{, if synchronized} \\ 0.8\, T_{\rm EHB} \left(\frac{\Omega_{\rm spin}}{\Omega_{\rm orb}}\right)^{-1}_{\rm final} & \text{, if not} \end{cases} \tag{5.9}$$

where t is the stellar age since the start of sdB core helium-burning. We then run a grid of spin–orbit evolution for both of our $0.47\,M_\odot$ and $0.37\,M_\odot$ sdB models, with initial orbital periods of $(1, 2, 3, 4, 5, 6, 7, 8)$ hours and companion masses of $(0.1, 0.2, 0.3, 0.4, 0.5, 0.6, 0.7, 0.8)$ solar-masses, and calculated their tidal synchronization timescale defined by Equation 5.9.

We show the interpolated results for the ratio $\bar{T}_{\rm sync}/T_{\rm EHB}$ based on this grid in the whole parameter space in Figure 5.4. On the y-axis we also label the typical companion masses for sdB+dM and sdB+WD binaries [66]. We see that this ratio ranges from $10^{-1.5}$ to $10^{1.5}$, with weak dependence on the masses of the companion star. This is an expected result from our tidal torque formula (Equation 5.1): the torque depends on the mass-ratio (hence the secondary mass) as $\tau_\alpha \propto q^2 a^{-6}$, where $a = (G(M_1 + M_2)/\Omega_{\rm orb}^2)^{1/3} \propto (1 + q)^{1/3}$, hence $\tau_\alpha \propto q^2/(1 + q)^2$. For typical sdB binaries, q ranges from 0.3 to 1.5, and the corresponding torque scaling is maximally different by only a factor of ~ 7. In contrast, $\bar{T}_{\rm sync}/T_{\rm EHB}$ varies by a factor of $\sim 10^3$ over the period range shown in Figure 5.4, due to its strong dependence on semi-major axis.

The blue colored regions in Figure 5.4 show the parameter space where $\bar{T}_{\rm sync}/T_{\rm EHB} < 1$, or where the binaries are expected to be synchronized. We see that for $0.47\,M_\odot$ sdB binaries, systems with initial orbital periods less than $\sim 0.15 - 0.22$ days have synchronization timescales shorter than the 164 Myrs sdB lifetime, while for $0.37\,M_\odot$ sdB this period becomes $\sim 0.10 - 0.17$ days for its 444 Myrs lifetime, depending on the companion masses. As binaries at these orbital periods produce

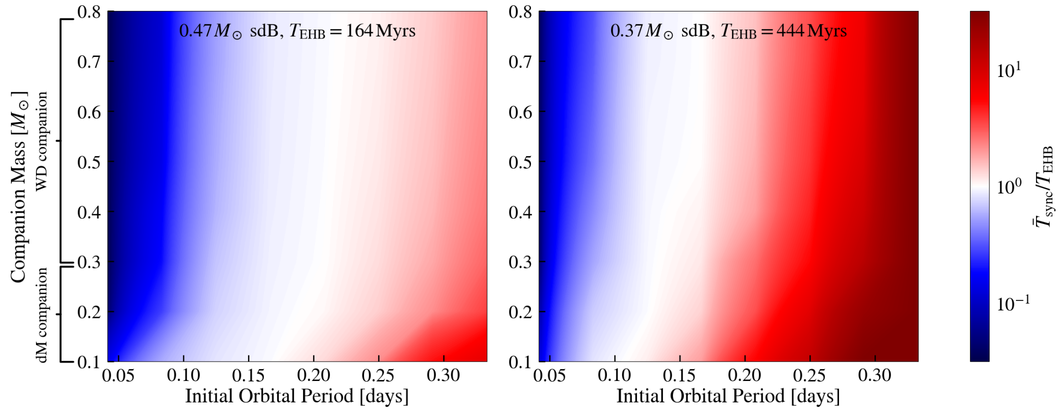

Figure 5.4: The ratio between the tidal synchronization timescale $\bar{T}_{\rm sync}$ and the the sdB lifetime $T_{\rm EHB}$ interpolated between different choices of companion masses and initial orbital periods. The blue regions show the parameter space where $\bar{T}_{\rm sync} < T_{\rm EHB}$. The brackets on the y axis indicate the typical companion masses for sdB+WD or sdB+dM systems [66]. **Left**: The results for the 0.47 $M_\odot$ sdB model, with $T_{\rm EHB} = 164$ Myrs. We see that for systems in orbits less than $\sim 0.15 - 0.22$ d, the synchronization timescale is less than the stellar lifetime, meaning these systems are likely to be observed as tidally synchronized. The results have weak dependence on companion masses. **Right**: The results for the 0.37 $M_\odot$ sdB model. The critical orbital period below which systems become synchronized now becomes $\sim 0.10 - 0.17$ d.

weak GW emission, their orbital periods are nearly constant, and these results confirm the critical orbital periods for synchronization shown in Figure 5.3.

We note from Figure 5.4 that, even though systems below the synchronization periods can reach tidal synchronization in the sdB lifetime, in most of the parameter space their synchronization timescales are not less than the corresponding sdB lifetime by one order of magnitude. This is especially true for sdB+dM binaries with $M_{\rm companion} \lesssim 0.3\,M_\odot$, and we can see that $\bar{T}_{\rm sync} < 0.1\,T_{\rm EHB}$ is only achieved for those binaries in $P_{\rm orb} \lesssim 0.05\,{\rm d} \approx 1$ hour orbits. This is consistent with the findings that sdB binaries with small companions (dMs or brown dwarfs) can be slightly sub-synchronized even at orbital periods less than ~ 2.5 hours (e.g., SDSS J162256.66+473051.1, a 64% synchronized system with $P_{\rm orb} = 1.67$ h, [65]; and SDSS J082053.53+000843.4, a 65% synchronized system with $P_{\rm orb} = 2.3$ h, [64]).

[64] further points out that synchronized binaries locate further away from the zero-age extreme horizontal branch (ZAEHB) on the $\log g - T_{\rm eff}$ diagram compared to these sub-synchronized systems, suggesting that those synchronized binaries might be older. Our findings that the tidal synchronization timescales at small orbital

periods are shorter than the sdB lifetime (but not by orders of magnitude), agrees with this explanation.

Historically, the orbital inclinations and companion masses are hard to acquire for non-eclipsing sdB binaries. Some works hence assume tidal synchronization for short-period binaries, and derive the orbital parameters from the orbital periods by setting $P_{\rm orb} = P_{\rm rot}$ (e.g., [25]). However, if we can assume tidal synchronization for systems with $\bar{T}_{\rm sync} < 0.1\,T_{\rm EHB}$, we see that this method should only apply to binaries with $P_{\rm orb} \lesssim 1\,{\rm h}$. This is much shorter than the synchronization period ($P_{\rm orb,\,sync} = 1.2\,{\rm d}$) assumed in [25], meaning that in their work the companion masses/inclinations might be over/underestimated.

Additionally, binaries with $P_{\rm orb} \lesssim 1\,{\rm h}$ can undergo significant orbital decay due to gravitational-wave radiation, and it is questionable whether these systems can *ever* reach 100% tidal synchronization, as tides at sub-synchronization may not be strong enough for $\Omega_{\rm spin}$ to fully catch up with $\Omega_{\rm orb}$ (as in the case of WD binaries, see, e.g., [67]). Mass-transfer may also happen for these binaries, making their evolution more complicated [7].

5.5 Discussion

Tidal Torque Scaling with Stellar Radii

We saw in Section 5.4 that the binary orbital period required to reach tidal synchronization is shorter for the $0.37\,M_\odot$ low-mass sdB, compared to the $0.47\,M_\odot$ canonical sdB. This means the tidal torque must be weaker for low-mass sdBs. To explain the reason, we consider an equal-mass binary ($q = 1$), and rewrite the mode torque of equation 5.1 as

$$\tau_\alpha = -f(\omega_{\rm f})\gamma_\alpha J_\alpha C_\alpha S(R_1)\,, \tag{5.10}$$

where

$$f(\omega_{\rm f}) \equiv \frac{\omega_{\rm f}^2}{(\omega_\alpha - \omega_{\rm f})^2 + \gamma_\alpha^2} \tag{5.11}$$

is a dimensionless function describing the resonance dependence of the torque on $\omega_{\rm f}$, whose scaling should be of similar order for different stellar models. The quantity

$$J_\alpha \equiv m\omega_\alpha M_1 R_1^2 \langle \xi_\alpha | \xi_\alpha \rangle \tag{5.12}$$

is the angular momentum of the oscillation mode α with azimuthal wave number m, which roughly scales as $J_\alpha \propto M_1 R_1^2$ for stars of similar structure at the same

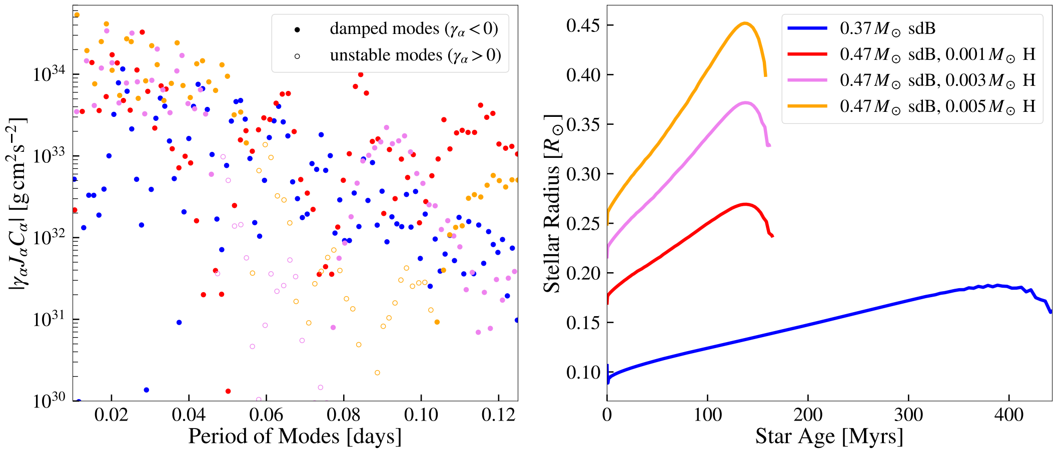

Figure 5.5: **Left**: The magnitude of $\gamma_\alpha J_\alpha C_\alpha$ (defined in the main text) for different sdB models. This quantity determines the tidal torque of each mode per unit tidal forcing strength, and we see that they are of similar orders of magnitude without clear dependence on the different stellar models. Hence, the physical torque should be roughly proportional to the tidal forcing strength which scales as R^6. Note that sdB models with hydrogen masses greater than $10^{-3}\,M_\odot$ have some unstable modes, and their tidal excitation can not be treated with our current method. **Right**: Stellar radii as a function of age for different sdB models. More massive systems with more hydrogen left in the envelope have larger radii, and the tidal torques are expected to be stronger based on the R^6 scaling.

mode frequency. For dissipating modes, the rate for mode α to dissipate its angular momentum (i.e., exerting a torque) is $\gamma_\alpha J_\alpha$. The quantity

$$C_\alpha \equiv \frac{|W_{lm} Q_\alpha|^2}{\langle \xi_\alpha | \xi_\alpha \rangle} \tag{5.13}$$

describes the dimensionless coupling of the tidal potential and the oscillation mode, and $S(R_1) \equiv (R_1/a)^{2(l+1)}$ is the scaling of the tidal forcing strength.

With this notation, we can see that the quantity $\gamma_\alpha J_\alpha C_\alpha$ represents the rate at which mode α deposits its angular momentum into the star (i.e., the tidal torque), per tidal forcing strength. We plot this quantity for the $0.47\,M_\odot$ and $0.37\,M_\odot$ sdB models in Figure 5.5, and we see that they have similar orders of magnitude without clear dependence on the different stellar models. This is expected as these sdB stars have very similar internal structures.

Therefore, the main scaling of the physical tidal torque comes from the forcing strength $S(R_1)$. As shown in right panel of Figure 5.5, the $0.37\,M_\odot$ sdB is more compact than the $0.47\,M_\odot$ sdB due to its lower mass, and its radius R_1 is smaller by a factor of ~ 2. For $l = 2$ modes, this produces a difference in the tidal torque by

$(R_{0.37}/R_{0.47})^6 \sim 1/64$. Since the 0.37 $M_\odot$ sdB has a smaller moment of inertia by a factor of a few, its synchronization time scale is about ten times longer. We can confirm this result from Figure 5.4: the tidal synchronization timescale at $P \sim 0.2$ d for 0.47 $M_\odot$ sdB binaries is $T_{\rm EHB,0.47} = 164$ Myrs, roughly 10 times shorter than the timescale of 0.37 $M_\odot$ sdB binaries at the same period (a few times $T_{\rm EHB,0.37} = 444$ Myrs).

The above analysis can also provide insight into the tidal torques for sdBs with different hydrogen envelope masses. Detailed sdB modeling has shown that hydrogen envelope masses range from 0.001 to 0.005 $M_\odot$ [38]. This small amount of hydrogen never affects the core structure of the helium-burning sdBs, but it can greatly change the stellar radius.

In the right panel of Figure 5.5 we show the stellar radii for some 0.47 $M_\odot$ sdB models that retained more hydrogen than $10^{-3}\,M_\odot$. Compared to the original $10^{-3}\,M_\odot$ hydrogen model, we can see even that a slight increase of hydrogen could increase the sdB radius by a factor of $\sim 1.5 - 2$. We further plot the $\gamma_\alpha J_\alpha C_\alpha$ calculated for these models in the left panel of Figure 5.5, and we see that despite some scatter, they are similar to the $10^{-3}\,M_\odot$ hydrogen model. We hence expect the $\tau \propto R^6$ scaling roughly holds for these models, and the tidal torque for these larger sdBs could be larger by a factor of $\sim 10-50$, which will increase the synchronization transitional period.

We note, however, there is a reason that we did not actually compute the tidal torques for these more extensive sdB models. We see in Figure 5.5 that for sdB models with $M_{\rm H} > 10^{-3}\,M_\odot$, there exist a period range where the mode growth rate γ_α is positive, i.e. where the modes are *unstable*. This is caused by the so-called κ-mechanism in these stars, where the partial ionization of iron creates an opacity bump, generating self-excited oscillations [11, 9]. Our torque in equation 5.1 only holds for damped oscillation modes, and it is unclear how these self-excited oscillations would interact with tidal forcing (see, e.g., [22]). These unstable modes have periods of $\sim 0.05-0.1$ days, so they could be very important for the tidal evolution of sdBs in $\sim 0.1 - 0.2$ day orbits. Future works should investigate how these modes will behave under tidal excitation.

The above analysis also explains the discrepancies between the tidal synchronization period we calculated and those estimated by [60], who applied Zahn's traveling wave limit. The synchronization periods we found for the 0.47 $M_\odot$ canonical sdB model are longer than the periods from their work, which means the tidal torque in our cases is stronger. This might be because [60] used an sdB model with only $10^{-4}\,M_\odot$ hydrogen left, whose radius is smaller than our model. Hence, even though the gravity waves are more damped with Zahn's traveling wave limit in their models, the tidal torque can still be weaker due to its strong dependence on the stellar radius.

Resonance Locking

In binary systems, if the tidal torque consists of many resonance peaks from individual modes, a process called resonance locking may occur [81, 82]. In this scenario, the forcing frequency of the binary enters a resonance with one of the oscillation modes α, and stays as

$$\omega_{\rm f} \equiv m(\Omega_{\rm orb} - \Omega_{\rm spin}) \simeq \omega_\alpha \tag{5.14}$$

throughout the binary lifetime. As ω_α evolves on its own timescale which is independent of the binary separation, this scenario may result in very different binary evolution history compared to other tidal theories.

To see whether resonance locking can happen for sdB binaries, we write the evolution of forcing frequency as

$$\dot{\omega}_{\rm f} = m\left(\frac{3(\tau_{\rm tide} + \tau_{\rm GW})}{I_{\rm orb}} - \frac{\tau_{\rm tide}}{I_{\rm spin}}\right), \tag{5.15}$$

where we substitute Equations 5.3, 5.4, 5.6 and 5.7, and neglect the $\dot{I}_{\rm spin}$ term as the stellar structure and moment of inertia only changes slowly during the evolution. To maintain a resonance lock, we must have $\dot{\omega}_{\rm f} = \dot{\omega}_\alpha$. For helium-burning subdwarfs, their g-mode frequency increases over time, hence the necessary (but not sufficient) condition for resonance locking to occur is $\dot{\omega}_{\rm f} > 0$, or

$$1 + \frac{\tau_{\rm GW}}{\tau_{\rm tide}} > \frac{I_{\rm orb}}{3I_{\rm spin}}\,. \tag{5.16}$$

For binaries of order-of-unity mass ratios, $I_{\rm orb} = \mu a^2 \sim M_1 a^2 \gg M_1 R_1^2 > I_{\rm spin}$. The above relation hence never holds for realistic sdB binaries, unless $\tau_{\rm GW} \gg \tau_{\rm tide}$. This can happen either for already close-to-synchronization binaries or wide binaries, where $\tau_{\rm tide}$ becomes very small in both cases. In the former case, the low-frequency oscillating g-modes that contribute most to the tidal torque should be very efficiently damped (see Section 5.4), which prevents resonance peaks from forming. In the latter case, tidal evolution is not important, because it would occur on a gravitational wave inspiral time which is very long for wide binaries. We hence do not expect resonance locking to happen for sdB binaries, which is confirmed with our numerical spin–orbit evolution calculations.

Differential Rotation

As we expect very efficient angular momentum transport inside the sdBs, we assume they are rigidly rotating in our spin–orbit evolution calculations. Observationally, asteroseismology can measure the internal rotation of stars via frequency splittings of g-mode and p-mode oscillations [1]. Since g-modes mainly probe the deeper region of the star, while p-modes probe the outer layers, a difference between the rotational rates derived from their frequency splittings may suggest the level of differential rotation between the stellar core and the outer layers.

With *Kepler*/K2, there have now been a handful of pulsating sdBs with both p-mode and g-mode frequency splitting measured. [35] reports that for the sdB+WD system KIC 11558725, the rotational rate derived from p-mode splitting is $P_{\mathrm{p}} = 40.2 \pm 0.3$ days, while the rate from g-mode splitting is found to be $P_{\mathrm{g}} = 45.1 \pm 7.8$ days, showing that KIC 11559725 is roughly rigidly-rotating. Similar results are found for for sdBs EPIC 220422705 ([44]; where $P_{\mathrm{p}} \sim 29$ days and $P_{\mathrm{g}} \sim 32$ days) and PG 0101+039 ([45]; where $P_{\mathrm{p}} = 8.60 \pm 0.16$ days and $P_{\mathrm{g}} = 8.81 \pm 0.06$ days). We note that the slightly faster rotation rates measured from p-mode splitting for these systems are consistent with our tidal spin-up picture with dissipating gravity waves: as gravity waves mostly dissipate in the outer envelopes of the star (Figure 5.1), they exert local tidal force mostly in the these regions, and angular momentum is subsequently transported inwards.

However, the above systems all have slow rotation rates compared to the typical rotational periods ($P_{\mathrm{rot}} \lesssim 0.3$ d) of tidal synchronization calculated from our models. This means the tidal torque should be weak for these systems. We pay particular attention to one system V1405 Ori (also EPIC 246683636 or KUV 04421+1416), which is an sdB+dM binary with an orbital period of 0.498 days [61]. [62] obtained the p-mode and g-mode splitting from K2 observations, and determined a p-mode derived rotation rate of 0.555 ± 0.029 days and (marginally) a g-mode derived rotation rate of 4.2 ± 0.4 days. If the P_{g} measurements are reliable, this appears to be an sdB with substantial differential rotation, whose envelope is almost synchronized while the interior is not. This means for strong tidal torques acting in the sdB outer envelope, the assumption of rigid rotation might break down. As the stellar core, which carries most of the stellar mass and moment of inertia, is weakly coupled to the envelope in this case, our calculated tidal synchronization orbital period might be shorter than that needed to synchronize the envelope.

While the current sample is limited, we expect further observations with TESS can provide us more sdB pulsators with differential rotation measured [5, 4, 75]. It is beyond the scope of this work to develop methods for the spin–orbit evolution of differentially rotating sdB models, but we comment that it might be a crucial factor to understand sdB tidal spin-up.

Implications for Rotation Periods of CO WDs

Rotating sdBs can potentially form rapidly rotating carbon–oxygen (CO) white dwarfs after their nuclear burning stops. If the spin angular momentum is conserved after the core-helium-burning phase, the rotation periods of CO WDs are then given by:

$$P_{\mathrm{rot,\,WD}} = \frac{I_{\mathrm{WD}}}{I_{\mathrm{sdB,\,end}}} P_{\mathrm{rot,\,end}}\,, \tag{5.17}$$

where $I_{\mathrm{sdB,\,end}}$ and $P_{\mathrm{rot,\,end}}$ are the the moment of inertia and the rotation period of the sdB at the end of its helium-burning phase (defined by the time when the central helium fraction drops below 1%), and I_{WD} is the moment of inertia of the CO WD. Evolving our $0.47\,M_{\odot}$ sdB model until it forms a CO WD, we find that the stellar moment of inertia decreases from $I_{\mathrm{sdB,\,end}} = 3\times10^{51}\ \mathrm{g\,cm^2}$ to $I_{\mathrm{WD}} = 1.8\times10^{50}\ \mathrm{g\,cm^2}$ in 50 Myrs, due to the shrinking of the star after nuclear burning stops.

Since tidal synchronization occurs at orbital periods less than ≈ 0.2 d, rapidly rotating CO WDs formed from tidally synchronized sdBs should have $P_{\mathrm{rot,\,WD}} \lesssim (1.8\times10^{50}/3\times10^{51})\times0.2\,\mathrm{d} \approx 17\,\mathrm{min}$. At orbital periods $P_{\mathrm{orb}} \lesssim 1\,\mathrm{h}$, the gravitational-wave decay timescale becomes less than the sdB lifetime, so the sdB does not form a WD before mass transfer with its companion. This gives a lower-limit of $P_{\mathrm{rot,\,WD}} \gtrsim (1.8\times10^{50}/3\times10^{51})\times1\,\mathrm{h} \approx 4\,\mathrm{min}$ if mass transfer has not occurred. We hence crudely estimate that rapidly rotating CO WDs formed from synchronized sdB stars can have rotation periods between 4 to 17 minutes. This corresponds to rotation rates roughly a hundred times larger than ordinary WDs.

In the above analysis, we ignored any tidal torques after the core-helium-burning phase. Since the star can rotate much faster than the orbit as it contracts, tidal dissipation may spin it back down, producing longer rotation periods than those listed above. Future works should investigate this scenario to have more realistic estimates of the rotation rates of CO WDs originating from sdB binaries. Nonetheless, future observations of rapidly rotating CO WDs in close binaries may indicate that they were tidally spun up during a sdB phase of evolution.

Limitations with the Mode Decomposition Method

Throughout this work, we calculate the total tidal torque by expanding it into a summation of tidal torques from individual oscillation modes (Equation 5.2). [72] recently pointed out a potential issue with this "mode decomposition" method. They found that the magnitude of off-resonance torques could be different from the magnitude calculated from direct solving of fluid equations under the same tidal potential. [15] further shows that the discrepancy might be caused by the fact that non-adiabatic mode solutions generally do not form a complete and orthogonal basis for the torque expansion. However, the correction they introduced for viscous damping cannot directly apply to the radiative dissipation of tidally excited g-modes.

Nevertheless, when tidal torques are dominated by resonant modes, the correction to the tidal torque magnitude is likely only significant when the tidal forcing frequency is off-resonance [72]. As the torques at these frequencies are typically orders of magnitude weaker than the on-resonance case (see Figure 5.2), we do not expect them to dominate the tidal evolution. Our results should still be valid as long as most tidal-spin up is caused by on-resonance torques.

When the tidal forcing is on resonance with one of the oscillation modes, the mode amplitude becomes so large that it can trigger nonlinear wave dissipation. In this scenario, the oscillation mode excites a number of nearby daughter and granddaughter modes, and the overall damping rate by this sea of coupled modes could be much larger than the radiative damping of individual modes [6, 80].

There are no theoretical works on estimating this nonlinear dissipation on core helium burning stars (except for some toy models, see, e.g., [43]). Nevertheless, because our calculated tidal synchronization periods match observed trends fairly well, we suspect nonlinear dissipation does not greatly increase mode damping rates. Future works should look into the nonlinear effects and their potential influence on sdB tidal spin-up.

Other Caveats

There are some other caveats with our methods. We calculate the oscillation modes based on pre-calculated non-rotating stellar models. As the star gets significant spin-up, the modes may start to behave differently. This matters the most when $\Omega_{\rm spin}$ becomes comparable with ω_α. As the the mode contributing mostly to the tidal torque is the one with $\omega_\alpha \approx \omega_{\rm f} \equiv m(\Omega_{\rm orb} - \Omega_{\rm spin})$, the rotational effects on mode solutions could be significant when $\omega_\alpha \sim \Omega_{\rm orb} \sim \Omega_{\rm spin}$, i.e., when the system is close to synchronization. However, the tidal torque becomes negligible when the system is synchronized, so we do not expect these rotational effects to change our results much.

We set the initial orbital periods of our binary systems as a unified $P_{\mathrm{orb}} = 60$ days, while in reality close-in sdB binaries can be born from two separate channels, namely a prior mass-transfer phase, or a common-envelope ejection. In general, sdB binaries born from these channels could have different initial spin periods, but the detailed outcome of these processes is highly uncertain. Nevertheless, we comment that, as long as tides are responsible for most of the sdB angular momentum for synchronized systems, our calculations should be insensitive to the initial orbital setup.

We did not include mass-transfer in the sdB evolution phase, even though it could happen for sdB binaries born at orbital periods less than 2−3 hours [7]. Mass-transfer may remove the sdB outer hydrogen envelope, and hence changes the strength of the tides (see discussion in Section 5.3). However, we suspect tidal synchronization will remain efficient for these stars since they fill their Roche lobes.

5.6 Conclusion

In this manuscript, we investigated the tidal spin-up of close-in subdwarf B (sdB) binaries. We considered the dissipation of tidally excited gravity waves in the envelopes of sdB stars, and calculated the tidal torques by directly computing the amplitudes of tidally driven oscillation modes in sdB stellar models. We integrated the coupled spin-orbit evolution of these binaries and calculated the resulting sdB rotation rates.

We showed that in contrast to the usual assumption that gravity waves are efficiently damped near the surface ("Zahn's traveling wave limit"), these waves can actually be less damped, and can reflect back to form standing waves in the radiative envelope of sdB stars. The resulting tidal torque is then significantly less than Zahn's theory predicted, and has a complicated resonant dependence on the frequency of the tidal force. At longer periods, the waves are more highly damped and the tidal torque approaches Zahn's limit.

For binaries containing a $0.47\,M_{\odot}$ canonical sdB, our models predict the system will be tidally synchronized if the orbit is less than ~ 0.2 days. For those with a $0.37\,M_{\odot}$ low-mass sdB, this tidal synchronization period becomes ~ 0.15 days. These values are very similar to the observed spin rates of sdB binaries (Figure 5.3), which are tidally synchronized at orbital periods less than ~ 0.2 days. The tidal synchronization timescale has weak dependence on the companion star mass, and is mostly determined by the orbital period.

We investigated how the amount of hydrogen in the sdB envelope could affect the strength of the tidal torque. Since sdBs with more hydrogen have larger radii, and the tidal torque magnitude could scale with the stellar radius as $\tau \propto R^6$, tidal torques may be stronger for stars with more hydrogen. However, the existence of unstable oscillations for our sdB models with thicker hydrogen envelopes complicate the calculation of tidal torques.

When tidally synchronized sdBs evolve into carbon–oxygen white dwarfs, we estimate their rotation periods to be between 4 to 17 minutes (if tidal effects after the core-helium-burning phase can be neglected), which corresponds to spin rates roughy a hundred times faster than typical white dwarfs. We pointed out that resonance locking cannot happen in the tidal spin-up phase of sdB binaries, and discussed the limitations of our mode decomposition method to calculate tidal torques. Differential rotation and rotational effects on oscillation may also be important. Future works should investigate the above scenarios, and compare to growing numbers of rotation rate measurements for sdBs in close binaries.

The agreement between our models and measurements for sdB binaries is very encouraging for the prospect of reliable tidal synchronization predictions. In particular, we expect the physics of tidal spin-up in sdBs to be very similar to that of more massive helium stars in close binaries [43], which are progenitors of gravitational wave sources and exotic supernovae. We believe the results of this paper increase the credibility of predictions for black hole spins presented in that work.

Acknowledgements

We thank Holly Preece for constructive comments on the manuscript. We thank Evan Bauer, Ylva Götberg, Rich Townsend, Emily Hu, Peter Scherbak, Reed Essick and Yuri Levin for helpful discussions. This work is partially supported by NASA through grant 20-XRP20 2-0147. L.M. is thankful for the Max Planck Institute for Astrophysics, where the 2023 Kavli Summer Program was hosted and many of the above discussions took place.

5.7 Appendix: Fixing MESA Profiles

To calculate the tidal response, we solve for internal stellar oscillations with the GYRE stellar oscillation code [73, 71, 27]. The code reads stellar snapshots from MESA as unperturbed background profiles of density, pressure, etc., and then solves the linear perturbation equations of stellar oscillations. The oscillation equations GYRE aims to solve are simplified by assuming hydrostatic equilibrium and mass conservation of the background stellar profile, hence the MESA snapshots provided to GYRE should satisfy the following equations:

$$\frac{dP}{dr} = -\rho g \,, \tag{5.18}$$

$$\frac{dM_r}{dr} = 4\pi r^2 \rho \,, \tag{5.19}$$

where P, ρ, M_r and $g = GM_r/r^2$ are the pressure, density, enclosed mass and gravity inside the star. Further, the Brunt-Väisälä frequency profile inside the stellar model should also satisfy the following equation by definition:

$$N^2 \equiv g\left(\frac{1}{\Gamma_1}\frac{d\ln P}{dr} - \frac{d\ln\rho}{dr}\right) = g\left(-\frac{g}{c_{\rm s}^2} - \frac{d\ln\rho}{dr}\right), \tag{5.20}$$

where we made use of $c_{\rm s}^2 \equiv \Gamma_1 P/\rho$. We rewrite the above equation into the following form:

$$\frac{d\ln\rho}{dr} = -\frac{N^2}{g} - \frac{g}{c_{\rm s}^2} \,, \tag{5.21}$$

and plot the ratios between the LHS and RHS of Equations 5.18, 5.19 and 5.21 for one of our MESA stellar snapshots in the upper panels of Figure 5.6. While they should all be unity, we notice that in the original MESA profile, the ratio between the LHS and RHS for equation 5.21 departs significantly from 1 at the density discontinuity near the convective core boundary at $0.025\,R_\odot$. In the radiative envelope, this ratio also departs from unity by a few percent at some radii. The GYRE oscillation solutions solved by assuming Equation 5.21 are hence problematic. In practice, we find that this inconsistency often causes the mode solutions to change drastically between successive MESA snapshots, while in principle we expect them to vary gradually as the modes evolve.

We hence need to fix the stellar profiles provided by MESA to get correct oscillation solutions. As g mode oscillations are most sensitive to the Brunt-Väisälä frequency profile, we aim to keep the value of N as output by MESA, and adjust the density and pressure profiles to satisfy Equations 5.18, 5.19 and 5.21. Hence, we rewrite

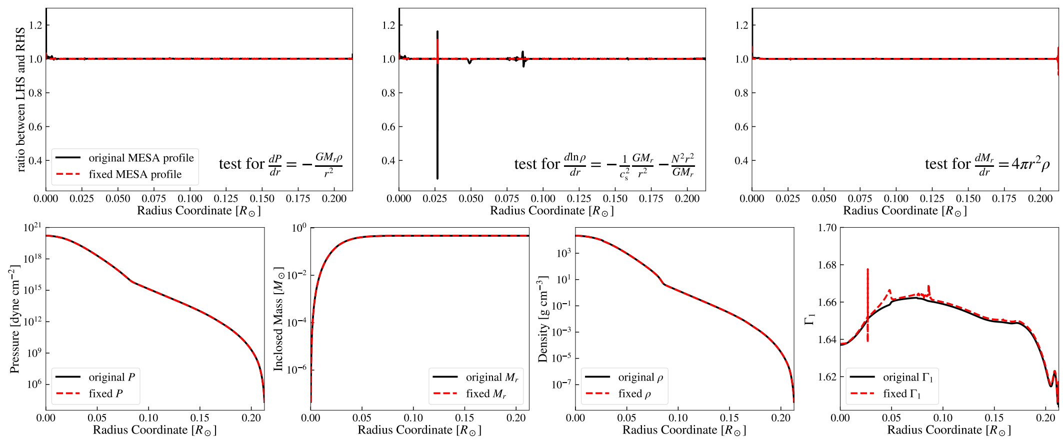

Figure 5.6: **Upper**: The ratios between the LHS and RHS of Equations 5.18, 5.19 and 5.21 for an example MESA snapshot, which should all be unity. We see that in the original stellar profile calculated from MESA, Equation 5.21 is sometimes not satisfied, with the largest discrepancy happening at the convective core boundary with a density discontinuity. We fix the P, M_r and ρ profiles by the method described in Appendix 5.7, and the fixed profiles satisfy Equation 5.21 better. **Lower**: The original and fixed P, M_r, ρ and Γ_1 profiles of the example MESA snapshot. The pressure, density and enclosed mass are almost identical to original MESA profiles, so the change of stellar structure after the fixing process is negligible. Γ_1 is different by a small amount in some regions of the star, which means that the energy processes in the fixed stellar model are in general not consistent.

these equations into the following matrix form:

$$\frac{d}{dr}\begin{bmatrix} P \\ \ln\rho \\ M_r \end{bmatrix} = \begin{bmatrix} -\dfrac{GM_r\rho}{r^2} \\ -\dfrac{N^2r^2}{GM_r} - \dfrac{GM_r}{r^2c_{\mathrm{s}}^2} \\ 4\pi r^2\rho \end{bmatrix} . \tag{5.22}$$

The equations then become a first order ordinary differential equation of the form $d\mathbf{y}/dr = f(\mathbf{y}, r; N^2, c_{\mathrm{s}}^2)$ where $\mathbf{y}(r) = [P(r), \ln\rho(r), M_r(r)]$ is an unknown function to be solved numerically, and N^2 and c_{s}^2 are the ODE parameters that can be fitted from the original stellar profile. To solve for $\mathbf{y}$, we need a set of boundary conditions for P, ρ and M_r, which is naturally given by the following physical requirements:

$$P(R_{\mathrm{star}}) = P_{\mathrm{original}}(R_{\mathrm{star}}) \quad \text{(original surface pressure)}\,; \tag{5.23}$$

$$\rho(0) = \rho_{\mathrm{original}}(0) \quad \text{(original central density)}\,; \tag{5.24}$$

$$M_r(0) = 0 \quad \text{(vanishing central enclosed mass)}\,. \tag{5.25}$$

We note that, however, the above boundary conditions can not be directly used by numerical solvers, as there exists a coordinate divergence at $r = 0$ for $f(\mathbf{y}, r; N^2, c_\mathrm{s}^2)$, as seen from Equation 5.22. Nevertheless, for sufficiently small $\epsilon > 0$, we can expand ρ and M_r at $r = \epsilon$ to the leading order:

$$\rho(\epsilon) \approx \rho(0) + \left(\frac{d\rho}{dr}\right)_{r=0} \epsilon \approx \rho(0)\,, \tag{5.26}$$

$$M_r(\epsilon) \approx M_r(0) + \left(\frac{dM_r}{dr}\right)_{r=0} \epsilon + \left(\frac{d^2 M_r}{dr^2}\right)_{r=0} \frac{\epsilon^2}{2} + \left(\frac{d^3 M_r}{dr^3}\right)_{r=0} \frac{\epsilon^3}{6} = \frac{4\pi\rho(0)}{3}\epsilon^3\,, \tag{5.27}$$

$$\tag{5.28}$$

where we made use of Equation 5.19 to calculate $d^3 M_r/dr^3$. This means Equation 5.22 can be solved on the interval $\epsilon \leq r \leq R_\mathrm{star}$ with the following boundary conditions:

$$P(R_\mathrm{star}) = P_\mathrm{original}(R_\mathrm{star})\,; \tag{5.29}$$

$$\rho(\epsilon) = \rho_\mathrm{original}(0)\,; \tag{5.30}$$

$$M_r(\epsilon) = \frac{4\pi\rho_\mathrm{original}(0)}{3}\epsilon^3\,, \tag{5.31}$$

such that the divergence at $r = 0$ can be avoided. Once the solutions are found, the values at $r = 0$ are acquired by $P(0) = P(\epsilon)$, $\rho(0) = \rho(\epsilon)$ and $M_r(0) = 0$, with Equations 5.26 and 5.27, and the relation $P(\epsilon) \approx P(0)$ by Taylor expansion of P near $r = 0$ to the leading order.

In practice, ϵ should be much smaller than the scale length of P, ρ and M_r, such that the higher-order terms in the expansions can be neglected. This condition is always satisfied for the scales of the spatial resolution in a valid stellar model. Therefore, we choose ϵ to be the spatial coordinate of the innermost grid in the MESA model, and we can then solve for Equation 5.22 with the boundary conditions described by Equations 5.29, 5.30 and 5.31.

We use the `integrate.solve_bvp` function in the SciPy python package [79] to solve for the fixed P, M_r and ρ profiles, using the original MESA profiles as our initial guess. We show the comparison between our fixed and original MESA profiles in Figure 5.6. The fixed P, M_r and ρ profiles are almost identical to the original density profile, but they more accurately satisfy Equation 5.21 in the radiative envelope. While there is still some inconsistency at the convective core boundary due to the density discontinuity, it is likely unimportant as gravity waves are evanescent in the convective core.

We note that, as the adiabatic index $\Gamma_1 \equiv \rho c_s^2/P$ is now calculated from the fixed P and ρ and the original sound speed profile, it can be different from the original Γ_1 by a small amount inside the star. Physically, this means the energy transport processes in this fixed stellar profile may not be consistent with its hydrostatic structure, and future works should investigate a more self-consistent way to deal with this problem. Nevertheless, we find that, after fixing the MESA profiles, GYRE is able to get oscillation solutions that vary gradually across nearby MESA snapshots.

References

[1] Conny Aerts, Jørgen Christensen-Dalsgaard, and Donald W. Kurtz. *Asteroseismology*. Springer, 2010. DOI: 10.1007/978-1-4020-5803-5.

[2] A. S. Baran et al. "A subsynchronously rotating pulsating subdwarf B star in a short-period binary with a white dwarf companion". In: *Astronomy & Astrophysics* 585, A66 (Jan. 2016), A66. DOI: 10.1051/0004-6361/201527182.

[3] A. S. Baran et al. "K2 observations of the sdBV + dM/bd binaries PHL 457 and EQ Psc". In: *Monthly Notices of the Royal Astronomical Society* 489.2 (Oct. 2019), pp. 1556–1571. DOI: 10.1093/mnras/stz2209.

[4] A. S. Baran et al. "Short-period pulsating hot-subdwarf stars observed by TESS II. Northern ecliptic hemisphere". In: *arXiv e-prints*, arXiv:2403.02384 (Mar. 2024), arXiv:2403.02384. DOI: 10.48550/arXiv.2403.02384. arXiv: 2403.02384 [astro-ph.SR].

[5] A. S. Baran et al. "Short-period pulsating hot-subdwarf stars observed by TESS. I. Southern ecliptic hemisphere". In: *Astronomy & Astrophysics* 669, A48 (Jan. 2023), A48. DOI: 10.1051/0004-6361/202244888. arXiv: 2211.09137 [astro-ph.SR].

[6] Adrian J. Barker and Gordon I. Ogilvie. "Stability analysis of a tidally excited internal gravity wave near the centre of a solar-type star". In: *Monthly Notices of the Royal Astronomical Society* 417.1 (Oct. 2011), pp. 745–761. DOI: 10.1111/j.1365-2966.2011.19322.x. arXiv: 1106.5001 [astro-ph.EP].

[7] Evan B. Bauer and Thomas Kupfer. "Phases of Mass Transfer from Hot Subdwarfs to White Dwarf Companions and Their Photometric Properties". In: *The Astrophysical Journal* 922.2, 245 (Dec. 2021), p. 245. DOI: 10.3847/1538-4357/ac25f0. arXiv: 2106.13297 [astro-ph.SR].

[8] D. Bossini et al. “Kepler red-clump stars in the field and in open clusters: constraints on core mixing”. In: *Monthly Notices of the Royal Astronomical Society* 469.4 (Aug. 2017), pp. 4718–4725. DOI: 10.1093/mnras/stx1135. arXiv: 1705.03077 [astro-ph.GA].

[9] S. Charpinet et al. “A Driving Mechanism for the Newly Discovered Class of Pulsating Subdwarf B Stars”. In: *The Astrophysical Journal Letters* 483.2 (July 1997), pp. L123–L126. DOI: 10.1086/310741.

[10] S. Charpinet et al. “Testing the forward modeling approach in asteroseismology. II. Structure and internal dynamics of the hot B subdwarf component in the close eclipsing binary system PG 1336-018”. In: *Astronomy & Astrophysics* 489.1 (Oct. 2008), pp. 377–394. DOI: 10.1051/0004-6361:200809907.

[11] S. Charpinet et al. “The Potential of Asteroseismology for Hot, Subdwarf B Stars: A New Class of Pulsating Stars?” In: *The Astrophysical Journal Letters* 471 (Nov. 1996), p. L103. DOI: 10.1086/310335. arXiv: astro-ph/9606069 [astro-ph].

[12] Jieun Choi et al. “Mesa Isochrones and Stellar Tracks (MIST). I. Solar-scaled Models”. In: *The Astrophysical Journal* 823.2, 102 (June 2016), p. 102. DOI: 10.3847/0004-637X/823/2/102. arXiv: 1604.08592 [astro-ph.SR].

[13] Thomas Constantino et al. “The treatment of mixing in core helium burning models - I. Implications for asteroseismology”. In: *Monthly Notices of the Royal Astronomical Society* 452.1 (Sept. 2015), pp. 123–145. DOI: 10.1093/mnras/stv1264. arXiv: 1506.01209 [astro-ph.SR].

[14] C. M. Copperwheat et al. “Radial-velocity measurements of subdwarf B stars”. In: *Monthly Notices of the Royal Astronomical Society* 415.2 (Aug. 2011), pp. 1381–1395. DOI: 10.1111/j.1365-2966.2011.18786.x. arXiv: 1103.4745 [astro-ph.SR].

[15] Janosz W. Dewberry and Samantha C. Wu. “On the damping of tidally driven oscillations”. In: *Monthly Notices of the Royal Astronomical Society* 527.2 (Jan. 2024), pp. 2288–2296. DOI: 10.1093/mnras/stad3164. arXiv: 2309.11502 [astro-ph.SR].

[16] H. Drechsel et al. “HS 0705+6700: A new eclipsing sdB binary”. In: *Astronomy & Astrophysics* 379 (Dec. 2001), pp. 893–904. DOI: 10.1051/0004-6361:20011376. arXiv: astro-ph/0110217 [astro-ph].

[17] Peter Eggleton. *Evolutionary Processes in Binary and Multiple Stars*. Cambridge University Press, 2006.

[18] Peter P. Eggleton, Ludmila G. Kiseleva, and Piet Hut. “The Equilibrium Tide Model for Tidal Friction”. In: *The Astrophysical Journal* 499.2 (May 1998), pp. 853–870. DOI: 10.1086/305670. arXiv: astro-ph/9801246 [astro-ph].

[19] Ekrem M. Esmer et al. "Revisiting the analysis of HW Virginis eclipse timing data. I. A frequentist data modeling approach and a dynamical stability analysis". In: *Astronomy & Astrophysics* 648, A85 (Apr. 2021), A85. DOI: 10.1051/0004-6361/202038640. arXiv: 2103.00062 [astro-ph.SR].

[20] G. Fontaine et al. "Observational Asteroseismology of Hot Subdwarf Stars with the Mont4K/Kuiper Combination at the Steward Observatory Mount Bigelow Station". In: *6th Meeting on Hot Subdwarf Stars and Related Objects*. Ed. by V. van Grootel et al. Vol. 481. Astronomical Society of the Pacific Conference Series. Apr. 2014, p. 19. DOI: 10.48550/arXiv.1307.3502. arXiv: 1307.3502 [astro-ph.SR].

[21] J. Fuller. "Heartbeat stars, tidally excited oscillations and resonance locking". In: *Monthly Notices of the Royal Astronomical Society* 472 (Dec. 2017), pp. 1538–1564. DOI: 10.1093/mnras/stx2135. arXiv: 1706.05054 [astro-ph.SR].

[22] Jim Fuller. "Inverse tides in pulsating binary stars". In: *Monthly Notices of the Royal Astronomical Society* 501.1 (Feb. 2021), pp. 483–490. DOI: 10.1093/mnras/staa3636. arXiv: 2011.06613 [astro-ph.SR].

[23] Jim Fuller and Wenbin Lu. "The spins of compact objects born from helium stars in binary systems". In: *Monthly Notices of the Royal Astronomical Society* 511.3 (Apr. 2022), pp. 3951–3964. DOI: 10.1093/mnras/stac317. arXiv: 2201.08407 [astro-ph.HE].

[24] Jim Fuller, Anthony L. Piro, and Adam S. Jermyn. "Slowing the spins of stellar cores". In: *Monthly Notices of the Royal Astronomical Society* 485.3 (May 2019), pp. 3661–3680. DOI: 10.1093/mnras/stz514. arXiv: 1902.08227 [astro-ph.SR].

[25] S. Geier et al. "Hot subdwarf stars in close-up view. I. Rotational properties of subdwarf B stars in close binary systems and nature of their unseen companions". In: *Astronomy & Astrophysics* 519, A25 (Sept. 2010), A25. DOI: 10.1051/0004-6361/201014465. arXiv: 1005.4785 [astro-ph.SR].

[26] S. Geier et al. "The MUCHFUSS project - searching for hot subdwarf binaries with massive unseen companions. Survey, target selection and atmospheric parameters". In: *Astronomy & Astrophysics* 530, A28 (June 2011), A28. DOI: 10.1051/0004-6361/201015316. arXiv: 1103.4045 [astro-ph.SR].

[27] J. Goldstein and R. H. D. Townsend. "The Contour Method: a New Approach to Finding Modes of Nonadiabatic Stellar Pulsations". In: *The Astrophysical Journal* 899.2, 116 (Aug. 2020), p. 116. DOI: 10.3847/1538-4357/aba748. arXiv: 2006.13223 [astro-ph.SR].

[28] Y. Götberg et al. "Spectral models for binary products: Unifying subdwarfs and Wolf-Rayet stars as a sequence of stripped-envelope stars". In: *Astron-*

omy & Astrophysics 615, A78 (July 2018), A78. DOI: 10.1051/0004-6361/201732274. arXiv: 1802.03018 [astro-ph.SR].

[29] Z. Han et al. "The origin of subdwarf B stars - I. The formation channels". In: *Monthly Notices of the Royal Astronomical Society* 336.2 (Oct. 2002), pp. 449–466. DOI: 10.1046/j.1365-8711.2002.05752.x. arXiv: astro-ph/0206130 [astro-ph].

[30] Z. Han et al. "The origin of subdwarf B stars - II". In: *Monthly Notices of the Royal Astronomical Society* 341.2 (May 2003), pp. 669–691. DOI: 10.1046/j.1365-8711.2003.06451.x. arXiv: astro-ph/0301380 [astro-ph].

[31] U. Heber. "Hot Subluminous Stars". In: *Publications of the Astronomical Society of the Pacific* 128.966 (Aug. 2016), p. 082001. DOI: 10.1088/1538-3873/128/966/082001. arXiv: 1604.07749 [astro-ph.SR].

[32] Ulrich Heber. "Hot Subdwarf Stars". In: *Annual Review of Astronomy and Astrophysics* 47.1 (Sept. 2009), pp. 211–251. DOI: 10.1146/annurev-astro-082708-101836.

[33] M. L. Humason and F. Zwicky. "A Search for Faint Blue Stars." In: *The Astrophysical Journal* 105 (Jan. 1947), p. 85. DOI: 10.1086/144884.

[34] Adam S. Jermyn et al. "Modules for Experiments in Stellar Astrophysics (MESA): Time-dependent Convection, Energy Conservation, Automatic Differentiation, and Infrastructure". In: *The Astrophysical Journal Supplement Series* 265.1, 15 (Mar. 2023), p. 15. DOI: 10.3847/1538-4365/acae8d. arXiv: 2208.03651 [astro-ph.SR].

[35] J. W. Kern et al. "Asteroseismic analysis of the pulsating subdwarf B star KIC 11558725: an sdB+WD system with divergent frequency multiplets and mode trapping observed by Kepler". In: *Monthly Notices of the Royal Astronomical Society* 474.4 (Mar. 2018), pp. 4709–4716. DOI: 10.1093/mnras/stx2893.

[36] Matthias U. Kruckow et al. "A Catalog of Potential Post-Common Envelope Binaries". In: *The Astrophysical Journal* 920.2, 86 (Oct. 2021), p. 86. DOI: 10.3847/1538-4357/ac13ac. arXiv: 2107.05221 [astro-ph.SR].

[37] R. P. Kudritzki and K. P. Simon. "Non-LTE analysis of subluminous O-star. The hydrogen-deficient subdwarf O-binary HD 49798." In: *Astronomy & Astrophysics* 70 (Nov. 1978), pp. 653–663.

[38] T. Kupfer et al. "Hot subdwarf binaries from the MUCHFUSS project. Analysis of 12 new systems and a study of the short-period binary population". In: *Astronomy & Astrophysics* 576, A44 (Apr. 2015), A44. DOI: 10.1051/0004-6361/201425213. arXiv: 1501.03692 [astro-ph.SR].

[39] Thomas Kupfer et al. "A New Class of Roche Lobe-filling Hot Subdwarf Binaries". In: *The Astrophysical Journal Letters* 898.1, L25 (July 2020), p. L25. DOI: 10.3847/2041-8213/aba3c2. arXiv: 2007.05349 [astro-ph.SR].

[40] Thomas Kupfer et al. "PTF1 J082340.04+081936.5: A Hot Subdwarf B Star with a Low-mass White Dwarf Companion in an 87-minute Orbit". In: *The Astrophysical Journal* 835.2, 131 (Feb. 2017), p. 131. DOI: 10.3847/1538-4357/835/2/131. arXiv: 1612.02019 [astro-ph.SR].

[41] Thomas Kupfer et al. "The First Ultracompact Roche Lobe-Filling Hot Subdwarf Binary". In: *The Astrophysical Journal* 891.1, 45 (Mar. 2020), p. 45. DOI: 10.3847/1538-4357/ab72ff. arXiv: 2002.01485 [astro-ph.SR].

[42] Doron Kushnir et al. "Dynamical tides reexpressed". In: *Monthly Notices of the Royal Astronomical Society* 467.2 (May 2017), pp. 2146–2149. DOI: 10.1093/mnras/stx255. arXiv: 1605.03810 [astro-ph.SR].

[43] Linhao Ma and Jim Fuller. "Tidal Spin-up of Black Hole Progenitor Stars". In: *The Astrophysical Journal* 952.1, 53 (July 2023), p. 53. DOI: 10.3847/1538-4357/acdb74. arXiv: 2305.08356 [astro-ph.HE].

[44] X. -Y Ma et al. "K2 Photometry on Oscillation Mode Variability: The New Pulsating Hot B Subdwarf Star EPIC 220422705". In: *The Astrophysical Journal* 933.2, 211 (July 2022), p. 211. DOI: 10.3847/1538-4357/ac75b8. arXiv: 2206.01887 [astro-ph.SR].

[45] X. -Y. Ma et al. "Amplitude and frequency variations in PG 0101+039 from K2 photometry. A pulsating hot B subdwarf star in an unsynchronized binary system". In: *Astronomy & Astrophysics* 680, A11 (Dec. 2023), A11. DOI: 10.1051/0004-6361/202347410. arXiv: 2309.11532 [astro-ph.SR].

[46] P. F. L. Maxted et al. "The binary fraction of extreme horizontal branch stars". In: *Monthly Notices of the Royal Astronomical Society* 326.4 (Oct. 2001), pp. 1391–1402. DOI: 10.1111/j.1365-2966.2001.04714.x. arXiv: astro-ph/0103342 [astro-ph].

[47] B. Mosser et al. "Spin down of the core rotation in red giants". In: *Astronomy & Astrophysics* 548, A10 (Dec. 2012), A10. DOI: 10.1051/0004-6361/201220106. arXiv: 1209.3336 [astro-ph.SR].

[48] R. Napiwotzki et al. "Close binary EHB stars from SPY". In: *Astrophysics and Space Science* 291.3 (June 2004), pp. 321–328. DOI: 10.1023/B:ASTR.0000044362.07416.6c. arXiv: astro-ph/0401201 [astro-ph].

[49] Anthony Noll, Sarbani Basu, and Saskia Hekker. "Effect of nuclear reactions rates and core boundary mixing on the seismology of red clump stars". In: *arXiv e-prints*, arXiv:2401.05519 (Jan. 2024), arXiv:2401.05519. DOI: 10.48550/arXiv.2401.05519. arXiv: 2401.05519 [astro-ph.SR].

[50] Herbert Pablo et al. "Seismic evidence for non-synchronization in two close sdb+dM binaries from Kepler photometry". In: *Monthly Notices of the Royal Astronomical Society* 422.2 (May 2012), pp. 1343–1351. DOI: 10.1111/j.1365-2966.2012.20707.x. arXiv: 1202.3649 [astro-ph.SR].

[51] B. Paxton et al. "Modules for Experiments in Stellar Astrophysics (MESA)". In: *The Astrophysical Journal Supplement Series* 192, 3 (Jan. 2011), p. 3. DOI: 10.1088/0067-0049/192/1/3. arXiv: 1009.1622 [astro-ph.SR].

[52] B. Paxton et al. "Modules for Experiments in Stellar Astrophysics (MESA): Binaries, Pulsations, and Explosions". In: *The Astrophysical Journal Supplement Series* 220, 15 (Sept. 2015), p. 15. DOI: 10.1088/0067-0049/220/1/15. arXiv: 1506.03146 [astro-ph.SR].

[53] B. Paxton et al. "Modules for Experiments in Stellar Astrophysics (MESA): Planets, Oscillations, Rotation, and Massive Stars". In: *The Astrophysical Journal Supplement Series* 208, 4 (Sept. 2013), p. 4. DOI: 10.1088/0067-0049/208/1/4. arXiv: 1301.0319 [astro-ph.SR].

[54] Bill Paxton et al. "Modules for Experiments in Stellar Astrophysics (MESA): Convective Boundaries, Element Diffusion, and Massive Star Explosions". In: *The Astrophysical Journal Supplement Series* 234.2, 34 (Feb. 2018), p. 34. DOI: 10.3847/1538-4365/aaa5a8. arXiv: 1710.08424 [astro-ph.SR].

[55] Bill Paxton et al. "Modules for Experiments in Stellar Astrophysics (MESA): Pulsating Variable Stars, Rotation, Convective Boundaries, and Energy Conservation". In: *The Astrophysical Journal Supplement Series* 243.1, 10 (July 2019), p. 10. DOI: 10.3847/1538-4365/ab2241. arXiv: 1903.01426 [astro-ph.SR].

[56] Ingrid Pelisoli et al. "A hot subdwarf-white dwarf super-Chandrasekhar candidate supernova Ia progenitor". In: *Nature Astronomy* 5 (July 2021), pp. 1052–1061. DOI: 10.1038/s41550-021-01413-0. arXiv: 2107.09074 [astro-ph.SR].

[57] Ingrid Pelisoli et al. "Alone but not lonely: Observational evidence that binary interaction is always required to form hot subdwarf stars". In: *Astronomy & Astrophysics* 642, A180 (Oct. 2020), A180. DOI: 10.1051/0004-6361/202038473. arXiv: 2008.07522 [astro-ph.SR].

[58] P. C. Peters. "Gravitational Radiation and the Motion of Two Point Masses". In: *Physical Review* 136.4B (Nov. 1964), pp. 1224–1232. DOI: 10.1103/PhysRev.136.B1224.

[59] Holly P. Preece, Christopher A. Tout, and C. Simon Jeffery. "Convection physics and tidal synchronization of the subdwarf binary NY Virginis". In: *Monthly Notices of the Royal Astronomical Society* 485.2 (May 2019),

pp. 2889–2894. DOI: 10.1093/mnras/stz547. arXiv: 1903.06176 [astro-ph.SR].

[60] Holly P. Preece, Christopher A. Tout, and C. Simon Jeffery. "Tidal Interactions of Close Hot Subdwarf Binaries". In: *Monthly Notices of the Royal Astronomical Society* 481.1 (Nov. 2018), pp. 715–726. DOI: 10.1093/mnras/sty2091. arXiv: 1808.00945 [astro-ph.SR].

[61] M. D. Reed et al. "An EC 14026 pulsator in a reflection binary". In: *Astrophysics and Space Science* 329.1-2 (Oct. 2010), pp. 83–86. DOI: 10.1007/s10509-010-0323-0.

[62] M. D. Reed et al. "K2 observations of the pulsating subdwarf B stars UY Sex and V1405 Ori". In: *Monthly Notices of the Royal Astronomical Society* 492.4 (Mar. 2020), pp. 5202–5217. DOI: 10.1093/mnras/staa144.

[63] S. Sanjayan et al. "Pulsating subdwarf B stars in the oldest open cluster NGC 6791". In: *Monthly Notices of the Royal Astronomical Society* 509.1 (Jan. 2022), pp. 763–777. DOI: 10.1093/mnras/stab2985. arXiv: 2111.09873 [astro-ph.SR].

[64] V. Schaffenroth et al. "A quantitative in-depth analysis of the prototype sdB+BD system SDSS J08205+0008 revisited in the Gaia era". In: *Monthly Notices of the Royal Astronomical Society* 501.3 (Mar. 2021), pp. 3847–3870. DOI: 10.1093/mnras/staa3661. arXiv: 2011.10013 [astro-ph.SR].

[65] V. Schaffenroth et al. "Binaries discovered by the MUCHFUSS project. SDSS J162256.66+473051.1: An eclipsing subdwarf B binary with a brown dwarf companion". In: *Astronomy & Astrophysics* 564, A98 (Apr. 2014), A98. DOI: 10.1051/0004-6361/201423377. arXiv: 1402.5263 [astro-ph.SR].

[66] V. Schaffenroth et al. "Hot subdwarfs in close binaries observed from space. I. Orbital, atmospheric, and absolute parameters, and the nature of their companions". In: *Astronomy & Astrophysics* 666, A182 (Oct. 2022), A182. DOI: 10.1051/0004-6361/202244214. arXiv: 2207.02001 [astro-ph.SR].

[67] Peter Scherbak and Jim Fuller. "Ultra–short-period WD Binaries Are Not Undergoing Strong Tidal Heating". In: *The Astrophysical Journal* 962.2, 185 (Feb. 2024), p. 185. DOI: 10.3847/1538-4357/ad1dd6. arXiv: 2401.14397 [astro-ph.SR].

[68] R. Silvotti et al. "EPIC 216747137: a new HW Vir eclipsing binary with a massive sdOB primary and a low-mass M-dwarf companion". In: *Monthly Notices of the Royal Astronomical Society* 500.2 (Jan. 2021), pp. 2461–2474. DOI: 10.1093/mnras/staa3332. arXiv: 2010.13524 [astro-ph.SR].

[69] Roberto Silvotti et al. “Filling the gap between synchronized and non-synchronized sdBs in short-period sdBV+dM binaries with TESS: TIC 137608661, a new system with a well-defined rotational splitting”. In: *Monthly Notices of the Royal Astronomical Society* 511.2 (Apr. 2022), pp. 2201–2217. DOI: 10.1093/mnras/stac160. arXiv: 2201.06559 [astro-ph.SR].

[70] J. H. Telting et al. “KIC 7668647: a 14 day beaming sdB+WD binary with a pulsating subdwarf”. In: *Astronomy & Astrophysics* 570, A129 (Oct. 2014), A129. DOI: 10.1051/0004-6361/201424169. arXiv: 1409.2345 [astro-ph.SR].

[71] R. H. D. Townsend, J. Goldstein, and E. G. Zweibel. “Angular momentum transport by heat-driven g-modes in slowly pulsating B stars”. In: *Monthly Notices of the Royal Astronomical Society* 475.1 (Mar. 2018), pp. 879–893. DOI: 10.1093/mnras/stx3142. arXiv: 1712.02420 [astro-ph.SR].

[72] R. H. D. Townsend and M. Sun. “Discrepant Approaches to Modeling Stellar Tides and the Blurring of Pseudosynchronization”. In: *The Astrophysical Journal* 953.1, 48 (Aug. 2023), p. 48. DOI: 10.3847/1538-4357/acdd5a. arXiv: 2306.06429 [astro-ph.SR].

[73] R. H. D. Townsend and S. A. Teitler. “GYRE: an open-source stellar oscillation code based on a new Magnus Multiple Shooting scheme”. In: *Monthly Notices of the Royal Astronomical Society* 435.4 (Nov. 2013), pp. 3406–3418. DOI: 10.1093/mnras/stt1533. arXiv: 1308.2965 [astro-ph.SR].

[74] B. Tripathi et al. “Predicting the Slowing of Stellar Differential Rotation by Instability-Driven Turbulence”. In: *arXiv e-prints*, arXiv:2403.07395 (Mar. 2024), arXiv:2403.07395. DOI: 10.48550/arXiv.2403.07395. arXiv: 2403.07395 [astro-ph.SR].

[75] Murat Uzundag et al. “A comprehensive search for hot subdwarf stars using Gaia and TESS I. Pulsating hot subdwarf B stars”. In: *arXiv e-prints*, arXiv:2401.17707 (Jan. 2024), arXiv:2401.17707. DOI: 10.48550/arXiv.2401.17707. arXiv: 2401.17707 [astro-ph.SR].

[76] Vilho Väisälä. “Über die Wirkung der Windschwankungen auf die Pilotbeobachtungen”. In: *Societus Scientiarum Fennica Commentationes Physico-Mathematicae* 2 (Jan. 1925), p. 19.

[77] V. Van Grootel et al. “Asteroseismology in action: a test of spin-orbit synchronism in the close binary system Feige 48”. In: *Astronomy & Astrophysics* 483.3 (June 2008), pp. 875–885. DOI: 10.1051/0004-6361:200809554.

[78] S. Vennes et al. “The Shortest Period sdB Plus White Dwarf Binary CD-30 11223 (GALEX J1411-3053)”. In: *The Astrophysical Journal Letters* 759.1, L25 (Nov. 2012), p. L25. DOI: 10.1088/2041-8205/759/1/L25. arXiv: 1210.1512 [astro-ph.SR].

[79] Pauli Virtanen et al. “SciPy 1.0: Fundamental Algorithms for Scientific Computing in Python”. In: *Nature Methods* 17 (2020), pp. 261–272. DOI: 10.1038/s41592-019-0686-2.

[80] Nevin N. Weinberg et al. “Nonlinear Tides in Close Binary Systems”. In: *The Astrophysical Journal* 751.2, 136 (June 2012), p. 136. DOI: 10.1088/0004-637X/751/2/136. arXiv: 1107.0946 [astro-ph.SR].

[81] M. G. Witte and G. J. Savonije. “Tidal evolution of eccentric orbits in massive binary systems. A study of resonance locking”. In: *Astronomy & Astrophysics* 350 (Oct. 1999), pp. 129–147. DOI: 10.48550/arXiv.astro-ph/9909073. arXiv: astro-ph/9909073 [astro-ph].

[82] M. G. Witte and G. J. Savonije. “Tidal evolution of eccentric orbits in massive binary systems. II. Coupled resonance locking for two rotating main sequence stars”. In: *Astronomy & Astrophysics* 366 (Feb. 2001), pp. 840–857. DOI: 10.1051/0004-6361:20000245.

[83] Maximilian Wolz et al. “Spectroscopic and Photometric Analysis of the HW Vir Star PTF1 J011339.09+225739.1”. In: *Open Astronomy* 27.1 (May 2018), pp. 80–90. DOI: 10.1515/astro-2018-0011.

[84] J. -P. Zahn. “The dynamical tide in close binaries.” In: *Astronomy & Astrophysics* 41 (July 1975), pp. 329–344.

[85] J. -P. Zahn. “Tidal friction in close binary systems.” In: *Astronomy & Astrophysics* 57 (May 1977), pp. 383–394.

[86] X. Zhang, X. Chen, and Z. Han. “The masses of hot subdwarfs”. In: *Astronomy & Astrophysics* 504.3 (Sept. 2009), pp. L13–L16. DOI: 10.1051/0004-6361/200912336. arXiv: 0909.2560 [astro-ph.SR].

Chapter 6

SPINNING BLACK HOLES BORN FROM TIDALLY INTERACTING BINARIES

[1] Linhao Ma and Jim Fuller. "Tidal Spin-up of Black Hole Progenitor Stars". In: *The Astrophysical Journal* 952.1 (2023), p. 53. DOI: 10.3847/1538-4357/acdb74.

Abstract

Gravitational wave observations indicate the existence of merging black holes (BHs) with high spin ($a \gtrsim 0.3$), whose formation pathways are still an open question. A possible way to form those binaries is through the tidal spin-up of a Wolf–Rayet (WR) star by its BH companion. In this work, we investigate this scenario by directly calculating the tidal excitation of oscillation modes in WR star models, determining the tidal spin-up rate, and integrating the coupled spin–orbit evolution for WR–BH binaries. We find that for short-period orbits and massive WR stars, the tidal interaction is mostly contributed by standing gravity modes, in contrast to Zahn's model of travelling waves which is frequently assumed in the literature. The standing modes are less efficiently damped than traveling waves, meaning that prior estimates of tidal spin-up may be overestimated. We show that tidal synchronization is rarely reached in WR–BH binaries, and the resulting BH spins have $a \lesssim 0.4$ for all but the shortest period ($P_{\rm orb} \lesssim 0.5\,{\rm d}$) binaries. Tidal spin-up in lower-mass systems is more efficient, providing an anti-correlation between the mass and spin of the BHs, which could be tested in future gravitational wave data. Nonlinear damping processes are poorly understood but may allow for more efficient tidal spin-up. We also discuss a new class of gravito-thermal modes that appear in our calculations.

6.1 Introduction

The spins of stellar-mass black holes (BHs) are still not fully understood. Most BHs detected from LIGO/Virgo events have low aligned components of their spins [1, 57, 28, 42, 58], which agrees with predictions of efficient angular momentum (AM) transport within the interiors of massive stars. Such processes remove the majority of AM from the stellar core, predicting slowly rotating remnants after core-collapse [16, 25]. These theories are approximately consistent with core-rotation rate measurements of low-mass red giants from asteroseismology [5, 29, 8, 9, 51, 18], with a few discrepancies [11]. Yet, among a small fraction of LIGO/Virgo BHs and a majority of high-mass X-ray binaries [27], high BH spins are measured. Therefore it still remains a theoretical challenge to explain the existence of these rapidly rotating objects (see, e.g. discussions in [39, 6, 12]).

A natural scenario to form high-spin BHs is through binary interactions, as nearly all BHs with spin measurements are found via BH mergers or X-ray binaries. One possible progenitor of BH binaries are Wolf–Rayet–BH binaries. Such a system is formed from an ordinary massive binary system, where the primary collapses to a (likely slowly rotating) BH, and then strips off the envelope of the secondary, making it a Wolf–Rayet (WR) star. Tidal interactions during the WR phase could possibly spin up the latter, forming a rapidly spinning BH. Many studies have investigated this scenario and made predictions for the spins of the second-born BHs [24, 38, 4, 7, 31, 15], finding they can be large for sufficiently close binary systems ($P_{\rm orb} \lesssim 1$ day).

However, in most of these studies, the tidal response of the WR star to the BH companion is not calculated directly. Instead, an effective tidal torque calculated from Zahn's theory of dynamical tides ([55, 56], see also [20]) is often assumed. The basic picture of Zahn's theory is as follows: gravity waves are tidally excited near the convective core-radiative envelope interface inside a star. The waves propagate outwards and damp due to radiative diffusion near the surface of the star. The damping is often so strong that the waves dissipate before reaching the surface and behave as travelling waves rather than standing waves. The energy and AM deposited by the waves can be calculated and translated to an effective tidal torque. While this picture is often assumed in studies of tidally excited waves, it has not been closely examined in binaries involving a WR star.

In this work, we directly solve for oscillation modes of WR stellar models, quantifying their tidal coupling strengths and dissipation rates. We then compute AM transfer rates and model their spin evolution and resulting BH spins, comparing to those from Zahn's theory. The plan of this paper is as follows: in §6.2 we review the basic formalism of dynamical tides for calculating tidal torques based on stellar evolution models, and we summarize the setups of our models of the WR stars; in §6.3 and §6.4 we present our analysis for the tidally excited modes and the stellar spin evolution. We discuss our results in §6.5 and conclude in §6.6.

6.2 Tidal Torques by Dynamical Tides

In classical tidal theory, tides can be decomposed into two components: equilibrium tides and dynamical tides. The former corresponds to the global distortion of the star, while the latter is composed of internal oscillations, which is believed to be a dominant cause of tidal dissipation. From [26], the energy dissipation rate of a tidally forced oscillation mode α excited by the tidal potential of an aligned and circular orbiting secondary is given by

$$\dot{E}_\alpha = \frac{m\omega_\alpha \Omega_{\rm orb}\gamma_\alpha q^2 M_1 R_1^2 |W_{lm} Q_\alpha|^2 \omega_{\rm f}^2}{(\omega_\alpha - \omega_{\rm f})^2 + \gamma_\alpha^2} \left(\frac{R_1}{a}\right)^{2(l+1)}, \tag{6.1}$$

where ω_α and γ_α are the mode frequency and damping rate, and $\omega_{\rm f} = m(\Omega_{\rm orb} - \Omega_{\rm spin})$ is the tidal forcing frequency (measured in the frame co-rotating with the primary), and $\Omega_{\rm spin}$ is the star's angular rotation frequency. M_1 and R_1 are the mass and radius of the primary, $q = M_2/M_1$ is the mass ratio of the secondary to the primary, a and $\Omega_{\rm orb}$ are the semi-major axis and the angular frequency of the orbit. l and m are the mode's angular and azimuthal wave numbers and W_{lm} is an expansion coefficient of the tidal potential. $Q_\alpha \equiv \langle \xi_\alpha | \nabla(r^l Y_{lm}) \rangle / \omega_\alpha^2$ is the dimensionless overlap integral describing the spatial coupling between the mode and the tidal potential, which is calculated by the relation $Q_\alpha = -(2l+1)\delta\Phi_\alpha/(4\pi\omega_\alpha^2)$ [13], where $\delta\Phi_\alpha$ is the surface gravity potential perturbation. The mode angular momentum dissipation rate is related to the energy dissipation by [13]

$$\dot{J}_\alpha = \frac{\dot{E}_\alpha}{\Omega_{\rm orb}}, \tag{6.2}$$

assuming a circular orbit. Hence, by solving for the internal oscillation modes (with ω_α, γ_α and Q_α) inside the primary, we are able to calculate the energy dissipation and tidal spin-up rate, given a companion mass and orbit.

Stellar Models

We built our WR star models with the MESA stellar evolution code [32, 34, 33, 35, 36]. Instead of using the binary options in MESA, we construct our models as follows: we start with a number of zero-age main-sequence (ZAMS) single star models with a variety of masses, summarized in Table 6.1. The stars evolve to core hydrogen depletion before the stripping-off process occurs. We simulate this process by artificially removing the outer hydrogen envelope immediately after hydrogen depletion (defined by the time when the central hydrogen fraction drops below 10^{-5}), producing a helium star as the initial setup for the WR star. We

model	M_{ZAMS}	M_{WR}	Dutch factor	desired Z
1	$15\,M_\odot$	$3\,M_\odot$	0.5	$10^{-2}Z_\odot$
2	$20\,M_\odot$	$5\,M_\odot$	0.5	$10^{-2}Z_\odot$
3	$30\,M_\odot$	$10\,M_\odot$	0.5	$10^{-2}Z_\odot$
4	$45\,M_\odot$	$18\,M_\odot$	0.5	$10^{-2}Z_\odot$
5	$60\,M_\odot$	$27\,M_\odot$	0.5	$10^{-2}Z_\odot$
6	$80\,M_\odot$	$38\,M_\odot$	0.5	$10^{-2}Z_\odot$
7	$100\,M_\odot$	$50\,M_\odot$	0.5	$10^{-2}Z_\odot$
8	$120\,M_\odot$	$62\,M_\odot$	0.5	$10^{-2}Z_\odot$
9	$15\,M_\odot$	$3\,M_\odot$	4.0	$Z_\odot$
10	$20\,M_\odot$	$5\,M_\odot$	4.0	$Z_\odot$
11	$30\,M_\odot$	$10\,M_\odot$	4.0	$Z_\odot$
12	$45\,M_\odot$	$18\,M_\odot$	4.0	$Z_\odot$
13	$60\,M_\odot$	$26\,M_\odot$	3.0	$Z_\odot$
14	$80\,M_\odot$	$38\,M_\odot$	2.0	$Z_\odot$
15	$100\,M_\odot$	$49\,M_\odot$	1.7	$Z_\odot$
16	$120\,M_\odot$	$61\,M_\odot$	1.5	$Z_\odot$

Table 6.1: Parameters of our Wolf–Rayet star models. We fixed the metallicities of all models to $Z = 0.01\,Z\odot$ and adapted their Dutch wind scaling factors to match the mass-loss rates for the desired metallicities. See discussions in the main text.

then restart the evolution until the end of core helium depletion (when the central helium fraction drops below 10^{-5}), and we output the stellar pulsation parameters to be used later for spin-evolution calculations. Example MESA inlists are available on Zenodo under an open-source Creative Commons Attribution license: https://doi.org/10.5281/zenodo.7935443, and the model parameters are summarized in Table 6.1.

During the helium burning phase, we compute the internal oscillations of the models with the GYRE stellar oscillation code [50, 49, 21]. We use the second order Magnus differential scheme to calculate non-adiabatic modes, as it proves to be the most reliable when dealing with low-frequency oscillations. We specify our search to $l = m = 2$ modes since this is the dominant part of the tidal potential in aligned and circular orbits, with the corresponding $W_{22} = \sqrt{3\pi/10}$. Example GYRE inputs are available on Zenodo under an open-source Creative Commons Attribution license: https://doi.org/10.5281/zenodo.7935443. Once we have the mode solutions, we integrate the spin–orbit evolution with Eq. 6.1 and 6.2, summing over all modes. We assume the primary remains rigidly rotating during the evolution, due to the strong AM diffusion inside WR stars [15]. We use our non-rotating mode solutions all along in the integration, as we will see that most systems never get to tidal synchronization, such that the rotational effects can be ignored.

An important process related to the spin–orbit evolution is the large wind mass loss experienced by WR stars (e.g., [44]), which removes AM from both the spin and the orbit. The mass loss rates of high-mass WR stars are somewhat uncertain [44, 52], especially at low-metallicity, hence there are few reliable observed/modelled values to compare with. We simulate the mass loss with the "Dutch" wind scheme [30] in MESA with $\eta = 0.5$ and include its effects in our integration. The mass-loss rate has a strong dependence on the metallicity of the star. However, we find that GYRE was unable to solve the oscillations correctly for some of our massive models at solar metallicity due to MESA's artificial treatment of super-Eddington near-surface layers. We hence used a universal metallicity $Z = 0.01\,Z_\odot$ in all our models so that the stellar structure can be more accurately modeled. Oscillations solved from these models are reasonable approximations since the mode properties are mostly determined by the deep internal structure of the stars which are not strongly dependent on metallicity.

To estimate the evolution and mass loss rates of higher metallicity stars, we increase the wind scaling factor to match the mass-loss rate of an alternative model with the desired metallicity. For instance, to simulate a $10\,M_\odot$ WR star at solar metallicity, we use a wind scaling factor of $\eta = 4$ for our $Z = 0.01\,Z_\odot$ model of the same mass, which produces roughly the same mass loss rate as a $Z = Z_\odot$ model with $\eta = 0.5$. In the following, we will simply reference the models with their desired metallicity, yet the readers should keep in mind that the underlying models actually have $Z = 0.01\,Z_\odot$ and adapted Dutch factors, which are summarized in Table 6.1.

6.3 Mode Morphology

Figure 6.1 shows some example mode eigenfunctions from a $10\,M_\odot$ WR star model at solar metallicity during the helium burning phase. We see that there is a distinction between the high-frequency ($P \lesssim 0.8$ d, green line) and low-frequency ($P \gtrsim 0.8$ d, blue and red lines) modes. For a typical high-frequency mode, the eigenfunction appears to be a standing low-order gravity wave trapped in the radiative envelope of the star. This is in contrast with the [55] model for travelling waves that damp near the stellar surface. When the tidal forcing frequency ω_f becomes close to the frequency of one of these modes, a resonance occurs and the energy/angular momentum dissipation becomes dominated by it (cf. Equation 6.1). The tidal torque

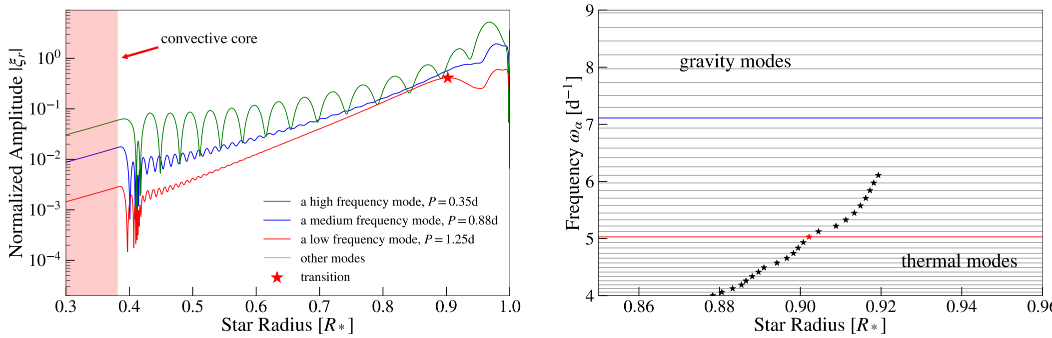

Figure 6.1: **Left**: Example mode eigenfunctions for a $10\,M_\odot$ Wolf–Rayet star model at solar metallicity during helium burning. For high-frequency modes, we see a standing g-mode (green line) excited near the convective core (red region) boundary, in contrast with Zahn's assumption of travelling waves. As the frequency decreases, the modes become travelling gravity waves (blue line), damping near the surface (Zahn's formalism). When the frequency continues to decrease, the modes become mixed modes with a travelling g-mode component and a thermal mode component. The red star marks the transition point, calculated by the local maximum of the eigenfunction. **Right**: A detailed look at the transition points between g-modes and thermal modes (stars). The lines show the frequencies of all modes and the colored lines correspond to the example modes in the left panel. The transition points agree well with the theoretically derived ones where $\omega_\alpha = \omega_{\rm crit}$ (the boundary between two propagation regions, cf. Appendix 6.7). At higher frequency the thermal mode region (shaded) gets narrower and disappears.

contributed by this standing mode is different from Zahn's theory, and we will see in §6.4 that Zahn's results on spin–orbit evolution are significantly altered.

At lower frequency, the modes turn to travelling waves (blue line) as Zahn assumed, since the g-mode dispersion relation indicates an imaginary wave number $\mathrm{Im}(k_r) \propto 1/\omega_\alpha^2$ (see Appendix 6.7), i.e., the spatial evanescence becomes larger at lower frequency. For even lower frequency, the eigenfunction becomes a mixed mode which can be separated into two components: a gravity wave inner region of the radiative envelope, and a thermal wave region in the outer envelope. We show in Appendix 6.7 and 6.7 that the transition occurs around a critical frequency $\omega_{\rm crit} \equiv (4\lambda N^2 \omega_{\rm T})^{1/3}$, where $\omega_T = \kappa/r^2$ is the thermal frequency, and $\kappa = 16\sigma_{\rm B} T^3/(3\rho^2 c_{\rm P} \kappa_{\rm R})$ is the thermal diffusivity. The thermal mode exists where $|\omega_{\rm crit}| > \omega_\alpha$, while the g-mode exists where $|\omega_{\rm crit}| < \omega_\alpha$, as seen in the right panel of Figure 6.1. For higher frequency waves the thermal mode region becomes narrower and disappears. Since the thermal mode components only exist near the very surface of the star, where the density is very low, we would expect that the mechanical

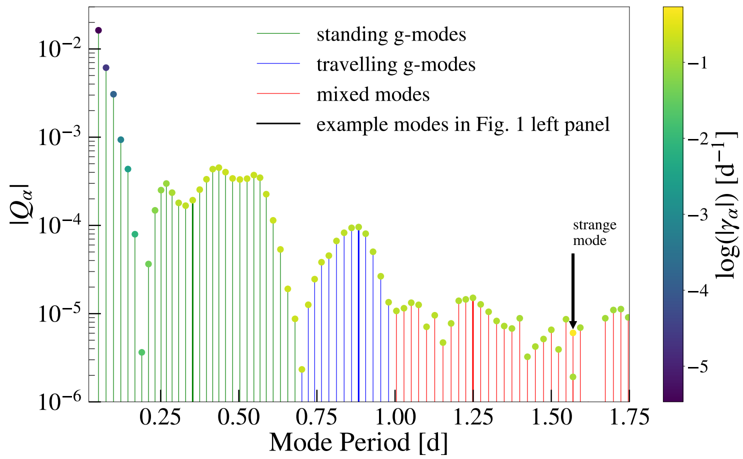

Figure 6.2: The overlap integral $|Q_\alpha|$ as a function of mode period from a $10\,M_\odot$ Wolf–Rayet star model at solar metallicity during helium burning (same as Figure 6.1). Circle colors indicate mode damping rates $|\gamma_\alpha|$, while line color indicates the mode type (the thick lines show the corresponding modes in Figure 6.1 left panel). "Strange mode" solutions often appear at long periods with excess damping rates and unusual period spacings (see Appendix 6.7).

torques are mostly contributed by the travelling g-mode component excited in the deep interior as Zahn's theory assumed. Hence at low tidal forcing frequency the tidal torques should be similar to Zahn's model, as we will see in §6.4.

Figure 6.2 shows the periods, damping rates and overlap integrals Q_α of all modes we solved for the same $10\,M_\odot$ model. We see that most modes have a nearly constant period spacing, matching the expectations for g-modes. The damping rates for most modes are at the same order of magnitude, except at high-frequency where the damping is significantly lower. This is due to their low radial wave numbers k_r and the damping rate $\gamma_\alpha \propto \int_{\rm star} k_r^2 \kappa |\xi_\alpha|^2 dm$. Low-frequency modes become traveling waves whose damping rate is roughly the wave crossing time.

The overlap integral $|Q_\alpha|$ typically decreases as the mode frequency decreases, but with significant scatter and with "hills and valleys" as the frequency decreases. Since the on-resonance AM dissipation $\dot{J}_\alpha \propto \gamma_\alpha |Q_\alpha|^2$, we expect to see the same "hills and valleys" features in the tidal synchronization rate, as the tidal forcing frequency is moving across different modes with varying Q_α. This is also different from Zahn's theory, which predicts a "smooth" power-law relation for the AM deposition rate as a function of orbital period ([24], or Equation 6.6 in this paper).

In the frequency ranges where mixed modes appear, we notice that GYRE suffers from numerical convergence problems as it starts looking for extremely high-order modes. We identified some of the mode solutions in that regime as "strange modes", and an example is labelled in Figure 6.2. These modes often have excess damping rates and unusual winding numbers (mode radial order), and do not obey the usual frequency spacing of g-modes. In addition, their eigenfunctions appear to be artificially truncated as they reach deeper inside the star, unlike other modes with an inner g-mode component at similar frequencies, which are truncated near the convective core boundary. We are not sure if these modes are physical or caused by numerical artifacts from GYRE, hence we do not include them in the spin–orbit integration. A detailed discussion of these modes is presented in Appendix 6.7.

6.4 Evolution of WR Spins

We integrate the spin–orbit evolution of WR–BH binaries from the WR star models and oscillations modes we have computed. Throughout the evolution, the orbital AM of the system is lost due to winds from the primary, gravitational radiation and tidal AM transfer:

$$\dot{J}_{\rm orb} = \dot{J}_{\rm wind,orb} - \dot{J}_{\rm GW} - \dot{J}_{\rm tide}\,, \tag{6.3}$$

where $\dot{J}_{\rm wind,orb} = \dot{M}_1 \Omega_{\rm orb} (M_2 a/(M_1+M_2))^2$ and $\dot{J}_{\rm tide}$ is given by summing over all modes from Equation 6.2. At short orbits, the orbital decay timescale by gravitational wave radiation is given by [37] (assuming circular orbits)

$$t_{\rm GW} \equiv \frac{a}{|\langle da/dt\rangle|} = \frac{5}{64(4\pi^2)^{4/3}} \frac{c^5(1+q)^{1/3}}{G^{5/3}M_1^{5/3}q} P_{\rm orb}^{8/3}\,, \tag{6.4}$$

where $q = M_2/M_1$ is the mass ratio. For equal mass binaries ($q = 1$), this gives $t_{\rm GW} \approx 206\,{\rm Myr} \times (M_1/10\,M_\odot)^{-5/3}(P_{\rm orb}/0.3\,{\rm d})^{8/3}$, much greater than the typical WR lifetime ($\lesssim 1$ Myr). Hence, gravitational radiation is not important in our case, but we still include the term $\dot{J}_{\rm GW} = (32/5)(G/a)^{7/2}c^{-5}M_1^2M_2^2\sqrt{M_1+M_2}$ in our evolution.

The primary receives spin AM from the orbit at $\dot{J}_{\rm tide}$, and it loses AM through winds:

$$\dot{J}_{\rm spin} = \dot{J}_{\rm tide} + \dot{J}_{\rm wind,spin}\,, \tag{6.5}$$

where $\dot{J}_{\rm wind,spin} = \dot{M}_1 \Omega_{\rm spin} R_1^2$. The spin of the primary may also change due to the changes of its internal structure and hence moment of inertia. Since the secondary is a BH in our case, its spin is not coupled.

For comparison, we also integrate each evolution based on Zahn's formalism, with an adapted AM transfer rate from [24]:

$$\dot{J}_{\rm tide,Zahn} = \frac{GM_2^2}{r_{\rm c}}\left(\frac{r_{\rm c}}{a}\right)^6 s_{\rm c}^{8/3}\frac{\rho_{\rm c}}{\bar{\rho}_{\rm c}}\left(1-\frac{\rho_{\rm c}}{\bar{\rho}_{\rm c}}\right)^2, \tag{6.6}$$

where $s_{\rm c} = \sqrt{3/\pi G\bar{\rho}_{\rm c}}|\Omega_{\rm orb}-\Omega_{\rm spin}|$, while $r_{\rm c}$, $\rho_{\rm c}$ and $\bar{\rho}_{\rm c}$ are the convective core radius, the density at the core boundary, and the average density of the core, respectively.

We construct the integration machinery of the spin–orbit evolution as follows: after generating a grid of stellar model snapshots throughout the star's evolution, we solve for oscillation modes for each snapshot with GYRE. We begin our integration at the start of the helium burning phase (defined by the instant when 2‰ of the core helium burning lifetime has passed). We carefully apply an adaptive time step control to avoid i) sudden crossing of resonance locations; ii) sudden changes of mode frequencies; iii) changes of more than 2‰ of the total evolution phase lifetime; and iv) sudden change of stellar spin by 2‰, in one time step. To evaluate physical quantities (e.g. mode frequencies, stellar masses) between two model snapshots, we estimate them by interpolating these snapshots and their corresponding GYRE solutions. In doing so, we track the modes by their radial orders $n_{\rm pg}$, and only include the mode eigenfunctions existing in both snapshots. We carried out resolution tests with half our selected timesteps and we confirm that the results are nearly identical.

Theories have suggested that the strong magnetic coupling between the stellar core and envelope (e.g. Taylor-Spruit dynamo, [45, 17]) removes the majority of core AM immediately after the main sequence [25], before the envelope can be stripped off. Hence, we assume initially non-rotating WR stars. We run models with initial orbital periods of 0.3, 0.5, or 0.8 days. We find that longer period orbits exhibit very little tidal spin-up.

In this work we specify our calculations to equal mass binaries ($q = 1$), since they are the most relevant for binary black holes. For cases with different mass ratios, one would expect from Equation 6.1 that the tidal dissipation rate (hence the tidal spin-up rate) naïvely scales as q^2, as we verified in some additional test runs. However, extreme mass ratios could allow for orbital decay and resulting processes such as resonance locking or binary mergers. We hope to generalize our calculations to such systems in future works.

Figure 6.3 shows the spin and orbital evolution for a few of the systems we studied. Since the WR primary burns helium and loses mass throughout the evolution, the

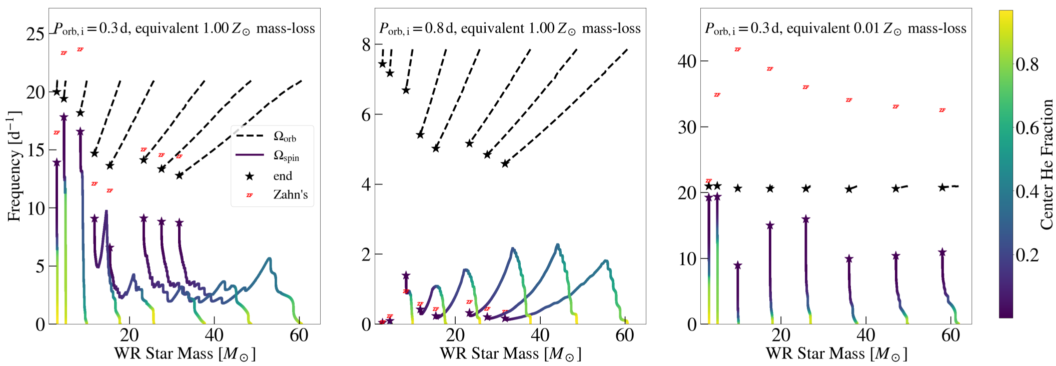

Figure 6.3: The spin and orbital evolution for our Wolf–Rayet–BH binaries. All systems have equal mass companions initially. The solid and dashed lines show the spin and orbital frequencies, respectively. Line colors indicate the evolving central helium mass fraction. The stars mark the end of evolution (core helium depletion), and the red "ZF" symbols show the spins if Zahn's formalism (Equation 6.6) is assumed. **Left**: Systems with initial orbital periods of 0.3 days and a mass-loss rate equivalent to solar metallicity. Mass loss is very significant for high-mass models and the final spins depart from Zahn's formalism for them. **Middle**: Systems with initial orbital periods of 0.8 days and a mass-loss rate equivalent to solar metallicity. Mass loss overpowers tidal spin-up and the primaries are not spun up much, consistent with Zahn's results. **Right**: Systems with initial orbital periods of 0.3 days and a mass-loss rate equivalent to 0.01 solar metallicity. Mass loss is negligible for most systems and the primaries are partially spun up, but not as much as Zahn's formalism predicts. None of these models reach tidal synchronization.

mass and central helium fraction can be seen as time coordinates, as shown. For systems with short initial orbits and high metallicities ($P_{\rm orb,i} = 0.3\,{\rm d},\ Z = Z_\odot$, left panel), we see that the primaries get significantly spun up, yet they are not tidally synchronized even at the end of evolution. In addition, the final spins of massive models are never higher than what one would expect from Zahn's theory.

When we increase the initial periods ($P_{\rm orb,i} = 0.8\,{\rm d}$, middle panel of Figure 6.3), the tidal torques decrease as expected. At these long periods, the tidal torque is dominated by traveling waves and the results agree well with Zahn's formalism. However, the tidal torque is unable to compete with mass loss, which almost completely removes the spin AM the star accumulated during the first half of the evolution, leaving a slowly spinning primary.

Tidal spin-up is followed by mass-loss induced spin-down in the middle of the evolution for solar-metallicity models (Figure 6.3, left and middle panel) due to an increase in the wind mass loss rate. This occurs when the helium envelope

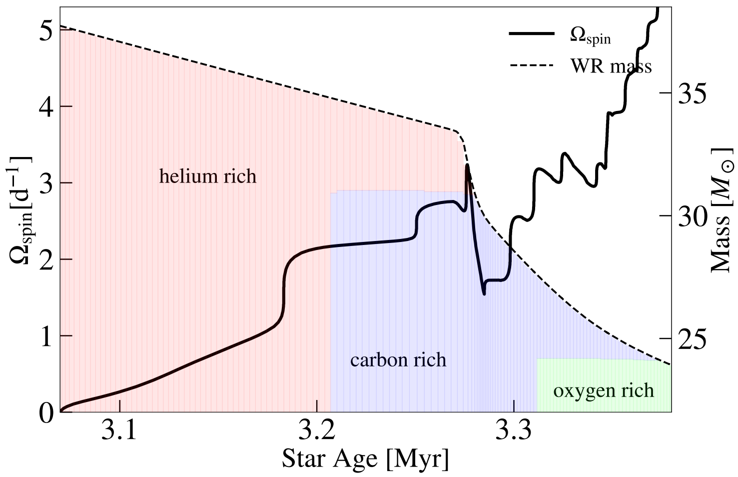

Figure 6.4: The mass and spin evolution of a $38\,M_\odot$ Wolf–Rayet star at solar metallicity, with an initial orbit of 0.3 days. The shaded regions show the dominant composition as a function of mass coordinate (right axis). At an age of $\sim 3.3\,$Myr, mass loss exposes the carbon-rich core, greatly enhancing the mass loss and spin down rates.

is lost completely, exposing the CO-rich core, and greatly increasing the mass loss rate according to the “Dutch" mass loss prescription (Figure 6.4). In several thousand years the winds remove the star’s spin AM until the mass loss rate decreases somewhat, allowing tidal spin-up to proceed. However, ongoing mass loss and a widened orbit prevent tides from spinning up the star to synchronization.

When we consider short initial periods but move to low-metallicity models ($P_{\mathrm{orb,i}} = 0.3\,\mathrm{d}$, $Z = 0.01\,Z_\odot$, right panel of Figure 6.3), the mass loss becomes negligible and the spin evolution is dominated by tidal effects. The orbits do not change significantly. We see that the primaries get significantly spun up, yet still not reaching tidal synchronization, and the resulting spin is much slower than Zahn’s prediction, except for the lowest mass models. This is because the transition period from standing modes to travelling waves increases as the stellar mass increases. Hence the evolution is more likely to depart from Zahn’s formalism for more massive primaries (see §6.5).

The evolution of spin frequencies show “step-like” features (most easily seen in Figure 6.3 middle panel) characterized by sudden increases in spin frequency. This is caused by the resonance-crossing of standing modes with the tidal forcing, as illustrated in Figure 6.5. When the tidal forcing frequency gets close to one of the mode frequencies, a near-resonance occurs (cf. Equation 6.1) and the tidal torque

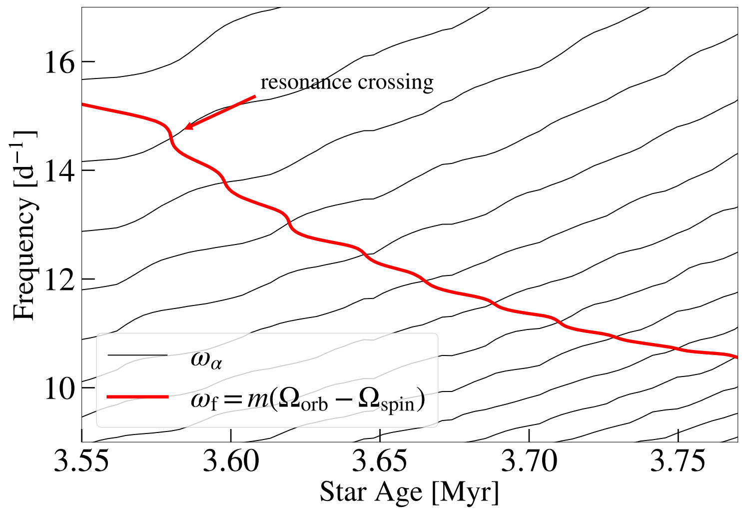

Figure 6.5: The evolution of the mode frequencies (black lines) and tidal forcing frequency (red line) of a WR–BH binary with a $26\,M_\odot$, $1.0\,Z_\odot$ WR star, an equal mass companion and an initial orbit of 0.8 days. The mode frequencies increase as the star evolves, while the forcing frequency decreases, preventing resonance locking. $\Omega_{\rm spin}$ increases rapidly while $\omega_{\rm f}$ decreases rapidly at resonance crossings, creating the "step-like" features we see in the spin frequency evolution (Figure 6.3).

drastically increases, leading to high spin-up rate. The occasional crossings of these resonances create the "step-like" features.

6.5 Discussion

Comparison to Zahn's Formalism

To understand why and how the tidal evolution differs from Zahn's formalism, in the upper panel of Figure 6.6 we show the tidal torques calculated for a $10\,M_\odot$ WR star model for different tidal forcing periods $P_{\rm tide} = 2\pi/\Omega_{\rm tide}$ with these two approaches. For short tidal periods, the tidal torque has sharp peaks at standing g-mode frequencies, in contrast to the power-law dependence of Zahn's prediction. This is caused by low damping rates of standing modes at short mode periods (cf. Figure 6.2 and Figure 6.6 lower right panel).

As the mode and orbital frequencies evolve, resonance crossings occur, hence the accumulated tidal spin-up must be evaluated by integrating $\dot{J}_{\rm tide}$ over time. Zahn's theory for travelling waves generally overestimates the tidal spin-up in this case, as the resonance peaks are narrow, and during the majority of evolution, the tidal torque is much less than what Zahn's formalism estimates. This helps to explain the departure of final spins shown in Figure 6.3 for short-period systems (left and right

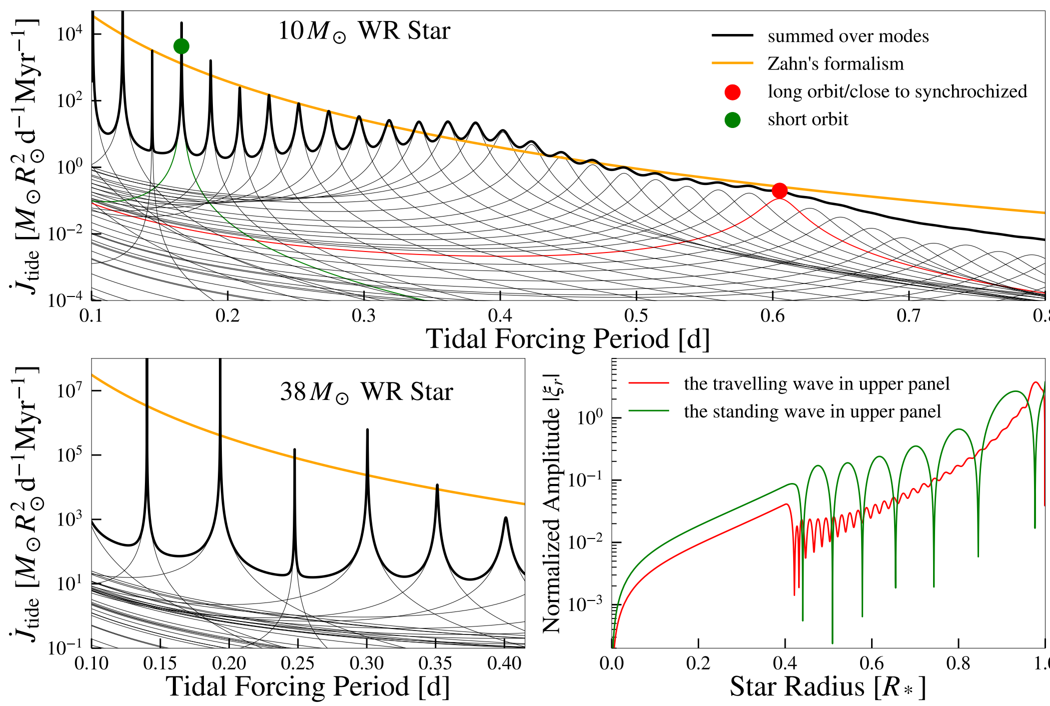

Figure 6.6: **Upper**: Our calculated $\dot{J}_{\rm tide}$ by summing over modes (thick black line) and by Zahn's formalism (thick orange line) as a function of tidal forcing period $P_{\rm tide} = 2\pi/\Omega_{\rm tide}$, for a $10\,M_\odot$ Wolf–Rayet model with 90% central helium abundance. The contributions from individual modes are represented by thin gray lines. At short tidal forcing periods $P_{\rm tide} \lesssim 0.35\,{\rm d}$ (e.g., the green dot), the tidal torque is dominated by resonance peaks from individual standing modes, and is very different from what Zahn predicts. At long forcing periods (e.g., the red dot), the tidal torque is no longer dominated by individual modes, but arises from a multitude of highly-damped travelling modes. This is exactly Zahn's assumption, and hence the torques are similar at long periods. **Lower Left**: The same as the upper panel but for a more massive $38\,M_\odot$ Wolf–Rayet model with 90% central helium abundance. We see that the mode-period spacing becomes larger, and the standing wave region extends to longer tidal forcing period. **Lower Right**: Eigenfunctions of the most resonant mode at the green and red dots in the upper panel. We see clearly that one is a standing mode while the other is a travelling mode.

panel) from Zahn's predictions.

When the systems are in long-period orbits, or already at a stage where $\Omega_{\rm spin}$ becomes comparable to $\Omega_{\rm orb}$ (close to tidal synchronization), the tidal forcing periods become long and the tidal torques are mostly contributed by modes at low frequencies. These modes, in contrast to their high-frequency partners, have large damping and are essentially travelling waves (cf. Figure 6.2 and Figure 6.6 lower right panel). Therefore, the tidal torque is no longer dominated by resonance with an individual mode, but instead has contributions from many strongly damped modes, effectively forming a "continuum" (Figure 6.6, red dot). This continuum formed by traveling waves is exactly what Zahn's formalism assumes, so the torques should be similar to Zahn's formalism, which is confirmed in Figure 6.6. This explains the consistency between our results and Zahn's for long-period initial orbits (Figure 6.3 middle panel).

We note, however, that the transition period between standing waves and travelling waves depends on the stellar mass: for higher mass models, the frequency range for standing waves extends to longer periods, as shown for the 38 $M_\odot$ model in the lower left panel of Figure 6.6. Hence, the tidal evolution of massive WR stars departs more strongly from Zahn's formalism, as we see in the left and right panels of Figure 6.3.

This distinction is caused by the different structures of low and high-mass WR stars. For higher mass stars, a larger fraction of the total internal pressure is contributed by radiation pressure since they are hotter and more luminous. Radiation pressure, however, contributes smaller buoyancy forces because the Brunt-Väisälä frequency N is zero for a star supported purely by radiation pressure. Indeed, the Brunt-Väisälä frequencies within our high-mass models are smaller than those within our low-mass models (Figure 6.7). This increases the g-mode period spacing (proportional to N^{-1}) of high-mass stars and decreases the radial wave number at the same frequency (as $k_r \propto N$). Hence, the mode damping rate $\gamma_\alpha \propto \int_{\rm star} k_r^2 \kappa |\xi_\alpha|^2 dm$ is also decreased. A secondary effect is that the convective cores are larger in more massive stars, making the radiative envelopes and g-mode cavities narrower. These combined effects make the resonance peaks narrower and more widely spaced for higher mass models, and further from the travelling wave limit of Zahn's formalism.

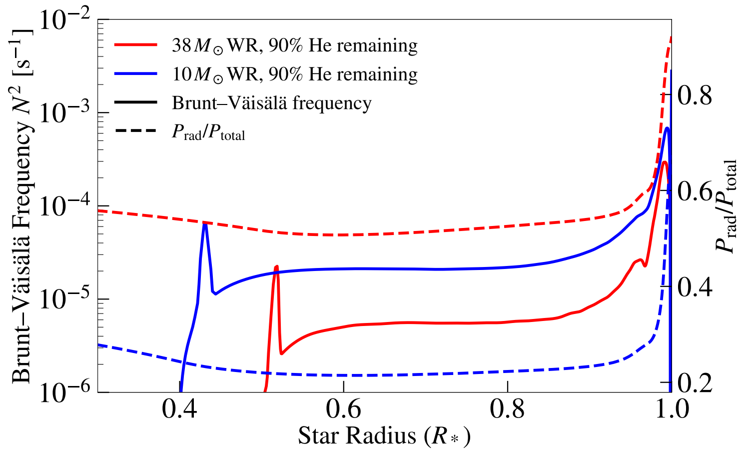

Figure 6.7: The Brunt-Väisälä frequency (solid lines) and the ratio of radiation pressure to total pressure (dashed lines) of two WR models of 10 (blue) and 38 $M_\odot$ (red), the same models in Figure 6.6. The radiation pressure fraction is higher for the more massive model, making its Brunt-Väisälä frequency lower. This causes its resonance peaks to be narrower and more separated, as seen in Figure 6.6.

Resonance Locking

When the tidal dissipation is dominated by resonant modes, an important process called resonance locking may occur [53]. However, we argue that this is unlikely to occur for WR–BH binaries. Resonance locking can happen when the mode's frequency evolves at the same rate as the tidal forcing frequency:

$$\dot{\omega}_\alpha = \dot{\omega}_{\rm f} = m(\dot{\Omega}_{\rm orb} - \dot{\Omega}_{\rm spin})\,. \tag{6.7}$$

We see from our example evolution tracks (Figure 6.3) that in most cases $\dot{\Omega}_{\rm orb} < 0$ and $\dot{\Omega}_{\rm spin} > 0$, which means $\dot{\omega}_{\rm f} < 0$, in contrast to the fact that $\dot{\omega}_\alpha > 0$ due to stellar evolution (Figure 6.5). Hence the above relation never holds and resonance locking can never happen. Instead, the system rapidly passes through resonances, creating the step-like features in Figure 6.3.

We note that when mass loss dominates the spin evolution, we could occasionally have $\dot{\Omega}_{\rm spin} < 0$ (Figure 6.3, left and middle panels) and resonance locking may happen during this phase. This may prevent a star from rapidly spinning down, but it cannot cause tidal spin-up. However we find that during these phases the Brunt-Väsäilä frequency of the star increases rapidly, such that $\dot{\omega}_\alpha$ exceeds $\dot{\omega}_{\rm f}$ even at resonance, in contrast to the resonance locking criterion. Hence, resonance locking does not appear to occur in any of our modeled systems.

Implications for BH Spins

A rapidly rotating WR star can probably collapse to a fast-spinning BH, forming a high-spin binary BH system. If angular momentum is conserved during the core-collapse process, the dimensionless spin parameter of the resulting BH is

$$a = \frac{cJ_{\rm WR}}{GM_{\rm BH}^2} \, . \tag{6.8}$$

In Figure 6.8, we show the resulting black-hole spins of our WR star models, assuming that they preserve their masses and angular momenta after helium burning and during the core-collapse process. We also show the predicted BH spins with Zahn's formalism. We see that lower-mass systems can form faster-spinning BHs, as their tidal spin-up is more efficient. It is only in ultra-short orbits that these systems form fast-spinning BHs. For solar metallicity systems, tidal spin-up cannot overcome AM loss from winds, resulting in low spins for systems starting at long ($P_{\rm orb,i} \gtrsim 0.5\,{\rm d}$) orbital periods. Low-metallicity ($1\%\,Z_\odot$) systems with $0.5\,{\rm d} \lesssim P_{\rm orb,i} \lesssim 1\,{\rm d}$ produce larger BH spins with $0.1 \lesssim a \lesssim 0.8$, compared to $a \sim 0.01$ predicted by single star evolution models [16]. For high-mass systems, the spins are much smaller than Zahn's predictions.

Our predicted BH spins are roughly compatible with some LIGO measurements with moderate spins ($0.1 \lesssim \chi_{\rm eff} \lesssim 0.5$) [1, 2, 3], but would have a tough time matching any events with large $\chi_{\rm eff}$. The relationship between orbital period, mass, and spin is different than what Zahn's theory predicts. Whereas we typically find higher spins for $M_{\rm BH} \lesssim 10\,M_\odot$, Zahn's theory predicts smaller spins for lower mass BHs. There may be an anti-correlation between mass and spin [43] which would support our new models. A mass-spin correlation from future LIGO-VIRGO data will help distinguish between these models. None of our high-mass models predict spins comparable to some high-spin measurements ($a \gtrsim 0.9$) from X-ray binaries [27], and the uncertainty of such measurements is still under debate [6, 12]. However, those measurements are for the first-born BH, while our models only apply to the second-born BH.

Previous works on tidal interactions between WR–BH binaries have predicted black hole spins similar to our "Zahn's results" in Figure 6.8, in which Zahn's formalism is assumed [38, 4, 7, 31, 15]. These results likely overestimate the black hole spins when standing waves are present, which applies primarily to massive BHs ($M_{\rm BH} \gtrsim 10\,M_\odot$). [10] also investigated tidal spin-up of WR stars, but used different prescriptions for tidal dissipation, winds, and orbital AM losses. Unlike our results

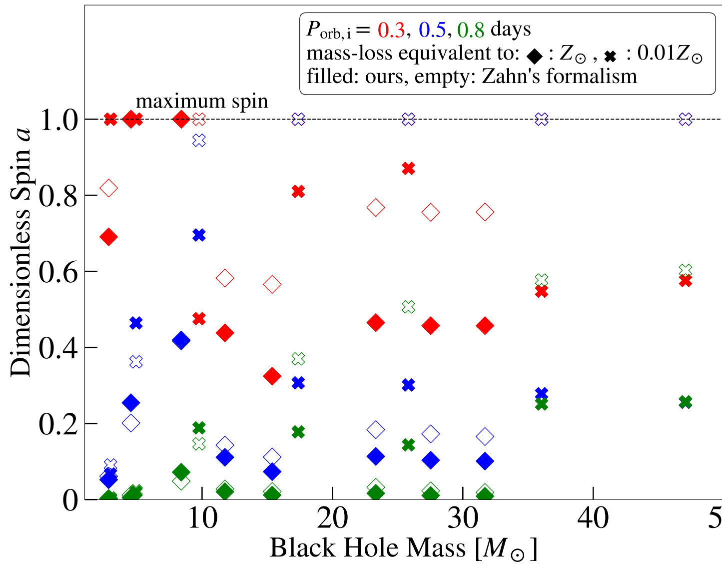

Figure 6.8: The dimensionless spin of resulting black holes for our Wolf–Rayet star models if their masses and angular momenta at the end of helium burning is preserved. Zahn's predictions for the same system are also shown, and are assumed 1 (maximum rotating) if the progenitors have $J > GM^2/c$. For short initial orbits, the models typically predict higher spins than individual stellar evolution models, where the spins could be as low as 10^{-2}. However, the spins are usually lower than Zahn's predictions, especially for high-mass systems.

and those listed above, they found that tidal spin-up coupled with mass loss frequently caused the orbits to decay and instigate mass transfer. This outcome is more likely with small companion masses (e.g., neutron stars) whose orbits must decay more in order to tidally spin-up the WR star.

Nonlinear dissipation

Throughout the paper, we have assumed that the tidally forced modes are linear. However, this is not true when a mode is close to resonance, especially for massive models with larger on-resonance mode amplitudes. To examine how nonlinearity may affect our conclusions, we estimate the nonlinear damping rate for a mode α in Appendix 6.7. For weakly nonlinear modes, an approximate nonlinear damping rate may be

$$\gamma_{\alpha,\rm NL} \sim \frac{(d\xi_{\alpha,r}/dr)_{\rm max}}{\tau_{\alpha,2}}, \tag{6.9}$$

where the numerator is the mode nonlinearity (i.e., the peak value of $d\xi_r/dr$ within the star, which is much less than unity for a weakly nonlinear mode) and the denominator is the wave crossing time of the envelope. We rerun our evolution

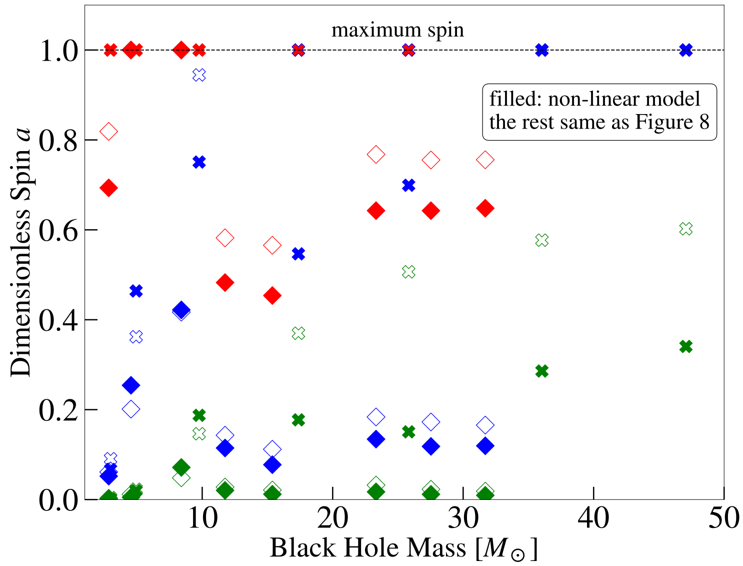

Figure 6.9: The dimensionless spin of resulting black holes for our Wolf–Rayet star models with the nonlinear damping rates we estimate in Appendix 6.7. Zahn's predictions are also shown. The black hole spins are significantly increased when including nonlinear damping, especially for high-mass black holes and short-period systems. Hence, nonlinear effects could be an important factor in these systems.

models with this nonlinear damping rate, and we find that nearly all models achieve more tidal spin-up compared to linear damping only.

In Figure 6.9, we show the predicted BH spins for our systems with nonlinear damping, compared to the predictions from Zahn's theory. We see that for very short-period orbits ($P \sim 0.3$ d), the strong tidal forcing triggers substantial nonlinear damping, spinning up the BHs to nearly the same rotation rates as predicted by Zahn's theory, where maximum damping occurs. Nonlinear effects are the most significant for low-metallicity and high-mass ($M \gtrsim 30\,M_\odot$) models, which have lower order g-modes dominating their tidal processes and less linear damping (see discussion in §6.5).

However, our nonlinear damping model is crude, so these predictions are not very reliable. A more detailed study of the nonlinear interactions has to be carried out to establish firm conclusions for the final BH spins.

Caveats

Throughout this paper, we have assumed very efficient angular momentum transport within the WR star, such that it remains rigidly rotating. This is justified by the asteroseismically callibrated models of magnetic angular momentum transport [16] that predict nearly rigid rotation during the helium-burning phase [15]. However, if angular momentum transport is inefficient, gravity waves damping near the stellar surface will preferentially spin up those layers until they are synchronized. This will create a critical layer at which subsequent waves are absorbed [20], synchronizing the star from the outside inwards. Recent works have investigated the formation of critical layers and subsequent absoroption of incoming waves [46, 22], though they do not include magnetic torques that may allow angular momentum transport to prevent critical layer formation. If a critical layer can form, it will absorb outgoing waves, such that Zahn's model applies once again.

We have ignored the influence of the Coriolis force in our calculations. This will become significant once the star's have been partially spun up and the tidal forcing frequency becomes smaller than the rotation frequency. However, the prograde $\ell = m = 2$ modes that dominate the tidal interaction have eigenfunctions that are only slightly changed by Coriolis forces (see, e.g., [14]), so we don't expect any of our conclusions to be greatly affected.

We have adopted the "Dutch" wind models with an artificial scaling factor to simulate the mass-loss rates for Wolf–Rayet stars at different metallicities. However, the wind physics for these stripped stars are highly uncertain [52], and different wind models could result different rates for the removal of spin angular momentum from the primary, introducing uncertainties in the final black hole spins. Nevertheless, we don't expect these uncertainties to exceed the differences between our solar-metallicity models and the 0.01 $Z_\odot$ models, as they represent extreme cases of large and negligible mass-loss, respectively. Hence, the final black hole spins with the "correct" wind physics should lie between the data points representing models with the same initial mass and periods but different metallicities in our Figure 6.8. The conclusion that these black holes are not spun up to maximal rotation appears robust.

Our stellar models were run at low metallicity in order to reliably calculate the near-surface structure and mode eigenfunctions. Higher metallicity stars will have somewhat different structure and mode eigenfunctions near the surface, particularly around the iron group opacity peak. If this significantly affects mode damping rates, then the tidal synchronization efficiency would be similarly altered. We set up additional test models with 0.02, 0.03 and 0.2 $Z_\odot$ and find that the oscillation mode parameters (frequencies, damping rates and overlap integrals) show no significant differences, nor specific trends towards higher metallicities, hence we expect our treatment to be appropriate. However, these models all have weak winds, while the strong winds in solar-metallicity models may also alter the eigenmode properties. [41, 40] present detailed models of the transition from the hydrostatic star the hydrodynamic wind in the near-surface layers. Future work should investigate how those types of stellar models affect mode eigenfunctions and damping rates.

Finally, our calculations are performed by summing up the contribution of individual tidally excited oscillation modes. If non-resonant modes outside our computed frequency range contribute to the tidal dissipation, or if our eigenmode calculations miss highly non-adiabatic thermal modes that contribute to the dissipation, then the tidal dissipation rate could possibly increase. It would be interesting to compare to calculations performed by directly computing the forced tidal response, as outlined in [47].

6.6 Conclusion

In this work, we investigate the dynamical tidal spin-up of Wolf–Rayet stars from black hole companions. We build Wolf–Rayet star models with different metallicities, and then calculate their oscillation mode frequencies, damping rates, and eigenfunctions. We use these to integrate the coupled spin–orbit evolution of the binary based on the tidal excitation of these oscillation modes. We also make predictions for the resulting BH spins upon core-collapse of the Wolf–Rayet star.

We study the properties of the oscillation modes and find that at shorter orbital period, the tidal forcing is mostly contributed by standing g-modes, in contrast to the usual assumption of travelling waves proposed by [55]. The standing g-mode spectra contributes a resonance structure, and during most of the spin–orbit evolution phase, the tidal response lies between resonances and the interaction strength is weaker than Zahn's prediction. The tidal forcing transits to Zahn's travelling wave limit at longer periods, in which Zahn's estimate is more accurate. However, the specific transition frequency depends on the stellar masses, and the structure for more massive stars (supported significantly by radiation pressure) tend to have lower transition frequencies, allowing systems in longer-period orbits to evolve differently compared to Zahn's prediction.

We find that it is difficult to tidally synchronize Wolf–Rayet stars during helium-burning. For solar-metallicity Wolf–Rayet stars, strong winds tend to remove the majority of angular momentum deposited by tides, leaving slowly spinning stars and black holes. At low metallicity, the stellar wind is weaker and the stars are significantly tidally spun up, yet still less than Zahn's prediction, especially for massive stars and short-period orbits.

Tidal interactions can significantly spin up the resulting BHs compared to single-star models. Yet the predicted black hole spins a are still $\lesssim 0.4$ for all but our shortest period ($P_{\rm orb} \lesssim 0.5\,\mathrm{d}$) models. These predictions are consistent with some low/moderate-spin measurements from LIGO/Virgo black hole merger events, but cannot explain high-spin X-ray binaries events since only the second-born black hole has large spin in these models.

We have discussed a new class of gravito-thermal modes that appear in our calculations, yet we do not reach a firm conclusion whether these modes are physical or caused by numerical artifacts. Future work should investigate the origins of these modes, and any effect they could have on tidal spin-up.

There are also caveats to our work. We have assumed rigid rotation of the Wolf–Rayet star during our spin–orbit evolution calculations, as expected if there are strong internal AM transport processes caused by magnetic torques. However, weak AM transport could enable surface critical layer formation, allowing Zahn's model to apply. We did not realistically calculate the near-surface structure of our solar-metallicity models, which could alter our estimate of the mode damping rates. We also point out that nonlinear damping effects could be significant for our most massive models, which can produce more tidal dissipation than our predictions from linear theory. This should be studied and improved in future work.

Acknowledgements

We thank the anonymous referee for a constructive report that helped to improve this work. We also thank Hang Yu, Rich Townsend, Emily Hu and Katie Breivik for helpful discussions. This work is partially supported by NASA through grant 20-XRP20 2-0147. J.F. is thankful for support through an Innovator Grant from The Rose Hills Foundation, and the Sloan Foundation through grant FG-2018-10515.

6.7 Appendix

Mode Dispersion Relation with Thermal Diffusion and Radiation Pressure

To understand the effects of thermal diffusion on stellar oscillation modes, we modify the derivations in the appendices of [25], assuming the stellar interior has a mixture of ideal gas and radiation pressure, and constant molecular weight. The internal energy density is given by

$$u = c_{\rm V,g} T + a T^4 \,, \tag{6.10}$$

where T is the temperature of the fluid, and $c_{\rm V,g} = nk_{\rm B}/(\gamma_{\rm g} - 1)$ is the heat capacity for gas at constant volume, and a is the radiation constant, n is the number density of gas particles and $\gamma_{\rm g}$ is the heat capacity ratio for ideal gas ($\gamma_{\rm g} = 5/3$ for mono-atomic gas). The pressure of the mixture is given by

$$P = P_{\rm gas} + P_{\rm rad} = nk_{\rm B}T + \frac{1}{3}aT^4\,. \tag{6.11}$$

Now we consider a change in entropy: from the first law of thermodynamics, we have $dS = (dU + pdV)/T$. This immediately leads to the change in entropy density

$$ds = nk_{\rm B}\left[\left(\frac{1}{\gamma_{\rm g}-1} + \frac{12\eta}{1-\eta}\right)d\ln T - \frac{1+3\eta}{1-\eta}d\ln\rho\right], \tag{6.12}$$

where we defined $\eta \equiv P_{\rm rad}/P$ and used $d\ln\rho = -d\ln V$, where ρ is the gas density. Taking the derivative of Equation 6.11, we have the following relation:

$$d\ln P = (1-\eta)d\ln\rho + (1+3\eta)d\ln T\,. \tag{6.13}$$

We substitute this relation into Equation 6.12 to have two alternative forms of the entropy derivative:

$$ds = nk_{\rm B}\left[\left(\frac{1}{\gamma_{\rm g}-1} + \frac{12\eta}{1-\eta} + \frac{(1+3\eta)^2}{(1-\eta)^2}\right)d\ln T - \frac{1+3\eta}{(1-\eta)^2}d\ln P\right], \tag{6.14}$$

and

$$ds = nk_{\rm B}\left[\left(\frac{1}{\gamma_{\rm g}-1} + \frac{12\eta}{1-\eta}\right)\frac{1}{1+3\eta}d\ln P - \left(\frac{1-\eta+12(\gamma_{\rm g}-1)\eta}{(\gamma_{\rm g}-1)(1+3\eta)} + \frac{1+3\eta}{1-\eta}\right)d\ln\rho\right]. \tag{6.15}$$

From Equations 6.14 and 6.15 we can calculate the following thermodynamic quantities:

$$c_{\rm P} \equiv T\left(\frac{\partial s}{\partial T}\right)_P = \left(\frac{\partial s}{\partial \ln T}\right)_P = \left(\frac{1}{\gamma_{\rm g}-1} + \frac{12\eta}{1-\eta} + \frac{(1+3\eta)^2}{(1-\eta)^2}\right)nk_{\rm B}\,, \tag{6.16}$$

$$\Gamma_1 \equiv \left(\frac{\partial\ln P}{\partial\ln\rho}\right)_s = 1-\eta + \frac{(\gamma_{\rm g}-1)(1+3\eta)^2}{1-\eta+12(\gamma_{\rm g}-1)\eta}\,. \tag{6.17}$$

We now derive the energy equation for the mixture of ideal gas and radiation. With thermal diffusion, the entropy changes at a rate

$$\frac{ds}{dt} = \frac{\partial s}{\partial t} + \mathbf{v}\cdot\nabla s = \frac{c_{\rm P}\kappa}{T}\nabla^2 T\,, \tag{6.18}$$

where κ is the thermal diffusivity. We assume a static and spherically symmetric stellar background and the usual harmonic time dependence of perturbations $\delta Q \propto e^{-\sigma t} = e^{-i\omega t}$. The above equation reduces to

$$-\sigma\left(\delta s + \xi_r \frac{\partial s}{\partial r}\right) = -c_\mathrm{P}\kappa k^2 \delta \ln T\,, \tag{6.19}$$

where ξ_r is the radial displacement and we used the WKB approximation $\nabla^2 \to -k^2$. From Equations 6.15 and 6.17, we have

$$\frac{\partial s}{\partial r} = \frac{1-\eta}{1+3\eta} c_\mathrm{P}\left(\frac{1}{\Gamma_1}\frac{\partial \ln P}{\partial r} - \frac{\partial \ln \rho}{\partial r}\right) = \frac{1-\eta}{1+3\eta}\frac{c_\mathrm{P}}{g} N^2\,, \tag{6.20}$$

where $N^2 \equiv g(\Gamma_1^{-1}\partial \ln P/\partial r - \partial \ln \rho/\partial r)$ is the Brunt-Väisälä frequency. We can further express δs and $\delta \ln T$ in terms of δP and $\delta\rho$ from Equations 6.15 and 6.13. We substitute them and the above equation into Equation 6.19, and arrive at our energy equation:

$$\left(1 - \frac{\kappa k^2}{\sigma}\right)\frac{\delta\rho}{\rho} = \left(\frac{1}{\Gamma_1} - \frac{\kappa k^2}{\sigma}\frac{1}{1-\eta}\right)\frac{\delta P}{P} + \frac{N^2}{g}\xi_r\,. \tag{6.21}$$

It is straightforward to verify that Equation 6.21 reduces to the energy equation in [25] when $\eta = 0$, i.e. radiation is neglected.

We now consider the dynamics of the fluid. The perturbed momentum equation reads:

$$\rho\omega^2\xi_r = ik_r\delta P + g\delta\rho\,, \quad \rho\omega^2\xi_\perp = \nabla_\perp \delta P\,, \tag{6.22}$$

where we again used the WKB approximation $\nabla_r \to ik_r$. The continuity equation with the incompressible approximation[1] gives

$$\nabla\cdot\xi \approx ik_r\xi_r + \nabla_\perp\cdot\xi_\perp = 0\,. \tag{6.23}$$

When the angular dependence of perturbation variables are expanded in spherical harmonics, we have $\nabla_\perp^2 \to -\lambda/r^2$ where $\lambda = l(l+1)$. Combining the above equations with the energy equation, we arrive at the dispersion relation

$$1 - \frac{\kappa k^2}{\sigma} + \frac{\lambda}{k^2 r^2}\frac{N^2}{\sigma^2} = \left(\frac{1}{\Gamma_1} - \frac{\kappa k^2}{\sigma}\frac{1}{1-\eta}\right)\frac{ik_r}{k^2 H}\,, \tag{6.24}$$

where $H \equiv P/(\rho g)$ is the pressure scale height. With the WKB approximation, $k \approx k_r$ and $k_r H \gg 1$, the first term in the bracket of the right hand side can be neglected, and the dispersion relation becomes

$$1 - \frac{\kappa k_r^2}{\sigma}\left(1 - \frac{1}{1-\eta}\frac{i}{k_r H}\right) \approx -\frac{\lambda}{k_r^2 r^2}\frac{N^2}{\sigma^2}\,. \tag{6.25}$$

[1] The result is similar without this approximation.

Gravity and Thermal Mixed Modes

When gas pressure is non-negligible, we always have $1-\eta \sim 1$ and the second term in the bracket of the left hand side of Equation 6.25 can usually be neglected under WKB approximation $k_r H \gg 1$. The dispersion relation hence reduces to the quadratic equation

$$\left(\frac{\omega_T}{\sigma}k_r^2 r^2\right)^2 - \left(\frac{\omega_T}{\sigma}k_r^2 r^2\right) - \frac{1}{4}\frac{\omega_{\rm crit}^3}{\sigma^3} = 0\,, \tag{6.26}$$

where $\omega_T = \kappa/r^2$ is the thermal frequency, and

$$\omega_{\rm crit} \equiv (4\lambda N^2 \omega_T)^{1/3} \tag{6.27}$$

is the critical frequency between different types of modes. The solution to Equation 6.26 is

$$k_r^2 r^2 \frac{\omega_T}{\sigma} = \frac{1}{2} \pm \frac{1}{2}\left(1 + \frac{\omega_{\rm crit}^3}{\sigma^3}\right)^{1/2}\,, \tag{6.28}$$

which has two important limits.

1. **High-frequency region**($|\omega_{\rm crit}| \ll |\sigma|$): the solution reduces to

$$k_r^2 r^2 \frac{\omega_T}{\sigma} \simeq \frac{1}{2} \pm \frac{1}{2}\left(1 + \frac{1}{2}\frac{\omega_{\rm crit}^3}{\sigma^3}\right). \tag{6.29}$$

   The "+" sign solution further reduces to the (radial) thermal diffusion solution $k_r^2\kappa \simeq \sigma$. The "−" sign solution reduces to $k_r^2 = -\lambda N^2/r^2\sigma^2$, which is the g-mode dispersion relation. With $\sigma = i(\omega + i\gamma)$, under the weakly damped limit $\gamma \ll \omega$, we have

$$k_r \approx \pm\frac{\sqrt{\lambda}N}{r\omega^2}(\omega - i\gamma)\,, \tag{6.30}$$

   which means the wave amplitude increases/decreases as it gets closer to the envelope, at a rate $\Im(k_r) = \pm\sqrt{\lambda}N\gamma/(r\omega^2)$.

2. **Low-frequency region**($|\omega_{\rm crit}| \gg |\sigma|$): The solutions reduce to

$$k_r^2 r^2 \simeq \pm\left(\frac{\lambda N^2}{\omega_T \sigma}\right)^{1/2}. \tag{6.31}$$

   Under the weakly damped limit, $\sigma = i(\omega + i\gamma) \approx i\omega$, we hence have

$$k_r \approx \frac{e^{i\theta}}{r}\left(\frac{\lambda N^2}{\omega_T \omega}\right)^{1/4}\,, \tag{6.32}$$

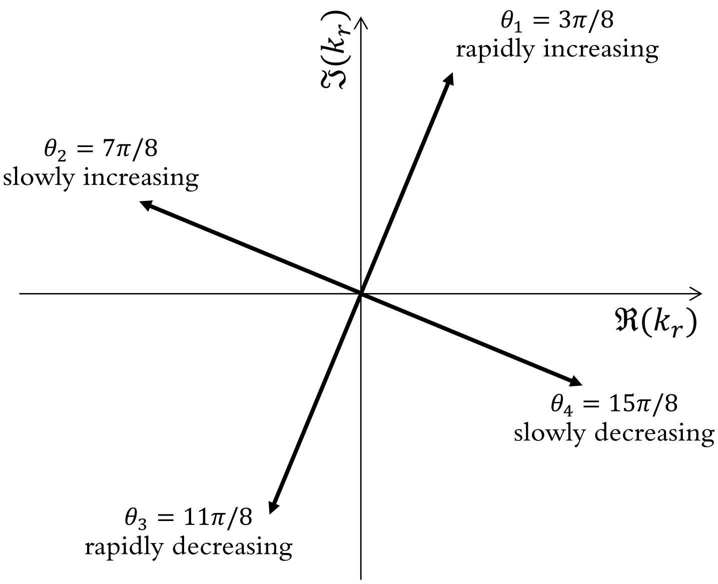

Figure 6.10: k_r for the thermal mode on the complex plane. The four solutions correspond to rapidly increasing, slowly increasing, rapidly decreasing and slowly decreasing thermal modes, respectively.

> where $\theta = 3\pi/8, 7\pi/8, 11\pi/8$ or $15\pi/8$, corresponding to the four solutions of rapidly increasing, slowly increasing, rapidly decreasing and slowly decreasing thermal modes, respectively (Figure 6.10). Physically, these waves are gravito-thermal modes in which both buoyancy and thermal diffusion play important roles. For the rapidly evanescent modes, $\Im(k_r) = \pm(\lambda N^2/\omega_T\omega)^{1/4}\cos(\pi/8)/r$, while for the slowly evanescent modes, $\Im(k_r) = \pm(\lambda N^2/\omega_T\omega)^{1/4}\sin(\pi/8)/r$, both of which are independent of γ.

Since $\omega_{\rm crit}$ explicitly depends on the local stellar properties, modes of a given frequency can behave as either gravity or thermal waves in different parts of the star, as we see in Figure 6.1. Modes can therefore behave as “mixed modes", with gravity mode character in the core of the star where thermal diffusion is unimportant, and thermal mode character near the surface of the star where thermal diffusion is very important. Such modes have rarely been examined in asteroseismology because their high damping rates mean that they will not be visible as stellar pulsation modes. However, these damping rates also mean they could be very important for energy dissipation via tidal excitation.

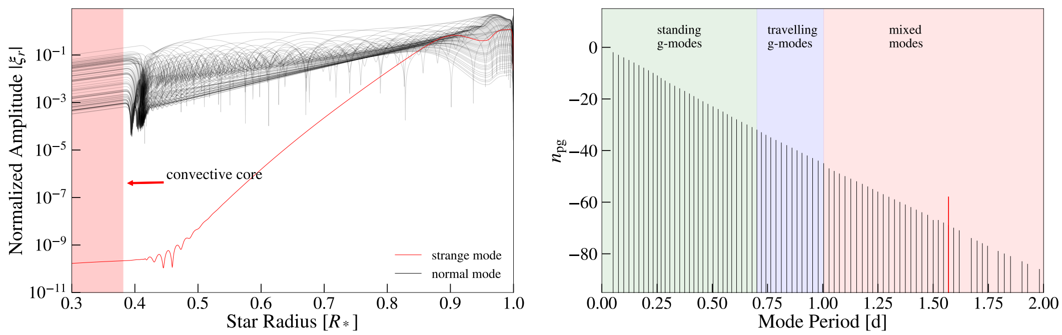

Figure 6.11: Left: All mode eigenfunctions for mode periods between 0.1 to 2 days solved by GYRE for a $10\,M_\odot$ Wolf–Rayet star model at solar metallicity during helium burning. In addition to the normal modes (black lines, including standing g-modes, travelling g-modes and mixed modes, discussed in §6.3), a strange mode solution (red line) exists. This mode has much higher damping rate because it is localized near the stellar surface, as indicated by its rapidly decreasing amplitude towards the core. **Right**: The periods and winding numbers (n_{pg}) for mode solutions, showing an outlying strange mode solution.

Strange Modes

When solving for high-order, low-frequency mixed modes, GYRE occasionally returns solutions which we identified as "strange modes". An example is given in Figure 6.11. The strange modes are usually distinct in the following aspects: 1) the modes have higher damping rates, often one order of magnitude larger than the normal modes. This causes stronger spatial evanescence as the waves propagate inwards, as seen from Equation 6.31. 2) The modes have unusual winding numbers n_{pg} (defined in [48], and treated as mode radial orders in GYRE), departing from the normal n_{pg}-period relation of normal modes (Figure 6.11, right panel). 3) The modes do not obey the uniform period spacing shared by normal g-modes. 4) The strange mode eigenfunctions seem to be artificially truncated in the radiative envelope, once they reach a minimum amplitude. We confirm that there are no special physical conditions inside the star where they are truncated. Resolution tests also show that the strange mode solutions do not converge even at very high spatial/frequency resolution.

We guess that the strange modes are effectively gravito-thermal mixed modes that are trapped in the near surface region where the waves behave as thermal waves ($|\omega_{crit}| \gg |\sigma|$). Because they are trapped in the surface layers, their damping rates are much larger than normal modes, similar to the acoustic strange modes found at high frequencies [19] . Because their eigenfunctions evanesce so rapidly towards the core, their amplitudes apparently drop below the numerical precision of GYRE near the core, causing the artificial behavior of the eigenfunction at small radii seen in Figure 6.11. This also causes the value of $n_{\rm pg}$ computed by GYRE to be incorrect, and explains why their exact frequencies/eigenfunctions do not converge at high spatial resolution.

In our calculations, the strange modes only exist in the low-frequency range of mode spectra. Hence, if actually physically present, these modes will only be relevant at the late stage of spin–orbit evolution, when the star has already been significantly spun up. Hence, we believe our main results to be robust against the uncertainties surrounding strange modes, but these modes should be studied in more detail in future work.

Nonlinear Damping of Modes

Our tidal calculations are based entirely on linear theory, yet under certain circumstances nonlinear effects could be important. The dominant nonlinear term in the fluid momentum equation is $\xi \cdot \nabla\xi \sim \xi(d\xi_r/dr)$, hence $d\xi_r/dr$ serves as an approximate measure of linearity, which only holds when $d\xi_r/dr \ll 1$. For our most massive models, the modes become nonlinear very close to resonance, so nonlinear effects will be important during resonance crossings. While developing a complete nonlinear theory is beyond the scope of this work, here we propose an ad-hoc estimate of the nonlinear damping rates of modes.

We have pointed out that the nonlinearity can be estimated by $d\xi_r/dr$. Specifically, we define

$$\phi_\alpha \equiv (d\xi_{\alpha,r}/dr)_{\rm max} = A_\alpha (d\bar{\xi}_{\alpha,r}/dr)_{\rm max} \tag{6.33}$$

as the parameter to characterize nonlinearity of mode α, where $\bar{\xi}_{\alpha,r}$ is the normalized eigenfunction solution of α and A_α is the mode amplitude due to linear driving, given by [13]:

$$A_\alpha = \frac{1}{2}\frac{W_{lm}Q_\alpha\omega_{\rm f}}{\sqrt{(\omega_\alpha-\omega_{\rm f})^2+(\gamma_\alpha+\gamma_{\alpha,\rm NL})^2}}\left(\frac{M_{\rm p}}{M_*}\right)\left(\frac{R_*}{a}\right)^{l+1}. \tag{6.34}$$

Note that we have replaced the damping rate by $\gamma_\alpha + \gamma_{\alpha,\rm NL}$, where we denote γ_α as the usual radiative damping rate we adopted in linear theory, and $\gamma_{\alpha,\rm NL}$ as the damping rate caused by nonlinear effects. From our convention, $\gamma_{\alpha,\rm NL}$ is a function of ϕ_α, i.e. $\gamma_{\alpha,\rm NL} = \gamma_{\alpha,\rm NL}(\phi_\alpha)$. While the detailed functional form of $\gamma_{\alpha,\rm NL}$ requires a thorough examination of the nonlinear damping mechanisms, physically we expect

$$\gamma_{\alpha,\rm NL}(0) = 0\,,\ \gamma_{\alpha,\rm NL}(\phi_\alpha \gtrsim 1) \simeq \gamma_{\alpha,\rm NL,max}\,, \tag{6.35}$$

i.e., no nonlinear damping when the mode amplitude is zero, and maximum damping when the ϕ_α parameter reaches 1. The maximum damping rate $\gamma_{\alpha,\mathrm{NL,max}}$ can be estimated by the inverse group travel time $\tau_{\alpha,2}$ defined in [26]:

$$\gamma_{\alpha,\mathrm{NL,max}} \simeq -\frac{1}{\tau_{\alpha,2}} = -\left(\frac{\sqrt{6}}{\omega_\alpha^2}\int_{\mathrm{rad}} \frac{N dr}{r}\right)^{-1}, \tag{6.36}$$

where the integral is carried out in the radiative zone of the star, and N is the Brunt-Väisälä frequency. Several authors suggest that the nonlinear damping rate should scale as $\gamma_{\alpha,\mathrm{NL}} \propto \sqrt{E_\alpha} \propto A_\alpha$ (see, e.g., [23, 54]). This suggests $\gamma_{\alpha,\mathrm{NL}}(\phi_\alpha)$ is linearly proportional to the mode amplitude, such that

$$\gamma_{\alpha,\mathrm{NL}}(\phi_\alpha) \simeq \min(1, \phi_\alpha)\gamma_{\alpha,\mathrm{NL,max}}\,. \tag{6.37}$$

Note that this ad-hoc expression 6.37 should most likely to hold when $\phi_\alpha \ll 1$ and $\phi_\alpha \gtrsim 1$, since we only know the properties of this function under these two limits. This further suggests we can assume $(\gamma_\alpha + \gamma_{\alpha,\mathrm{NL}})^2 \simeq \gamma_\alpha^2 + \gamma_{\alpha,\mathrm{NL}}^2$, since one of the two terms will always dominate the expression under these two limits. With this convention, combining Equations 6.33, 6.34 and 6.37, we have a quadratic equation for A_α^2 (when $\phi_\alpha < 1$)

$$(A_\alpha^2)^2 + 2B_\alpha A_\alpha^2 - C_\alpha = 0\,, \tag{6.38}$$

where

$$B_\alpha =((\omega_\alpha - \omega_\mathrm{f})^2 + \gamma_\alpha^2)/(2\bar{\gamma}_\alpha^2)\,, \tag{6.39}$$

$$C_\alpha =W_{lm}^2 Q_\alpha^2(\omega_\mathrm{f}/2\bar{\gamma}_\alpha)^2(M_\mathrm{p}/M_*)^2(R_*/a)^{2(l+1)}\,, \tag{6.40}$$

and $\bar{\gamma}_\alpha \equiv (d\bar{\xi}_{\alpha,r}/dr)_\mathrm{max}\gamma_{\alpha,\mathrm{NL,max}}$. The positive solution of A_α^2 gives

$$A_\alpha = (\sqrt{B_\alpha^2 + C_\alpha} - B_\alpha)^{1/2}\,. \tag{6.41}$$

Hence the nonlinear damping rate is given by

$$\gamma_{\alpha,\mathrm{NL}} = -\min\left[1, \left(\sqrt{B_\alpha^2 + C_\alpha} - B_\alpha\right)^{1/2}(d\bar{\xi}_{\alpha,r}/dr)_\mathrm{max}\right]\tau_{\alpha,2}^{-1}\,. \tag{6.42}$$

References

[1] B. P. Abbott et al. “Binary Black Hole Population Properties Inferred from the First and Second Observing Runs of Advanced LIGO and Advanced Virgo”. In: *The Astrophysical Journal Letters* 882.2, L24 (Sept. 2019), p. L24. DOI: `10.3847/2041-8213/ab3800`. arXiv: `1811.12940 [astro-ph.HE]`.

[2] B. P. Abbott et al. “GWTC-1: A Gravitational-Wave Transient Catalog of Compact Binary Mergers Observed by LIGO and Virgo during the First and Second Observing Runs”. In: *Physical Review X* 9.3, 031040 (July 2019), p. 031040. DOI: 10.1103/PhysRevX.9.031040. arXiv: 1811.12907 [astro-ph.HE].

[3] R. Abbott et al. “GWTC-2: Compact Binary Coalescences Observed by LIGO and Virgo during the First Half of the Third Observing Run”. In: *Physical Review X* 11.2, 021053 (Apr. 2021), p. 021053. DOI: 10.1103/PhysRevX.11.021053. arXiv: 2010.14527 [gr-qc].

[4] Simone S. Bavera et al. “The origin of spin in binary black holes. Predicting the distributions of the main observables of Advanced LIGO”. In: *Astronomy & Astrophysics* 635, A97 (Mar. 2020), A97. DOI: 10.1051/0004-6361/201936204. arXiv: 1906.12257 [astro-ph.HE].

[5] P. G. Beck et al. “Fast core rotation in red-giant stars as revealed by gravity-dominated mixed modes”. In: *Nature* 481 (Jan. 2012), pp. 55–57. DOI: 10.1038/nature10612. arXiv: 1112.2825 [astro-ph.SR].

[6] K. Belczynski, C. Done, and J. -P. Lasota. “All Apples: Comparing black holes in X-ray binaries and gravitational-wave sources”. In: *arXiv e-prints* (Nov. 2021), arXiv:2111.09401. arXiv: 2111.09401 [astro-ph.HE].

[7] K. Belczynski et al. “Evolutionary roads leading to low effective spins, high black hole masses, and O1/O2 rates for LIGO/Virgo binary black holes”. In: *Astronomy & Astrophysics* 636, A104 (Apr. 2020), A104. DOI: 10.1051/0004-6361/201936528. arXiv: 1706.07053 [astro-ph.HE].

[8] S. Deheuvels et al. “Seismic constraints on the radial dependence of the internal rotation profiles of six Kepler subgiants and young red giants”. In: *Astronomy & Astrophysics* 564, A27 (Apr. 2014), A27. DOI: 10.1051/0004-6361/201322779. arXiv: 1401.3096 [astro-ph.SR].

[9] S. Deheuvels et al. “Seismic evidence for a weak radial differential rotation in intermediate-mass core helium burning stars”. In: *Astronomy & Astrophysics* 580, A96 (Aug. 2015), A96. DOI: 10.1051/0004-6361/201526449. arXiv: 1506.02704 [astro-ph.SR].

[10] R. G. Detmers et al. “Gamma-ray bursts from tidally spun-up Wolf-Rayet stars?” In: *Astronomy & Astrophysics* 484.3 (June 2008), pp. 831–839. DOI: 10.1051/0004-6361:200809371. arXiv: 0804.0014 [astro-ph].

[11] P. Eggenberger et al. “Asteroseismology of evolved stars to constrain the internal transport of angular momentum. II. Test of a revised prescription for transport by the Tayler instability”. In: *Astronomy & Astrophysics* 631, L6 (Nov. 2019), p. L6. DOI: 10.1051/0004-6361/201936348. arXiv: 2001.11525 [astro-ph.SR].

[12] Maya Fishbach and Vicky Kalogera. "Apples and Oranges: Comparing Black Holes in X-Ray Binaries and Gravitational-wave Sources". In: *The Astrophysical Journal Letters* 929.2, L26 (Apr. 2022), p. L26. DOI: 10.3847/2041-8213/ac64a5. arXiv: 2111.02935 [astro-ph.HE].

[13] J. Fuller. "Heartbeat stars, tidally excited oscillations and resonance locking". In: *Monthly Notices of the Royal Astronomical Society* 472 (Dec. 2017), pp. 1538–1564. DOI: 10.1093/mnras/stx2135. arXiv: 1706.05054 [astro-ph.SR].

[14] J. Fuller. "Saturn ring seismology: Evidence for stable stratification in the deep interior of Saturn". In: *Icarus* 242 (Nov. 2014), pp. 283–296. DOI: 10.1016/j.icarus.2014.08.006. arXiv: 1406.3343 [astro-ph.EP].

[15] Jim Fuller and Wenbin Lu. "The spins of compact objects born from helium stars in binary systems". In: *Monthly Notices of the Royal Astronomical Society* 511.3 (Apr. 2022), pp. 3951–3964. DOI: 10.1093/mnras/stac317. arXiv: 2201.08407 [astro-ph.HE].

[16] Jim Fuller and Linhao Ma. "Most Black Holes Are Born Very Slowly Rotating". In: *The Astrophysical Journal Letters* 881.1, L1 (Aug. 2019), p. L1. DOI: 10.3847/2041-8213/ab339b. arXiv: 1907.03714 [astro-ph.SR].

[17] Jim Fuller, Anthony L. Piro, and Adam S. Jermyn. "Slowing the spins of stellar cores". In: *Monthly Notices of the Royal Astronomical Society* 485.3 (May 2019), pp. 3661–3680. DOI: 10.1093/mnras/stz514. arXiv: 1902.08227 [astro-ph.SR].

[18] C. Gehan et al. "Core rotation braking on the red giant branch for various mass ranges". In: *Astronomy & Astrophysics* 616, A24 (Aug. 2018), A24. DOI: 10.1051/0004-6361/201832822. arXiv: 1802.04558 [astro-ph.SR].

[19] Wolfgang Glatzel and Hans Oliver Kaltschmidt. "The non-radial stability of Wolf-Rayet stars". In: *Monthly Notices of the Royal Astronomical Society* 337.2 (Dec. 2002), pp. 743–748. DOI: 10.1046/j.1365-8711.2002.05965.x.

[20] P. Goldreich and P. D. Nicholson. "Tidal friction in early-type stars". In: *The Astrophysical Journal* 342 (July 1989), pp. 1079–1084. DOI: 10.1086/167665.

[21] J. Goldstein and R. H. D. Townsend. "The Contour Method: a New Approach to Finding Modes of Nonadiabatic Stellar Pulsations". In: *The Astrophysical Journal* 899.2, 116 (Aug. 2020), p. 116. DOI: 10.3847/1538-4357/aba748. arXiv: 2006.13223 [astro-ph.SR].

[22] Zhao Guo, Gordon I. Ogilvie, and Adrian J. Barker. "Tidally excited gravity waves in the cores of solar-type stars: resonances and critical-layer formation". In: *Monthly Notices of the Royal Astronomical Society* 521.1 (May

2023), pp. 1353–1373. doi: 10.1093/mnras/stad569. arXiv: 2210.12880 [astro-ph.SR].

[23] Pawan Kumar and Jeremy Goodman. "Nonlinear Damping of Oscillations in Tidal-Capture Binaries". In: *The Astrophysical Journal* 466 (Aug. 1996), p. 946. doi: 10.1086/177565. arXiv: astro-ph/9509112 [astro-ph].

[24] Doron Kushnir et al. "Dynamical tides reexpressed". In: *Monthly Notices of the Royal Astronomical Society* 467.2 (May 2017), pp. 2146–2149. doi: 10.1093/mnras/stx255. arXiv: 1605.03810 [astro-ph.SR].

[25] Linhao Ma and Jim Fuller. "Angular momentum transport in massive stars and natal neutron star rotation rates". In: *Monthly Notices of the Royal Astronomical Society* 488.3 (Sept. 2019), pp. 4338–4355. doi: 10.1093/mnras/stz2009. arXiv: 1907.03713 [astro-ph.SR].

[26] Linhao Ma and Jim Fuller. "Orbital Decay of Short-period Exoplanets via Tidal Resonance Locking". In: *The Astrophysical Journal* 918.1, 16 (Sept. 2021), p. 16. doi: 10.3847/1538-4357/ac088e. arXiv: 2105.09335 [astro-ph.EP].

[27] M. Coleman Miller and Jon M. Miller. "The masses and spins of neutron stars and stellar-mass black holes". In: *Physics Reports* 548 (Jan. 2015), pp. 1–34. doi: 10.1016/j.physrep.2014.09.003. arXiv: 1408.4145 [astro-ph.HE].

[28] Simona Miller, Thomas A. Callister, and Will M. Farr. "The Low Effective Spin of Binary Black Holes and Implications for Individual Gravitational-wave Events". In: *The Astrophysical Journal* 895.2, 128 (June 2020), p. 128. doi: 10.3847/1538-4357/ab80c0. arXiv: 2001.06051 [astro-ph.HE].

[29] B. Mosser et al. "Spin down of the core rotation in red giants". In: *Astronomy & Astrophysics* 548, A10 (Dec. 2012), A10. doi: 10.1051/0004-6361/201220106. arXiv: 1209.3336 [astro-ph.SR].

[30] T. Nugis and H. J. G. L. M. Lamers. "Mass-loss rates of Wolf-Rayet stars as a function of stellar parameters". In: *Astronomy & Astrophysics* 360 (Aug. 2000), pp. 227–244.

[31] A. Olejak and K. Belczynski. "The Implications of High Black Hole Spins for the Origin of Binary Black Hole Mergers". In: *The Astrophysical Journal Letters* 921.1, L2 (Nov. 2021), p. L2. doi: 10.3847/2041-8213/ac2f48. arXiv: 2109.06872 [astro-ph.HE].

[32] B. Paxton et al. "Modules for Experiments in Stellar Astrophysics (MESA)". In: *The Astrophysical Journal Supplement Series* 192, 3 (Jan. 2011), p. 3. doi: 10.1088/0067-0049/192/1/3. arXiv: 1009.1622 [astro-ph.SR].

[33] B. Paxton et al. “Modules for Experiments in Stellar Astrophysics (MESA): Binaries, Pulsations, and Explosions”. In: *The Astrophysical Journal Supplement Series* 220, 15 (Sept. 2015), p. 15. DOI: 10.1088/0067-0049/220/1/15. arXiv: 1506.03146 [astro-ph.SR].

[34] B. Paxton et al. “Modules for Experiments in Stellar Astrophysics (MESA): Planets, Oscillations, Rotation, and Massive Stars”. In: *The Astrophysical Journal Supplement Series* 208, 4 (Sept. 2013), p. 4. DOI: 10.1088/0067-0049/208/1/4. arXiv: 1301.0319 [astro-ph.SR].

[35] Bill Paxton et al. “Modules for Experiments in Stellar Astrophysics (MESA): Convective Boundaries, Element Diffusion, and Massive Star Explosions”. In: *The Astrophysical Journal Supplement Series* 234.2, 34 (Feb. 2018), p. 34. DOI: 10.3847/1538-4365/aaa5a8. arXiv: 1710.08424 [astro-ph.SR].

[36] Bill Paxton et al. “Modules for Experiments in Stellar Astrophysics (MESA): Pulsating Variable Stars, Rotation, Convective Boundaries, and Energy Conservation”. In: *The Astrophysical Journal Supplement Series* 243.1, 10 (July 2019), p. 10. DOI: 10.3847/1538-4365/ab2241. arXiv: 1903.01426 [astro-ph.SR].

[37] P. C. Peters. “Gravitational Radiation and the Motion of Two Point Masses”. In: *Physical Review* 136.4B (Nov. 1964), pp. 1224–1232. DOI: 10.1103/PhysRev.136.B1224.

[38] Y. Qin et al. “The spin of the second-born black hole in coalescing binary black holes”. In: *Astronomy & Astrophysics* 616, A28 (Aug. 2018), A28. DOI: 10.1051/0004-6361/201832839. arXiv: 1802.05738 [astro-ph.SR].

[39] Ying Qin et al. “On the Origin of Black Hole Spin in High-mass X-Ray Binaries”. In: *The Astrophysical Journal Letters* 870.2, L18 (Jan. 2019), p. L18. DOI: 10.3847/2041-8213/aaf97b. arXiv: 1810.13016 [astro-ph.SR].

[40] Stephen Ro. “The Wolf-Rayet Stellar Response To The Iron Opacity Bump: Envelope Inflation, Winds, and Microturbulence”. In: *The Astrophysical Journal* 873.1, 76 (Mar. 2019), p. 76. DOI: 10.3847/1538-4357/ab0421. arXiv: 1904.01703 [astro-ph.SR].

[41] Stephen Ro and Christopher D. Matzner. “On the Launching and Structure of Radiatively Driven Winds in Wolf-Rayet Stars”. In: *The Astrophysical Journal* 821.2, 109 (Apr. 2016), p. 109. DOI: 10.3847/0004-637X/821/2/109. arXiv: 1602.07318 [astro-ph.SR].

[42] Javier Roulet et al. “Distribution of effective spins and masses of binary black holes from the LIGO and Virgo O1-O3a observing runs”. In: *Physical Review D* 104.8, 083010 (Oct. 2021), p. 083010. DOI: 10.1103/PhysRevD.104.083010. arXiv: 2105.10580 [astro-ph.HE].

[43] Mohammadtaher Safarzadeh, Will M. Farr, and Enrico Ramirez-Ruiz. "A Trend in the Effective Spin Distribution of LIGO Binary Black Holes with Mass". In: *The Astrophysical Journal* 894.2, 129 (May 2020), p. 129. DOI: 10.3847/1538-4357/ab80be. arXiv: 2001.06490 [gr-qc].

[44] Andreas A. C. Sander and Jorick S. Vink. "On the nature of massive helium star winds and Wolf-Rayet-type mass-loss". In: *Monthly Notices of the Royal Astronomical Society* 499.1 (Nov. 2020), pp. 873–892. DOI: 10.1093/mnras/staa2712. arXiv: 2009.01849 [astro-ph.SR].

[45] H. C. Spruit. "Dynamo action by differential rotation in a stably stratified stellar interior". In: *Astronomy & Astrophysics* 381 (Jan. 2002), pp. 923–932. DOI: 10.1051/0004-6361:20011465. arXiv: astro-ph/0108207 [astro-ph].

[46] Yubo Su, Daniel Lecoanet, and Dong Lai. "Physics of tidal dissipation in early-type stars and white dwarfs: hydrodynamical simulations of internal gravity wave breaking in stellar envelopes". In: *Monthly Notices of the Royal Astronomical Society* 495.1 (June 2020), pp. 1239–1251. DOI: 10.1093/mnras/staa1306. arXiv: 2002.11118 [astro-ph.SR].

[47] Meng Sun, R. H. D. Townsend, and Zhao Guo. "gyre_tides: Modeling Binary Tides within the GYRE Stellar Oscillation Code". In: *The Astrophysical Journal* 945.1, 43 (Mar. 2023), p. 43. DOI: 10.3847/1538-4357/acb33a. arXiv: 2301.06599 [astro-ph.SR].

[48] Masao Takata. "Analysis of Adiabatic Dipolar Oscillations of Stars". In: *Publications of the Astronomical Society of Japan* 58 (Oct. 2006), pp. 893–908. DOI: 10.1093/pasj/58.5.893.

[49] R. H. D. Townsend, J. Goldstein, and E. G. Zweibel. "Angular momentum transport by heat-driven g-modes in slowly pulsating B stars". In: *Monthly Notices of the Royal Astronomical Society* 475.1 (Mar. 2018), pp. 879–893. DOI: 10.1093/mnras/stx3142. arXiv: 1712.02420 [astro-ph.SR].

[50] R. H. D. Townsend and S. A. Teitler. "GYRE: an open-source stellar oscillation code based on a new Magnus Multiple Shooting scheme". In: *Monthly Notices of the Royal Astronomical Society* 435.4 (Nov. 2013), pp. 3406–3418. DOI: 10.1093/mnras/stt1533. arXiv: 1308.2965 [astro-ph.SR].

[51] S. A. Triana et al. "Internal rotation of 13 low-mass low-luminosity red giants in the Kepler field". In: *Astronomy & Astrophysics* 602, A62 (June 2017), A62. DOI: 10.1051/0004-6361/201629186. arXiv: 1702.07910 [astro-ph.SR].

[52] Jorick S. Vink. "Theory and Diagnostics of Hot Star Mass Loss". In: *Annual Review of Astronomy and Astrophysics* 60 (Aug. 2022), pp. 203–246. DOI: 10.1146/annurev-astro-052920-094949. arXiv: 2109.08164 [astro-ph.SR].

[53] M. G. Witte and G. J. Savonije. “Tidal evolution of eccentric orbits in massive binary systems. A study of resonance locking”. In: *Astronomy & Astrophysics* 350 (Oct. 1999), pp. 129–147. eprint: astro-ph/9909073.

[54] Hang Yu, Nevin N. Weinberg, and Jim Fuller. “Non-linear dynamical tides in white dwarf binaries”. In: *Monthly Notices of the Royal Astronomical Society* 496.4 (Aug. 2020), pp. 5482–5502. DOI: 10.1093/mnras/staa1858. arXiv: 2005.03058 [astro-ph.SR].

[55] J.-P. Zahn. “The dynamical tide in close binaries”. In: *Astronomy & Astrophysics* 41 (July 1975), pp. 329–344.

[56] J.-P. Zahn. “Tidal friction in close binary stars”. In: *Astronomy & Astrophysics* 57 (May 1977), pp. 383–394.

[57] Matias Zaldarriaga, Doron Kushnir, and Juna A. Kollmeier. “The expected spins of gravitational wave sources with isolated field binary progenitors”. In: *Monthly Notices of the Royal Astronomical Society* 473.3 (Jan. 2018), pp. 4174–4178. DOI: 10.1093/mnras/stx2577. arXiv: 1702.00885 [astro-ph.HE].

[58] Michael Zevin et al. “One Channel to Rule Them All? Constraining the Origins of Binary Black Holes Using Multiple Formation Pathways”. In: *The Astrophysical Journal* 910.2, 152 (Apr. 2021), p. 152. DOI: 10.3847/1538-4357/abe40e. arXiv: 2011.10057 [astro-ph.HE].

Chapter 7

SUMMARY

In this thesis, I study the physical processes of dynamical friction and tidal dissipation, and investigated how they will affect the dynamics of stars, planets, and black holes.

I derive a new discrete expression for the dynamical friction force. This formula is specifically designed for application to numerical simulations, either in post-processing, or "on the fly" when the dynamical friction forces cannot be resolved. I develop a new discrete dynamical friction estimator based on this formula, which is directly implementable into N-body simulations.

The formula I derived has a large number of advantages compared to the traditional Chandrasekhar's analytic expression, which is often used for sub-grid dynamical friction modeling. These advantages include: (1) it allows for an arbitrary distribution function, without requiring an infinite homogeneous time-invariant medium with constant density, Maxwellian velocity distribution, etc.; (2) it is designed specifically for simulations so it is represented only as a sum over quantities which are always well-defined in the simulation for all N-body particles (e.g. positions, velocities, masses), and does not require the expensive and fundamentally ill-defined evaluation of quantities like density, background mean velocity/dispersion/distribution function, Coulomb logarithm, etc.; (3) it trivially incorporates force softening exactly consistent with how it is treated in-code, and generalizes to arbitrary multi-component N-body simulations with different species and an arbitrary range of particle masses; (4) it manifestly conserves total momentum, unlike N-body implementations of Chandrasekhar's formula; (5) it can be evaluated directly alongside the normal gravitational forces with negligible cost, and automatically inherits all of the desired convergence and accuracy properties of the N-body solver.

I implemented the dynamical friction estimator in GIZMO, and verified that it agrees well with the N-body simulations, and that the computational overhead of evaluating it alongside gravity in the tree is immeasurably small.

There are still uncertainties in this work. In the derivation of the discrete formula, an approximate integral kernel is inserted, which is not necessarily unique or best-behaved. I found that even if the discrete estimator closely agrees with the calibrated-Chandrasekhar dynamical friction estimator in the test problems, it still differs from the the high-resolution simulation results in terms of the detailed particle trajectories, which might be related to the fundamental Chandrasekhar-like assumptions made in the formula. I also note that it remains an open question how to accurately avoid "double counting" when some of the dynamical friction may be captured self-consistently by the N-body code while additional dynamical friction is modeled using the sub-grid model. This is especially the case when the system evolves (such as when a super-massive black hole (SMBH) grow) and the fraction of resolved dynamical friction changes with time.

I study the dynamics of black hole seeds at high-redshift with high-resolution cosmological galaxy formation simulations. This helps to understand their implications for super-massive black hole formation and growth. The simulations and semi-analytic dynamical friction calculations show that black hole seeds cannot efficiently sink to galactic centers or be retained at high redshifts, unless they are extremely massive already ($M > 10^8\,M_\odot$, i.e. already super-massive black holes). I show that this threshold is at least an order-of-magnitude higher than what one would expect in a spherically-symmetric smooth galaxy potential, as commonly adopted in analytic or older simulation calculations which could not resolve the complex, clumpy, time-dependent sub-structure of these galaxies. For smoother galaxies, this mass threshold reduces to $10^7\,M_\odot$, which does not change the key conclusion.

I qualitatively conclude that the chaotic nature of high-redshift galaxies, coupled to the very short Hubble times ($\lesssim 1\,\mathrm{Gyr}$) make it impossible for any lower-mass seeds to efficiently migrate from $\gtrsim 1\,\mathrm{kpc}$ scales to galactic centers at $z > 7$. As the formation models of super-massive black holes often require their seeds to be placed in the galactic center, I hence point out that the non-sinking of them provides a great challenge in explaining the formation and growth of the first SMBHs with masses $\gg 10^9\,M_\odot$ in the centers of the earliest galaxies.

I also show that even the most massive sinking BHs ($\gtrsim 10^8\,M_\odot$) do not sink to the same location at sub-kpc scales, where their migration stalls. This has potentially profound implications for LISA detection of SMBH-SMBH mergers in high-redshift galaxies. I also discuss two possible scenarios which may solve this sinking problem.

The first solution states that seed black holes may form in-situ when the massive bulge finally forms and creates a deep central potential, or a large number of seeds may form so that a small fraction of them may have just the right orbital parameters to be captured by this bulge. However, I show that this deep central potential well does not form until redshift $z \lesssim 9$, from gas and stars which are already highly metal-enriched ($Z \gtrsim 0.1\,Z_{\odot}$). This means popular speculative black hole seed formation channels like Pop III relics or direct collapse from hyper-massive quasi-stars could not provide the origin of the SMBHs. Moreover, stellar-relic black holes, if primarily growing by accretion in these massive bulges that do not exist until $z \lesssim 9$, must grow with sustained highly super-Eddington accretion, which is also a challenge for their accretion mechanisms.

The second solution states that seed black holes may have enormous effective masses when they are trapped in structures like star clusters, so that they can sink early and may remain trapped in the growing galaxy center. However, for $z > 7$ galaxies, the overwhelming majority of the clusters form in-situ in the galaxy as it evolves from in-situ gas, or the massive clusters which formed later. This will limit the time for these seed black holes to grow in these clusters.

I study the orbital decay of short-period exoplanets via tidal resonance locking, where planets fall into resonance with stellar oscillation modes and migrate along with the resonant locations. When resonance locking between planets and stellar gravity (g) modes operates, I find that planetary orbits typically decay on a mode evolution timescale, which is usually similar to the star's main-sequence lifetime. The tidal migration time scale is nearly independent of planet mass and orbital period, such that the effective tidal quality factor Q' decreases toward longer orbital periods and lower-mass planets.

I show that resonance locking can be prevented by nonlinear damping that saturates (or eliminates) resonant mode excitation. Both the stellar structure and the planet mass influence the nonlinearity of the tidally excited g modes. For solar-type host stars with radiative cores, nonlinear effects could become very important near the center of the star, wiping out resonances. Hot Jupiters of $M \gtrsim 0.3\,M_{\mathrm{J}}$ trigger efficient nonlinear dissipation of gravity modes, and more massive planets ($M \gtrsim 3\,M_{\mathrm{J}}$) cause wave breaking. In either case, energy dissipation has a very strong power-law dependence on orbital frequency, with the tidal migration timescale increasing sharply with orbital period. On the other hand, resonance locking can likely operate for planets of any mass that orbit massive host stars with convective cores, which prevent gravity waves from reaching the stellar center.

Based on stellar spin measurements, some studies inferred a strong period dependence of the tidal quality factor Q' of hot Jupiter host stars. If resonance locking occurs in hot Jupiter systems, I show that it produces a remarkably similar power-law dependence of Q', which could provide evidence in favor of resonance locking. However, since nonlinear dissipation likely prevents resonance locking from occurring in these systems, other potential explanations should be explored. I suggest that many moderately rotating hot Jupiter hosts (which were inferred to have been tidally spun up, thereby placing a constraint on Q') are instead simply younger than average. In this scenario, their more rapid rotation stems primarily from their youth, and only a lower limit of Q' can be inferred. Future age constraints for those systems may determine which explanation is more likely.

I apply resonance locking to 15 observed hot Jupiter systems and predict that these systems generally have Q's in the range $10^6 - 10^9$, which is typically $2 - 3$ orders of magnitude higher than observed lower limits. This means their orbital decay will be hard to measure if resonance locking is operating, as expected for stars with convective cores. However, nonlinear damping likely operates in host stars possessing radiative cores, leading to much smaller Q's, like that measured for WASP-12b. Further observations of these systems can thus help to improve the understanding of which tidal process operates.

I examine the long-term orbital evolution of exoplanets, combining theories based on resonance locking and nonlinear dissipation/wave breaking. I predict that hot Jupiters migrate inwards via nonlinear wave damping and are frequently destroyed during the main sequence for solar-type host stars. This may help to explain the finding that hot Jupiter host stars are on average slightly younger than field stars. For hot Neptunes and super-Earths, I predict that resonance locking can operate, driving inward migration on a stellar evolution time scale. This can result in a tidal quality factor of $Q' \lesssim 10^5$, causing much more orbital decay than prior expectations. However, the corresponding quality factor at short orbital periods can exceed $Q' \gtrsim 10^7$, allowing the planets to survive at ultrashort periods for extended lengths of time, consistent with the observed old ages of ultrashort-period planet hosts.

Since nonlinear dissipation occurs for massive planets orbiting stars with radiative cores, I predict a sharp decline in the population of short-period ($P_{\rm orb} \lesssim 2\,$days) hot Jupiters orbiting solar-type host stars. I predict a more gradual decline for low-mass planets and host stars with convective cores, where resonance locking is at work, producing a much smoother distribution with orbital period. Future observations will help test this prediction, provided that effects of tidal migration can be distinguished from the birth-period distribution.

I investigate the tidal spin-up of close-in subdwarf B (sdB) binaries. I consider the dissipation of tidally excited gravity waves in the envelopes of sdB stars, and calculate the tidal torques by directly computing the amplitudes of tidally driven oscillation modes in sdB stellar models. I integrate the coupled spin-orbit evolution of these binaries and calculated the resulting sdB rotation rates.

I show that in contrast to the usual assumption that gravity waves are efficiently damped near the surface ("Zahn's traveling wave limit"), these waves can actually be less damped, and can reflect back to form standing waves in the radiative envelope of sdB stars. The resulting tidal torque is then significantly less than Zahn's theory predicted, and has a complicated resonant dependence on the frequency of the tidal force. At longer periods, the waves are more highly damped and the tidal torque approaches Zahn's limit.

For binaries containing a 0.47 $M_\odot$ canonical sdB, my models predict the system will be tidally synchronized if the orbit is less than ~ 0.2 days. For those with a 0.37 $M_\odot$ low-mass sdB, this tidal synchronization period becomes ~ 0.15 days. These values are very similar to the observed spin rates of sdB binaries, which are tidally synchronized at orbital periods less than ~ 0.2 days. The tidal synchronization timescale has weak dependence on the companion star mass, and is mostly determined by the orbital period.

I investigate how the amount of hydrogen in the sdB envelope could affect the strength of the tidal torque. Since sdBs with more hydrogen have larger radii, and the tidal torque magnitude could scale with the stellar radius as $\tau \propto R^6$, tidal torques may be stronger for stars with more hydrogen. However, the existence of unstable oscillations for the sdB models with thicker hydrogen envelopes complicate the calculation of tidal torques.

I point out that resonance locking cannot happen in the tidal spin-up phase of sdB binaries, and discussed the limitations of the mode decomposition method to calculate tidal torques. Differential rotation and rotational effects on oscillation may also be important. Future works should investigate the above scenarios, and compare to growing numbers of rotation rate measurements for sdBs in close binaries.

I also investigate the dynamical tidal spin-up of Wolf–Rayet stars from black hole companions. I build Wolf–Rayet star models with different metallicities, and then calculate their oscillation mode frequencies, damping rates, and eigenfunctions. I use these results to integrate the coupled spin–orbit evolution of the binary based on the tidal excitation of these oscillation modes. I also make predictions for the resulting BH spins upon core-collapse of the Wolf–Rayet star.

I study the properties of the oscillation modes and find that at shorter orbital period, the tidal forcing is mostly contributed by standing g-modes, in contrast to the usual assumption of travelling waves proposed by Zahn. The standing g-mode spectra contributes a resonance structure, and during most of the spin–orbit evolution phase, the tidal response lies between resonances and the interaction strength is weaker than Zahn's prediction. The tidal forcing transits to Zahn's travelling wave limit at longer periods, in which Zahn's estimate is more accurate. However, the specific transition frequency depends on the stellar masses, and the structure for more massive stars (supported significantly by radiation pressure) tend to have lower transition frequencies, allowing systems in longer-period orbits to evolve differently compared to Zahn's prediction.

I find that it is difficult to tidally synchronize Wolf–Rayet stars during helium-burning. For solar-metallicity Wolf–Rayet stars, strong winds tend to remove the majority of angular momentum deposited by tides, leaving slowly spinning stars and black holes. At low metallicity, the stellar wind is weaker and the stars are significantly tidally spun up, yet still less than Zahn's prediction, especially for massive stars and short-period orbits.

I show that tidal interactions can significantly spin up the resulting BHs compared to single-star models. Yet the predicted black hole spins a are still $\lesssim 0.4$ for all but the shortest period ($P_{\rm orb} \lesssim 0.5\,{\rm d}$) models. These predictions are consistent with some low/moderate-spin measurements from LIGO/Virgo black hole merger events, but cannot explain high-spin X-ray binaries events since only the second-born black hole has large spin in these models.